ÉNERGIE MATÉRIAUX TÉLÉCOMMUNICATIONS

PHOTONICS-BASED TIME-FREQUENCY ANALYSIS AND PROCESSING OF HIGH-SPEED ELECTROMAGNETIC WAVES

Par

Xinyi Zhu

Thèse présentée pour l'obtention du grade de
Philosophiae Doctor (Ph.D.)
en Télécommunication

Jury d'évaluation

Président du jury et examinateur interne	Tarek Djerafi INRS-EMT, Montreal, Canada
Examinateur externe	Hossein Asghari Loyola Marymount University
Examinateur externe	François Blanchard École de technologie supérieure
Directeur de recherche	José Azaña INRS-EMT, Montreal, Canada

REMERCIEMENTS

Pursuing my Ph.D. at the Institut National de la Recherche Scientifique (INRS) in Montreal has been an incredible journey, enriched by the unique experiences of living in this beautiful, diverse, and romantic city. The opportunity to immerse myself in a different culture has been profoundly rewarding, and I have come to love Montreal for its distinctive charm and vibrant community.

First and foremost, I would like to express my deepest gratitude to my supervisor, Prof. José Azaña, who gave me the opportunity to work in his group. His invaluable help, guidance, and mentorship have been important throughout my doctoral research. Professor Azaña granted me the freedom to explore my ideas and pursue my research interests, always providing me with the time and resources to learn and understand. His unique blend of visionary thinking and contemporary relevance, coupled with a balanced approach to both theoretical and practical aspects of research, has greatly enriched my academic experience. Working with him has been a unique and rewarding experience, and I am profoundly grateful for his unwavering support. His patience in explaining every aspect of our research, no matter how straightforward the question, has been particularly beneficial. His encouragement and support have given me the confidence to persist in my research endeavors. I am particularly thankful for the opportunities and encourage from Prof. José Azaña to attend numerous international conferences. These experiences have significantly boosted my confidence, allowed me to establish a professional network, and broadened my understanding of various research areas. Moreover, Prof. Azaña has not only supported my research work but also generously shared his experiences and provided assistance to make my daily life smoother.

I would like to express my deepest appreciation to my boyfriend, Hao Sun. We came to Montreal together to pursue our Ph.D. studies. We are exploring this beautiful and romantic city together while embracing a new culture has been an incredibly enriching experience. His constant companionship and encouragement have been a source of strength throughout this journey. Hao has stood by my side through all the highs and lows, providing unwavering emotional support and motivation. His tolerance, understanding, and comforting presence have been pillars of support, especially during challenging times like the COVID-19 pandemic. Thank you, Hao, for your unwavering support and for making this journey so much more meaningful and unforgettable. Your love and encouragement have been essential to my life, and I am deeply grateful for everything you have done for me.

In addition, I thank the group members: Dr. Luis Romero Cortes, Dr. Reza Maram, Dr. Saikrishna Reddy Konatham, Dr. Xiaozhou Li, Dr. Saket Kaushal, Benjamin Crockett, Afsaneh Shoeib, Majid Goodarzi, and Geunweon Lim, who have enriched my time in Montreal. Especially, I would like to thanks Benjamin Crockett who provide improtant help with the French summary of my thesis.

I would also like to express my gratitude to the core committee for my Ph.D thesis: Prof. Tarek Djerafi, Prof. Hossein Asghari, and Prof. François Blanchard. Thank you for your time and efforts in reviewing and evaluation of my thesis.

I also wish to acknowledge my whole family and my best friends, Chenlu Gao and Wei Qiu, for their unconditional love and support. Even from afar, their encouragement has been a constant source of inspiration and motivation, reminding me of the importance of perseverance and dedication.

RÉSUMÉ

MÉTHODES PHOTONIQUES POUR L’ANALYSE TEMPS-FRÉQUENCE ET LE TRAITEMENT DES ONDES ÉLECTROMAGNÉTIQUES À HAUTE VITESSE

L'analyse et le traitement temps-fréquence (T-F) d'une onde électromagnétique (EM), allant des micro-ondes au domaine optique, sont indispensable dans divers domaines. La distribution T-F d'un signal révèle l’évoluent dans le temps, cruciale pour caractériser les signaux non stationnaires et décrire les états des canaux de télécommunication et les cibles en détection. Manipuler l'évolution temporelle des composantes spectrales d'une onde électro-magnétiques (EM) est critique pour résoudre de nombreux problèmes scientifiques et techniques, comme la sélection de canaux, la réduction du bruit/interférences et l'amélioration de l'efficacité spectrale.

Les applications pratiques, incluant les systèmes de télécommunication de nouvelle génération et les plateformes Radar/Lidar, exigent une analyse T-F en temps réel de signaux dynamiques à haute vitesse (jusqu'à plusieurs dizaines de GHz de bande passante) avec une flexibilité définie par l'utilisateur. Réaliser une analyse spectrale et un traitement en temps réel avec ces spécifications reste un défi.

Dans cette thèse, je développe une méthode pour analyser et manipuler les propriétés T-F des ondes EM adaptée aux signaux à haute vitesse. J'introduis l'équivalence entre la modulation par lentille temporelle et la propagation par dispersion du second ordre, offrant ainsi un aperçu de la relation temps-fréquence entre ces deux concepts. Sur cette base, je propose une architecture photonique pour un analyseur temps-fréquence, utilisant la modulation de phase temporelle et un milieu dispersif. Cette méthode permet de capturer le spectrogramme du signal entrant directement dans le domaine temporel, offrant un accès en temps réel à l’évolution des composantes spectrales du signal large bande. Cela est démontré avec les spécifications pratiques requises, permettant l'analyse des signaux à haute vitesse sur une bande passante complète approchant 100 GHz, incluant la capacité d'intercepter des signaux rapides aléatoires, avec une résolution temporelle de la nanoseconde et une résolution fréquentielle de l'ordre du MHz.

Le spectrogramme cartographié dans le temps permet une manipulation via des techniques de modulation temporelle disponibles. Comme le spectre dynamique du signal est raporté le long du domaine temporel, on peut manipuler directement les composantes spectrales dynamiques en utilisant ces méthodes. Les opérations de cartographie temporelle peuvent être inversées pour reconstruire le signal traité T-F. En utilisant des composants de télécommunication disponibles, je démontre un contrôle arbitraire de la distribution T-F des signaux à haute vitesse programmable à l'échelle de la nanoseconde. Cette méthode représente une avancée significative dans la manipulation des propriétés T-F des ondes EM, répondant aux exigences strictes de nombreuses applications modernes et émergentes.

Mots-clés: transformation de Fourier à court terme (STFT), analyse spectrale en temps réel, filtre photonique à micro-ondes, traitement du signal, dispersion de la vitesse de groupe, lentille temporelle.

ABSTRACT

Time-frequency (T-F) analysis and processing of electromagnetic (EM) waves, ranging from the microwave to optical domains, are desired for various fields. The joint T-F distribution of a signal gives key information on how the frequency components change over time, providing a powerful tool to characterize non-stationary signals. This is essential for a wide range of fields, for instance to describe the states of telecommunication channels or target information in sensing. Moreover, manipulating the temporal evolution of an EM wave's frequency components is crucial for solving many scientific and engineering problems. The capability of processing at will non-stationary signals is essential for channel selection, noise/interference mitigation, and improving spectral efficiency in communication and sensing systems. Practical applications, including next-generation telecommunication systems, Radar/Lidar platforms, require real-time T-F analysis and processing of dynamic signals at high speeds (up to tens of GHz bandwidth) with user-defined versatility. Achieving real-time spectral analysis and processing with these specifications remains challenging.

In this thesis, I develop a method for analyzing and manipulating the T-F properties of arbitrary EM waves, suited for high-speed signals. I firstly introduce the equivalence between time-lens modulation and second-order dispersion propagation, providing insight into the time-frequency relationship between these two units. Based on this, I propose a photonic-based architecture for a time-frequency analyzer, using temporal phase modulation and dispersive medium. This method enables capturing the spectrogram of the incoming signal directly in the temporal domain, providing real-time access to the evolving frequency spectrum of the input broadband signal. This is demonstrated with the practical required specifications, i.e., enabling high-speed signals analysis over a full bandwidth approaching 100 GHz, including the capability of intercepting random fast signals, with nanosecond time resolution and MHz-level frequency resolution.

The time-mapped spectrogram paves the way for user-defined manipulation via widely-available temporal modulation techniques. As the dynamic spectrum of the signal is consecutively mapped along the time domain, one can directly manipulate the time-varying frequency contents using available temporal modulation methods. The time-mapping operations can then be inverted to reconstruct the T-F-processed signal. Using off-the-shelf telecommunication components, I demonstrate arbitrary control of the T-F distribution of high-speed signals with nanosecond-scale programmability. This scheme is further applied for mitigating rapidly changing frequency interference and the direct synthesis of fast waveforms with customized T-F distributions. The method represents a significant advancement in manipulating the T-F properties of EM waves and it fulfils the stringent requirements for many modern and emerging applications.

Keywords: Short-time Fourier transform (STFT), real-time spectral analysis, microwave photonic filter, signal processing, group-velocity dispersion, time lens.

SOMMAIRE RÉCAPITULATIF

01. INTRODUCTION

La connaissance précise des caractéristiques spectrales évolutives d'une forme d'onde est fondamentale pour un large éventail de domaines, y compris la photonique micro-ondes, les technologies Radar/Lidar, les télécommunications et la biomédecine [1], [2], [3], [4], [5]. Pour obtenir la représentation la plus complète d'un signal d'intérêt, l'analyse doit généralement être effectuée en temps réel et sans aucune interruption dans l'acquisition et le traitement du signal. Cela correspond effectivement à mesurer la représentation conjointe temps-fréquence (T-F) ou le spectrogramme (SP) [5], [6], [7], [8], [9], [10], de sorte que les caractéristiques spectrales du signal testé (*Signal under test,* SUT) sont analysées sur des échelles de temps compatibles avec la bande passante de la forme d'onde analysée. Les techniques d'analyse spectrale de Fourier en temps réel (*Real-time spectral analysis,* RT-SA) sont nécessaires lorsque l'accès aux informations spectrales dynamiquement changeantes d'un signal entrant non stationnaire est requis. Cette technique est particulièrement importante dans les applications où une compréhension immédiate du contenu spectral du signal est nécessaire et est largement utilisée pour l'analyse d'une grande variété de signaux rencontrés dans de nombreux problèmes scientifiques et d'ingénierie. De plus, les techniques RT-SA sont des outils indispensables pour étudier et capturer le signal d'intérêt en une seule prise avec une faible latence. Pour analyser efficacement ces signaux dynamiques, l'analyse spectrale doit être effectuée de manière continue, en temps réel et sans interruption. Une autre exigence clé pour de nombreuses applications est que le spectre doit également être capturé avec une définition spectrale suffisamment élevée, correspondant à une résolution de fréquence fine. Pourtant, il demeure très difficile de capturer le spectrogramme complet des ondes électromagnétiques sur une large bande passante d'analyse (par exemple, dans la gamme des dizaines de GHz et au-delà) tout en conservant une résolution de fréquence élevée (par exemple, jusqu'au régime du MHz). Dans le cas des signaux radio et micro-ondes, les solutions les plus courantes reposent sur le post-traitement numérique électronique pour implémenter plusieurs algorithmes de transformée de Fourier rapide (*Fast Fourier transform,* FFT). Bien qu'elles puissent facilement accéder à des résolutions de fréquence jusqu'au régime du kHz, la bande passante instantanée d'exploitation (ou la plage de fréquences) de cette technique reste limitée à quelques centaines de MHz [11]. D'autre part, le traitement analogique photonique peut surmonter la limitation de la bande passante d'analyse des méthodes basées sur l'électronique [6], [7], [8], [9], [10], [12], [13], [14], [15], mais au prix d'une résolution temporelle ou fréquentielle considérablement réduite. Ainsi, l'analyse et le traitement spectral en temps réel avec ces spécifications restent encore difficiles. Dans cette thèse, nous nous intéressons particulièrement à la RT-SA des signaux avec des bandes passantes instantanées supérieures à la gamme des GHz. Les formes d'onde à bande passante GHz se trouvent le plus souvent dans le spectre électromagnétique allant des micro-ondes au domaine optique, incluant également les ondes millimétriques et THz [16]. De nombreuses tâches importantes nécessitent la RT-SA de ces formes d'onde temporelles à haute vitesse, y compris les communications à large bande [17], les plateformes radar [18], la caractérisation ultra-rapide, la détection et la spectroscopie, et la recherche en radioastronomie [19], etc. Ces applications pratiques nécessitent une RT-SA effectuée de manière continue et sans interruption, avec un ensemble de spécifications répondant aux exigences pratiques, y compris des bandes passantes instantanées bien supérieures à la gamme des GHz, avec des résolutions temporelles de l'ordre de la nanoseconde ou même plus courtes, et avec des résolutions fréquentielles fines jusqu'au niveau du MHz.

D'autre part, la manipulation linéaire complète de la distribution T-F conjointe d'un signal entrant donné devient de plus en plus importante dans de nombreuses applications modernes et émergentes, y compris les systèmes de télécommunications de prochaine génération [17], [20] et les plateformes de détection à distance intelligentes (Radar et Lidar) [4], [18], [21]. Par exemple, pour améliorer l'efficacité spectrale des systèmes de communication modernes, des schémas de radio cognitive et optiques sont de plus en plus utilisés [22], [23], nécessitant des architectures définies par logiciel qui permettent une allocation et un contrôle dynamiques du spectre. Des stratégies de codage sophistiquées sont également nécessaires, où les informations souhaitées sont encodées le long des variations conjointes T-F de l'onde de manière rapidement adaptable, comme dans le cas des systèmes de saut de fréquence ultrarapides [24]. Les systèmes radar fonctionnent souvent dans des environnements dynamiques et difficiles où une manipulation reconfigurable du spectre de fréquence des ondes capturées est fortement souhaitée pour améliorer les performances, la polyvalence et l'adaptabilité [4], [25]. Dans ces applications, les opérations de traitement des ondes requises peuvent inclure la sélection ou la désélection d'un ensemble de bandes de fréquences [26], le filtrage de certaines interférences ou composants indésirables de type bruit provenant de l'onde entrante [27], ou d'autres manipulations plus sophistiquées sur le spectre complexe de l'onde [28]. La caractéristique clé est que ces opérations de filtrage dédiées doivent être reconfigurées à une très grande vitesse, à l'échelle de la nanoseconde ou même plus rapide [28], [29], tout en offrant un ensemble de spécifications conformes aux performances cibles, y compris une opération sur des bandes passantes larges et avec les résolutions temporelles et fréquentielles nécessaires [30].

Pour réaliser une manipulation temps-fréquence définie par l'utilisateur, un filtre linéaire est requis, dans lequel on peut programmer et reconfigurer la réponse spectrale du filtre de manière arbitraire, définie par l'utilisateur, et à une vitesse aussi rapide que la résolution de fréquence offerte par le filtre [31]. Le filtrage T-F conjoint arbitraire peut être facilement implémenté en utilisant le traitement numérique du signal (DSP). Cependant, cela nécessite la détection et la numérisation du profil d'onde complexe, suivies de la conversion du profil numérique traité en une onde analogique. De plus, pour une manipulation d'onde en temps réel, cette procédure est très difficile lorsque les variations de l'onde sont plus rapides que quelques centaines de MHz [32]. En alternative, des filtres radiofréquence (RF) [33], [34] ont été démontrés permettant un réglage discret de certaines caractéristiques de la réponse spectrale du filtre (par exemple, fréquence centrale et bande passante), bien que sur une bande passante d'exploitation limitée, jusqu'à quelques GHz. Le filtrage optique offre des bandes passantes d'exploitation beaucoup plus larges, et des technologies sont disponibles permettant une reconfigurabilité versatile de la réponse spectrale du filtre [35], [36]. Cependant, la vitesse de reconfigurabilité de ces schémas (généralement dans la gamme des kHz) reste des ordres de grandeur plus lente que la résolution de fréquence qu'ils peuvent offrir (généralement dans la gamme des GHz), les rendant ainsi inadaptés aux tâches de manipulation générale des signaux T-F. En tant que tel, il y a eu des efforts récents importants vers le développement de filtres micro-ondes à variation temporelle (TVF) reconfigurables mis en œuvre directement dans le domaine des ondes analogiques. Une solution particulièrement intéressante est celle basée sur les systèmes de filtres photoniques micro-ondes (MPF), qui peuvent offrir des bandes passantes d'exploitation supérieures à des dizaines de GHz, et un degré important de flexibilité et de reconfigurabilité au-delà de celui de leurs homologues en filtres électriques [37]. Pourtant, les MPF restent limités en termes de vitesse de réglage pratique et/ou de degré de reconfigurabilité. Un filtrage T-F continu avec une très grande vitesse de réglage basé sur la modulation temporelle d'un spectrogramme cartographié dans le temps basée sur le principe de Talbot pulsé a été proposé précédemment [38]. Cependant, conformément aux contraintes discutées ci-dessus pour cette méthode d'analyse de spectrogramme, la bande passante de traitement de cette approche est intrinsèquement limitée à quelques GHz avec seulement quelques points d'analyse de fréquence. Une technique également récemment proposée est basée sur la diffusion Brillouin stimulée (SBS). En utilisant cette méthode, un MPF a été démontré pour fournir une sélectivité de fréquence fine (par exemple, des dizaines de MHz) [39], mais seule la fréquence centrale peut être ajustée et l'exigence d'un signal de contrôle du filtre introduirait des composants non linéaires supplémentaires. D'autre part, l'utilisation de peignes de fréquences optiques a conduit à des avancées en matière de vitesse de réglage rapide et de flexibilité [40]. Cependant, la possibilité de réglage de fréquence et la reconfigurabilité de la bande passante peuvent difficilement être réalisées simultanément en utilisant cette méthodologie. Récemment, un circuit photonique programmable basé sur des réseaux de guides d'ondes et des déphaseurs a produit des filtres avec plusieurs réponses [41]. Cependant, le réglage est relativement complexe car il nécessite de contrôler chaque actionneur de phase séparément pour obtenir la réponse souhaitée du filtre, et la vitesse de réglage est intrinsèquement limitée par l'actionneur thermo-optique (échelles de microsecondes). Ainsi, il reste difficile pour n'importe lequel des MPF proposés à ce jour de fournir la combinaison complète de spécifications de performance souhaitée. Certaines de ces méthodes sont pratiquement limitées en ce qui concerne leur degré de reconfigurabilité [39], [40], et/ou leur bande passante d'exploitation, à quelques GHz au mieux [39], [42].

02. OBJECTIFS, CONTRIBUTIONS ET ORGANISATION DE LA THÈSE

L'objectif principal de cette thèse est de concevoir, étudier et démontrer expérimentalement une approche assistée par photonique pour l'analyse et le traitement spectral en temps réel des formes d'onde à large bande, capable de fournir les spécifications de performance cibles suivantes :

- Bande passante instantanée en temps réel de plusieurs dizaines de GHz,
- Spécifications définies par l'utilisateur pour les tâches d'analyse et de traitement,
- Vitesse de réglage rapide, à l'échelle de la nanoseconde ou plus rapide, pour la manipulation spectrale,
- Résolution temporelle dans la gamme des nanosecondes,
- Résolution fréquentielle fine jusqu'au niveau du MHz.

Dans ce but, cette thèse propose un cadre pour l'analyse et la manipulation en temps réel définies par l'utilisateur de la distribution conjointe T-F des ondes électromagnétiques (EM) directement dans le domaine analogique, idéalement adapté au fonctionnement sur les ondes à haute vitesse. En utilisant ce concept, nous concevons et démontrons un schéma photonique pour l'analyse et le traitement T-F des signaux micro-ondes et optiques. L'approche proposée combine la polyvalence de l'approche DSP avec la performance (par exemple, vitesse de traitement et bande passante) d'une solution photonique. La stratégie implique de mapper la distribution T-F de l'onde entrante le long du domaine temporel basé sur la phase de l'illuminateur de réseau de Talbot (*Talbot array illuminator,* TAI), de manière continue et sans interruption, ce qui permet à son tour une manipulation définie par l'utilisateur de la distribution T-F de l'onde grâce aux techniques de modulation temporelle disponibles. En vue de cet objectif déclaré, les contributions centrales de cette thèse sont les suivantes :

- Une étude théorique détaillée du concept central de notre proposition sera discutée. L'équivalence entre la modulation de phase temporelle et la modulation spectrale temporelle sera évaluée à travers des équations et sera également validée par des résultats numériques et expérimentaux. Cela fournit une compréhension approfondie du concept derrière la proposition fondamentale.
- La proposition et l'étude théorique incluent la dérivation de toutes les principales équations de conception pour l'analyse de signal basée sur la photonique pour l'analyse spectrale en temps réel, basée sur une transformée de Fourier à court terme (*short-time Fourier transform,* STFT) cartographiée temporellement.
- Validation numérique du concept de spectrogramme cartographié temporellement proposé et de ses principales spécifications de performance et compromis.

- Démonstration expérimentale du spectrogramme cartographié temporellement basé sur la photonique de signaux micro-ondes à large bande arbitraires, fournissant l'ensemble suivant de spécifications de performance:
  - Bande passante d'analyse en temps réel jusqu'à ~100 GHz,
  - Résolution temporelle dans le régime de la nanoseconde,
  - Résolution fréquentielle fine jusqu'au niveau du MHz,
  - Spécifications reconfigurables définies par l'utilisateur.
- Étude théorique et analyse du filtrage temps-fréquence proposé basé sur le spectrogramme cartographié temporellement obtenu.
- Démonstration expérimentale de la manipulation temps-fréquence des signaux arbitraires qui ont été analysés avec succès par l'étape d'analyse du spectrogramme. Nous présenterons les capacités suivantes du filtrage proposé :
  - Bande passante d'exploitation en temps réel jusqu'à ~100 GHz,
  - Vitesse de réglage rapide jusqu'au régime de la nanoseconde,
  - Résolution fréquentielle fine jusqu'à quelques centaines de MHz,
  - Reconfigurabilité arbitraire, en termes de fréquence centrale, de bande passante, de bande passante et de forme de la réponse spectrale TVF,
  - Atténuation des interférences aléatoires.

03. ÉQUIVALENCE ENTRE LA DISPERSION DE VITESSE DE GROUPE ET LA LENTILLE TEMPORELLE

03.1. EQUIVALENCE MATHÉMATIQUE ENTRE GVD ET TL

Je commence par fournir un aperçu de la modélisation mathématique du processus de propagation d'impulsions à travers une dispersion du second ordre. Les signaux impliqués sont supposés être centrés à la fréquence angulaire ω_0. La dispersion totale du second ordre est définie comme $\ddot{\Phi}_0 = \beta_2 z$, où $\ddot{\Phi}_0 = \beta_2 z$, β_2 et z sont respectivement le coefficient de dispersion et la longueur du milieu. Le processus de dispersion de vitesse de groupe (*Group velocity dispersion,* GVD) peut être modélisé comme un filtrage spectral uniquement en phase, correspondant à une fonction de transfert en fréquence $\widehat{H}(\omega) = exp(-j\frac{1}{2}\ddot{\Phi}_0\omega^2)$ sur toute la bande passante de la forme d'onde. Ici, nous ignorons le délai de propagation global subi par le paquet d'ondes, les termes de dispersion d'ordre supérieur et les pertes. Ainsi, la réponse impulsionnelle temporelle associée $\hat{h}\ (t)$ peut être obtenue par transformation de Fourier inverse de $\widehat{\mathrm{H}}(\omega)$, c'est-à-dire, $\hat{h}\,(t) = exp\left(j\frac{1}{2\ddot{\Phi}_0}t^2\right)$, où t est la variable temporelle relative au délai de groupe du milieu à ω_0.

Lorsqu'une forme d'onde pulsée optique se propage à travers un tel milieu dispersif de second ordre, l'amplitude de l'enveloppe complexe de sortie peut être écrite comme:

$$\begin{aligned} |a_{out}(t)| &= \left|\int_{-\infty}^{+\infty} \hat{a}_{in}(\tau)\, exp\left(j\frac{1}{2\ddot{\Phi}_0}(t-\tau)^2\right) d\tau\right| \\ &= \left|\int_{-\infty}^{+\infty} \hat{a}_{in}(\tau)\, exp\left(j\frac{1}{2\ddot{\Phi}_0}\tau^2\right) exp\left(-j\frac{1}{\ddot{\Phi}_0}\tau t\right) d\tau\right| \\ &= \left|\mathcal{F}\left[\hat{a}_{in}(\tau) exp\left(j\frac{1}{2\ddot{\Phi}_0}\tau^2\right)\right]_{\omega=\frac{t}{\ddot{\Phi}_0}}\right| \end{aligned} \tag{1}$$

où $\mathcal{F}$ désigne la transformée de Fourier. Ainsi, sous l'effet de la GVD, la forme d'onde de sortie subit une distorsion et, en particulier, son enveloppe temporelle est proportionnelle à la transformée de Fourier de la forme d'onde de l'impulsion d'entrée modulée par une phase quadratique, dont le résultat est évalué à $\omega = \frac{t}{\ddot{\Phi}_0}$.

Nous anticipons que le profil temporel d'une forme d'onde dispersée sera proportionnel au spectre de fréquence de la forme d'onde temporelle d'entrée modulée par une phase temporelle quadratique appropriée. La modulation requise (amplitude plate, phase quadratique) peut être effectuée à l'aide d'une lentille temporelle (*Time-lens,* TL) [43]. En pratique, la TL peut être mise en œuvre sur une impulsion optique en

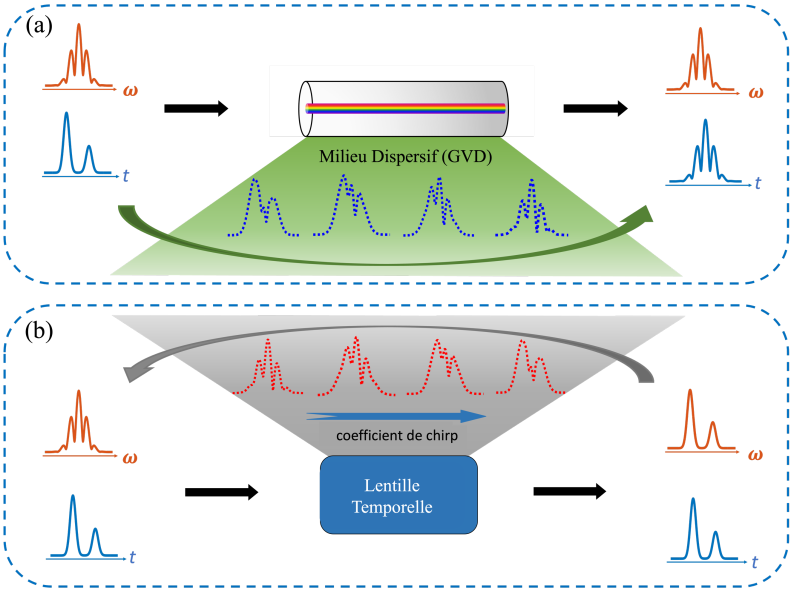

Fig. 1. Illustration du principe proposé, montrant l'évolution de (a) l'enveloppe temporelle d'une forme d'onde entrante lors de sa propagation à travers un milieu dispersif d'ordre deux prescrit (t : variable temporelle), et (b) le spectre de fréquence de la même forme d'onde d'entrée lorsqu'elle subit une TL (ω : variable de fréquence radiale).

utilisant un modulateur électro-optique (*Electro-optic phase modulator,* PM) piloté par un signal radio-fréquence (RF) sinusoïdal. Cette modulation est localement quadratique autour du minimum ou de la cuspide de la sinusoïde dans l'ouverture temporelle [44]. Ainsi, l'amplitude du spectre de sortie est simplement la transformée de Fourier du signal modulé [45]:

$$|A_{out}(\omega)| \propto |\mathcal{F}[\hat{a}_{in}(t)\exp(j\varphi(t))]|$$
$$= \left|\mathcal{F}\left[\hat{a}_{in}(t)\exp\left(j\frac{\ddot{\varphi}_t}{2}t^2\right)\right]\right| \quad (2)$$

En comparant les Eqs. (1) et (2), nous concluons que si le coefficient de chirp de la TL et la dispersion à émuler satisfont la condition suivante :

$$\ddot{\varphi}_t = \frac{1}{\ddot{\Phi}_0} \quad (3)$$

le spectre de fréquence de la forme d'onde modulée en phase présente la même forme que celle de la forme d'onde temporelle dispersée, sous le facteur de cartographie (ou mappage) temps-fréquence

$$\Delta\omega_t = \frac{\Delta t}{\ddot{\Phi}_0} \quad (4)$$

Où $\Delta\omega_t$ est la variable de fréquence relative à la fréquence optique centrale du signal et Δt est la variable temporelle relative au centre de la forme d'onde de sortie. Par conséquent, la relation entre le coefficient de chirp $\ddot{\varphi}_t$ de la lentille temporelle et la dispersion à émuler est cruciale pour obtenir une correspondance exacte entre le spectre de fréquence de la forme d'onde modulée en phase et la forme d'onde temporelle disperse, Fig. 1.

03.2. DÉMONSTRATION EXPÉRIMENTALE

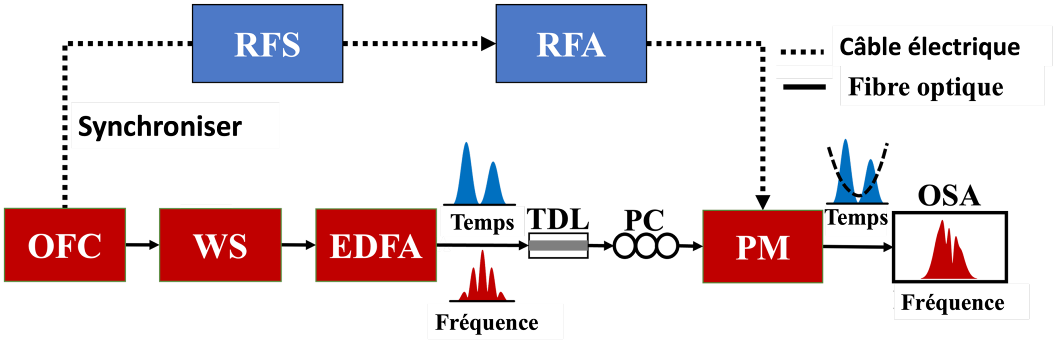

Fig. 2. Schéma de l'installation expérimentale. RFS : synthétiseur de radiofréquence ; RFA : amplificateur de radiofréquence ; OFC : peigne de fréquence optique ; WS : façonneur d'onde ; EDFA : amplificateur à fibre dopée erbium ; TDL : ligne à retard accordable ; PC : contrôleur de polarisation ; PM : modulateur de phase ; OSA : analyseur de spectre optique.

La Fig. 2 montre le montage expérimental. Un train d'impulsions optiques a été utilisé comme source optique, suivi par un WaveShaper (WS) pour générer la forme d'onde d'impulsion cible. Pour réaliser l'opération de la TL, nous avons utilisé un PM avec une V_π moyenne d'environ 3.5 V, piloté par un signal RF sinusoïdal. La synchronisation du signal RF et de la source optique d'entrée a été réalisée en ajustant une ligne à retard réglable (*Tuneable delay line,* TDL). Enfin, le signal modulé a été directement capturé par un analyseur de spectre optique avec une résolution de 1.25 GHz.

Pour démontrer le concept introduit, nous considérons d'abord une impulsion optique en forme de sinc comme entrée. Les Fig. 3 (a) et (b) montrent le spectre de fréquence mesuré et le profil temporel numérique correspondant. La largeur à mi-hauteur (*Full-width at half maximum,* FWHM) de la source optique d'entrée est d'environ 100 GHz. Ici, nous fixons la puissance du signal RF modulant à 22 dBm, ce qui donne un décalage de phase de pointe d'environ 2.5 rad dans le processus de modulation. Le coefficient de chirp de modulation $\ddot{\varphi}_t$ de la TL est ensuite contrôlé en ajustant continuellement la fréquence du signal RF pour émuler différentes quantités de dispersion. Les Fig. 3 (c)-(e) montrent le spectre de fréquence mesuré du signal modulé (tracés rouges pleins), comparé à la forme d'onde temporelle attendue correspondante après dispersion (tracés bleus en pointillés) et au spectre simulé à la sortie du PM lorsqu'il est piloté par la modulation sinusoïdale idéale, pour trois des cas évalués. La forme d'onde dispersée est analysée numériquement en supposant une propagation à travers une fibre monomode (*Single-mode fiber,* SMF) avec un coefficient de dispersion de $\beta_2 = -21.6\ \mathrm{ps}^2/(\mathrm{rad} \cdot \mathrm{km})$. Pour les cas montrés dans la Fig. 3, la fréquence de modulation est fixée à 6 GHz (c), 8 GHz (d) et 10 GHz (e), respectivement. Dans la simulation, les longueurs des sections SMF correspondantes sont de 12.8 km (c), 7.22 km (d) et 4.62 km (e), respectivement, telles que déterminées par l'équation (3). Notez que les axes temporels et de fréquence des résultats représentés sont mis à l'échelle selon la relation entre les deux variables de l'équation (4). Les résultats expérimentaux valident le fait que le spectre de fréquence d'une forme d'onde donnée (d'entrée), après une modulation de phase temporelle sinusoïdale appropriée, présente la même forme que celle d'une version dispersée de la même forme d'onde temporelle après propagation à travers une quantité prescrite de dispersion, suivant le facteur de cartographie fréquence-temps.

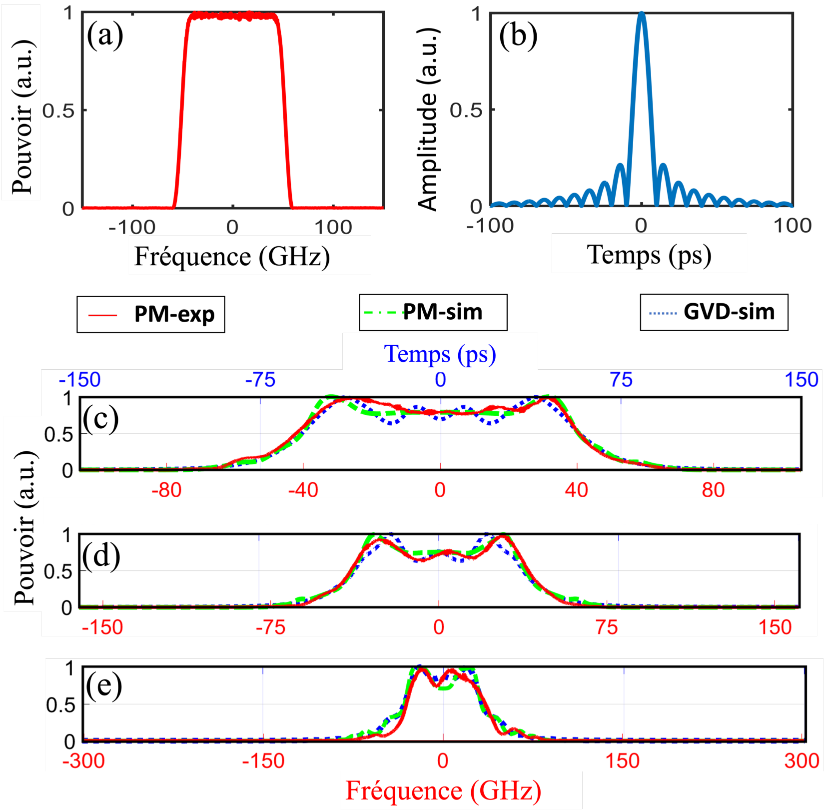

Fig. 3. Résultats expérimentaux: (a) spectre mesuré de l'impulsion façonnée en entrée ; (b) et forme d'onde temporelle simulée ; (c)-(e) spectres mesurés (courbe rouge continue, échelle inférieure) à la sortie du modulateur de phase (PM), comparés aux formes d'onde temporelles simulées après la quantité correspondante de dispersion (courbe bleue en pointillés, échelle supérieure) et au spectre simulé à la sortie du PM lorsqu'il est commandé par les signaux sinusoïdaux correspondants (courbe verte en pointillés, échelles inférieures), avec l'échelle de fréquence relative et de temps définie dans le texte.

04. ANALYSE SPECTRALE CARTOGRAPHIÉE DANS LE TEMPS

04.1. PRINCIPE DE FONCTIONNEMENT

Un spectrogramme basé sur le principe de l'effet Talbot a été proposé, offrant une manière simple de cartographier temporellement un STFT sans interruption d'un signal entrant de manière totalement continue et en temps réel [8], [46]. Le principe implique d'échantillonner le SUT (c'est-à-dire un signal micro-onde) avec un train périodique de courtes impulsions optiques (généralement non chirpées) selon le critère de Nyquist, suivi par une propagation linéaire à travers une ligne dispersive de groupe-vitesse adaptée. Plus précisément, la ligne dispersive est conçue pour satisfaire une condition d'auto-imagerie de Talbot entier par rapport au taux d'échantillonnage des impulsions. Le système permet de cartographier dans le domaine temporel les spectres de sections temporelles consécutives et fortement superposées du SUT à la sortie du système, chaque spectre cartographié dans le temps s'étendant sur une durée égale à la période

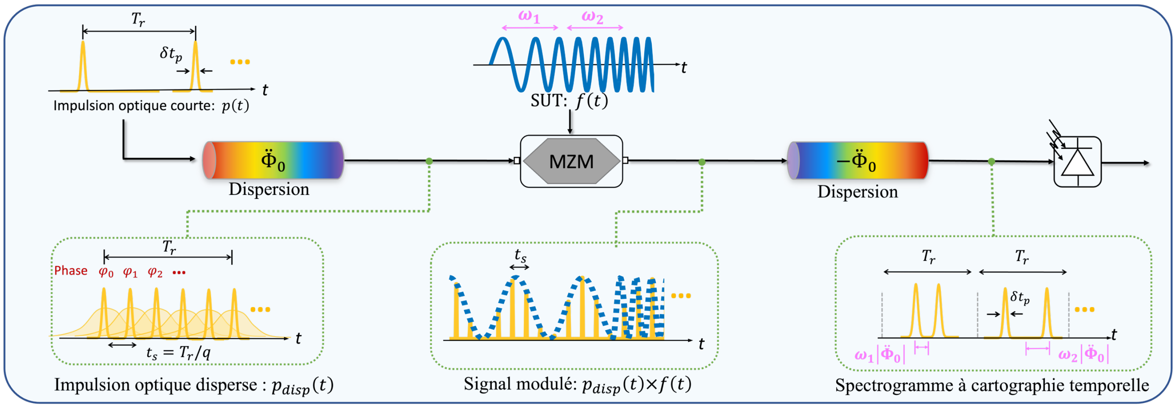

Fig. 4. Principes de base des schémas basés sur Talbot fractionné pour le spectrogramme à cartographie temporelle, impliquant l'échantillonnage temporel du SUT micro-ondes avec un train d'impulsions optiques conditionné par phase Talbot à haut débit, suivi de la dispersion de groupe-vitesse (GVD) en fibre optique et de la photodétection.

d'échantillonnage des impulsions. Cependant, l'inconvénient principal du schéma de Talbot entier est la bande passante opérationnelle limitée (quelques GHz au mieux) et le nombre limité de points d'analyse dans le domaine fréquentiel (généralement inférieur à ~10 points d'analyse).

Pour remédier à cela, nous proposons de concevoir les lignes dispersives pour fonctionner sous des conditions de Talbot fractionnel [47], de sorte que le signal optique sur lequel l'UTS est modulé soit en fait une copie multipliée du train d'impulsions optiques d'entrée. Le schéma résultant est illustré dans la Fig. 4. Pour fonctionner sous une condition de Talbot fractionnel, la dispersion de groupe de la ligne doit satisfaire la condition suivante [48]:

$$\ddot{\Phi}_0 = \frac{s}{q}\frac{{T_r}^2}{2\pi} \qquad (5)$$

avec q étant un nombre naturel quelconque et s étant un entier co-premier avec q. Remarquez que l'équation. (5) avec $q = 1$ représente la condition de Talbot entier. Sous cette condition, le train d'impulsions d'entrée est exactement reproduit à la sortie de la première ligne dispersive dans le schéma général illustré à la Fig. 4. Sous la condition de Talbot fractionnel de l'équation (5) (avec $q \geq 2$), le train d'impulsions d'entrée est également auto-imagé après propagation à travers la première ligne dispersive, de manière à ce que le signal optique dispersé soit un autre train d'impulsions dans lequel les impulsions individuelles sont des répliques exactes de celles d'entrée, avec une enveloppe définie par $p(t)$, mais se répétant à un taux accru par le facteur q. Cela signifie que la période de répétition du train d'simpulsions auto-imagé après dispersion est $t_s = T_r/q$. Dans une conception pratique, l'utilisation de $|s| = 1$ garantit la condition de conception la moins stricte expérimentallement. Pour assurer la production d'un train d'impulsions uniformément multiplié, la période de répétition réduite doit toujours être plus longue que la largeur temporelle complète de chaque impulsion individuelle $\Delta\nu_p$, à savoir, $t_s > 1/\Delta\nu_p$. Le SUT est

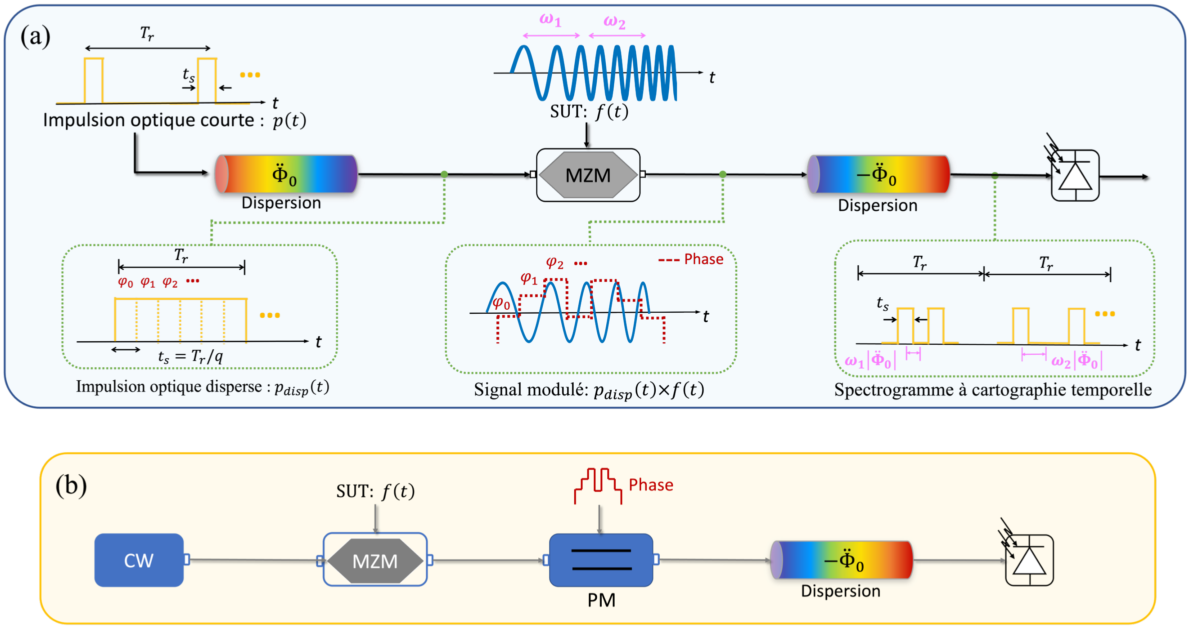

Fig. 5. Principe du schéma de spectrogramme basé sur TAI proposé. (a) Schéma de la configuration proposée basée sur l'illuminateur à réseau de Talbot (TAI) pour l'analyse en temps réel du spectrogramme. (b) Implémentation pratique du design de la Fig. 5(a) utilisant la modulation de phase électro-optique (PM) du SUT sur un support optique, suivie de la dispersion de groupe-vitesse en fibre optique et de la photodétection.

ensuite échantillonné de manière uniforme par ce train d'impulsions courtes avec un taux accru (par le facteur q par rapport au taux des impulsions d'entrée). Compte tenu du facteur de cartographie fréquence-temps discuté précédemment, $\Delta\omega_t \rightarrow \Delta t/\ddot{\Phi}_0$, déterminé également par le facteur de dispersion $\ddot{\Phi}_0$, la T-F cartographiée dans le temps de n'importe quelle section du SUT s'étend sur une durée maximale de $|\ddot{\Phi}_0|\Delta\omega_{SUT}$, où $\Delta\omega_{SUT}$ est la largeur de bande spectrale totale du SUT. Ces deux conditions de conception centrales peuvent être mathématiquement exprimées simultanément comme suit:

$$\frac{1}{\Delta\nu_p} < t_s < \frac{1}{\Delta\upsilon_{SUT}} \qquad (6)$$

où $\Delta\upsilon_{SUT} = \Delta\omega_{SUT}/2\pi$ est la largeur de bande spectrale totale du SUT exprimée en unités de fréquence naturelle. L'inégalité à droite garantit qu'il n'y a pas de chevauchement entre les spectres cartographiés dans le temps consécutifs à la sortie du système. Cette inégalité correspond au critère de Nyquist qui doit être respecté lors de l'échantillonnage d'un signal dont la bande passante est plus large que $\Delta\upsilon_{SUT}$ [49].

Une caractéristique clé d'un train d'impulsions produit par auto-imagerie fractionnel de Talbot est qu'un décalage de phase déterministe est induit impulsion par impulsion le long du train multiplié en taux. Le profil de phase temporelle discret et restreins est basé sur le cadre de l'illuminateur de réseau temporel de Talbot (TAI), selon l'expression suivante [50]:

$$\varphi_n = -\sigma\pi n^2 \frac{p}{q} \qquad (7)$$

où $\sigma = \pm 1$, n est un indice entier définissant le numéro temporel de l'impulsion, et le paramètre entier p dépend du facteur de multiplication de taux q et du paramètre s dans l'équation (5). En particulier, les paramètres p et s doivent satisfaire la relation de congruence suivante : $ps = 1 + qe_q$, avec $e_q = 1$ si q est impair et $e_q = 0$ si q est pair. Cette caractéristique d'un train d'impulsions fractionnel de Talbot suggère une mise en œuvre alternative pour la génération de la séquence d'impulsions utilisée pour l'échantillonnage du SUT. Ce train d'échantillonnage pourrait être produit par modulation de phase temporelle d'une séquence d'impulsions optiques verrouillées en mode générée directement avec une période de répétition t_s, où la phase est décalée impulsion par impulsion selon le motif de l'équation (7).

Le design fractionnel de Talbot proposé peut être encore simplifié en suivant le schéma illustré dans la Fig. 5 (a). Supposons que les impulsions optiques individuelles présentent une forme rectangulaire idéale avec une largeur temporelle égale à la période de répétition cible à la sortie, $t_s = T_r/q$. Mathématiquement, l'enveloppe individuelle de l'impulsion peut alors être écrite comme $p(t) \propto \mathrm{rect}(t/t_s)$, où $\mathrm{rect}(t/X))$ est une fonction rectangulaire idéale de durée X, c'est-à-dire $\mathrm{rect}(t/X) = 1$ pour $(-X/2) \leq t \leq (X/2)$, et $\mathrm{rect}(t/X) = 0$ pour toute autre valeur de t. Dans ce cas, le train d'impulsions fractionnel de Talbot à la sortie de la ligne dispersive présente une distribution uniforme de lumière avec un motif de phase temporelle discret suivant l'équation (7), comme indiqué dans la Fig. 5 (a). Cela implique que le SUT doit ensuite être modulé en phase selon le profil temporel dans l'équation (7). Cela évite le besoin d'un échantillonnage temporel de l'intensité du SUT et du processus de modulation d'amplitude correspondant. La Fig. 5 (b) montre une implémentation pratique proposée du design résultant. Le SUT est d'abord modulé dans un support optique, par exemple, une lumière continue (CW). En général, le système proposé effectuerait une analyse T-F de l'enveloppe complexe temporelle d'une forme d'onde optique entrante. Le SUT optique est ensuite modulé en phase suivant le profil défini dans l'équation (7). Cela peut être mis en œuvre en utilisant par exemple un PM piloté par un générateur de formes d'onde arbitraires électroniques (*arbitrary waveform generator,* AWG). Le signal de modulation de l'AWG devrait être programmé pour implémenter la modulation de phase selon le profil dans l'équation (7). Comme illustré dans la Fig. 5 (a), chaque niveau de phase discret devrait avoir une valeur uniforme s'étendant sur une durée égale à la période de répétition t_s du train d'impulsions multiplié en taux équivalent. Pour éviter une accumulation de phase importante, nécessitant une excursion de modulation de phase importante, les phases dans l'équation (7) sont plus facilement implémentées modulo 2π, comme illustré dans la Fig. 5. Cette phase restreinte surmonte les limitations associées aux contraintes sur l'excursion maximale de phase possible avec un dispositif de modulation temporelle pratique. Dans ce cas, le motif de phase résultant est périodique avec une période égale à q (si le produit pq est un nombre pair) ou $2q$ (si le produit pq est un nombre impair) [21], c'est-à-dire que le profil de modulation de phase temporelle résultant se répète périodiquement avec une période égale à $T_r = qt_s$ou $2T_r = 2qt_s$, respectivement. Nous rappelons qu'en général, le facteur s est déterminé par la relation de congruence : $ps = 1 + qe_q$. En pratique, les meilleures performances sont obtenues lorsque le facteur s dans l'équation (5) est fixé avec une magnitude égale à 1. Par exemple, lorsque s = 1, le facteur p dans l'équation (7) doit être fixé comme suit : $p = 1$ si q est pair, ou $p = q + 1$si q est impair. Ici, nous avons choisi q comme impair, de manière à ce que le motif de phase dans l'équation (7) se répète tous les q niveaux de phase, ou avec une période $T_r = qt_s$. La phase temporelle résultante TAI qui est modulée sur l'PM peut alors être écrite comme suit :

$$\varphi_n = -\sigma\pi n^2 \frac{q-1}{q} \tag{8}$$

Cette fonction de phase est enveloppée à 2π et permet toujours une modulation équivalente à une lentille temporelle conventionnelle avec une excursion totale de phase de $\frac{\pi q}{4}$.

Ensuite, le SUT modulé en phase se propage à travers une ligne dispersive linéaire avec un GVD égal à $-\ddot{\Phi}_0$ qui satisfait la condition suivante:

$$\ddot{\Phi}_0 = \sigma \frac{q{t_s}^2}{2\pi}. \tag{9}$$

En pratique, ce filtrage de phase spectrale peut être implémenté en utilisant une simple ligne dispersive de groupe-vitesse (par exemple, une longueur appropriée de fibre optique monomode). Le signal temporel résultant correspond aux spectres consécutifs cartographiés dans le temps du signal après un photodiode. Ce schéma calcule la transformée de Fourier (FT) sur chaque section consécutive de durée T_r du SUT d'entrée, de manière à ce que les spectres consécutifs résultants soient cartographiés le long du domaine temporel, chacun s'étendant sur une plage de temps de durée T_r. Ce mappage est produit selon la loi de cartographie fréquence-temps $\Delta\omega = \Delta t/\ddot{\Phi}_0$, décrite dans l'équation (4).

04.2. LES SIMULATIONS NUMÉRIQUES

Nous rapportons d'abord les résultats des simulations numériques pour l'analyse en temps réel du spectrogramme basée sur TAI proposée, comme illustré dans la Fig. 6. Le SUT micro-onde est d'abord modulé sur la lumière CW à travers un modulateur Mach-Zehnder (*Mach-Zehnder modulator,* MZM). Ensuite, le SUT optique est modulé en phase selon le profil temporel dans l'équation (8) avec les paramètres suivants. La largeur temporelle de chaque niveau de phase discret est supposée être $t_s = 25$ ps, et les paramètres définissant le motif de phase fractionnel de Talbot sont fixés à $s = -1$ et $q = 401$, ce qui se traduit par une période de répétition $T_r = t_s \times q \approx 10$ ns.. La ligne dispersive suivante introduit la quantité requise de GVD selon l'équation (9), à savoir, $-\ddot{\Phi}_0 = -\frac{q{t_s}^2}{2\pi} = 2.5 \times \frac{10^5}{2\pi} \mathrm{ps}^2/\mathrm{rad}$. Ces paramètres mappent consécutivement chaque composantes spectrales calculées sur une période de 10-ns avec q = 401 points d'analyse, correspondant à une résolution optimale de fréquence d'environ 100 MHz.

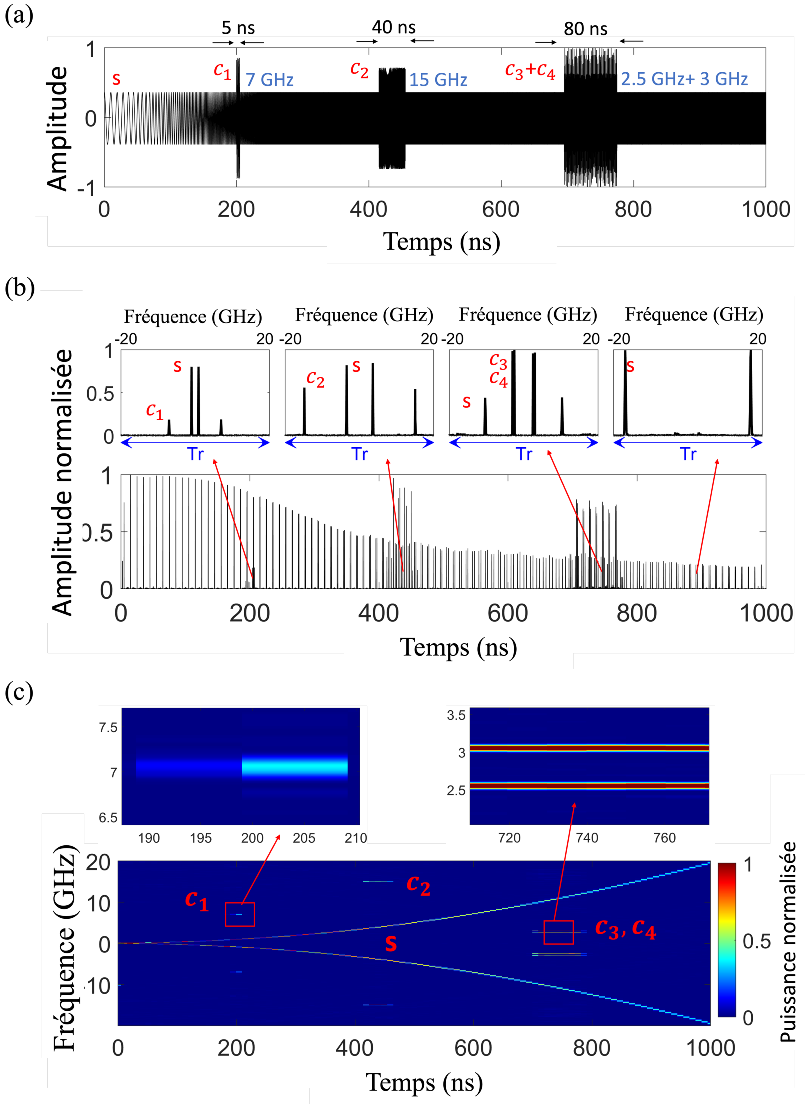

Fig. 6. Simulations numériques de l'analyse de spectrogramme temporellement cartographié basée sur TAI d'un signal micro-onde. (a) Trace temporelle du signal sous test (SUT). (b) Amplitude moyenne de la forme d'onde temporelle à la sortie du système de spectrogramme temporellement cartographié. (c) Représentation 2D de la distribution d'énergie T-F conjointe du signal (SP) récupérée à partir de la trace temporelle de sortie.

La Fig. 6 (a) montre le SUT micro-onde d'une durée de 1 µs, composé d'une sinusoïde à chirp de fréquence quadratique croissante, avec une fréquence augmentant de 100 MHz à 20 GHz, ainsi que des interférences isolées avec différents contenus fréquentiels et durées temporelles. La Fig. 6 (b) montre l'amplitude moyenne de la forme d'onde temporelle à la sortie du système spectrogramme TAI. Remarquez que le système proposé cartographie le long du domaine temporel le spectre de fréquence complet (double bande latérale) correspondant chaque T_r, incluant à la fois les côtés positif et négatif du spectre d'entrée de l'UTS, conformément à la loi de cartographie fréquence-temps définie ci-dessus, $\Delta\omega = \Delta t/\ddot{\Phi}_0$. L'axe des

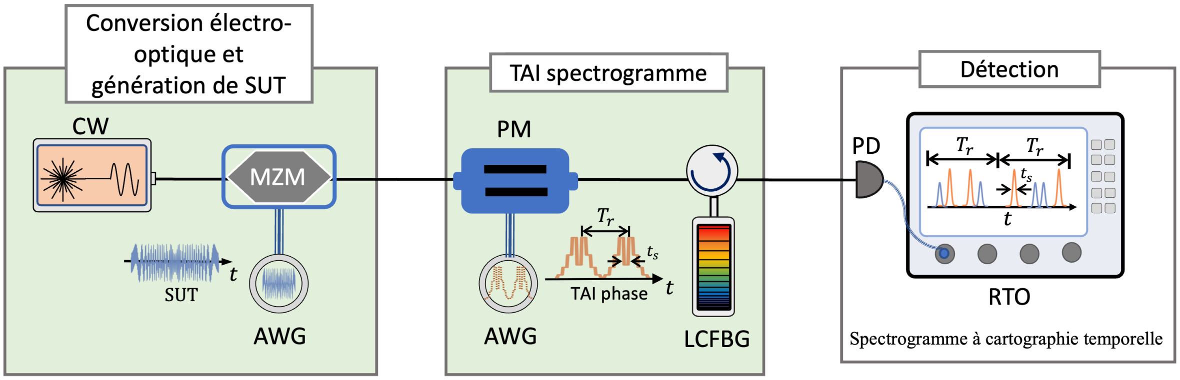

Fig. 7. Principe et configuration expérimentale proposée pour le spectrogramme basé sur TAI.

fréquences correspondant pour chacune des traces montrées dans les encarts est représenté dans l'axe horizontal supérieur.

Comme prédit, et comme on peut l'observer dans les encarts de la Fig. 6 (b), la cartographie temporelle permet d'identifier les composantes fréquentielles de l'UTS, à savoir le terme de chirp de fréquence croissante quadratique (désigné par ‘s’) et les interférences de fréquence isolées (désignées par ‘c_i’ avec i = 1, 2, 3, 4, …) aux emplacements temporels attendus. La Fig. 6 (c) montre une représentation 2D de la distribution d'énergie T-F conjointe du signal récupérée à partir de la trace temporelle de sortie. Le FT du signal changeant dans notre exemple est calculé tous les 10 ns, c'est-à-dire à une vitesse de 100×10^6 FTs par seconde.

04.3. RÉSULTATS EXPÉRIMENTAUX DE PREUVE DE CONCEPT

04.3.1. SPECTROGRAMME CARTOGRAPHIÉ DANS LE TEMPS DE SIGNAUX MICRO-ONDES NON STATIONNAIRES SUR UNE BANDE PASSANTE DE 92 GHZ

Pour vérifier expérimentalement le concept de spectrogramme en temps réel basé sur TAI proposé, un schéma simple basé sur la photonique est conçu. La configuration expérimentale est illustrée dans la Fig. 7, suivant le même schéma général utilisé pour les simulations ci-dessus. Les signaux sont générés à l'aide d'un générateur de formes d'onde arbitraires (AWG) électronique, puis modulés sur le support optique à travers un modulateur Mach-Zehnder électro-optique (bande passante de 40 GHz). Le SUT optique entre ensuite dans l'unité de spectrogramme TAI, composée d'un PM (bande passante de 40 GHz) piloté par un autre canal du même AWG. La phase temporelle modulée est conçue selon le motif de phase multi-niveaux Talbot requis qui satisfait l'équation (8). Ensuite, un réseau de Bragg à fibre chirpée linéairement réfléchissant (*Linearly-chirped fiber Bragg grating,* LCFBG) est utilisé pour fournir la quantité désirée de dispersion de groupe-vitesse. Le signal temporel obtenu à la sortie du milieu dispersif, capturé par un photodétecteur (PD) de 50 GHz connecté à un oscilloscope de 28 GHz, correspond à des spectres consécutifs cartographiés dans le temps du SUT d'entrée pendant la période d'analyse T_r.

Dans une première expérience, la phase TAI est réglée avec t_s~ 10.8 ps, q = 139, T_r = 1.5 ns, permettant une bande passante de fonctionnement de $1/t_s$ ~ 92 GHz et une résolution théorique de fréquence d'environ 660 MHz. Le signal modulé en phase se propage ensuite à travers un LCFBG réfléchissant

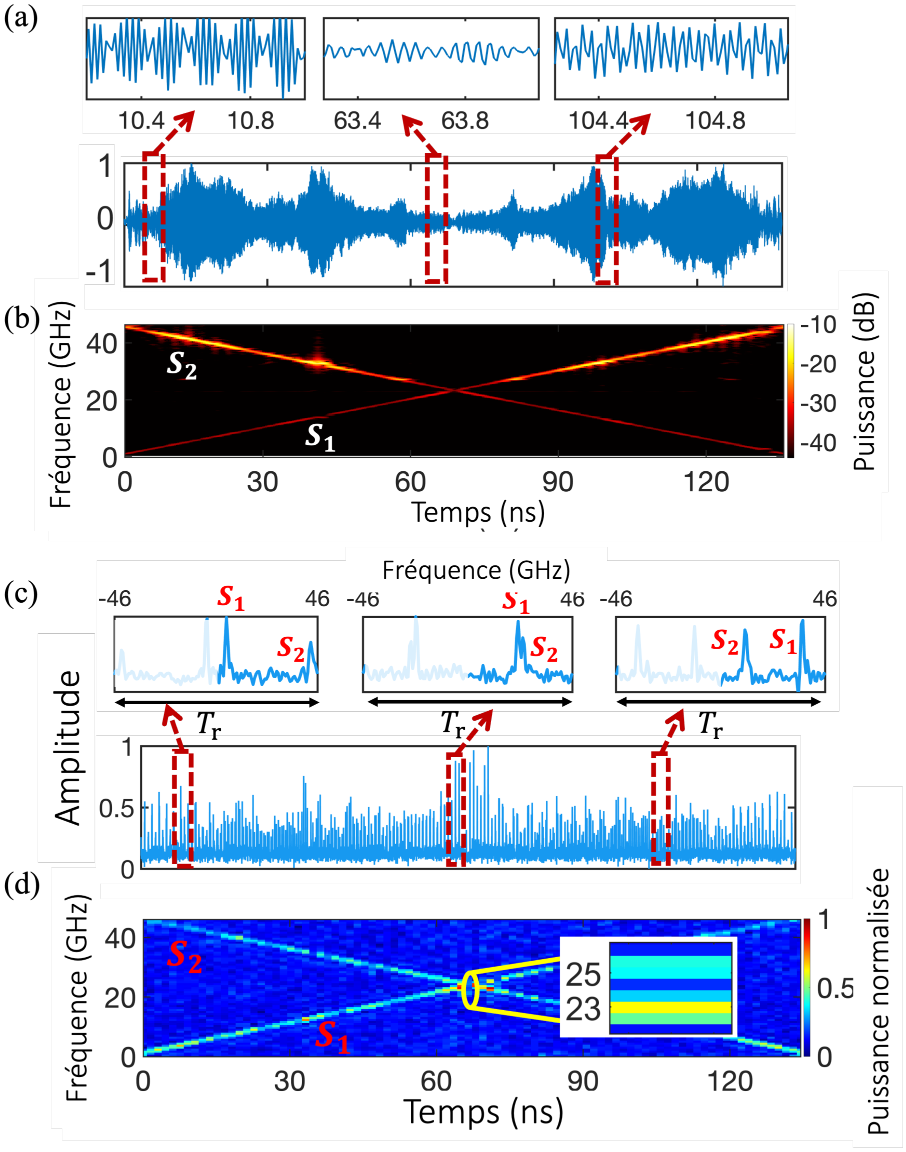

Fig. 8. Démonstration de la proposition avec une bande passante de 92 GHz. (a) Trace temporelle du SUT. (b) Intensité du spectrogramme obtenu numériquement du SUT. (c) TM-SP mesuré avec plusieurs zooms autour de trois périodes d'analyse temporelle pertinentes différentes. (d) Représentation 2D de la distribution T-F conjointe du signal qui est redimensionnée numériquement à partir de la trace temporelle mesurée en sortie de c.

fournissant une dispersion de groupe-vitesse $\ddot{\Phi}_0 \sim 2{,}600\ \mathrm{ps}^2/\mathrm{rad}$. Ainsi, le FT du signal est calculé toutes les 1.5 ns, soit à une vitesse de 666×10^6 FTs par seconde. La Fig. 8 (a) montre la forme d'onde temporelle du SUT, s'étendant sur une gamme de fréquences d'environ 46 GHz (largeur de bande optique totale d'environ 92 GHz). L'intensité du spectrogramme obtenu numériquement du SUT micro-onde est montrée dans la Fig. 8 (b). Le signal temporel à la sortie de l'unité de spectrogramme TAI est montré dans la Fig. 8 (c). Comme prévu, le système proposé cartographie le spectre de fréquence complet (double bande latérale) correspondant le long du domaine temporel chaque T_r, selon la loi de cartographie fréquence-temps définie ci-dessus. Comme prédit, et comme cela peut être observé à partir des encarts, la cartographie temporelle identifie clairement les composantes de fréquence des deux chirps, à savoir l'augmentation linéaire (désignée par S_1) et la diminution (c'est-à-dire S_2), dans chaque fenêtre d'analyse.

Le signal temporel capturé peut être transformé numériquement en une représentation spectrogramme 2D tel que communément utilisé, illustrée dans la Fig. 8 (d), montrant clairement l'évolution du contenu fréquentiel des chirps individuels (c'est-à-dire S_1 et S_2) avec une très haute définition. Le spectrogramme récupéré est en excellent accord avec celui attendu pour le SUT d'entrée. En théorie, chaque spectre est mesuré avec $q = 139$ points d'analyse. Les résultats confirment la capacité de la configuration démontrée à fournir une analyse spectrale en temps réel sans interruption avec une largeur de bande de fréquence instantanée approchant 100 GHz, une résolution de fréquence de 660 MHz et une résolution temporelle de 1.5 ns, à une vitesse de 666×10^6 FTs par seconde, dépassant les capacités des plateformes actuelles basées sur DSP électronique.

04.4. LA POLYVALENCE DU SPECTROGRAMME TAI PROPOSE

Nous notons que les spécifications du spectrogramme temporel (*Time-mapped spectrogram,* TM-SP) peuvent également être obtenues en ajustant simultanément la phase temporelle et la dispersion. Pour ce faire, nous remplaçons le LCFBG par une dispersion plus importante $\ddot{\Phi}_0 \sim 15{,}494\ \mathrm{ps}^2/\mathrm{rad}$. Le modèle de modulation de phase temporelle est conçu avec $q = 836$ niveaux de phase, chacun ayant une longueur de $t_s \sim 10.8\ \mathrm{ps}$ et la longueur de la période est $T_r = 9\ \mathrm{ns}$. Cela nous permet d'obtenir une résolution de fréquence plus étroite (c'est-à-dire $\delta\omega_{res} \sim 2\pi \times 110\ \mathrm{MHz}$) tout en maintenant la largeur de bande d'analyse complète à $1/t_s$~~92 GHz, ce qui correspond à ~836 points d'analyse par spectre. Comme le montre la Fig. 9 (a) et (b), le SUT est constitué de deux chirps linéaires croisés, l'un variant de 0.12 à 10 GHz et vice versa pour l'autre dans l'intervalle de temps de 0 à 1 μs, et avec différentes interférences de fréquence (c1-c4) de durées temporelles variables. La fréquence des interférences varie de 8 GHz à 20 GHz.

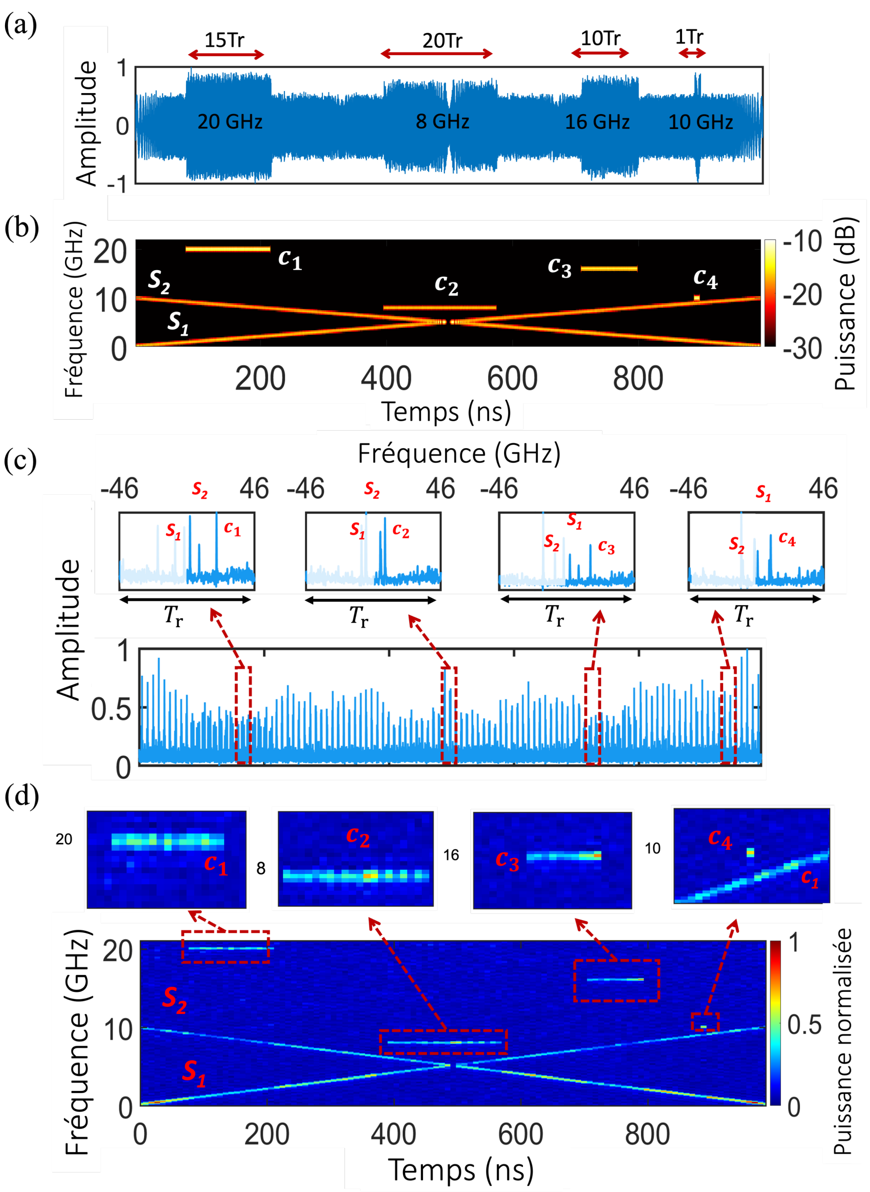

Fig. 9. Démonstration expérimentale d'une résolution de fréquence fine. (a) Forme d'onde temporelle mesurée du SUT. (b) Intensité du STFT numérique, ou spectrogramme, du SUT. (c) Trace TM-SP mesurée à la sortie du schéma STFT. (d) Une représentation 2D du TM-SP mesuré et les gros plans des sections d'interférence.

Comme le montrent les Fig. 9 (c) et (d), le TM-SP permet une identification précise des chirps individuels (c'est-à-dire S_1 et S_2) et des interférences de fréquence de l'objet sous test aux emplacements temporels et fréquentiels prescrits, avec les gros plans des sections d'interférence. L'axe supérieur de chaque graphique zoomé correspond à l'axe de la fréquence relative équivalente. Ce résultat confirme la polyvalence du spectrogramme temporel proposé.

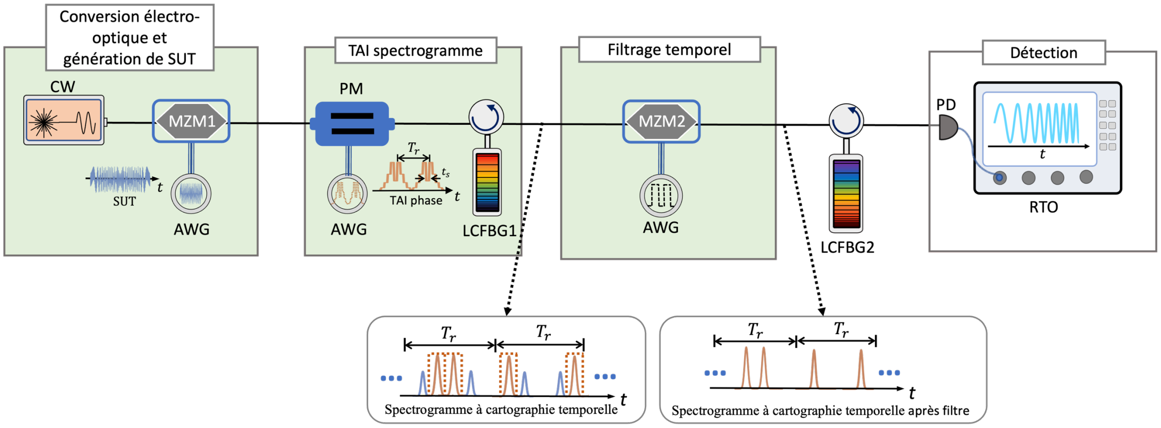

Fig. 10. Principe et configuration expérimentale du système de filtrage de fréquence variant dans le temps proposé. Le schéma implique (i) la conversion du signal électrique vers le domaine optique, (ii) TM-SP basé sur TAI et (iii) le filtre de fréquence variant dans le temps. Les lignes en pointillés montrent la forme d'onde de filtrage temporel conçue pour filtrer les composants cibles (c'est-à-dire l'un des composants de la chirp) dans le domaine temps-fréquence.

05. MANIPULATION TEMPS-FRÉQUENCE

Dans cette section, nous proposons une manipulation en temps réel, définie par l'utilisateur, du spectrogramme obtenu en utilisant les techniques de modulation temporelle disponibles.

Comme décrit ci-dessus, nous avons réussi à cartographier le spectre du SUT dans le domaine temporel. Ainsi, nous avons un accès direct aux informations spectrales changeantes des signaux, ce qui permet une manipulation précise du contenu fréquentiel variable dans le temps du signal en utilisant les méthodes de modulation temporelle disponibles, par exemple un MZM électro-optique. Pour traiter la forme d'onde STFT cartographiée dans le temps, les modèles de modulation temporelle sont prédéfinis conformément à la loi de mappage fréquence-temps évoquée ci-dessus. En général, le masque de filtrage temporel peut être exprimé mathématiquement comme suit :

$$h(t) = \sum_p \sum_k \left[a_{pk} \operatorname{rect}\left(\frac{t-\frac{T_r}{2}\pm\Delta t_{pk}+pT_r}{\Delta t_{filt}}\right) + \operatorname{rect}\left(\frac{t-\frac{T_r}{2}+pT_r}{\Delta t_{filt}}\right)\right]_{\Delta t_{pk}=\Delta\omega_{pk}/\ddot{\phi}} \qquad (10)$$

où t définit la variable temporelle du modèle temporel, $\operatorname{rect}\left(\frac{t-T}{\Delta t}\right)$ désigne une fonction rectangulaire centrée sur T et s'étendant sur une durée totale de Δt, et pT_r identifie la position temporelle centrale de chacune des périodes d'analyse (avec $p = 0, \pm 1, \pm 2, \ldots$).

05.1. DÉMONSTRATION EXPÉRIMENTALE DE LA FRÉQUENCE CENTRALE ACCORDABLE

Une expérience de validation du concept est réalisée sur la base de la conception illustrée à la Fig. 10. Dans l'expérience, nous utilisons la même configuration que pour le spectrogramme temporel du SUT

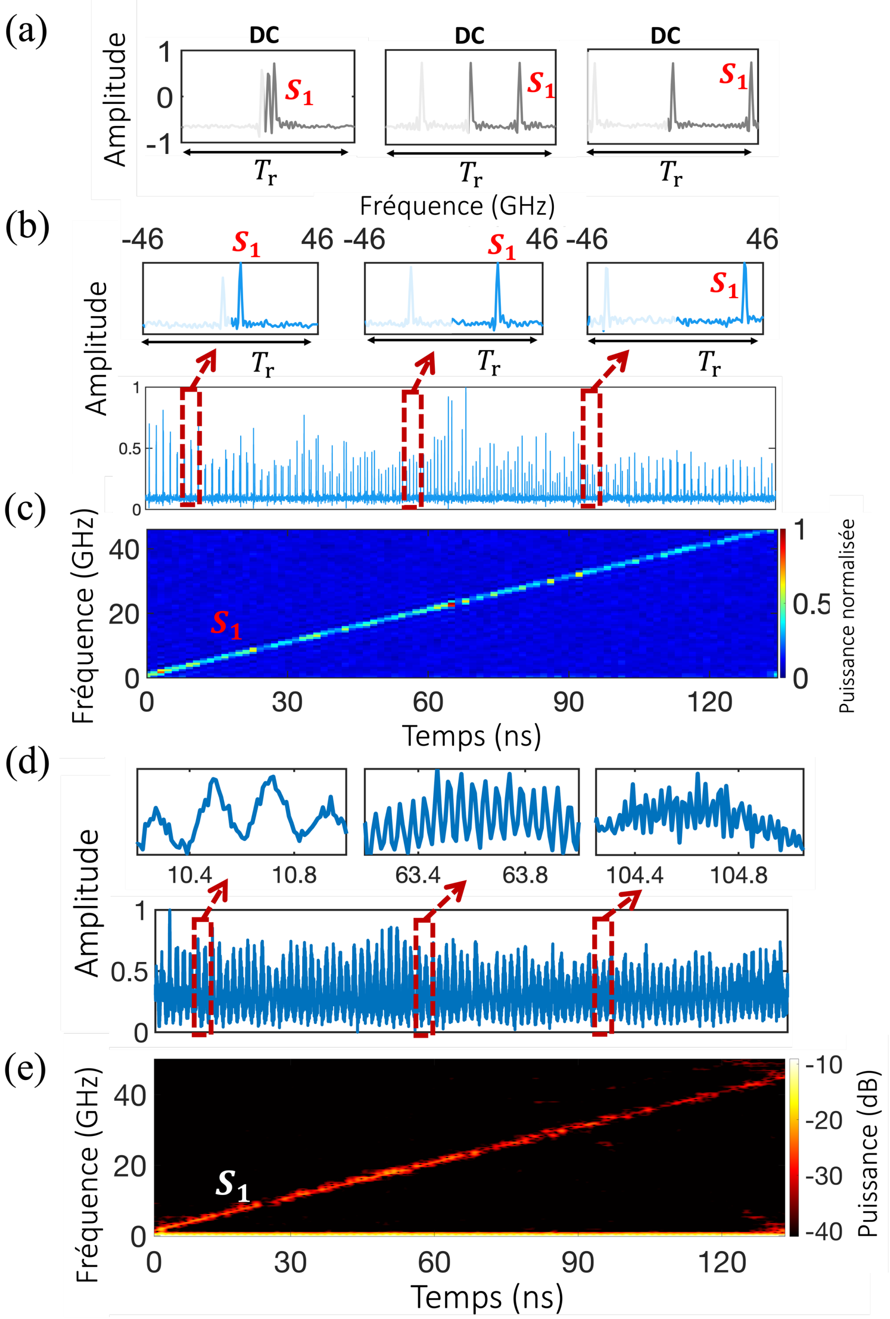

Fig. 11. Résultats expérimentaux du filtrage temps-fréquence. (a) Trois zooms du motif de filtrage temporel. (b) Le spectrogramme temps-cartographié après le filtrage T-F. (c) Représentation 2D du spectrogramme temps-cartographié filtré. (d) Le signal récupéré après le second élément dispersif. (e) Spectrogramme STFT numérique du signal récupéré.

illustré à la Fig. 7, avec les mêmes spécifications des dispositifs. Le modèle de filtrage temporel est généré à partir du même AWG modulé sur le spectrogramme temporel, en utilisant un deuxième MZM avec une largeur de bande de 40 GHz. Ensuite, la forme d'onde filtrée temporellement se propage à travers un deuxième milieu dispersif mis en œuvre via un autre LCFBG avec une dispersion exactement opposée à celle du premier et le signal filtré résultant est enregistré à la sortie.

Nous ciblons d'abord le filtrage (c'est-à-dire la sélection) d'une seule composante de chirp linéaire à partir du signal hyperfréquence à double chirp illustré à la Fig. 8. Pour réaliser l'opération de filtrage T-F souhaitée, le masque de filtrage temporel, illustré à la Fig. 11 (a), est conçu pour sélectionner les impulsions correspondantes. Le modèle de filtrage est ensuite reconfiguré tous les T_r, c'est-à-dire à une vitesse d'accord de $1/T_r$~660 MHz. La Fig. 11 (a) montre trois zooms du schéma de filtrage temporel, avec chaque largeur d'impulsion de t_s~ 10.8 ps, reconfigurée toutes les T_r = 1.5 ns. La Fig. 11 (b) montre la forme d'onde temporelle mesurée à la sortie du MZM utilisé pour le filtrage T-F. Les impulsions représentant les composantes de fréquence de S_2 sont fortement réduites par rapport aux composantes de S_1, comme le montre la représentation du TM-SP résultant dans la Fig. 11 (c). Enfin, la forme d'onde micro-ondes filtrée

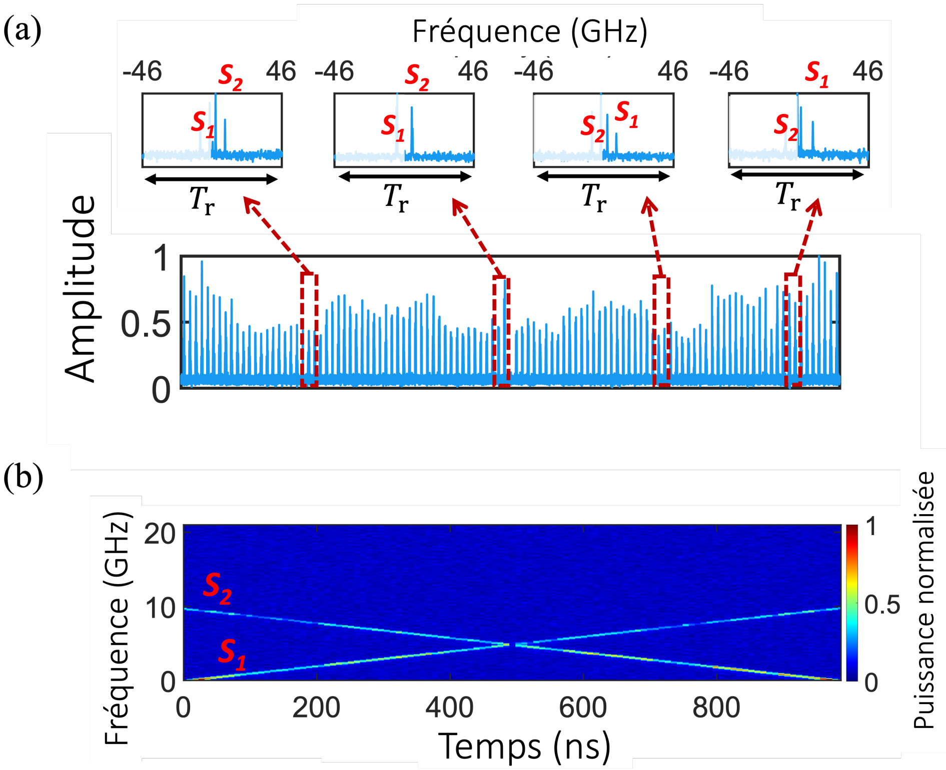

Fig. 12. Résultats expérimentaux de la manipulation temps-fréquence. (a) Le spectrogramme temps-cartographié après le filtrage T-F. (b) Représentation 2D du spectrogramme temps-cartographié filtré.

par T-F est récupérée en passant à travers un deuxième LCFBG avec une dispersion de $\ddot{\Phi}_0 \sim -2{,}600\ \mathrm{ps}^2/\mathrm{rad}$ et le signal micro-ondes traité mesuré est représenté à la Fig. 11 (d). Le spectrogramme numérique correspondant du signal mesuré traité est également illustré à la Fig. 11 (e). Si l'on compare avec les résultats de la Fig. 8, il est évident que S_2 est presque supprimé et qu'un chirp linéaire pur avec une fréquence croissante (composante S_1) est récupéré avec succès.

Le résultat suivant vise à réaliser un filtre temps-fréquence avec une sélectivité de fréquence fine (c'est-à-dire 110 MHz). Pour faciliter l'évaluation, les résultats capturés dans la Fig. 9 sont utilisés pour le filtrage temporel suivant. Nous visons ici à supprimer un ensemble d'interférences spectrales indésirables changeant le long d'un signal doublement chirpé à large bande. Afin de sélectionner les deux formes d'onde chirpées (S_1 et S_2), deux impulsions rectangulaires dont les positions temporelles varient en fonction du facteur de mappage fréquence-temps sont mises en œuvre dans chaque fenêtre temporelle d'analyse T_r. La largeur temporelle de chaque impulsion de filtrage est fixée à $t_s \sim 10.8$ ps pour manipuler avec précision la forme d'onde correspondante cartographiée dans le temps. Les Fig. 12 (a) et (b) montrent la trace TM-SP mesurée après le processus de filtrage temporel, ainsi que la représentation 2D correspondante. Comme prévu, le système présente une sélectivité suffisamment élevée pour éliminer efficacement l'interférence c_4 qui est espacé de 1 GHz par rapport à la forme d'onde doublement chirpé.

06. ÉVALUATION DE LA RÉPONSE EN FRÉQUENCE DU FILTRE TEMPS-FRÉQUENCE

Pour fournir des preuves supplémentaires sur la reconfigurabilité de la réponse spectrale fournie par le schéma de filtrage dynamique, en termes de forme de bande passante, de largeur de bande et de fréquence de réglage, nous avons réalisé une caractérisation standard de la réponse spectrale RF du schéma de photonique micro-ondes figurant à la Fig. 13. Un analyseur de réseau vectoriel (VNA) à bande passante de 50 GHz a été utilisé pour fournir le signal RF avec une fréquence balayée de 10 MHz à 50 GHz. Afin de démontrer la caractérisation du filtre proposé avec la plus grande largeur de bande de fonctionnement, la phase TAI est réglée avec $t_s \sim$ 10.8ps, T_r = 1.5 ns. Et une paire de LCFBGs avec la dispersion correspondante est utilisée. Le signal micro-onde récupéré est connecté à l'entrée du VNA pour mesurer la réponse en fréquence du système.

Les paramètres S_{21} mesurés par le VNA pour différentes réponses de filtrage sont présentés à la Fig. 14. Dans la Fig. 14 (a), nous programmions la forme d'onde de filtrage temporel pour qu'elle consiste en une impulsion de forme rectangulaire, avec une largeur temporelle de $5 \times t_s$ et une localisation temporelle

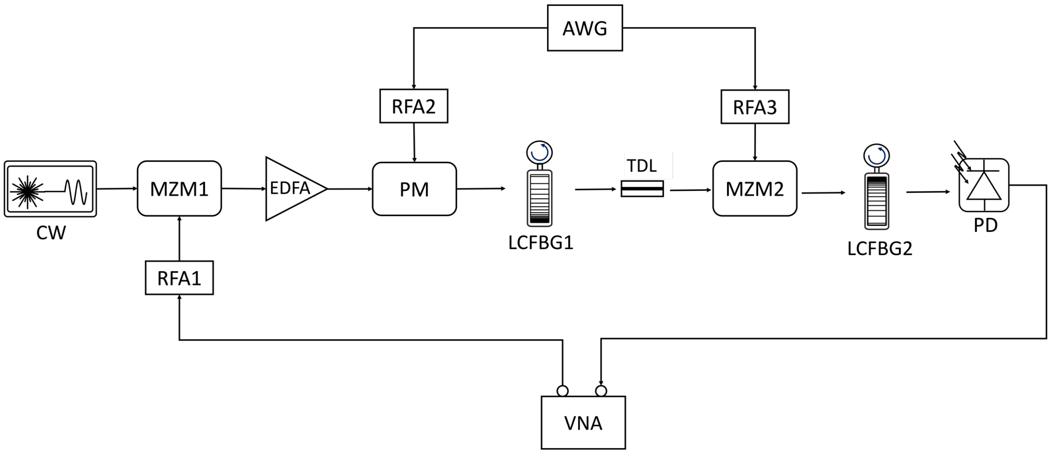

Fig. 13. La configuration pour mesurer la réponse d'amplitude spectrale du filtre photonique micro-onde implémenté à l'aide d'un schéma standard basé sur un VNA. MZM : Modulateur électro-optique Mach-Zehnder, EDFA : Amplificateur à fibre dopée erbium, PM : Modulateur de phase électro-optique, RFA : Amplificateur RF, AWG : Générateur de forme d'onde arbitraire, LCFBG : Réseau de Bragg à fibre à chirpement linéaire, TDL : Ligne à retard optique accordable, PD : Photodiode, RTO : Oscilloscope en temps réel, VNA : Analyseur de réseau vectoriel.

réglable, ce qui correspond à une réponse spectrale passe-bande avec une bande passante à 3 dB de 4 GHz et une fréquence centrale réglable de 10 à 46 GHz. La réponse en fréquence mesurée montre clairement le réglage de la fréquence centrale avec une bande passante de 4 GHz. Pour mettre en évidence davantage la polyvalence de notre schéma proposé, c'est-à-dire la capacité de répondre à une forme de réponse et une largeur de bande de fréquence reconfigurables, nous avons redéfini le motif de filtrage avec une impulsion de forme semblable à une fonction sinc. Les résultats à la Fig. 14 (b) confirment que la réponse en fréquence correspondante du système suit également une forme semblable à une fonction sinc avec une bande passante réglable de 1 GHz à 3 GHz.

Ainsi, nous avons démontré que le système de filtrage proposé présente une large bande passante d'opération anticipée et une réponse en fréquence reconfigurable en termes de fréquence centrale, de bande passante, de forme et de vitesse de réglage. Il convient de noter que le réglage de fréquence et de bande passante est effectué par étapes discrètes dans la Fig. 14, bien que généralement, un réglage continu pourrait être réalisé en concevant correctement le motif de filtrage.

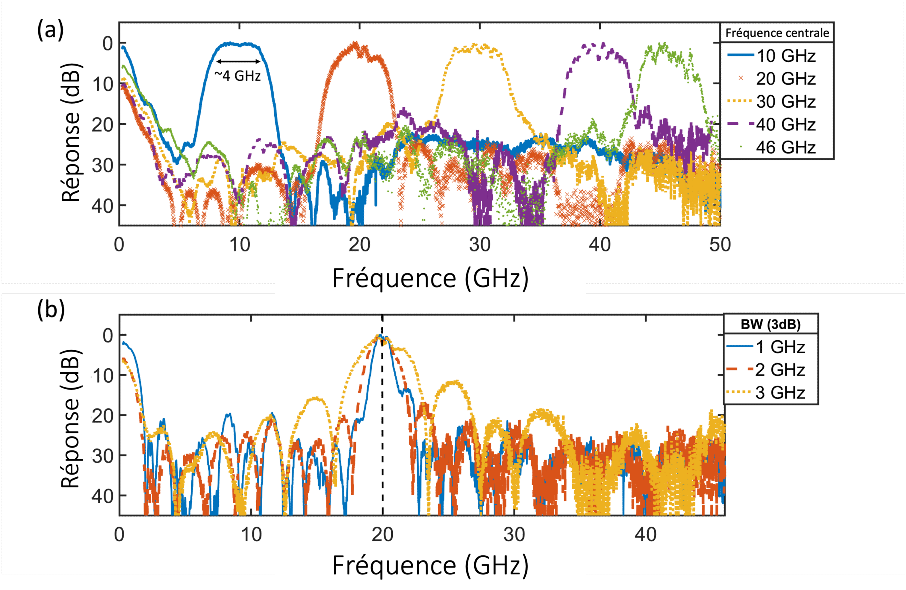

Fig. 14. Réponse en fréquence mesurée du filtre de photonique micro-onde démontré, avec (a) fréquence centrale reconfigurable, (b) largeur de bande et forme.

07. RÉSUMÉ

Cette thèse introduit le principe mathématique des deux principaux dispositifs : le milieu dispersif du second ordre et la lentille temporelle, utilisés dans la méthode proposée d'analyse et de traitement du signal. Le mécanisme physique, les caractéristiques principales et les implémentations pratiques ont été analysés, fournissant une compréhension approfondie de ces deux unités. Ensuite, la relation entre le temps et la fréquence a été explorée et l'équivalence entre la propagation du GVD et la modulation TL pour tout signal d'entrée donné a été proposée.

Sur cette base, une plateforme photonique pratique pour l'analyse en temps réel du spectrogramme a été proposée et démontrée, en utilisant les deux unités, c'est-à-dire la lentille temporelle et le milieu dispersif. L'analyse mathématique générale et les compromis du spectrogramme basé sur TAI ont été discutés. Un certain nombre de résultats numériques et expérimentaux ont été réalisés pour vérifier les caractéristiques du schéma proposé. Le spectrogramme basé sur TAI démontré a atteint des spécifications de performance sans précédent, à savoir :

- Largeur de bande d'analyse en temps réel jusqu'à ~100 GHz,
- Résolution temporelle dans le régime des nanosecondes,
- Fine résolution fréquentielle jusqu'au niveau des MHz,
- Spécifications reconfigurables définies par l'utilisateur.

Ces spécifications de performance répondent aux exigences strictes de l'analyse temps-fréquence pour une large gamme d'applications, notamment dans les domaines des communications, des technologies Radar/Lidar, des télécommunications et de la biomédecine. De plus, les spécifications de performance du spectrogramme basé sur TAI atteintes dans ce projet doctoral peuvent facilement être améliorées pour des bandes passantes d'analyse instantanée beaucoup plus élevées, jusqu'au domaine des térahertz, en utilisant des modulateurs de phase électro-optiques ultralarges [1] ou des mécanismes de modulation de phase temporelle non linéaires, tels que ceux basés sur la modulation croisée à phase croisée Kerr ou le mélange à quatre ondes dans des fibres ou guides d'ondes hautement dispersifs [2].

La distribution temps-fréquence obtenue a ensuite été manipulée en utilisant un modulateur Mach-Zehnder électro-optique. Comme la distribution T-F (la transformée de Fourier à court terme) de l'onde entrante a été cartographiée le long du domaine temporel, de manière continue et sans écart, cela permet ensuite une manipulation définie par l'utilisateur de la distribution T-F directement dans le domaine temporel. La manipulation temps-fréquence a été démontrée avec une large bande passante d'opération, de hautes résolutions temporelles et fréquentielles, ainsi qu'un degré de polyvalence sans précédent. Une application de ce schéma pour la mitigation des termes d'interférence de fréquence changeant rapidement le long d'une onde à grande vitesse et la synthèse directe de formes d'onde rapides avec des distributions T-F personnalisées a également été démontrée. La méthode rapportée représente une avancée significative dans la manipulation des propriétés T-F des ondes EM et répond aux exigences strictes de nombreuses applications modernes et émergentes.

Références

[1] L. R. Chen, P. Moslemi, Z. Wang, M. Ma, and R. Adams, "Integrated Microwave Photonics for Spectral Analysis, Waveform Generation, and Filtering," *IEEE Photonics Technol. Lett.*, vol. 30, no. 21, pp. 1838–1841, Nov. 2018, doi: 10.1109/LPT.2018.2861703.

[2] L. R. Cortés, D. Onori, H. G. de Chatellus, M. Burla, and J. Azaña, "Towards on-chip photonic-assisted radio-frequency spectral measurement and monitoring," *Optica*, vol. 7, no. 5, pp. 434–447, May 2020, doi: 10.1364/OPTICA.383247.

[3] X. Zou, B. Lu, W. Pan, L. Yan, A. Stöhr, and J. Yao, "Photonics for microwave measurements," *Laser Photonics Rev.*, vol. 10, no. 5, pp. 711–734, 2016, doi: 10.1002/lpor.201600019.

[4] Shilong Pan and Y. Zhang, "Microwave Photonic Radars," *J. Light. Technol.*, vol. 38, no. 19, pp. 5450–5484, Oct. 2020.

[5] P. G. Stoica, R. Moses, P. Stoica, and R. L. Moses, *Spectral analysis of signals*. Upper Saddle River, NJ: Pearson, Prentice Hall, 2005.

[6] P. Zuo, D. Ma, and Y. Chen, "Short-Time Fourier Transform Based on Stimulated Brillouin Scattering," *J. Light. Technol.*, vol. 40, no. 15, pp. 5052–5061, Aug. 2022, doi: 10.1109/JLT.2022.3174552.

[7] C. Zhang, J. Xu, P. C. Chui, and K. K. Y. Wong, "Parametric spectro-temporal analyzer (PASTA) for real-time optical spectrum observation," *Sci. Rep.*, vol. 3, no. 1, p. 2064, Jun. 2013, doi: 10.1038/srep02064.

[8] S. R. Konatham *et al.*, "Real-time gap-free dynamic waveform spectral analysis with nanosecond resolutions through analog signal processing," *Nat. Commun.*, vol. 11, no. 1, p. 3309, Jul. 2020, doi: 10.1038/s41467-020-17119-2.

[9] B. Crockett, M. L. Connor Rowe, and J. Azaña, "Real-time spectral characterization of THz-bandwidth waveforms by unwrapping a time-lens spectrogram," in *2023 Photonics North (PN)*, Jun. 2023, pp. 1–2. doi: 10.1109/PN58661.2023.10223063.

[10] X. Xie, J. Li, F. Yin, K. Xu, and Y. Dai, "STFT Based on Bandwidth-Scaled Microwave Photonics," *J. Light. Technol.*, vol. 39, no. 6, pp. 1680–1687, Mar. 2021.

[11] B. Crockett, L. R. Cortés, R. Maram, and J. Azaña, "Optical signal denoising through temporal passive amplification," *Optica*, vol. 9, no. 1, pp. 130–138, Jan. 2022, doi: 10.1364/OPTICA.428727.

[12] J. Huh and J. Azana, "All-Optical Reconfigurable Signal Processing Based on Cross Phase Modulation Time Lensing," *IEEE Photonics Technol. Lett.*, vol. 29, no. 10, pp. 826–829, May 2017, doi: 10.1109/LPT.2017.2687826.

[13] H. Guillet De Chatellus, L. R. Cortés, and J. Azaña, "Optical real-time Fourier transformation with kilohertz resolutions," *Optica*, vol. 3, no. 1, p. 1, Jan. 2016, doi: 10.1364/OPTICA.3.000001.

[14] A. Mahjoubfar, D. V. Churkin, S. Barland, N. Broderick, S. K. Turitsyn, and B. Jalali, "Time stretch and its applications," *Nat. Photonics*, vol. 11, no. 6, pp. 341–351, Jun. 2017, doi: 10.1038/nphoton.2017.76.

[15] H. Huang *et al.*, "Experimental observation of the spectral self-imaging effect with a four-wave mixing time lens," *Opt. Lett.*, vol. 48, no. 6, pp. 1522–1525, Mar. 2023, doi: 10.1364/OL.485428.

[16] J. Norgard and G. L. Best, "The Electromagnetic Spectrum," in *National Association of Broadcasters Engineering Handbook*, 11th ed., Routledge, 2017.

[17] Y. I. A. Al-Yasir, N. Ojaroudi Parchin, R. A. Abd-Alhameed, A. M. Abdulkhaleq, and J. M. Noras, "Recent Progress in the Design of 4G/5G Reconfigurable Filters," *Electronics*, vol. 8, no. 1, Art. no. 1, Jan. 2019, doi: 10.3390/electronics8010114.

[18] P. Ghelfi *et al.*, "A fully photonics-based coherent radar system," *Nature*, vol. 507, no. 7492, Art. no. 7492, Mar. 2014, doi: 10.1038/nature13078.

[19] W. A. Majid *et al.*, "A Bright Fast Radio Burst from FRB 20200120E with Sub-100 Nanosecond Structure," *Astrophys. J. Lett.*, vol. 919, no. 1, p. L6, Sep. 2021, doi: 10.3847/2041-8213/ac1921.

[20] H. Sun, A. Nallanathan, C.-X. Wang, and Y. Chen, “Wideband spectrum sensing for cognitive radio networks: a survey,” *IEEE Wirel. Commun.*, vol. 20, no. 2, pp. 74–81, Apr. 2013, doi: 10.1109/MWC.2013.6507397.

[21] H. Shao *et al.*, “An Investigation of Spectral Band Selection for Hyperspectral LiDAR Technique,” *Electronics*, vol. 9, no. 1, Art. no. 1, Jan. 2020, doi: 10.3390/electronics9010148.

[22] B. Wang and K. J. R. Liu, “Advances in cognitive radio networks: A survey,” *IEEE J Sel Top Signal Process*, vol. 5, no. 1, pp. 5–23, Feb. 2011, doi: 10.1109/JSTSP.2010.2093210.

[23] I. de Miguel *et al.*, “Cognitive dynamic optical networks,” *J. Opt. Commun. Netw.*, vol. 5, no. 10, pp. A107–A118, Oct. 2013, doi: 10.1364/JOCN.5.00A107.

[24] Q. Liu and M. P. Fok, “Ultrafast and Wideband Microwave Photonic Frequency-Hopping Systems: A Review,” *Appl. Sci. Res.*, vol. 10, no. 2, Art. no. 2, Jan. 2020, doi: 10.3390/app10020521.

[25] G. Serafino *et al.*, “Toward a New Generation of Radar Systems Based on Microwave Photonic Technologies,” *J. Light. Technol.*, vol. 37, no. 2, pp. 643–650, Jan. 2019, doi: 10.1109/JLT.2019.2894224.

[26] S. R. Thummaluru, M. Ameen, and R. K. Chaudhary, “Four-Port MIMO Cognitive Radio System for Midband 5G Applications,” *IEEE Trans. Antennas Propag.*, vol. 67, no. 8, pp. 5634–5645, Aug. 2019, doi: 10.1109/TAP.2019.2918476.

[27] D. Ma and Y. Chen, “Time-varying microwave photonic filter for arbitrary waveform signal-to-noise ratio improvement,” *Opt. Lett.*, vol. 47, no. 9, pp. 2186–2189, May 2022, doi: 10.1364/OL.455019.

[28] H.-J. Kim, D. E. Leaird, and A. M. Weiner, “Rapidly Tunable Dual-Comb RF Photonic Filter for Ultrabroadband RF Spread Spectrum Applications,” *IEEE Trans. Microw. Theory Tech.*, vol. 64, no. 10, pp. 3351–3362, Oct. 2016, doi: 10.1109/TMTT.2016.2599162.

[29] Y. Sun, S. Wang, J. Chen, and G. Wu, “Fast and large-range frequency hopping receiving based on simultaneous photonic filtering and digitizing,” *Opt. Lett.*, vol. 46, no. 4, pp. 749–752, Feb. 2021, doi: 10.1364/OL.415003.

[30] E. H. W. Chan and R. A. Minasian, “High-Resolution Tunable RF/Microwave Photonic Notch Filter With Low-Noise Performance,” *J. Light. Technol.*, vol. 29, no. 21, pp. 3304–3309, Nov. 2011, doi: 10.1109/JLT.2011.2167957.

[31] B. Boashash, *Time-Frequency Signal Analysis and Processing: A Comprehensive Reference*. Academic Press, 2015.

[32] “RSA7100B.” Accessed: Jun. 22, 2024. [Online]. Available: https://www.tek.com/en/datasheet/rsa7100b-rsa7100b-spectrum-analyzer-datasheet

[33] F. Khan and M. I. Younis, “RF MEMS electrostatically actuated tunable capacitors and their applications: a review,” *J. Micromechanics Microengineering*, vol. 32, no. 1, p. 013002, Dec. 2021, doi: 10.1088/1361-6439/ac3cd5.

[34] K. Song, W. Chen, S. R. Patience, Y. Chen, A. M. Iman, and Y. Fan, “Compact Wide-Frequency Tunable Filter With Switchable Bandpass and Bandstop Frequency Response,” *IEEE Access*, vol. 7, pp. 47503–47508, 2019, doi: 10.1109/ACCESS.2019.2908453.

[35] A. M. Weiner, “Ultrafast optical pulse shaping: A tutorial review,” *Opt. Commun.*, vol. 284, no. 15, pp. 3669–3692, Jul. 2011, doi: 10.1016/j.optcom.2011.03.084.

[36] D. Pérez-López, A. López, P. DasMahapatra, and J. Capmany, “Multipurpose self-configuration of programmable photonic circuits,” *Nat. Commun.*, vol. 11, no. 1, Art. no. 1, Dec. 2020, doi: 10.1038/s41467-020-19608-w.

[37] J. Yao, “Photonics to the Rescue: A Fresh Look at Microwave Photonic Filters,” *IEEE Microw. Mag.*, vol. 16, no. 8, pp. 46–60, Sep. 2015, doi: 10.1109/MMM.2015.2441594.

[38] S. Reddy, R. Maram, and J. Azaña, “On-the-Fly Time Mapped Full Spectrogram Analysis of High-Speed Non-Stationary Microwave Signals,” in *2018 European Conference on Optical Communication (ECOC)*, Sep. 2018, pp. 1–3. doi: 10.1109/ECOC.2018.8535112.

[39] D. Ma and Y. Chen, “Time-varying microwave photonic filter for arbitrary waveform signal-to-noise ratio improvement,” *Opt. Lett.*, vol. 47, no. 9, pp. 2186–2189, May 2022, doi: 10.1364/OL.455019.

[40] V. R. Supradeepa *et al.*, “Comb-based radiofrequency photonic filters with rapid tunability and high selectivity,” *Nat. Photonics*, vol. 6, no. 3, Art. no. 3, Mar. 2012, doi: 10.1038/nphoton.2011.350.

[41] D. Pérez-López, A. López, P. DasMahapatra, and J. Capmany, “Multipurpose self-configuration of programmable photonic circuits,” *Nat. Commun.*, vol. 11, no. 1, Art. no. 1, Dec. 2020, doi: 10.1038/s41467-020-19608-w.

[42] S. R. Konatham, B. Crockett, L. R. Cortés, and J. Azaña, “On-the-fly continuous time varying frequency filtering of broadband microwave signals,” in *45th European Conference on Optical Communication (ECOC 2019)*, Sep. 2019, pp. 1–4. doi: 10.1049/cp.2019.0837.

[43] B. H. Kolner and M. Nazarathy, “Temporal imaging with a time lens,” *Opt. Lett.*, vol. 14, no. 12, pp. 630–632, Jun. 1989, doi: 10.1364/OL.14.000630.

[44] J. Azaña, N. K. Berger, B. Levit, and B. Fischer, “Spectral Fraunhofer regime: time-to-frequency conversion by the action of a single time lens on an optical pulse,” *Appl. Opt.*, vol. 43, no. 2, pp. 483–490, Jan. 2004, doi: 10.1364/AO.43.000483.

[45] X. Zhu, L. R. Cortés, and J. Azaña, “Group-velocity dispersion emulator using a time lens,” *Opt. Lett.*, vol. 46, no. 23, pp. 5974–5977, Dec. 2021, doi: 10.1364/OL.444211.

[46] J. Azaña and X. Zhu, “Optical Time-Mapped Spectrograms (I): From the Time-Lens Fourier Transformer to the Talbot-Based Design,” *J. Light. Technol.*, vol. 41, no. 14, pp. 4609–4623, Jul. 2023, doi: 10.1109/JLT.2023.3243531.

[47] L. Romero Cortés, R. Maram, H. Guillet de Chatellus, and J. Azaña, “Arbitrary Energy-Preserving Control of Optical Pulse Trains and Frequency Combs through Generalized Talbot Effects,” *Laser Photonics Rev.*, vol. 13, no. 12, p. 1900176, 2019, doi: 10.1002/lpor.201900176.

[48] J. Azaña, X. Zhu, C. Rowe, and B. Crockett, “Optical Time-Mapped Spectrograms (II): Fractional Talbot Designs,” *J. Light. Technol.*, pp. 1–12, 2023, doi: 10.1109/JLT.2023.3260706.

[49] A. V. Oppenheim, A. S. Willsky, and S. H. Nawab, *Signals & Systems*. Pearson Educación, 1997.

[50] J. Azaña and X. Zhu, “Optical Time-Mapped Spectrograms (I): From the Time-Lens Fourier Transformer to the Talbot-Based Design,” *J. Light. Technol.*, vol. 41, no. 14, pp. 4609–4623, Jul. 2023, doi: 10.1109/JLT.2023.3243531.

TABLE DES MATIÈRES

LISTE DES FIGURES

LISTE DES ABRÉVIATIONS

EM	Electromagnetic
SUT	Signal Under Test
RF	Radio Frequency
CW	Continuous-Wave
PM	Phase Modulator
MZI	Mach–Zehnder Interferometer
MZM	Mach-Zehnder Modulator
I/Q	In-phase/Quadrature
BW	BandWidth
ER	Extinction Ratio
FT	Fourier Transform
RC	Resistor-Capacitor
CMOS	Complementary Metal-Oxide Semiconductor
MPF	Microwave Photonic Filter
T-F	Time-Frequency
STFT	Short-Time Fourier Transform
SP	Spectrogram
RT-SA	Real-time Fourier Spectral Analysis
TVF	Time-Varying filter
DSP	Digital Signal Processing
MWP	Microwave Photonics
ADC	Analog-to-Digital Converter
FFT	Fast Fourier Transforms
FIR	Finite Impulse Response
IIR	Infinite Impulse Response
DAC	Digital-to-Analog Converter
RT-FT	Real-Time Fourier Transformation
SLM	Spatial Light Modulator
WS	WaveShaper
FBG	Fiber Bragg Grating
LCFBG	Linear Chirped fiber Bragg Grating
OFC	Optical Frequency Combs
SBS	Stimulated Brillouin Scattering

DCF	Dispersion Compensation Fiber
GVD	Group-Velocity Dispersion
TL	Time Lens
XPM	Cross-Phase Modulation
SMF	Single Mode Fiber
FWHM	Full-Width at Half-Maximum
TDL	Tunable Delay Line
TAI	Talbot Array Illuminator
AWG	Arbitrary Waveform Generator
T-TAI	Temporal Talbot Array Illuminator
PD	Photo-Detector
TM-SP	Time-Mapped Spectrogram
EDFA	Erbium-Doped Fiber Amplifier
RFA	RF Amplifier
RTO	Real-Time Oscilloscope
VNA	Vector Network Analyzer
SNR	Signal to Noise Ratio
TPM	Temporal Phase Modulation
FWM	Four-Wave Mixing

ASSOCIATED PUBLICATIONS

Journal Articles

[J1] **X. Zhu**, and et. al., "Agile manipulation of the time-frequency distribution of high-speed electromagnetic waves." Nature Communication, under 2nd round reviewing.

[J2] **X. Zhu**, and et. al., "Group-velocity dispersion emulator using a time lens." *Optics Letters* 46, no. 23 (2021): 5974-5977.

[J3] J. Azaña, and **X. Zhu**. "Optical time-mapped spectrograms (I): from the time-lens Fourier transformer to the Talbot-based design." *Journal of Lightwave Technology* (2023).

[J4] J. Azaña, **X. Zhu**, C. ML Rowe, and B. Crockett. "Optical time-mapped spectrograms (II): Fractional Talbot designs." Journal of Lightwave Technology 41, no. 16 (2023): 5284-5295.

Conference Papers

[C1] **X. Zhu**, and et. al., “Broadband Microwave Photonic Filter with Full Reconfigurability and GHz-level Tuning Speed,” 2024 Summer Topicals Meeting Series (SUM).

[C2] **X. Zhu**, and et. al., “‘Time-varying Microwave Photonic Filter over 46-GHz Bandwidth with High Tuning Speed,” 2024 IEEE Research and Applications of Photonics in Defense Conference (RAPID).

[C3] **X. Zhu**, and et. al., "Microwave Photonic Filter with user-defined reconfigurability and high frequency-selectivity," 2023 International Topical Meeting on Microwave Photonics (MWP), Nanjing, China, pp. 1-4, 2023.

[C4] **X. Zhu**, and et. al, "Photonics-Based Real-Time Spectral Analysis Over 40-GHz Bandwidth with Fine Frequency Resolution," 2023 IEEE Research and Applications of Photonics in Defense Conference (RAPID), Miramar Beach, FL, USA, pp. 1-2, 2023.

[C5] **X. Zhu**, and et. al., “Photonics-enabled Nanosecond Scale Real-time Spectral Analysis with 92-GHz Bandwidth and MHz resolution”, Optical Fiber Communication Conference (OFC), 2023.

[C6] **X. Zhu**, and et. al., “Broadband and Fine-resolution Microwave Photonic Filtering with High-Speed Electronic Reconfigurability”, Optical Fiber Communication Conference (OFC), 2023.

[C7] **X. Zhu**, and et. al., “Microwave Photonic Filter with Rapid Tunability and Arbitrary Reconfigurability”, European Conference on Optical Communication (ECOC), 2023.

[C8] **X. Zhu**, and et. al., "Demonstration of dispersive waveform propagation tracking with a temporal phase modulator," 2020 IEEE Photonics Conference (IPC), Vancouver, BC, Canada, pp. 1-2, 2020.

[C9] **X. Zhu**, and et. al., "Experimental Demonstration of Dispersion Tracking Using a Temporal Phase Modulator," 2020 Photonics North (PN), Niagara Falls, ON, Canada, pp. 1-1, 2020.

[C10] **X. Zhu** and et. al., "Tracking the Dispersive Propagation of a Fast Waveform using a Temporal Phase Modulator," 2019 IEEE Photonics Conference (IPC), San Antonio, TX, USA, pp. 1-2, 2019.

Other publications not directly related to the thesis

[1] C. M.L. Rowe, B. Crockett, **X. Zhu**, J. Azaña, “Versatile Photonics Spectrograms for Ultrafast Real-Time Broadband Microwave Signal Analysis,” IEEE Transactions on Microwave Theory and Techniques. (2nd- round review).

[2] C. M.L. Rowe, B. Crockett, **X. Zhu**, J. Azaña, “Super-Bandwidth Detection using a Real-Time, Gapless Broadband Photonics Spectrogram with High Frequency Resolution,” 2024 IEEE Research and Applications of Photonics in Defense Conference (RAPID).

[3] M. Goodarzi, M. P. Fernandez, **X. Zhu** and J. Azaña, "Narrowband Optical Signal Denoising Through All-Fiber Temporal Talbot Effects," 2023 International Topical Meeting on Microwave Photonics (MWP), Nanjing, China, pp. 1-4, 2023.

[4] M. Goodarzi, M. P. Fernandez, **X. Zhu** and J. Azaña, "Narrowband Noise Filtering of Arbitrary Waveforms by Reversible In-Fiber Temporal Talbot Sampling,” Optical Fiber Communication Conference (OFC), 2023.

1 INTRODUCTION

This chapter reviews some preliminary methods and the concepts for signal analysis and processing that form the central part of the Thesis. It discusses the motivation for time-frequency analysis and manipulation and outlines various photonic-based methods for time-frequency analysis and dynamic filtering functions that enable time-frequency manipulation. The goals of the Thesis are established with the aim of overcoming some of the key limitations of previous time-frequency analysis and processing methods. The author's original contributions are briefly presented, and the structure of the thesis is outlined.

1.1 Signal Analysis and Processing

Electromagnetic (EM) waves serve as fundamental carriers of information across various applications. The core principle of this functionality is that information is often encoded in the variations of an EM wave. These variations may manifest as changes in amplitude, phase, frequency, or a combination of them, effectively carrying the information that is referred to as a signal. Typical variations in an EM wave that encode information occur either along the time domain or the frequency domain. The most intuitive variation is in time domain; in this case, the information is encoded in the properties of the wave—such as amplitude and phase—changing over time. For instance, the amplitude of the wave reflects how the signal energy is distributed along the time axis, while the phase corresponds to the temporal position of the information being encoded. These time-domain variations enable dynamic representation and transmission of data, which is crucial for real-time communication systems. On the other hand, encoding information in the frequency domain involves manipulating the relative weights of the different frequencies or colors of the EM wave. This means that instead of focusing on how the wave changes over time, this approach shows how the different frequency components are distributed. Specifically, a signal can be represented as a sum of sine waves of different frequencies, each weighted by a coefficient that indicates how the signal's energy is distributed over a range of frequencies. The frequency domain representation is particularly useful for understanding the spectral content of a signal and is often described by the signal's amplitude and/or phase as a function of frequency.

Once information is embedded within EM waves through various modulation techniques, one can extract and optimize the signal under test (SUT) for numerous applications, i.e., signal analysis and processing. Signal analysis involves the measurement and extraction of specific information or features from the waveform. This is typically necessary to identify and interpret target characteristics, content or properties of the signal. It provides a useful and important way to obtain deep insights into the desired information, including detecting patterns in time domain and identifying specific frequencies in the signal's spectrum. For instance, in radar systems, analysis is employed to detect echoes from targets, determine their distances, and ascertain their velocities based on the properties (amplitude, phase, etc.,) of reflected signals [1].

Signal processing, on the other hand, refers to the manipulation and enhancement of signal information, through various techniques and algorithms to modify, filter, and/or transform the signal to achieve specific objectives. This is essential in the field such as telecommunications. Where it is used to extract data from noisy channels to ensure reliable and high-quality communications [2]. Additionally, signal processing enables multiple functionalities, high performance, and fine-resolution capability for sensing, metrology, and quantum systems [3], [4], [5].

Thus, signal analysis and processing are essential for many important applications, particularly in communication systems, where signals are transmitted, received, and processed to enable seamless communication over long distances [6], [7]. Within these fields, the regime of signals from the microwave (radio frequency, RF) to the optical domain is of particular interest because these waves enable information encoding and manipulations at high speeds.

1.1.1 Temporal Signal Analysis and Processing

The manipulation of signal properties, such as amplitude and phase information along the time domain, is fundamental in signal analysis and processing, often achieved through temporal modulation methods. Temporal modulation of an EM wave can be accomplished through various mechanisms, enabling the efficient encoding and transmission of information across different media [8], [9], [10], [11], [12], [13], [14], [15]. Generally, temporal modulation involves alterting the amplitude and/or phase variation of an incoming signal along the time domain. Mathematically, the electric field of a continuous-wave (CW) light beam, or optical carrier, can be expressed as:

$$c(t) = A_0 e^{j(\omega_c t + \varphi_c)}, \tag{1.1}$$

where e is the Euler constant and $j = \sqrt{-1}$. A_0 is the amplitude of the carrier and ω_c is the angular frequency, and φ_c denotes the phase. Assuming a modulating signal $m(t)$ containing the information to be transmitted, the resulting modulated signal is the product of the optical carrier and the modulating signal:

$$y(t) = c(t) \cdot m(t). \tag{1.2}$$

Amplitude modulation varies the amplitude of the carrier signal in accordance with the modulating data or signal, while keeping the phase and frequency unchanged. To simplify the illustration shown in Fig. 1.1, the carrier signal can be described as the real part of $c(t)$, where $c(t)$ is complex-valued description used in the mathematical analysis throughout the thesis. Thus, the optical carrier manifests as a continuous sinusoidal wave with high angular frequency ω_c and constant amplitude A_0. In the example presented, the modulating signal is a sinusoidal wave with lower frequency. The resulting modulated signal exhibits a time-domain envelope resembling a copy of the modulating signal, while the central frequency remains the same as the carrier. Conversely, phase modulation introduces changes in phase to convey information. By encoding data into the phase of the carrier wave, phase modulation offers advantages such as robustness against amplitude variations, efficient use of bandwidth, and resilience to noise and interference. Due to the simplicity of envelope detection and processing, temporal modulation is widely used in optical fiber communications, signal processing, and sensing systems [16], [3], [15], [17], [18], [19], [20], [21] [22], [23], [24], [25]. Among these applications, a well-known technique involving temporal modulation is arbitrary waveform generation. Through modulating or shaping the complex (amplitude and/or phase) temporal profile of the incoming light wave, the output waveform exhibits the corresponding properties of

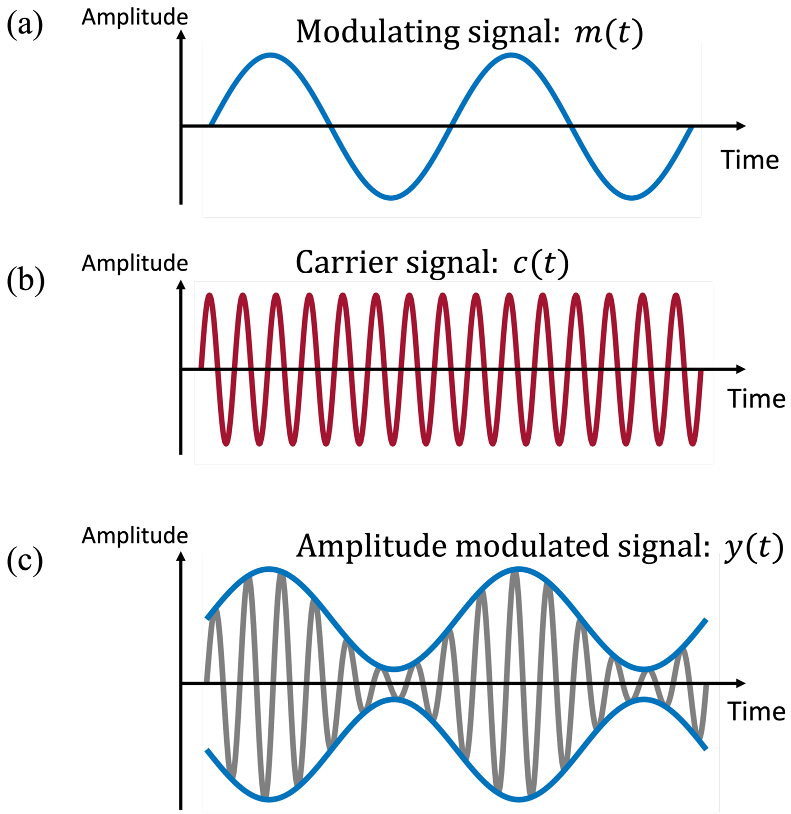

Figure 1.1. Illustration of temporal modulation. (a) Temporal waveform of the modulating signal. (b) Real part of the carrier signal. (c) Resulting amplitude modulated signal.

the modulating signal. This enables the generation of various output waveforms with desired features, achieving arbitrary waveform generation [26], [27], [28].

Optical or light waves are typically modulated using the nonlinearity of the materials. Specifically, optical modulation is often based on the electro-optic effect, where the refractive index of the material changes in response to the applied electric fields, thereby changing the phase of an optical carrier propagating through material. The refractive index change is directly proportional to the applied electric field magnitude [16]. This effect is known as Pockels effect and one of the most widely used material for the electro-optic effect is Lithium Niobate ($LiNbO_3$) crystal [29]. This allows customized phase modulation of the optical carrier with a phase shift that is directly proportional to the applied electrical voltage, known as electro-optic phase modulator (PM). To obtain intensity modulation, a Mach–Zehnder interferometer (MZI) structure is typically used. The input light is split into two arms of the MZI, and the optical wave in each arm undergoes different phase shifts induced by the applied voltages, respectively. When the optical waves from both arms recombine at the output, the phase difference between them causes constructive or destructive interference. This interference pattern converts the phase modulation into intensity modulation and this device is known as a Mach-Zehnder modulator (MZM), shown in Fig. 1.2. In more advanced communication systems, complex modulation schemes are generated using in-phase/quadrature (I/Q) modulators, which allow simultaneous modulation of amplitude and phase, enabling sophisticated modulation formats [30], [31].

Modulator performance is typically quantified by several key metrics, including modulation bandwidth (BW), extinction ratio (ER), half-wave voltage (V_π), etc [29], [32]. The BW of a modulator is typically defined as the range of frequencies over which the modulator can operate with acceptable performance, usually measured as the -3 dB bandwidth where the frequency response drops to half of its maximum value. Modulation BW is of utmost importance as it determines the ability to handle rapid variations of the modulating electric signal. This directly correlates with the highest bit rate that the modulator can support, which is essential for high-speed applications. Extinction ratio measures the contrast between the high-transmission (on) and low-transmission (off) levels, indicating the maximum depth of the modulation for a time-varying voltage. A higher ER is especially important in communication systems where accurate data transmission is required, ensuring the on and off states are distinctly different to minimize errors and avoid performance degradation. The required voltage to yield a phase change of π is known as the half-wave voltage or switching voltage V_π. The half-wave voltage directly influences the efficiency of the modulation process, and a lower V_π is preferred to reduce power consumption and optimize the performance of the modulator. Note that V_π is frequency-dependent and typically increases at high driving frequencies, affecting the modulator's effectiveness across different operational bandwidths [33].

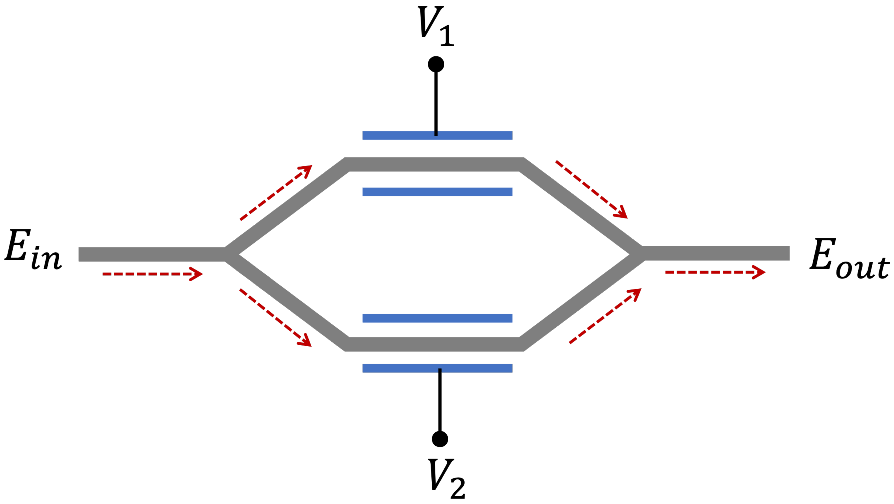

Figure 1.2. Schematic of Mach-Zehnder modulator (MZM). The MZM consists of two arms, with applied voltages V_1 and V_2, respectively.

Properly biasing the MZM is also crucial for achieving the required task. In order to ensure the MZM operates in a linear region, the bias is set at the quadrature bias point, where the phase difference between the two arms of the modulator is equal to π. $LiNbO_3$-based modulators offer large operation bandwidth far beyond 100 GHz [14], [34], [35], low power consumption with V_π down up to 1.4 V [14], [31], and a compact footprint [36], [37], making them an optimal choice for various applications in high-speed optical communications.

1.1.2 Frequency Spectrum Analysis and Processing

On the other hand, a temporal wave is often described using its frequency-domain (or Fourier transform) representation, which describes the relative complex weights among the frequency components of a wave [38]. Many important tasks (multiplexing, impairment mitigation etc. [4], [39], [40], [41]) require the wave to be manipulated in the frequency domain rather than in its temporal representation [1], [3], [42]. Manipulating the frequency spectrum of an input signal most often involves imposing a relative amplitude and/or phase weight among the different frequency components of the signal. This type of manipulation is time-invariant and is usually referred to as linear frequency filtering.

To manipulate the frequency components of a signal, it is essential to decompose the signal of interest into a sum of complex exponential components. To address this, Fourier transform (FT) is a fundamental mathematical tool that establishes the link between the time and frequency domain of representations [43]. The FT decomposes a temporal function or signal into a set of sine and cosine functions of varying frequencies, as shown in Fig. 1.3. Specifically, the frequency representation of a time domain signal $x(t)$ can be obtained through the FT using the following equation:

$$X(\omega) = FT(x(t)) = \int_{-\infty}^{+\infty} x(t)e^{-j\omega t}\, dt, \tag{1.3}$$

Here, $x(t)$ represents the variation over time of the signal under analysis and $X(\omega)$ is the frequency spectrum of $x(t)$. Access to the spectral components of a given signal allows one to manipulate/modify the characteristics of its characteristics in the frequency domain. By applying specific weights to the amplitude and phase of the target frequency components, we can tailor the output signal to meet the desired characteristics. This process can be mathematically described using the concept of a spectral transfer function. The spectral transfer function, denoted as $H(\omega)$, is a complex function that characterizes the filter's effect on the input signal in the frequency domain. It provides insight into how each frequency component of the input signal is processed in terms of both amplitude and phase. Since FT decomposes any arbitrary signal into a sum of complex exponentials weighted by its Fourier coefficients, the response of a linear frequency filter to an arbitrary input signal can be viewed as the modification of these Fourier coefficients according to the frequency response of the filter. The relationship between the input signal $X(\omega)$ and the output signal $Y(\omega)$ in the frequency domain is given by:

$$Y(\omega) = X(\omega) \cdot H(\omega), \tag{1.4}$$

where $Y(\omega)$ represents the output signal. $X(\omega)$ is the Fourier transform of the input signal, representing the signal in the frequency domain, as described in Eq. (1.3). $H(\omega)$ is the spectral transfer function of the filter, detailing the amplitude and/or phase modifications applied to the frequency components.

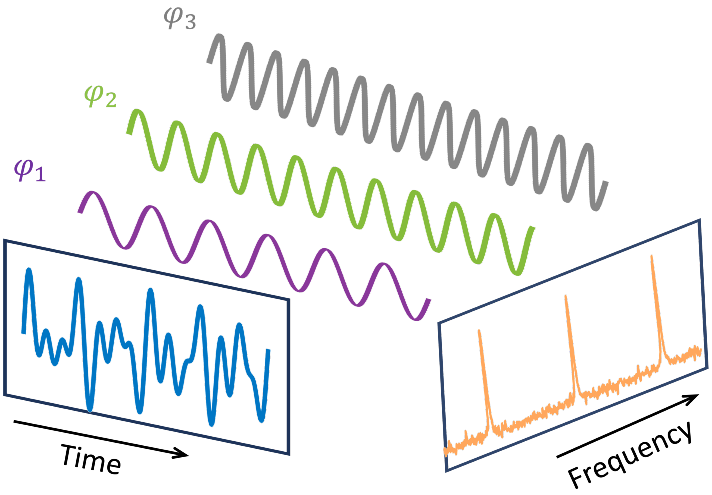

Figure 1.3. The concept of Fourier transform. The Fourier transform decomposes a signal into a sum of sinusoidal components of different frequencies.

This fundamental relationship unlocks many advanced techniques in signal processing and analysis, enabling precise control over the signal's spectral characteristics.

A practical example of frequency spectrum processing is the bandpass filter. A bandpass filter is a device that manipulates frequency contents, allowing specific frequencies within a given band to pass though while blocking signals outside the desired band. In general, filters can be classified into three types: low-pass, high-pass, and band-stop. By controlling the transfer function of the frequency filters, it enables signal manipulation, noise reduction, and signal conditioning in diverse applications such as communication, radar systems and instrumentation [44], [45]. Over the decades, a considerable number of frequency filters have been proposed and demonstrated across RF/microwave, and optical domain [1], [44], [46], [47], [48], [49], [50], [51]. Microwave filters can be realized through various structure types, including resistor-capacitor (RC) circuits [52], PIN diode-based tunable RF filter [53], and complementary metal-oxide semiconductor (CMOS) technologies [54]. On the other hand, optical filters are fundamental components in the manipulation of optical waves, typically based on thin-film [55], fiber-Bragg grating [56], and ring resonators [57]. These optical filters leverage the properties of light, offering capabilities in the THz frequency range and exceptional versatility [58]. The advantages of optical filters have been extended to the manipulation of microwave/RF signals through microwave photonic techniques. The unique feature of this method is the ability to process the microwave/RF signals directly in the optical domain, using photonic technologies to provide functions in microwave systems [59]. Various microwave photonic filters (MPFs) have been developed, utilizing nonlinear effect [60], [61], optical delay lines [62], or optical combs [63], providing the manipulation of microwave signals with high speed (i.e., over tens of GHz), advanced reconfigurability, and Immunity to electromagnetic interference [1].

1.1.3 Time-frequency (T-F) Analysis and Processing

While significant analysis and processing tasks can be accomplished using time (T) domain or frequency (F) domain techniques, many crucial tasks involving sophisticated manipulations of the time-frequency properties of waves remain challenging. The time-domain representation lacks direct information about the temporal location of the signal frequency components, whereas the frequency spectrum does not indicate when these components occur. Moreover, the manipulations associated to each of these two methods are limited in achieving fully arbitrary control and processing of the signal’s time-frequency properties.

In practice, the frequency spectrum of an incoming signal is rarely stationary, but changes over time. As such, for a full, comprehensive manipulation of an arbitrary waveform, it is necessary to perform joint

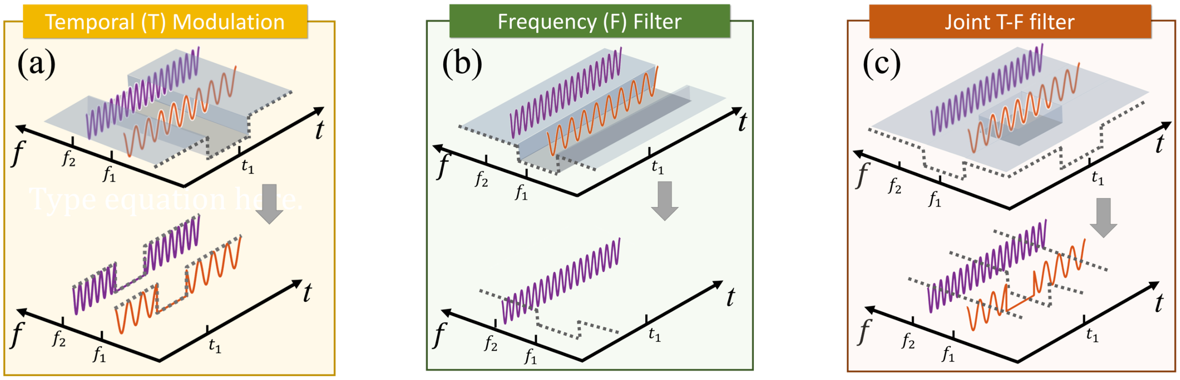

Figure 1.4. Comparation between different types of modulation. (a) temporal modulation, (b) frequency filter, and (c) joint time-frequency (T-F) manipulation.

time-frequency (T-F) analysis and processing, where time and frequency variations are analyzed and manipulated simultaneously. This is in sharp contrast with temporal modulation and frequency filtering methods in which the corresponding signal variations (as a function of time and frequency) are treated separately and independently. An example is illustrated in Fig. 1.4, where we target to eliminate a single frequency tone around a prescribed time t_1 from an incoming signal, which is composed of two different single-frequency components (f_1 and f_2, shown with orange and purple curves, respectively). This operation cannot be achieved using temporal modulation (a) or frequency filtering (c) or any combination of them. To accomplish this, we need manipulation of the joint T-F energy distribution of the wave.

1.1.3.1 Joint Time-frequency (T-F) Representation

A joint T-F distribution of a temporal signal offers a very intuitive and comprehensive representation, providing a precise picture of the time evolution of the signal energy spectrum [64], [65], [66]. It describes the temporal and spectral behaviour of a signal simultaneously. As such, T-F signal analysis and processing is important across a wide range of fields, from speech or sound analysis to communications, information processing, computing, remote sensing etc. using radio-frequency (RF, i.e., microwave to mm-wave), terahertz or optical waveforms [67], [68], [69], [70]. There are many algorithms for realizing the T-F representation. Among those, a widely used approach is the short-time Fourier transform (STFT), also known as the spectrogram. The process of this method is illustrated in Fig. 1.5, the input temporal signal is segmented into consecutive short intervals using a window function (analysis window) of predefined duration. To ensure that no signal information is lost in the process, these segments are typically adjacent or partially overlap (gap-free analysis). For each small segment, we do the Fourier transforming to extract the frequency information within the corresponding time slot. This procedure results in a changing spectrum over time, yielding a 2D T-F distribution known as the spectrogram (SP) [71]. Mathematically, the STFT of a time-varying signal $s(t)$ is written as:

$$STFT\{(s(t))\} = S(\tau, \omega) = \int_{-\infty}^{\infty} s(t)h(t-\tau)e^{-j\omega t}dt, \tag{1.4}$$

where ω is the angular frequency variable, $h(\tau)$ represents the window function, commonly a Hann, Hamming, or Gaussian window [72]. τ is the time-delay for the STFT analysis, corresponding to the time variable of the resulting T-F distribution. $S(\tau, \omega)$ is the FT of each segment $S(\tau, \omega) = \mathrm{FT}(h(t-\tau)s(t))$. The SP is then calculated as the squared magnitude of the STFT, providing a detailed representation of the signal's energy distribution across the joint T-F plane, as shown in Fig. 1.5 (b).

Several key specifications are usually considered for evaluating a spectrogram: analysis bandwidth, time resolution and frequency resolution, and the number of analysis points. The analysis bandwidth is dictated by the Nyquist sampling rate that is required to represent the signal, with higher sampling rates accommodating larger operation bandwidths. The choice of the window function significantly influences time resolution, which defines the smallest discernible time events in the signal. According to Eq. 1.4, time resolution is determined by the time width of the temporal window $h(\tau)$. Thus, selecting an appropriate time window is crucial for different incoming signals. Frequency resolution dictates the smallest frequency interval distinguishable between two spectral components. According to the uncertainty principle of FT, the frequency spectrum of each truncated signal segment exhibits a resolution that is inversely proportional to the STFT's time resolution [71]. The time and frequency resolution cannot be arbitrary sharp, but rather, they are bounded by the uncertainty principle. This principle restricts the sharpness of both time and frequency resolutions, underscoring the importance of carefully designing the time window in T-F analysis

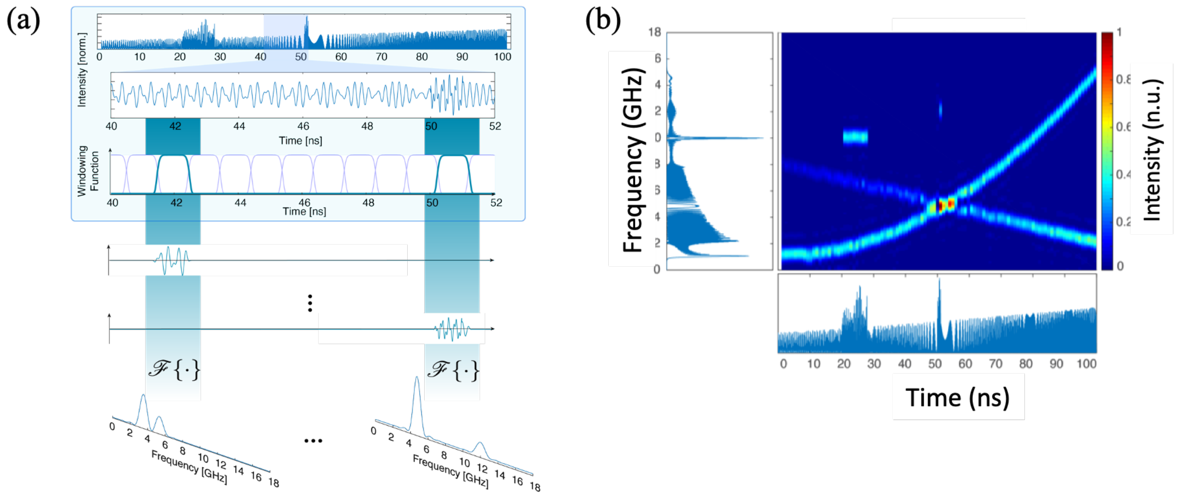

Figure 1.5. The concept of short-time Fourier transform (STFT) and spectrogram. (a) The temporal waveform of the signal is divided into a set of small segments by introducing a window function. The Fourier transform of each segment is computed to obtain the STFT of the signal. (b) The square magnitude of the STFT gives the spectrogram (SP).

to meet various application needs. The window must be narrow enough to capture short-duration events in time yet wide enough to resolve distinct frequencies effectively. In practice, the STFT may exhibit artifacts due to the uncertainty principle, depending on the duration of the windowing function. Implementations of this method require the window to be easily adjustable to detect a wide range of signal types effectively. The ratio between analysis bandwidth and frequency resolution provides an estimate of the number of points per analysis window used in spectral analysis, offering insights into the resolution capabilities of the analysis technique. These considerations are crucial for optimizing spectrogram performance across diverse applications and signal types.

Real-time Fourier spectral analysis (RT-SA) techniques are essential when there is a need to access the dynamically changing spectral information of an incoming nonstationary signal. This technique is particularly important in applications where immediate insight into the signal's spectral content is necessary, spanning a wide array of scientific and engineering disciplines. RT-SA techniques are indispensable tools for studying and capturing the signal of interest in a single-shot manner with low latency. To effectively analyze dynamic signals, spectral analysis must be performed in a real-time, continuous, and gap-free manner. Gap-free refers to the capability to implement the desired spectral analysis without any interruptions or dead time in the acquisition and processing of the signal of interest. This ensures that no information is missing, providing an accurate representation of the signal's behavior at every moment.The real-time capability of RT-SA allows for the immediate observation and analysis of signal characteristics, making it an essential tool in both research and practical applications. It facilitates quick identification and response to signal anomalies, ensuring critical information is captured and analyzed as it occurs. In this case, the bandwidth of signals that can be analyzed in real-time is often referred to as the instantaneous bandwidth, describing the frequency range that the system can process without delay.

In this thesis, we are particularly interested in RT-SA of signals with instantaneous bandwidths above the GHz range. Such high-speed waveforms are prevalent across the electromagnetic spectrum - from the microwave to the optical domain, also including millimeter and THz waves [73]. Many important tasks require RT-SA of these high- speed temporal waveforms, including broadband communications [74], radar platforms [75], ultra-fast characterization, sensing and spectroscopy and radio astronomy research [76], etc. These practical applications necessitate RT-SA to be performed in a continuous and gap-free manner, with a set of specifications meeting practical requirements, including instantaneous bandwidths well above GHz, high time resolutions in the nanosecond scale or even shorter, and fine frequency resolutions down to the MHz level.

1.1.3.2 Practical Requirements and Applications of T-F Processing

As mentioned above, considering that most waves encountered in practice are nonstationary, there is a fundamental interest in finding ways to analyse and manipulate at will their joint T-F distribution. Concerning T-F manipulation, realization of this wave processing paradigm requires implementation of a dynamic or *time-varying filtering* (TVF) process, in contrast to the (quasi-) static time-invariant filtering that is implemented by conventional frequency filters Fig. 1.6 illustrates an example of a joint T-F filtering process. The input consists of a target chirped signal, whose frequency changes with time, along with some undesired signal components occurring at random time locations with different frequencies. Here we use different colours to represent different frequencies. It is clear that the interference components are temporally overlapped with the target signal while sharing the same frequency range. To extract the target signal from the background noise, the manipulation of its T-F distribution is needed. This can be realized by implementing a TVF whose spectral transfer function can be tuned along with time, make it possible to manipulate the time-changing spectrum, as shown in the red dotted curve. The centre of the pass-band is altered in different time position to ensure the target signal can be maintained while the other components are eliminated. Such technique provides a complete processing and synthesis of non-stationary signals and is extensively used for a wide variety of signals encountered in scientific and engineering problems. Thus, to facilitate the required time-frequency processing, the implemented filters need to have main specifications that is used to evaluate the versatile capabilities, tunability and reconfigurability. The tunability refers to the dynamic shift of the central frequency of the filter's response. The reconfigurability describes to what degree the filter shape can be changed, such as switching the response between bandpass and band-stop, altering the number of passbands, changing the frequency bandwidth etc. Moreover, tuning speed is also important for practical applications. Tuning speed refers to the ability of a filter to change its spectral shaping parameters in response to control signals. It is a measure of how quickly the device can

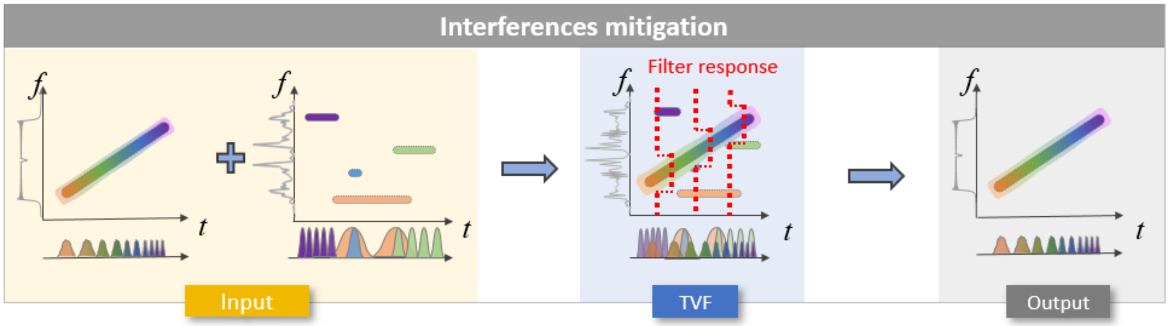

Figure 1.6. Illustration of time-varying filter (TVF). The incoming signal consists of a target linear-chirped signal, along with random interferences that appear at random time location with different frequencies. In order to eliminate the interferences, a TVF with dynamic response is implemented to the input and the output signal consisting of only the chirp component.

adjust the amplitude and phase characteristics of the optical signal. The faster the tuning speed, the more responsive and flexible the filter is in handling real-time signal processing tasks.

A considerable work and progress have been carried out to achieve the desired advanced functionalities and overall performance in many modern and emerging applications, including next-generation telecommunication systems [74], [77] and intelligent remote sensing platforms (Radar and Lidar) [5], [75], [78]. For instance, towards improving the spectral efficiency of modern communication systems, cognitive radio and optical schemes are increasingly being employed [79], [80], requiring software-defined architectures that enable dynamic spectrum allocation and control. The ability of real-time spectral detection and reconfigurable processing, with frequency resolution of MHz and wide-band spectrum analysis over several GHz bandwidths, are extremely important that enable the user to select the desired spectrum and avoid the interference from the congested channels [79], [80]. Sophisticated coding strategies are also needed where the desired information is encoded along the joint T-F variations of the wave in a rapidly adaptable manner, such as for the case of ultrafast frequency-hoping systems [81], [82] , as illustrated in Fig. 1.7. This requires the capability of the real-time analysis with over several GHz bandwidths, as well as the instantaneous rapid processing with flexibility and reconfigurability to precisely manipulate the desired hopping contents. Radar systems often operate in dynamic and challenging environments where reconfigurable manipulation of the frequency spectrum of the captured waves are highly desired to enhance the performance, versatility, and adaptability [5], [83], [84]. In dynamic practical environments, involving 5G and automotive radar systems[85], [86], [87], interference or jamming can significantly impact detection or sensing performance. In automotive radar systems, the mutual interference from other radars can degrade sensitivity and detection capabilities, potentially leading to hazardous situations[86]. These radar systems typically operate in the millimeter-wave range (with potential instantaneous bandwidth exceeding 30 GHz) [88] and necessitate real-time mitigation of interferences and noise. In these applications, the required wave processing operations may include selecting or deselecting a set of frequency bands [89], filtering out some undesired interference or noise-like components from the incoming wave [60], or other more sophisticated manipulations on the complex wave spectrum [90], [91]. The key feature is that these dedicated operations need to be processed at a very high speed, in a nanosecond scale or even faster [82], [90], while offering a set of specifications commensurate with the target performance, including operation over broad frequency bandwidths, well above the GHz range [92], [74]. Additionally, in these practical applications where the timely and accurate response is critical, processing must be performed with exceptionally low latency. In such contexts, high latency can have significant and potentially detrimental consequences [85]. For instance, real-time analysis and processing is essential in radar systems to ensure operational effectiveness and safety, as delays can impact response times and tracking accuracy. Similarly, next-generation networks face increasing demands for low-latency processing due to rising data rates and growing number of users. It is generally accepted that in the 6G communication framework, these applications would require latencies in the sub-ms or even μs range [93].

1.2 Methods and Technologies for Time-frequency Analysis and Processing

Theoretically, the aforementioned STFT offers a comprehensive analysis of signal attributes such as amplitude, phase, and frequency components across different time windows/positions, dynamically capturing their variations. This T-F distribution opens avenues for further signal processing through TVF, enabling targeted frequency component extraction/elimination over specific time intervals. To implement the T-F analysis and manipulation in practical applications, diverse methodologies have emerged over recent decades, showcasing remarkable advancements in operational bandwidth, frequency resolution, and reconfigurability. In general, current T-F analysis and manipulation approaches can be classified into 2 categories: digital signal processing (DSP) and analog signal processing. DSP approaches provide excellent reconfigurability, but are limited in processing speed, typically operating in the range of several megahertz (MHz) and can hardly be used for real-time signal processing [66], [68]. On the other hand, analog signal processing can be divided into two categories: (i) T-F filtering of electrical/RF microwave signals using the RF filter: This method involves using RF filters for manipulating electrical signals. It offers lower latency and can hendle higher-speed signals up to ~ few GHz, yet the filter responses can hardly be fully reconfigured [53], [94]. (ii) T-F manipulation of RF/microwave signals through photonic technologies, known as microwave photonics (MWP), this approach utilizes photonic techniques to achieve T-F analysis and manipulation. MWP techniques can operate over wider bandwidths, extending into tens of GHz, and hold promise for real-time signal processing applications, particularly in emerging 5G and 6G communication systems. However, current photonics/MWP T-F analysis and manipulation techniques still suffer from severe trade-offs between bandwidth, frequency resolution, and reconfigurability. Each of these techniques—DSP, electrical T-F filtering, and photonic-based T-F manipulation—offers distinct advantages and trade-offs. The following sections will delve into their operational principles, strengths, limitations, and performance characteristics to provide a comprehensive understanding of their capabilities and limitations.

1.2.1 Digital Signal Processing

The DSP approach to T-F analysis and manipulation is conceptually illustrated in Fig. 1.8. Initially, the incoming signal, e.g., audio, video, or signals from an antenna or optical waveforms photo-detected in a communication or sensing system, is first sampled by an analog-to-digital converter (ADC) with a sampling rate of f_s. According to the Nyquist sampling theorem, f_s must be at least twice the bandwidth of the incoming signal to accurately capture all signal information and allow for full signal recovery [95]. Within the ADC, the continuous analog signal/waveform is converted into discrete digital waveforms (data stream/samples) marked by the red dot lines shown in Fig. 1.8. These discrete waveforms or data samples are then analyzed and processed in a DSP unit, involving a large number of mathematical operations and

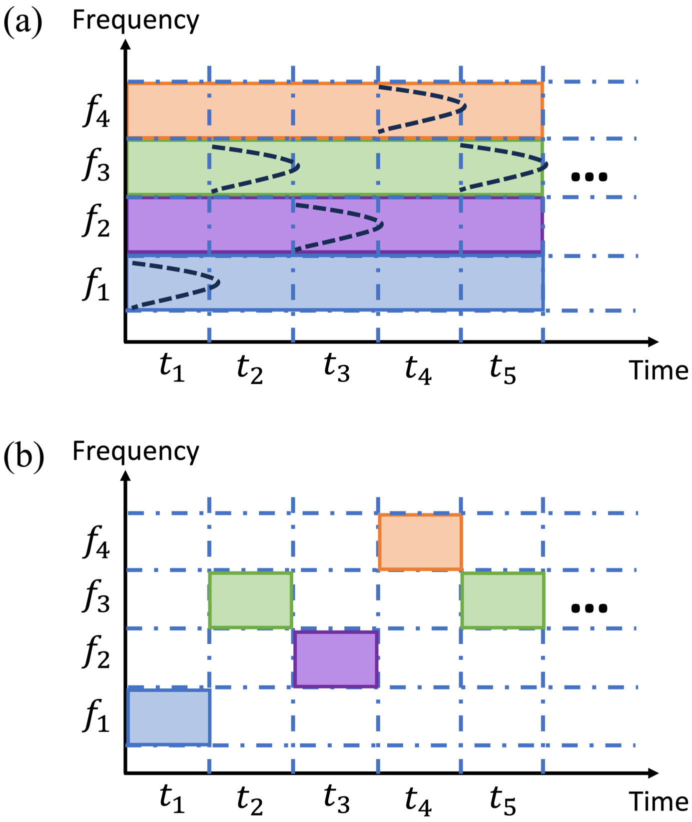

Figure 1.7. Practical applications of time-frequency processing. Frequency-hopping carrier generation based on time-varying filter.

algorithms, such as multiply-accumulates operations, fast Fourier transforms (FFT) [96], finite impulse response (FIR) filters, and infinite impulse response (IIR) filters etc.[97], [98], [99], [100], [101], [102]. Fig. 1.8 shows two functionalities: spectrogram analysis and time-varying filtering, both essential for T-F analysis and manipulation. Specifically, the T-F distribution of the sampled waveform is analyzed through the spectrogram, indicating specific frequency components along each analysis time window. Subsequently, a digital time-varying filter can be designed at will to perform any desired further T-F manipulation. In the example shown, the T-F analysis enables the extraction of a linearly chirped signal while suppressing undesired frequency components using a digital time-varying filter with its response depicted by the red dashed lines. The discrete/digital STFT/spectrogram is usually computed through the FFT algorithm [96] while the digital time-varying filters can be implemented using FIR or IIR digital filters [97], [98], [99], [100], [101], [102]. Finally, depending on the specific application, the processed digital waveform may need to be reconverted back into the analog domain using a digital-to-analog converter (DAC).

DSP approaches offer extraordinary versatility in tailoring the time-varying filter responses by readily programming the coefficient of the FIR or IIR filters. Parameters such as bandwidth, center frequency, and filter shape (e.g., rectangular, Gaussian) can be easily adjusted to meet specific requirements. Another key advantage of the DSP-based T-F analysis and manipulations is the ability to achieve high frequency resolution Δf. This parameter is determined by the sampling rate of the ADC f_s and the length of the time window N, given by $\Delta f = f_s/N$. As such, a longer recorded/sampled signal will yield a finer frequency resolution. Current DSP implementations for RF signals can achieve frequency resolutions in the range of MHz, assuming f_s in the GHz range and $N = 1024$. However, the processing speed of the DSP approach is inherently limited by its clock (in the range of several GHz) and the physical latency, hindering real-time applications in the above-mentioned modern systems requiring rapid signal processing, such as frequency hopping and radar systems operating beyond tens of GHz range. For example, the latency of the DSP unit reported in Ref. [103] is ~ 100 ns with a sampling rate of 100 MS/s, and it can be hardly applied for the high-speed applications. Another critical constraint of the DSP unit is the high-power consumption. For example, the power consumption of the ADC with a sampling rate of 400 MS/s is ~ 3W, and higher sampling rates will lead to even greater power demands [104]. On the other hand, a longer sampled waveform require more memory and computation operations, increasing the overall processing time and the energy consumption [104]. While advancements in CMOS technology have led to lower power consumption—such as reducing total power to 197 mW at 1.2 GHz with 28 nm CMOS—their higher cost and limited clock speeds still hinder the further application in the real-time signal, especially for high-speed dynamic signals [54]. It should be noted that the power consumption of the DSP unit highly depends on the

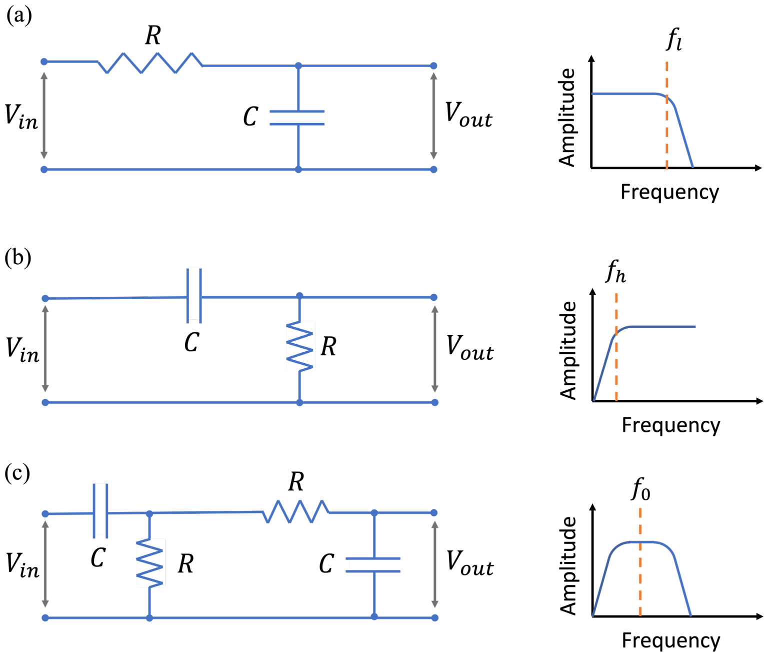

Figure 1.9. Schematic of RC-based filters with different response: (a) low-pass, (b) high-pass, and (c) band-pass.

applications, time complexity of the DSP algorithms, and unit architecture, e.g., general-purpose DSP units tend to consume more power compared to those optimized for specific functionalities [105].

1.2.2 Analog RF Signal Processing

Over the past few decades, significant efforts have been devoted to reducing latency and improving power consumption through advancements in analog RF filters. Conventional RF filters typically rely on configurations of capacitors (C) and resistors (R) to achieve various filtering functionalities such as low-pass, high-pass, and bandpass filtering [52]. For instance, a classic low-pass filter design resembles a series RC circuit, as depicted in Fig. 1.9 (a). The cutoff frequency of such a filter is determined by the values of the resistance R and capacitance C, given by $f_l = 1/2\pi RC$. By interchanging the positions of the resistor and capacitor, a high-pass filter can be easily implemented to effectively attenuate low-frequency components (Fig. 1.9 (b)), with a cutoff frequency $f_h = 1/2\pi RC$. Additionally, a bandpass filter can be constructed by cascading low-pass and high-pass filters, as shown in Fig. 1.9 (c). The bandwidth B of the bandpass filter can be expressed as $B = f_l - f_h$, and the centre frequency is defined as the geometric mean, $f_0 = \sqrt{f_l \times f_h}$. To obtain more complex filter responses, adjustments in capacitance or resistance allow for tunability in frequency responses. However, filters based on RC modelling are inherently limited to low frequency, usually well below 1 GHz [106]. To achieve a higher operation bandwidth (in the range of GHz), several innovative approaches have been developed, including PIN diode-based tunable RF filter [53], microelectromechanical systems based tunable capacitors [94], and the diode-based RF filters [107]. These technologies enable tunability in center frequency and bandwidth. However, their tuning speed remain below MHz, limiting adjustments primarily to center frequency and bandwidth. Furthermore, the operational bandwidth is still often limited to a few GHz at best. The limitations in tuning speed and operational bandwidth pose challenges for realizing TVFs that require rapid adjustment capabilities. Despite advancements, these constraints hinder broader applications in scenarios demanding fast-tuning capabilities for dynamic signal processing.

1.2.3 Photonic-based Signal Processing

Depending on the signal complexity and speed, the analysis and processing tasks often require substantial computing resources. This represents a crucial challenge in applying signal processing to many important problems, particularly those involving high-speed (i.e., broadband) temporal waveforms. It remains challenging for DSP methods to perform a processing task extending over a frequency bandwidth just exceeding a few GHz, particularly if the analysis is to be performed in a gap-free and real-time fashion. Processing based on analog electronic devices and sub-systems have been explored to overcome the limitations of the DSP approach. Yet, as discussed above, these systems offer limited capabilities for highly adaptive and reconfigurable operations.

In contrast, photonic technologies have emerged as a powerful alternative for processing optical signals, leveraging their inherent advantage of large bandwidth. Photonic methods provide a direct and effective means to analyze and manipulate signal, making them particularly suited for high-speed applications. These advantages extend beyond optical signals to encompass electronic, RF, and microwave signals, which can be modulated onto optical carriers using techniques like electro-optic modulation, forming the basis of MWP. MWP is an interdisciplinary field that combines radio frequency and optical domain, attracting significant interest and undergoing substantial development in both research and industry sectors over the past decades. MWP methods allow the realization of important signal analysis and processing functionalities with a performance that may not be possible using purely electronic methods. Key advantages of the MWP approach include its inherent low loss, immunity to electromagnetic interference, ultra-broad bandwidth (over 100 GHz) operation, fast tunability and programmability [108], [109], [110], [111]. In MWP systems, the initial step involves modulating the electrical signal onto an optical carrier, facilitating subsequent analysis and processing tasks within the optical domain. This approach enables implementing many important functionalities, including filtering, arbitrary waveform generation, beam-steering, and frequency measurements, with unparalleled speed, efficiency, and high reconfigurability [110], [111]. The processed optical signal is then converted back to the electrical domain through photodetection. Recent advancements in this field have focused on developing real-time joint T-F analysis and processing methods based on photonic techniques [69], [112], [113], [114], [115], [116]. These efforts underscore the potential of photonic approaches to revolutionize signal processing capabilities, offering new avenues for complex and demanding applications across various domains.

1.3 Photonic-based Time-frequency Analysis and Processing

A set of photonic approaches have been developed that provide a powerful tool with unprecedented performance towards the realization of practical performance requirements. In the following subsections, I will provide a brief overview of some main photonic techniques for time-frequency analysis (1.3.1) and processing (1.3.2) and their key features and limitations.

1.3.1 Photonic-based Time-mapped Spectrogram Analysis Methods

Several photonic methods have been developed for time-frequency analysis, aiming to overcome limitations encountered by DSP [113], [117], [118], [119]. Generally, these techniques rely on upconverting the electrical signal into the optical domain through electro-optic modulation, leveraging the large bandwidth available of photonics technologies, where even bandwidths of tens of GHz are considered relatively narrowband. One notable method relies on stimulated Brillouin scattering (SBS), which surpasses DSP capabilities by achieving up to 12 GHz bandwidth while maintaining impressive frequency resolution. However, its time resolution remains comparable to that provided by digital technologies [113]. Another photonics method involves manipulating the SUT on chirped waveforms, followed by dispersive propagation in fiber loops, improving time resolution down to 30 ns. Nevertheless, this method is constrained to sub-GHz maximum bandwidths [120].

In this thesis, we are particularly interested in the scheme for time mapping a full STFT (or SP) of the SUT in a continuous and gap-free manner. Fig. 1.10 (a) shows a schematic of the conventional design for real-time Fourier transformation (RT-FT) of a temporal microwave signal [121]. The analyzed scheme first involves dispersive propagation of a short optical pulse. The dispersed, temporally stretched optical pulse is then modulated by the SUT (using for instance an electro-optic MZM), and the resulting waveform is finally propagated through a second dispersive line. For realization of the desired RT-FT operation, the two dispersive lines must provide a predominant second-order group-velocity or chromatic dispersion (corresponding to a group delay profile that varies linearly as a function of frequency) of the same magnitude but opposite sign, i.e., $-\ddot{\Phi}_0$ and $+\ddot{\Phi}_0$, respectively, where each of these factors is defined as the slope of the corresponding group delay profile as a function of the relative radial frequency variable (around ω_0) [122]. As such, the scheme produces a temporal waveform that is proportional to the FT of a temporal section of the SUT. Specifically, the SUT is first temporally windowed by the dispersed pulses and the frequency spectrum corresponding to this SUT section is then mapped along the time domain with a frequency-to-time mapping law determined by the dispersion coefficient. The frequency axis is mapped along the temporal axis of the output waveform following the scaling law

$$\Delta\omega_t \rightarrow \Delta t/\ddot{\Phi}_0 \tag{1.5}$$

where $\Delta\omega_t$ is the input frequency variable relative to the signal's central optical frequency and Δt is output time variable relative to the center of the output waveform.

We recall that the STFT is a two-dimensional function of the time (τ) and frequency (ω) variables, simply defined as the FT of consecutive time-windowed sections of the SUT [116]:

$$STFT(\tau,\omega) = \ FT\{h(t-\tau) \times s(t)\} \tag{1.6}$$

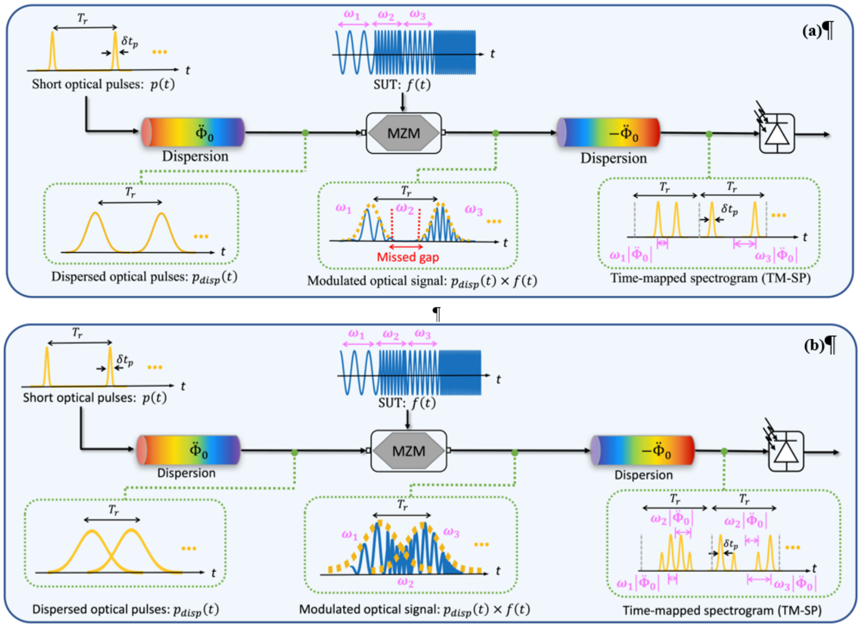

Figure 1.10. Basic principle of the real-time Fourier transformation (RT-FT) scheme. (a) A conventional design of the Fourier transformer of microwave signals, enabling the acquisition of the frequency spectra of windowed sections of the signal under test (SUT) that are sufficiently spaced along the time axis; this design necessarily misses some of the incoming signal information. (b) Extension of this scheme for a full real-time and gap-free spectrogram analysis of a continuously incoming nonstationary SUT. In the examples shown here, the SUT is a sinusoidal function with a frequency that is linearly increased along time.

The spectrogram (SP) is defined as the squared magnitude of the STFT. The function $h(t)$ in Eq. (1.6) defines the temporal window that is used for consecutive truncation of the SUT. In the considered scheme, Fig. 1.10 (a), we assume that we launch an infinite train of input pulses that are periodically spaced by T_r. Considering that the scheme in Fig. 1.10 (a) is a linear system, the overall output is determined by the sum of the outputs corresponding to each of the individual pulses at the system input. In turn, the output for each individual pulse is the time-mapped FT of the corresponding windowed section of the SUT and the window function used for calculation of the STFT is the dispersed pulse envelope. As the input pulses are spaced by the period T_r, any two consecutive windowed sections of the SUT, and their corresponding output time-mapped FT profiles, are delayed by this same period, T_r. Thus, each calculated FT is mapped along the time domain, with the resulting consecutive spectra being spaced by this same period T_r.

A main assumption in Fig. 1.10 (a), is that the optical pulses must be sufficiently spaced to avoid overlapping among the dispersed pulses at the output of the first dispersive line [121], [123], [124]. This would impose temporal gaps between consecutive analysis windows, implying that certain sections of the signal will not be processed, and their corresponding information will not be captured by the STFT, as illustrated in Fig. 1.10 (a). Thus, a STFT is implemented in a real-time manner, but information of the SUT is unavoidably lost. To overcome this drawback, a system with overlap among the consecutive analysis windows is designed, as illustrated in Fig. 1.10 (b). By properly design [116], the system introduces a significant overlapping among consecutive dispersed pulses (or time lenses) while still ensuring that the corresponding successive time-mapped FTs are well separated along the time domain. This enables implementation of a gap-free STFT analysis of the SUT in a continuous and real-time manner.

To further improve it, a scheme has been recently proposed and demonstrated for time-mapped STFT analysis of high-speed signals [114], [115] using a dispersive line designed according to the Talbot self-imaging conditions [125]. This scheme simplifies the design described above in that it does not require the first dispersive line. In other words, the Talbot scheme simply involves temporal sampling of the SUT with a periodic train of optical pulses followed by dispersive propagation [114]. The temporal self-imaging effect comprises a set of phenomena observed in the problem of dispersive propagation of a periodic train of pulses [125]. This scheme can be easily interpreted as a particular case of the above-described time-mapped STFT design. Specifically, as represented in Fig. 1.11 (a), we consider the case of a train of short optical pulses temporally spaced by a period T_r, which propagates through a second-order dispersive line characterized by a dispersion coefficient $\ddot{\Phi}_0$. Each of the individual pulses is temporally distorted and broadened, such that for a sufficiently high amount of dispersion, consecutive dispersed pulses interfere with each other. In the particular case when the dispersion coefficient satisfies the condition defined by:

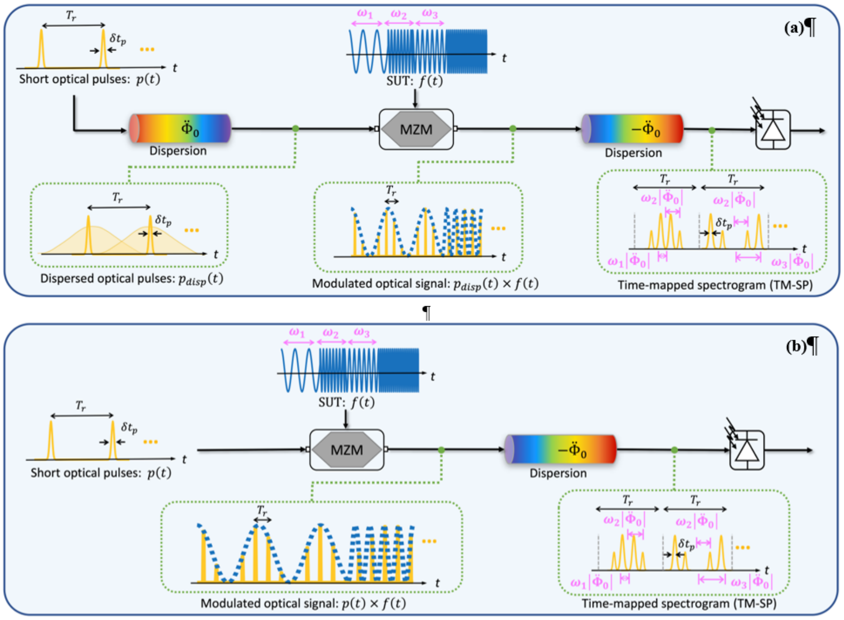

Figure 1.11. Interpretation of the integer Talbot-based STFT design. (a) General time-mapped SP design based on the dispersive Fourier transform, with the dispersion lines satisfying an integer Talbot self-imaging condition with respect to the input optical pulse train period. As illustrated, the input pulse train is exactly self-imaged in the first dispersive line. As a result, this first dispersive unit is then unnecessary and it can be omitted, leading to the simplified scheme shown in (b) for a time-mapped SP analysis of a continuously incoming SUT.

$$\ddot{\Phi}_0 = \frac{s}{q}\frac{T_r^2}{2\pi} \tag{1.7}$$

with $s = \pm 1, \pm 2, \ldots$. The output pattern reproduces an exact image of the input pulse train, as if the input pulses had not been dispersed at all [125]. This is referred to as a temporal integer Talbot (or self-imaging) effect, as illustrated in Fig. 1.11 (a). Then considering that under the integer Talbot condition, the dispersed pulse train is identical to the input pulse train, the first dispersive line can be entirely omitted, see Fig. 1.11 (b). This represents an important simplification in the resulting scheme. It is also very striking that this simplified scheme inherently produces the desired time lens effect on the SUT without the need to implement an actual quadratic temporal phase modulation process (as imposed by the linear frequency chirp of the individual dispersed pulses). Specifically, the action of the array of overlapping time lenses on the SUT is implemented by simply sampling the SUT with a suitable periodic train of short (generally, unchirped) pulses.

As discussed above, in real-time spectral analyzers, several main specifications have to be considered, such as instantaneous operation frequency bandwidth, time and frequency resolution, and the number of analysis points. The time (frequency) resolution of a given spectrogram distribution is defined as the minimum spacing between two different temporal (spectral) events of the SUT that can be clearly resolved in the obtained spectrogram [64]. The ratio between instantaneous bandwidth and resolution provides an estimate of the number of points of the performed spectral analysis. The time and frequency resolution parameters are inversely related, such that a sharper time resolution necessarily translates into a poorer frequency resolution, and vice versa [64].

As discussed before, time resolution δt_{sp} in STFT analysis is determined by the duration of the temporal window used for calculation of the STFT, which is given by the dispersed optical pulse envelope. Hence, the time resolution δt_{sp} of the performed spectrogram analysis can be estimated as the width $\delta\omega_p$ of the energy spectrum of the input optical pulses multiplied by the frequency-to-time scaling factor magnitude:

$$\delta t_{sp} \approx \left|\ddot{\Phi}_0\right| \delta\omega_p \tag{1.8}$$

Different metrics can be used for the time resolution estimates (e.g., standard deviation or others) [64], [126]. Eq. (1.8) implies that the time-mapped spectrogram is produced with a sharper temporal resolution (enabling to resolve closer temporal events along the SUT) when using either a narrower spectral pulse bandwidth or a smaller dispersion amount.

Another main specification of the performed spectrogram analysis is the frequency resolution of the calculated spectra, defined as the minimum spacing between two different spectral events of the SUT that can be clearly resolved [64]. The frequency resolution ($\delta\omega_{res}$) also determines the number of points N_{freq} used for representation of each of the calculated spectra. Mathematically, the number of frequency points $N_{freq} < \varDelta\omega_{SUT}/\delta\omega_{res}$, where $\varDelta\omega_{SUT}$ is the full-width spectral bandwidth of the SUT and $\delta\omega_{res}$ is an estimate of the frequency resolution of the spectrogram captured at the system output. The best frequency resolution $\delta\omega_{res}^{optimal}$ offered by a spectrogram distribution is ultimately limited by the uncertainty principle of the Fourier transform [64], [126]. This resolution is inversely proportional to the temporal duration of the analysis window used for the STFT calculation (which in turns determine the spectrogram time resolution, as discussed above). A key parameter that needs to be evaluated in practice is the photo-detection bandwidth, which will ultimately limit the achievable frequency resolution or number of frequency points in the analysis.

The general time-mapped STFT design, Fig. 1.10, offers a remarkable versatility to tailor the performance specifications of the obtained time-frequency analysis, e.g., in terms of operation bandwidth, processing speed, time and frequency resolutions. Specifically, the general scheme can be configured to achieve the combined set of performance specifications defined above, i.e., tens-of-GHz instantaneous bandwidths, MHz frequency resolutions, and the corresponding ultrahigh processing speeds, using widely available, realistic fiber-optics component technologies. However, to ensure gap-free SP analysis, dispersed consecutive pulses must overlap with each other, in such a way that the SUT is modulated on an interference-like optical pattern. In the most general case, this pattern exhibits arbitrary intensity variations along the time domain, such that the SUT is generally sampled in a sub-optimal (non-uniform) fashion. This means that some sections of the signal may be more strongly attenuated (or emphasized) than others, possibly affecting the performance (e.g., dynamic range) of the implemented time-frequency analysis. This is in sharp contrast to the integer Talbot design, Fig. 1.11, for which the SUT is directly modulated on the input optical pulse train under the Nyquist criterion, ensuring an optimal, fully uniform temporal sampling process. However, the additional design conditions that need to be imposed in the Talbot scheme significantly affect the versatility of this scheme to tailor the specifications of the performed SP analysis. Specifically, a photo-detection bandwidth capable of resolving the input short optical pulses is required. The bandwidth must be notably broader than the SUT bandwidth and the increase is by N times, where N is the number of analysis points in the captured spectra per analysis time slot. In practice, the integer Talbot scheme is just suited for processing modest speed signals (with a bandwidth of a few GHz at best) and with a limited number of analysis points along the frequency domain (typically, lower than ~10 analysis points) even using a photo-detection bandwidth exceeding 40 GHz [115]. Thus, none of these methods can be implemented for gap-free RT-SA with the required specifications of large bandwidth (over tens of GHz), nanosecond time resolution and MHz frequency resolution.

1.3.2 Photonic-based Time-varying Frequency Filtering Methods

In modern optical systems, the ability to selectively control and manipulate the spectral properties of optical signals play an important role. Optical filters, which allow specific wavelengths to pass while blocking others, are critical components in applications ranging from telecommunications and signal processing to spectroscopy and sensing [127]. As discussed above, to facilitate dynamic manipulation of the time-frequency distribution of an incoming signal, optical filters with high flexibility and tunable responses are necessary. Numerous methods have been proposed and demonstrated for reconfigurable optical filters [55], [128], [129], [130]. A well-known scheme based on spatial light modulator (SLM) to arbitrarily shape optical waveforms, also called waveshaper (WS). An input light first propagates through a spectral disperser (e.g., diffraction grating) and a lens, which spatially separates frequency components along one dimension at the back focal plane of the lens. Subsequently, a spatially patterned mask is placed to manipulate the phase and amplitude, and sometimes the polarization of the spatially dispersed optical spectral components. These manipulated components are then recombined by a second lens to form the output waveform. The filtering mask can be implemented by the programmable SLM or programmable liquid crystal modulator arrays [51], enabling reprogrammable waveform filtering under electronic control.

However, the tuning speed is typically limited to kHz level, with a frequency resolution in the range of a few GHz. This is insufficient for many practical applications that demand higher speed and finer frequency resolution, as discussed above.

On the other hand, when processing microwave/RF signals in the optical domain, MWP techniques are required as discussed above. Among them, MPFs have emerged as prominent units due to their large operational bandwidth, reconfigurability and rapid tuning capabilities. These filters are often constructed using a delay line configuration, categorized as either a FIR filter or an IIR filter. In what follows, I will primarily discuss the FIR-MPFs approaches, which offer superior tunability of their frequency response compared to IIR-MPFs.

In a FIR filter, the underlying concept involves subjecting the input signal to a series of time delays, weighting coefficients, and subsequent summation to produce the output. Fig. 1.12 depicts a typical diagram of the FIR delay-line-based microwave photonic filter. It consists of an optical source, a modulator, a delay-line element, and a photodetector. The RF signal can be modulated onto the optical carrier through a MZM or a PM as described above. The modulated optical signal is then evenly divided into *N* outputs, with the subsequent set of delay-lines used to implement the delay or weight functions. These delay lines can be implemented using an array of fiber Bragg gratings (FBGs), an arrayed waveguide, a linear chirped FBG (LCFBG), or a dispersive fiber [1], [131]. All the delayed signals interfere with each other at the output and

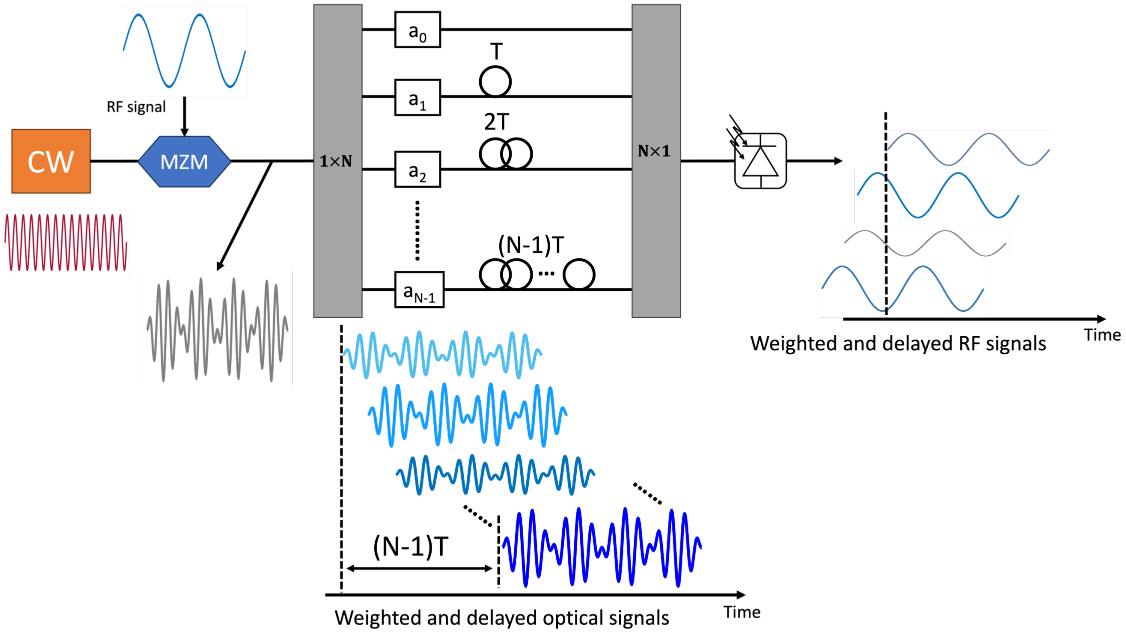

Figure 1.12. Basic principle of microwave photonic filter.

are then converted back to the final output RF signal using a photodiode. The output of the N-tap filter is described by the following equation:

$$g(t) = \sum_{i=0}^{N-1} a_i x(t - i \cdot T)\,, \tag{1.9}$$

where a_i are the coefficients of the N taps and $x(t)$ denotes the input signal. T represents the time delay between the two adjacent taps. The corresponding frequency domain output can be obtained by applying a Fourier transform:

$$G(\omega) = \sum_{i=0}^{N-1} a_i X(\omega) e^{j\omega(iT)}, \tag{1.10}$$

$X(\omega)$ is the Fourier transform of the input signal $x(t)$ as described in Eq. (1.3). Thus, the transfer function of the filter is

$$H(j\omega) = \frac{G(\omega)}{X(\omega)} = \sum_{i=0}^{N-1} a_i\, e^{j\omega(iT)} \tag{1.11}$$

This clearly indicates that the transfer function of the filter can be customized to a certain extent by suitably changing the nominal time delay and the tap coefficients.

MPFs offers a promising way for T-F processing with the main key specifications, such as tunability, reconfigurability, and rapid tunning speed. Tunability refers to the capability of adjusting the central frequency of the response to adapt to varying requirements or conditions. This is accomplished by tuning either the time delay or the wavelength spacing between consecutive optical carriers. A straightforward approach to vary the time delay is based on the LCFBG and a switched dispersive delay line [1], [62]. For the scheme based on LCFBGs, a tunable light source is required as described below. The use of optical fiber as a delay medium in the MPF is more attractive and simpler. The basic idea behind the tunable MPF with a switched dispersive delay line is to implement tunable optical switches [62], as illustrated in Fig. 1.13. A broadband optical light is transmitted through a spectrum shaper to obtain the sliced spectrum and

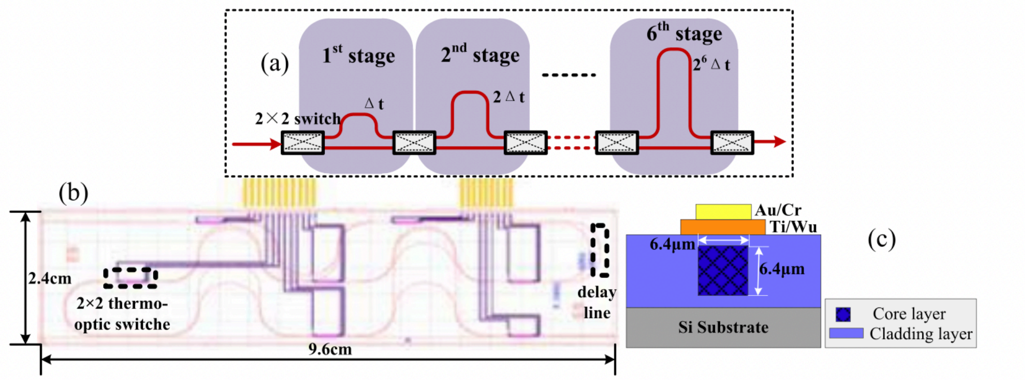

Figure 1.13. Tunable microwave photonic filter based on switched delay lines.

is then modulated by an RF signal. The spectrum shaper, a silica integrated light waveguide device, is composed of several delay elements interconnected using thermos-optic switches. By simply changing the state of each switch through controlling the driving voltage, the optical signal is tapped and delayed accordingly. As such, the tunability of the filter can be achieved by configuring the switches to change the time delay between the signals propagating through the delay lines [62]. However, the tunability remains relatively limited as the dispersive elements are difficult to modify once fabricated and the tuning speed is typically limited to kHz.

Alternative methods for tuning the central frequencies of the optical carriers have been proposed and demonstrated, including the use of wavelength tunable laser arrays, such as using multiple laser diodes [132], multi-mode mode locked lasers [133], or optical frequency combs (OFC) [63], [134]. Using these schemes, one can tune the central frequency of the implemented MPFs at speeds within the kHz range (corresponding to microsecond delays). In this set of methods, each carrier acts as a filter tap, where the wavelength and the output power of each optical carrier can be independently adjusted. The time delay between two adjacent taps is achieved by transmitting a microwave modulated optical signal through optical paths of varying physical lengths or through a dispersive element exhibiting linearly chromatic dispersion, e.g., a single fiber or a LCFBG. To give an example, let us consider a scenario where the dispersion parameter of the dispersive fiber is denoted as D (ps/ns/km) and the length of the fiber is z. Assuming a wavelength spacing between adjacent wavelengths of $\Delta\lambda$, then after passing through the fiber, a time delay $T = \Delta\lambda \cdot D \cdot z$ between each two adjacent taps will be implemented. As such, the tunability of the MPF can be achieved by tuning the wavelength spacing. In [135], several tunable lasers are implemented to generate multiple optical carriers. By simply changing the center wavelength of these carriers, different time delays are realized, enabling a band-pass filter with configurable center frequency response. Another scheme based on phase shift for each tap has been proposed [132] to tune the central frequency of the filter response. This is realized by controlling the wavelength and power of each optical carrier combined and using an FBG-based phase-shifted filter to obtain different phase-shifts for each tap of the filter. However, laser arrays usually lead to complicated schemes, which cannot be easily scaled up for realization of a large number of taps in the MPFs. To address this problem, many methods have been reported, such as using OFC [136], SBS techniques [61] and phase-modulation to intensity-modulation conversion [137], achieving highly efficient tunable microwave filters with high selectivity. However, the central-frequency tuning speed of all these schemes remains limited to the kHz range and slower.

Another important specification for MPFs is the reconfigurability, which refers to its ability to dynamically adjust filtering characteristics such as bandwidth, and shape. As predicted by Eq. 1.11, the response shape can generally be reconfigured through controlling the coefficient of each tap a_i and the number of taps *N*. This is usually realized via adjusting the optical spectral shape or through phase filtering. Many techniques have been explored and developed for implementing microwave photonic filters with high reconfigurability. One approach is based on an optical frequency comb and a programmable optical filter, e.g., a WS [138], [139]. A schematic of this approach is shown in Fig. 1.14: A broadband OFC is modulated by an MZM biased at quadrature point. The modulated comb lines are then temporally separated by a spool of dispersion compensation fiber (DCF). Then by programming the optical filter, i.e., a WS, one can manipulate the OFC spectrum and/or the number of comb lines. Hence, this configuration offers the possibility to tailor the filter spectral response to exhibit various different shapes of practical interest, e.g., Gaussian, sinc-shaped, and flap-top responses. A similar reconfigurable MPF using a diffraction-grating-based SLM has been also reported [140]. To further increase the reconfigurability of the MPF, many approaches have been presented to have multi-passband with selectable and switchable passbands by introducing a Lyot loop filter [141], [142], or by cascading MZI [143], [144].

The tuning and reconfigurable speed of the filter is another critical factor as it determines how fast the spectral response of the MPFs can be adjusted. While the approaches described above enable center frequency tuning or shape reconfigurability to a certain extent, their tuning mechanisms typically rely on slow thermal or mechanical control of the laser wavelengths, optical switches, or programmable optical filters. These methods are usually operated with a tuning speed in the kHz range or slower. Certain applications, however, require a faster tuning speed, on the order of MHz or even faster, to dynamically switch the frequency or shape of the filter in rapidly changing RF environment, such as the aforementioned frequency hopping manipulation in telecommunication and noise mitigation in Rada systems. Innovations such as ultrafast passband reconfiguration, utilizing optically controlled polarization rotation [145], have

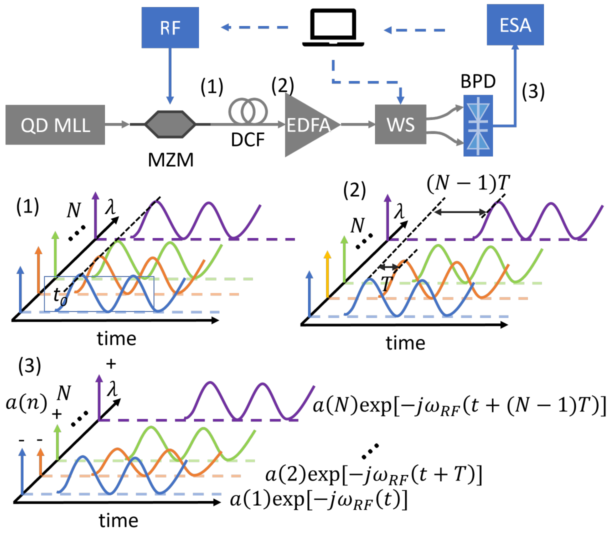

Figure 1.14. Reconfigurable microwave photonic filter based on a programmable optical filter.

been proposed. A GHz tuning speed has been demonstrated through this method. Leveraging the ultra-fast electro-optics Pockels effect has enabled the realization of RF switches with tens of GHz frequency tuning capability [146]. Another notable advancement involves the use of frequency combs and an analog RF phase shifter, yielding unprecedent performance and enabling simultaneous fast tunability, bandwidth reconfiguration, and high stopband attenuation [63].

Although various microwave photonic techniques with good flexibility are well developed, and existing MPF technologies offer an important degree of reconfigurability, their performance is still largely insufficient to enable *a full arbitrary and real-time control of the wave joint T-F distribution*, either because of their intrinsically slow reconfiguration speed [147], [148], [149], because fast tuning is restricted to some of the filter's main specifications only (e.g., central frequency) [60], [61], [63], [146], and/or because they are limited to implementing a very specific T-F filtering operation [150]. No comprehensive solution has been envisioned to achieve joint T-F filtering of high-speed signals (with GHz bandwidth and above) with an arbitrary user-defined response, i.e., with full reconfigurability, and rapid tuning speed. Continued research and innovation in this field are essential to address these challenges and unlock the full potential of photonic filtering technologies, that is implemented for the discussed emerging applications, to have user-defined reconfigurability in terms of central frequency, pass band, bandwidth, and response shape. The key ewquirement is that these operations need to be reconfigured at a very high speed, in a nanosecond scale or even faster, while offering a set of desired performance, including operation over tens of GHz bandwidth and MHz frequency resolution.

1.4 Objectives, Contributions and Organization of the Thesis

The main goal of this thesis is to design, study and experimentally demonstrate a photonic-assisted approach for real-time spectral analysis and processing of broadband waveforms, capable of providing the following target performance specifications:

- Real-time instantaneous bandwidth over tens of GHz,
- User-defined specifications for both the analysis and processing tasks,
- Rapid tuning speed, in a nanosecond scale and faster, for the spectral manipulation,
- Temporal resolution in the nanosecond range,
- Fine frequency resolution down to the MHz level

Towards this aim, this thesis proposes a general framework for user-defined real-time analysis and manipulation of the joint T-F distribution of EM waves directly in the analogue domain, ideally suited for operation on high-speed waves. Using this concept, we conceive and demonstrate a photonics scheme for T-F analysis and processing of microwave and optical signals. The proposed approach combines the versatility of the DSP approach with the performance (e.g., processing speed and bandwidth) of a photonic solution. The strategy involves mapping the T-F distribution (the STFT) of the incoming wave along the time domain based on Talbot array illuminator (TAI) phase, in a continuous and gapless manner, which in turns enables a user-defined manipulation of the wave's T-F distribution through available temporal modulation techniques. Since the time-mapped STFT is achieved using two consecutive phase transformations (along the temporal and spectral domains, respectively), the processed wave can be recovered by simply applying the opposite phase manipulations. This platform allows us to achieve the analysis and user-defined manipulation of the joint T-F distribution of arbitrary input microwave signal over a large bandwidth and with a fine frequency resolution. Towards this stated goal, the central contributions of this thesis are the following:

- A detailed theoretical study of the central concept of our proposal will be discussed. The equivalence between the temporal phase modulation and temporal spectral modulation will be evaluated through equations and will be also validated with numerical and experimental results. This provides an insightful understanding of the concept behind the fundamental concept of the proposal.
- The proposal and theoretical study including derivation of all main design equations for the photonic-based signal analysis for real-time spectral analysis, based on a time-mapped STFT. The proposed signal processing architecture involves two widely available signal processing units, namely, temporal phase modulation and group-delay dispersion. The design conditions of this scheme to perform a time-mapped STFT analysis of the incoming signal will be derived and discussed in this Thesis.
- Numerical validation of the proposed time-mapped spectrogram concept and its main performance specifications and trade-offs. The proposed architecture is found to be particularly interesting when implemented for broadband waveforms, offering performance specifications superior to the existing solutions.
- Experimental demonstration of the photonic-based time-mapped spectrogram of arbitrary broadband microwave signals, providing the following set of performance specifications:
    - Real-time analysis bandwidth up to ~ 100 GHz,
    - Temporal resolution into the nanosecond regime,
    - Fine frequency resolution down to the MHz level,
    - User-defined reconfigurable specifications.

- Theoretical study and analysis of the proposed time-frequency filtering that is based on the achieved time-mapped spectrogram. The time-mapped spectrogram effectively implements the short-time Fourier transform of the signal along the time domain, providing an straightforward mechanism to manipulate the spectrum directly in time domain. The design conditions and practical requirements for the user-defined spectrogram manipulation will be addressed in this thesis.
- Experimental demonstration of the time-frequency manipulation of the arbitrary signals that have been successfully analyzed through the spectrogram analysis step. We will showcase the following capabilities of the proposed filtering:
    - Real-time operation bandwidth up to ~ 100 GHz,
    - Rapid tuning speed up to the nanosecond range,
    - Fine frequency resolution down to a few hundreds of MHz,
    - Arbitrary reconfigurability, in terms of the central frequency, bandwidth, passband, and shape of the TVF spectral response,
    - Mitigation of random interferences.

The outline of this Thesis is as follows: In Chapter 2, I will give a deep discussion of the central components, i.e., phase modulation and group velocity dispersion, that will be used in the subsequent chapters. I will first present the mathematical description of equivalence between the temporal phase modulation of a time lens and the spectral phase modulation induced by the dispersive medium. Some numerical simulations and experimental demonstrations will be presented to validate the findings. In Chapter 3, I will give a detailed mathematical description of the proposed time-mapped spectrogram analysis. The proposal will be demonstrated through numerical simulations and experimental results to analyse various signals with reconfigurable specifications. A large operation bandwidth up to ~ 100 GHz will be validated. In Chapter 4, the following signal processing of the time-mapped spectrogram will be presented. The demonstrated experimental configuration can manipulate the 2D T-F distribution information of incoming signals directly through custom-designed temporal modulation. The proof-of-the concept experiments demonstrate the capability of this system to implement a fully reconfigurable user-defined spectral response with unprecedented performance. Some unique features of the time-frequency filter, which are of particular interest to interference mitigation applications and implementation of user-defined arbitrary responses, will be demonstrated. This Thesis then concludes with Chapter 5, pointing to existing challenges and unprecedented opportunities that the proposed time-mapped spectrogram analysis and processing brings to practical applications.

2 EQUIVALENCE BETWEEN GVD AND TL

This chapter presents the basic concepts of the central elements (i.e., second-order or group-velocity dispersive medium and time lens) that will be subsequently used for the signal analysis and processing strategies discussed in this Thesis. I will first describe the fundamentals of each of these two elements. This will be followed by pointing out a useful and interesting mathematical equivalence between the second-order dispersion propagation and the temporal phase modulation induced by a time lens. An important finding of this equivalence is that the temporal evolution of an input waveform as it propagates through a group-velocity dispersion medium can be evaluated by tracking the evolution of the signal frequency spectrum following application of a suitable temporal lens modulation. Some numerical and experimental results are reported to verify this proposal, and the implications and potential uses of this finding are also discussed.

2.1 Introduction

Group-velocity dispersion (GVD) is a fundamental physical mechanism observed in the propagation of a temporal waveform through a dielectric medium, which is caused by the variation of the group delay undergone by the propagating waveform as a function of frequency [151]. In optical systems, GVD is induced as a broadband signal propagates through mediums such as optical fibers [152], integrated dielectric waveguides [153], or chirped fiber/waveguide Bragg gratings [154], among others. Optical GVD plays a key role in a wide range of applications, including data transfer in fiber-optics telecommunication links [155], pulse compression and shaping [156], [157], waveform generation [158], analysis, processing and manipulation of pulses [159], and optical metrology and spectroscopy [160], etc.

In a dispersive medium, different frequency components of the propagating waveform travel with different group velocities. As a result, the temporal output waveform is not only broadened, but it is also distorted according to the outcome of a complex diffraction-like integral, e.g., a Fresnel diffraction integral for the case of second-order dispersion/GVD [161], [162]. In general, the distorted temporal output waveform depends upon the complex-field profile of the input signal and the dispersion introduced by the dispersive medium. Specifically, a given dispersion process can be modeled as a phase-only spectral filtering process, in which the input signal spectral phase is modified by considering the phase shift per frequency along the signal bandwidth corresponding to the prescribed dispersion profile [151]. We consider here the most general case of an arbitrary dispersion profile, including second and high-order dispersion

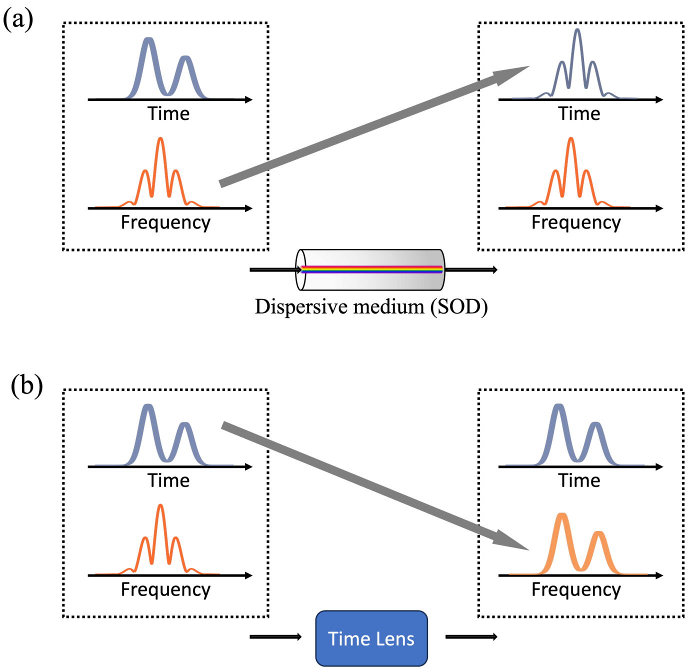

Figure 2.1. Dual Fraunhofer regimes: (a) frequency-to-time conversion using second-order dispersion, (b) time-to-frequency conversion based on a time lens.

terms, though in many cases, only the lowest order dispersion terms (such as the GVD) may be important [1].

When the GVD is strong enough to satisfies the time-domain Fraunhofer approximation for a given input, the output waveform envelope is proportional to the Fourier transform of the input, as shown in Fig. 2.1 (a) [163]. This is based on the analogy between paraxial diffraction of beams in the far-field (Fraunhofer) regime and the dispersive propagation of temporal waveforms, known as space-time duality [164], [165]. As such, the frequency spectrum (i.e., Fourier transform) of the signal is directly mapped along the time-domain (or frequency-to-time mapping) when transmitted through a dispersive medium with significant GVD. This mapping represents a fundamental technique for real-time spectrum analysis, as discussed in Chapter 1: the output temporal waveform resembles the shape of the Fourier transform of the input signal, allowing one to capture the input signal frequency spectrum in a purely real-time manner using a single high-speed photodetection apparatus.

The space-time duality can be extended to the functionality of a time lens (TL). This is an element that introduces a phase shift along the temporal profile of the signal, a process that is equivalent to the action of a spatial thin lens on a light beam in space. Specifically, it applies a quadratic or nearly-quadratic phase modulation to the input signal, analogous to the effect of a parabolic lens in space. This quadratic phase modulation imparts a temporal chirp to the signal, effectively stretching or compressing its waveform in time. While GVD causes a quadratic spectral phase modulation to the signal, a TL introduces a quadratic temporal phase modulation [166]. In practice, TL can be realized using a PM [29], or based on nonlinear optics such as cross-phase modulation (XPM) methods or parametric processes [167], [168], [169]. Similar to the Fraunhofer dispersion process described above, the frequency spectrum of the output of an TL represents an image of the temporal intensity distribution of the input waveform, when the induced phase modulation satisfies an equivalent condition, i.e., the spectral Fraunhofer condition. This achieves a time-to-frequency conversion process, as illustrated in Fig. 2.1(b) [170]. TLs have been widely used in signal processing tasks, e.g., pulse generation [171], waveform measurement [172], and time-lens Fourier transform [173].

GVD and TL are central to this thesis proposal and are widely utilized in many of the signal analysis and processing methods discussed in the previous chapter. Initially, a comprehensive mathematical model will be provided for the propagation of pulses through a GVD medium, focusing on GVD, and for temporal phase modulation using TLs. Subsequently, the thesis will formalize the mathematical equivalence between GVD propagation and TL modulation for any given input signal. This equivalence reveals a significant finding: the frequency spectrum of a waveform that is temporally modulated by a suitable quadratic phase function, i.e., a TL with a suitably designed chirp coefficient [170], [174], exhibits a similar shape to that of the temporal envelope of the same input after propagation through a prescribed second-order GVD amount. This mathematical equivalence is particularly intriguing as it offers deep insights into the GVD and TL processes that form the essence of this thesis. Moreover, beyond this fundamental interest, the equivalence holds practical implications. For instance, one could continuously follow the temporal shape evolution of a dispersed waveform by simply tracking the output frequency spectrum of the signal after passing through a suitable TL, in which the emulated GVD amount can be easily reconfigured (e.g., electronically reconfigurable using an electro-optics time lens, as detailed below). Numerical evaluation of a dispersive process generally requires a precise knowledge of the amplitude and phase profiles of the input waveform; however, this information is not always readily available and may be difficult to obtain in practice. Notice that gaining access to the complex (amplitude and phase) profile of an input optical wavefield is generally challenging, particularly for broadband signals (with frequency bandwidths exceeding just above 100 GHz) extending over long durations. Here I show how the introduced GVD-TL mathematical equivalence can be used for a continuous analysis of the temporal evolution of an arbitrary complex waveform as it propagates through a GVD medium, by using a single-frequency-driven phase modulator, providing a direct and simple way to analyze/track the amplitude of a dispersed temporal waveform.

2.2 Equivalence Between Group-Velocity Dispersion and Time-lens

2.2.1 Mathematical Modelling of Group-Velocity Dispersion (GVD)

I begin with a review of the mathematical modelling of the process of pulse propagation through a second-order dispersive medium, such as a spool of optical fiber. In a standard single mode fiber (SMF), the dispersion is characterized by the GVD coefficient β_2 that describe the accumulated dispersion per unit propagation distance, typically measured in the units of $\mathrm{ps}^2/(\mathrm{rad}\cdot\mathrm{km})$ [151]. Let z represent the total length of the optical fiber medium. The magnitude of the GVD coefficient β_2 increases linearly with the propagation length, such that the total GVD accumulated after propagating through the distance of z is defined as $\ddot{\Phi}_0 = \beta_2 z$, depicted in Fig. 2.2 (a). In such a medium, the GVD coefficient β_2 is defined as the slope of group delay curve as a function of frequency and is quadratically related to the frequency of the wave, resulting different frequency components of the propagating wave travel at different velocities. This leads to the broadening and distortion of the output waveform and this phenomenon is referred to as GVD. The supported transmission bandwidth is the specific wavelength range that the dispersive medium is able to operate across most effectively. Note that the sign of β_2 (positive or negative) depends on whether the optical wave experiences normal or anomalous dispersion, respectively.

As discussed earlier, the GVD process can be modelled as a spectral phase-only filtering of the input waveform with a quadratic phase response, corresponding to a frequency transfer function $\widehat{H}(\omega) = exp(-j\frac{1}{2}\ddot{\Phi}_0\omega^2)$ over the full waveform bandwidth. In this notation, the involved signals are assumed to be centered at the angular frequency ω_0, ω is the baseband radial frequency variable, with respect to the central optical frequency ω_0, and $\ddot{\Phi}_0$ is the total GVD of the medium. Here, we ignore the overall propagation delay undergone by the wavepacket, higher order dispersion terms, and insertion loss of the

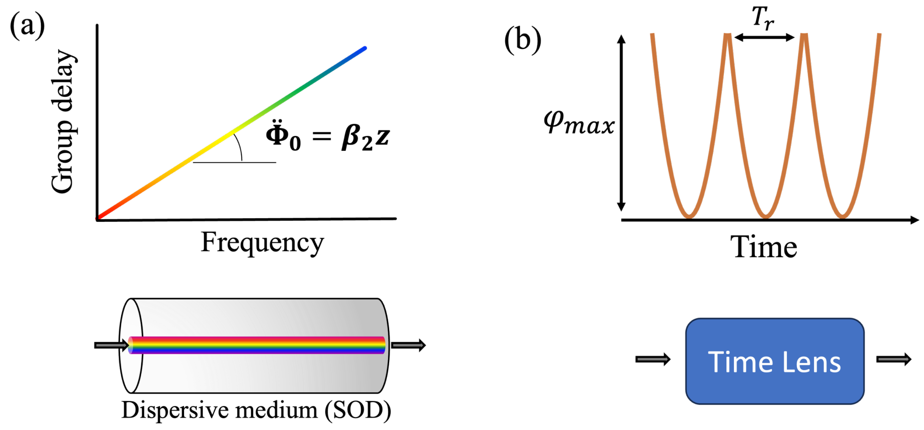

Figure 2.2. Schematic of second-order dispersion and time lens.

dispersive medium, assuming then that the transfer function has a constant amplitude. Considering that dispersive propagation is then modelled as a linear time-invariant process characterized by the above-defined spectral transfer function, this process can then be described through a temporal impulse response [175]. Specifically, the temporal impulse response $\hat{h}\ (t)$ of a dispersive line can then be obtained by inverse Fourier transform of $\widehat{H}(\omega)$, i.e., $\hat{h}\ (t) = exp\left(j\frac{1}{2\ddot{\Phi}_0}t^2\right)$, where t is the time variable relative to the medium's group delay at ω_0.

When an optical pulsed waveform propagates through such a second-order dispersive medium, the output can be described as the convolution between the complex temporal envelope of the input waveform, $\hat{a}_{in}(t)$, and the impulse response function $\hat{h}\ (t)$. The magnitude of the output complex envelope can be written as

$$\begin{aligned} |a_{out}(t)| &= \left|\int_{-\infty}^{+\infty} \hat{a}_{in}(\tau)\, exp\left(j\frac{1}{2\ddot{\Phi}_0}(t-\tau)^2\right) d\tau\right| \\ &= \left|\int_{-\infty}^{+\infty} \hat{a}_{in}(\tau)\, exp\left(j\frac{1}{2\ddot{\Phi}_0}\tau^2\right) exp\left(-j\frac{1}{\ddot{\Phi}_0}\tau t\right) d\tau\right| \\ &= \left|\mathcal{F}\left[\hat{a}_{in}(\tau) exp\left(j\frac{1}{2\ddot{\Phi}_0}\tau^2\right)\right]_{\omega=\frac{t}{\ddot{\Phi}_0}}\right| \end{aligned} \qquad (2.1)$$

where $\mathcal{F}$ denotes the Fourier transform. Hence, under the effect of GVD, the output waveform undergoes a distortion, and in particular, its temporal envelope is proportional to the Fourier transform of the input pulse waveform modulated by a quadratic phase, the result of which is evaluated at $\omega = \frac{t}{\ddot{\Phi}_0}$. As expected, in the most common case of an optical fiber, the output is determined by the dispersion coefficient β_2 and the length *z* of the dispersive fiber, such that access to the dispersive line at different positions along propagation would be needed for a continuous tracking of the temporal evolution of the propagating waveform. As noted above, the sign of β_2 stands for the type of chirp that a pulse undergoes as it propagates through the fiber. When $\beta_2 > 0$, the fiber exhibits normal dispersion, in which higher frequency components of the signal travel faster than lower frequency components. Conversely, in the anomalous dispersion (i.e., $\beta_2 < 0$) the pulse will experience negative chirp over time, where the lower frequency components have a faster speed than the high frequency components. Thus, the sign of β_2 is crucial in determining the propagation characteristics of the signal in the dispersive medium.

2.2.2 Mathematical Modelling of a Time Lens (TL)

As previously mentioned, while GVD induces a quadratic spectral phase modulation on a signal, a TL introduces a quadratic temporal phase modulation [166]. A TL can be implemented in practice using a PM [167], or based on nonlinear optics [113], [167], [168]. Among these, the most straightforward and efficient approach involves using a PM driven by a sinusoidal radio-frequency (RF) tone, inducing a phase shift that can be partially approximated as quadratic near the minima and maxima point, following a Taylor expansion of the sinusoidal phase profile [170] [167]:

$$\varphi(t) = \pm(\frac{\pi V_m}{V_\pi})cos(\omega_{mod}t)$$

$$\approx \pm(\frac{\pi V_m}{V_\pi})(1-\frac{\omega_{mod}^2 t^2}{2}), \qquad (2.2)$$

where V_m and ω_{mod} is the amplitude and the angular frequency of the modulated voltage, respectively, and V_π is the half-wave voltage of the modulator. The sign of the phase modulation in Eq. (2.2) determines the nature of the time lens effect, either focusing or defocusing the signal in the time domain, analog to how a spatial lens imposes a quadratic phase curvature on an optical wavefront. When the quadratic phase has a positive sign, it is similar to the phase near the valley point of the driving sinusoidal RF tone. Conversely, a quadratic phase modulation with negative sign corresponds to the phase near the peak point. When applied to a chirped signal, a time lens can modify the chirp rate (the rate of change of frequency with time) or the duration of the chirped signal [156]. Several important characteristics of a time lens include the length of time aperture, chirp coefficient, and total frequency excursion induced by the time-lens modulation. Time-lens aperture length T_r is the time window in which the phase approximation remains quadratic and this indicates the maximum duration of the input signal that can be effectively captured by the time lens. Signals longer than this temporal window will not be fully captured or effectively manipulated by the lens due to aberrations introduced by the approximation in Eq. (2.1), which in turn results in distortions in the output signal. These distortions are tolerable only over a limited duration, which is referred to as the time aperture, as depicted in Fig. 2.2 (b). Thus, to ensure a quadratic phase modulation, the phase profile should be in the nearly aberration-free region, and the transmission amplitude should ideally be flat across the aperture of the time lens. Chirp coefficient is a parameter describing the strength of the time lens and is defined as $\ddot{\varphi}_t \approx \pm A{\omega_{mod}}^2$, with $A = \frac{\pi V_m}{V_\pi}$ and ω_{mod} being the amplitude and frequency of the sinusoidal signal driving the PM, respectively. Thus, the temporal phase induced by the TL can be expressed as $\varphi(t) = \ddot{\varphi}_t \frac{t^2}{2}$. The linear variation of instantaneous angular frequency is given by the derivative of the quadratic phase

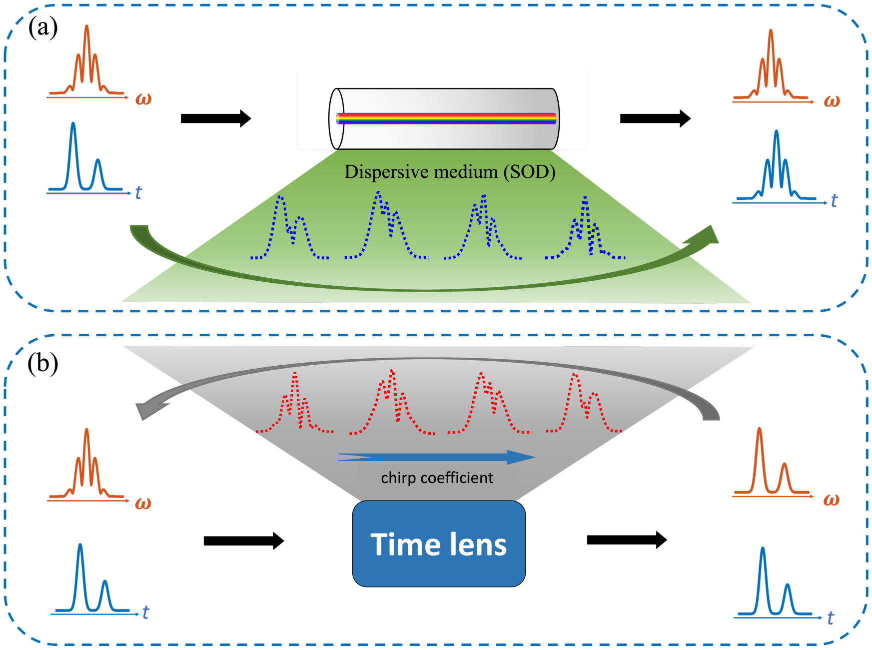

Figure 2.3. Illustration of the proposed principle, showing the evolution of (a) the temporal envelope of an incoming waveform as it propagates through a prescribed second-order dispersive medium (t: time variable), and (b) the frequency spectrum of the same input waveform as it undergoes a TL (ω: radial frequency variable).

$\varphi(t)' \sim \ddot{\varphi}_t t$. The total frequency excursion, indicating the maximum phase shift can be achieved over the time lens aperture T_r, is given by $\varphi_{max} = \frac{\ddot{\varphi}_t}{8} {T_r}^2$. It also implies that a larger phase shift can be achieved by increasing the modulation frequency or voltage. However, a higher modulation frequency will decrease the size of the time aperture T_r of the TL and the amount of voltage that can be safely applied is typically limited by the threshold of the modulator. Therefore, careful design of the modulation frequency and amplitude is necessary to avoid significant aberrations or damage to the modulator.

2.2.3 Mathematical Equivalence Between GVD and TL

From Eq. (2.2), we anticipate that the temporal profile of a dispersed waveform under test will be proportional to the frequency spectrum of the input temporal waveform modulated by a suitable quadratic temporal phase. As described above, the required modulation (flat amplitude, quadratic phase) can be performed using a TL [174]. In practice the TL can be implemented on an optical pulse using a PM driven by a sinusoidal RF signal. This modulation is locally quadratic around the minimum or cusp of the sinusoid within the time-aperture, [170]. As such, an input pulsed (time-limited) waveform will undergo the desired quadratic phase modulation after passing through the TL, and the magnitude of the output spectrum is simply the Fourier transform of the modulated signal [176]

$$|A_{out}(\omega)| \propto |\mathcal{F}[\hat{a}_{in}(t) exp\ (j\varphi(t))]|$$
$$= \left|\mathcal{F}\left[\hat{a}_{in}(t) exp\ (j\frac{\ddot{\varphi}_t}{2}t^2)\right]\right| \tag{2.3}$$

By comparing Eqs. (2.1) and (2.3), we conclude that if the chirp coefficient of the TL and the dispersion to be emulated satisfy the following condition:

$$\ddot{\varphi}_t = \frac{1}{\ddot{\Phi}_0} \tag{2.4}$$

the frequency spectrum of the phase-modulated waveform exhibits the exact same shape as that of the dispersed temporal waveform, under the frequency-to-time mapping factor

$$\Delta\omega_t = \frac{\Delta t}{\ddot{\Phi}_0} \tag{2.5}.$$

Where $\Delta\omega_t$ is the frequency variable relative to the signal's central optical frequency and Δt is time variable relative to the center of the output waveform. A key aspect of this finding is that the amount of emulated GVD could then be easily reconfigured through the time-lens chirp coefficient. Specifically, in an EO time lens, this can be reconfigured electronically by varying the amplitude and/or frequency of the driving modulation signal. As illustrated in Fig. 2.3 (a), the temporal shape of an input waveform is distorted as the amount of GVD is increased. An analogue evolution is obtained along the frequency domain when the same input waveform is modulated through a TL as the chirp coefficient is decreased, see Fig. 2.3 (b). From a practical application perspective, this concept would enable a continuous tracking of the temporal shape of an incoming pulsed waveform as it propagates through a dispersive medium without knowing the complex-field information of the input signal and without the need of gaining access to the dispersive medium at different propagation lengths. Specifically, for a sufficiently large amount of GVD, the dispersed temporal waveform is known to approach a time-mapped version of the input waveform spectrum (temporal Fraunhofer conditions) [177], see the output in Eq. (2.1); this corresponds with a phase modulation factor that is so small that the TL has a negligible effect on the input waveform spectrum. Recall that the dispersion $\ddot{\Phi}_0$ and the temporal phase shift $\ddot{\varphi}_t$ can be either positive or negative, depending on the type of dispersive medium and the characteristics of the modulating signal. Thus, the equivalence can allow emulation of both signs of dispersion when the modulated temporal phase satisfies Eq. (2.4). Specifically, for negative dispersion, the TL must have a negative chirp coefficient. In this case, the time-mapped frequency axes are reversed in comparison to increasing time. Therefore, the relationship between the chirp coefficient of the time lens and the dispersion to be emulated is crucial for achieving an exact match between the frequency spectrum of the phase-modulated waveform and the dispersed temporal waveform.

2.3 Numerical Simulation of the GVD Emulation

Several numerical simulations have been performed to validate the theory mentioned above. The TL is realized by a phase modulator which is driven by a sinusoidal RF signal, yielding a locally quadratic phase modulation along the nominal TL aperture [167]. Firstly, a waveform consisting of two consecutive and partially overlapped Gaussian pulses without initial phase was considered as the input signal. The temporal waveform and spectrum of this signal are depicted in Fig. 2.4 (a) and (b), respectively. The two pulses with 8-ps full-width at half-maximum (FWHM) time width are separated by 30 ps. As a result, the bandwidth at 1% of the full width of the input is around 100 GHz. Here, we set the modulation amplitude of the TL at 15.1 rad. As discussed in Chapter 1, the half-wave voltage of the electro-optic modulator is frequency-dependent, which will influence the total phase shift induced by the TL. However, in this case, the variation of half-wave voltage can be negligible because of the narrow bandwidth of the input signal. Therefore, the chirp-coefficient of TL can be controlled by modifying the frequency of the RF modulation, a strategy that is relatively easy to realize in practice.

To directly demonstrate the feasibility of this approach, the output spectrum of the TL and the corresponding output temporal waveform following dispersive propagation are shown in the same figure. It is worth noting that the comparison is analyzed after changing the scale according to the frequency-to-time mapping factor mentioned above $\omega = \frac{t}{\ddot{\Phi}_0}$. In Fig. 2.4 (c), a sinusoidal RF signal with frequency of 7 GHz is used to drive the modulator, and the input optical pulse is centered around a peak of the sinusoidal

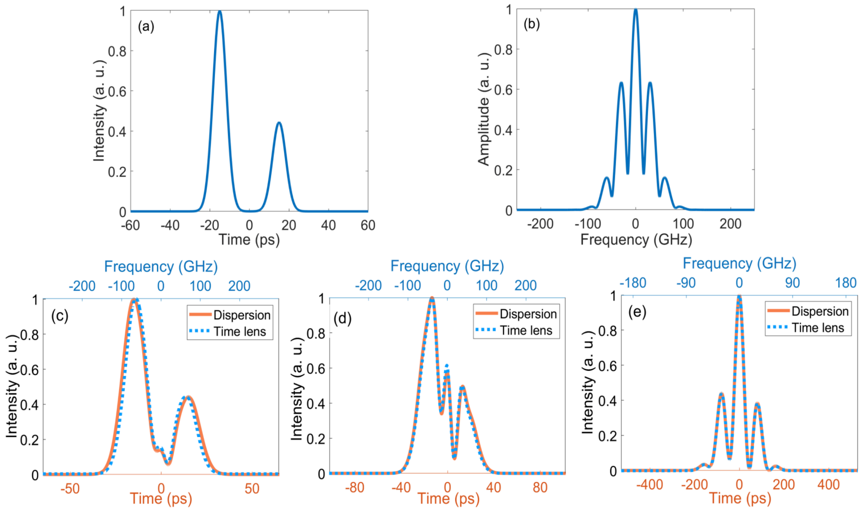

Figure 2.4. Simulation results. (a) Temporal waveform of the input signal; (b) Spectrum waveform of the input; (c)-(e) Output spectrum from the time lens with different modulation frequencies from 7GHz to 2GHz (dotted curve, top scale), compared with the temporal waveform from a single-mode fiber (solid curve, bottom scale) with the corresponding equivalent amount of dispersion, under with the relative frequency and time scaling defined in the text.

RF signal, which introduces a chirp-coefficient $\ddot{\varphi}_t = -15.1\,\mathrm{rad}\cdot(2\pi\cdot 7\mathrm{GHz})^2 \approx -29171\,\mathrm{GHz}^2\cdot\mathrm{rad}$. Owing to the large chirp-coefficient of the TL, the envelope of the output spectrum is similar to the input temporal waveform (dotted curve). To emulate the negative temporal phase induced by the TL, we consider propagation through a SMF with a GVD coefficient per unit length of -21.6 $\mathrm{ps}^2/(\mathrm{rad}\cdot\mathrm{km})$. According to the relationship between the TL chirp-coefficient and dispersion coefficient, $\frac{1}{\ddot{\Phi}_0} = \ddot{\varphi}_t$, this TL modulation process emulates the result of propagation of the considered input signal through a 1.6 km SMF with a total dispersion coefficient of -34.28 $\mathrm{ps}^2/\mathrm{rad}$. It can be seen that the frequency spectrum at the output of the TL exhibits nearly the same envelope as that of the temporal waveform after the corresponding amount of dispersion. In order to illustrate the waveform evolution, different modulation frequencies are applied on the TL, corresponding to different amounts of dispersions, see for instance the results shown in Fig. 2.4 (d) and (e). In these plots, the frequency of the sinusoidal RF signal is set to be 5 GHz and 3 GHz, respectively, inducing a chirp-coefficient $\ddot{\varphi}_t$ of -14883 $\mathrm{GHz}^2\cdot\mathrm{rad}$ and -2381.3 $\mathrm{GHz}^2\cdot\mathrm{rad}$, corresponding to a dispersivefiber length of 3.1 km and 19.5 km, respectively. In Fig. 2.4 (e), the output spectrum shows a profile similar to the input spectrum because the modulated temporal phase induced by the TL is small. However, for the temporal waveform at the output of the corresponding SMF, it approaches the time-mapped version of the input waveform spectrum due to the large amount of dispersion, which nearly satisfies the temporal Fraunhofer condition. Thus, we obtained an intermediate image of the dispersed waveform along the optical fiber and a waveform which is nearly reaching the far-field regime.

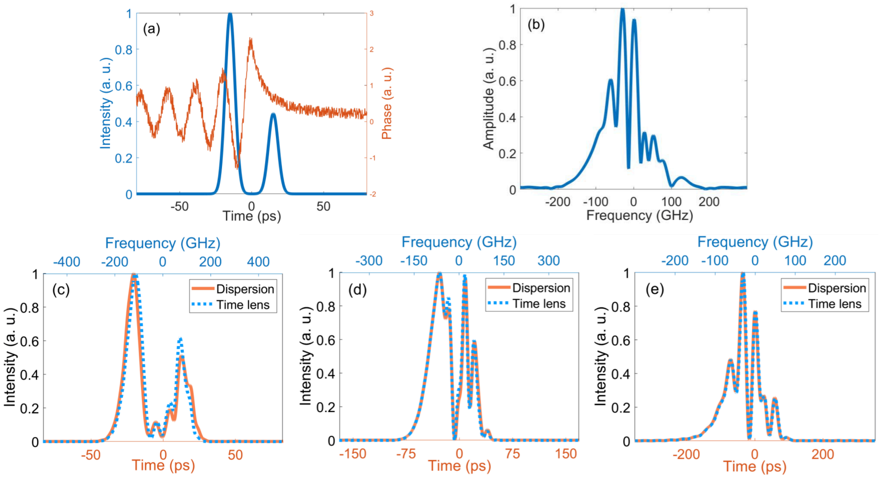

Figure 2.5. Simulation results of the input with initial nonuniform temporal phase. (a) Temporal waveform (solid curve, left scale) and the phase (dotted curve, right scale) of the input pulse; (b) Spectrum waveform of the input; (c)-(e) Output temporal waveforms from SMF with different lengths (solid curve, bottom scale) and output spectrum from the time lens with varying modulation frequency and amplitude of 15.1 rad (dotted curve, top scale);

For completeness, we finally considered the same input pulse as in the previous simulations but having an initial nonuniform temporal phase profile. In Fig. 2.5 (a), the blue curve represents the temporal waveform of the input, while the orange line shows the initial phase profile. This results in a spectrum with a bandwidth extending to ~200 GHz, defined at 1% of the full width of the signal, as depicted in Fig. 2.5 (b). In this case, the modulation amplitude remains the same as before and the evaluation is based on different modulation frequencies and dispersions. In Fig. 3(c)~(e), the output spectrum of the time lens with driving signal frequencies of 8 GHz, 5 GHz, and 3 GHz are shown with blue, dotted curves, while the orange curves show the corresponding temporal output waveforms after propagating through SMFs with lengths of 1.2 km, 3.1 km, and 8.6 km, respectively. As predicted, we obtained the expected waveforms along propagation through the considered dispersive fiber. This latest result confirms that the proposed equivalence is also valid for signals with initial phase.

2.4 Experimental Results of the GVD Emulation

Based on the equivalence discussed above, in proof-of-concept experiments, we follow the dispersion-induced temporal evolution of different picosecond optical waveforms (e.g., a sinc-like temporal pulse and a double-pulse waveform) and observe the obtained dynamics along the optical frequency domain. Fig. 2.6 shows the experimental setup of the demonstration. A frequency comb with a repetition rate of 250 MHz was used as the optical source, followed by a Waveshaper (WS) to generate the target input pulsed waveform. To realize the TL operation, we utilized a PM with an average V_π of ~3.5 V driven by a sinusoidal RF signal. Finally, the modulated signal was directly captured by an optical spectrum analyzer (APEX AP2440A) with a resolution of 1.25 GHz.

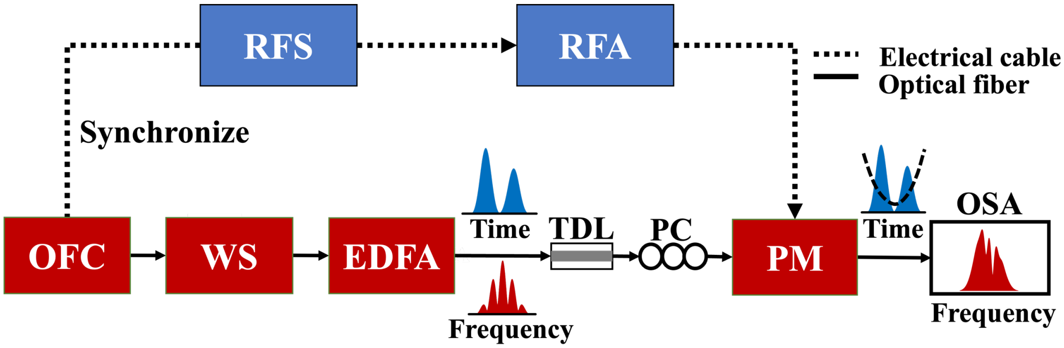

Figure 2.6. Schematic of the experimental setup. RFS: radio-frequency synthesizer; RFA: radio-frequency amplifier; OFC: optical frequency comb; WS: wave-shaper; EDFA: erbium-doped fiber amplifier; TDL: tunable delay line; PC: polarization controller; PM: phase modulator; OSA: optical spectrum analyzer.

To demonstrate the introduced concept, we first consider a sinc-shaped optical pulse (corresponding to a rectangular frequency-spectrum profile) as the input. Fig. 2.7 (a) and (b) show the measured frequency spectrum and the corresponding temporal profile. The latest was obtained numerically since the used optical source, Menlo Systems optical frequency comb (FC1500-250-ULN), is known to exhibit no spectral phase distortion. The FWHM bandwidth of the input optical source is ~100 GHz. Here, we fix the power of the modulating RF signal to 22 dBm, yielding a peak phase shift of ~2.5 rad in the modulation process. The modulation chirp coefficient $\ddot{\varphi}_t$ of the TL is then controlled by continuously tuning the frequency of the RF signal to emulate different amounts of dispersion. It is worth noting that the optical signal is centered at the peak of the modulating sinusoidal signal and the phase of the RF signal is slightly tuned in order to ensure a good synchronization with the input optical pulses. Figs. 2.7 (c)-(e) show the measured frequency spectrum of the modulated signal (solid red traces), compared with the corresponding expected temporal waveform after dispersion (dotted blue traces) and the simulated spectrum at the PM output when driven

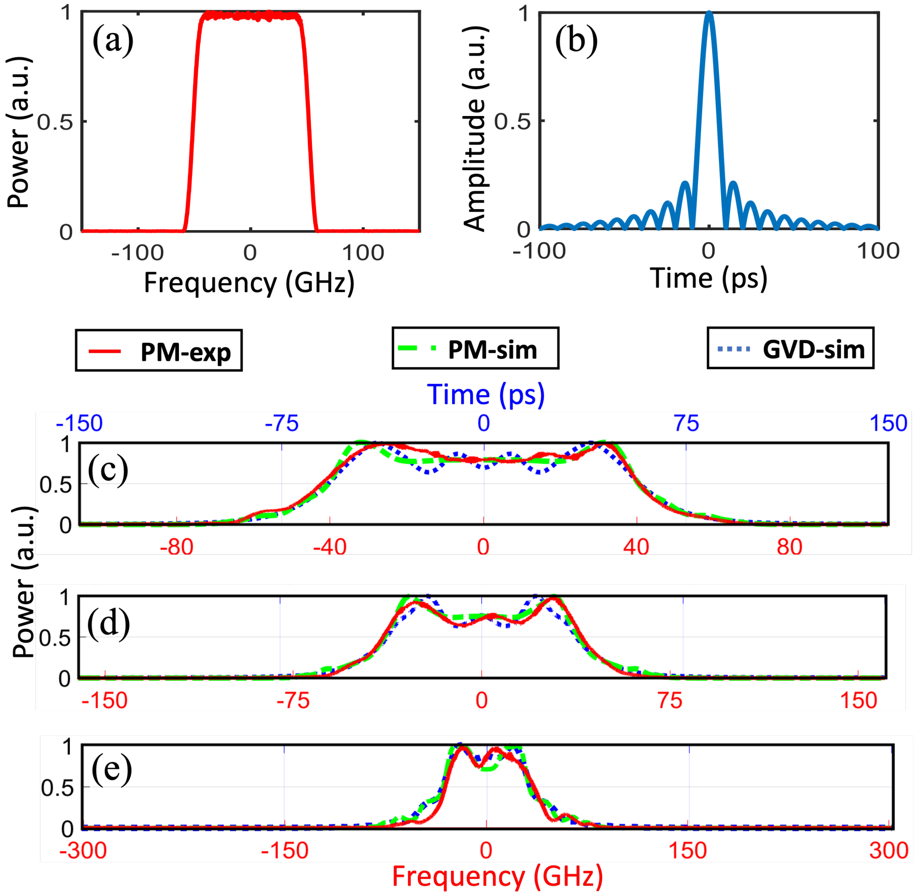

Figure 2.7. Experimental Results. (a) measured spectrum of the input shaped pulse; (b) and the simulated temporal waveform; (c)-(e) measured spectra (solid red curve, bottom scales) at the output of the PM, compared with the simulated temporal waveforms after the corresponding amount of dispersion (dotted blue curve, top scale) and the simulated spectrum at the output of the PM when driven by the corresponding sinusoidal signals (dash dotted green curve, bottom scales), with the relative frequency and time scaling defined in the text.

by the ideal sinusoidal modulation, for three of the evaluated cases. The time and frequency axis are marked at the top and bottom of the plot, respectively. The dispersed waveform is numerically analyzed assuming propagation through a SMF with dispersion coefficient of $\beta_2 = -21.6\ \text{ps}^2/(\text{rad}\cdot\text{km})$. For the cases shown in Fig. 2.7, the modulating frequency is set to 6 GHz (c), 8 GHz (d) and 10 GHz (e), respectively. In the simulation, the lengths of the corresponding SMF sections are 12.8 km (c), 7.22 km (d), and 4.62 km (e), respectively, as determined by Eq. (2.4). Notice that the time and frequency axis of the represented results are scaled as per the relationship between the two variables in Eq. (2.5). The optical spectra are represented around the waveform's central frequency (193.5 THz), whereas the reference time is fixed at the waveform's middle point. To give an example, in Fig. 2.7 (c), the RF frequency of the PM drive is set at 6 GHz, which introduces a chirp-coefficient of $\ddot{\varphi}_t = -2.5\ \text{rad}\cdot(2\pi\cdot 6\ \text{GHz})^2 \approx -3616.9\ \text{GHz}^2\cdot\text{rad}$. As anticipated, for small modulation factors, the output spectrum closely resembles the input spectrum with only slight distortion. The experimental results validate the theoretical predictions, with the output spectral waveform of the PM closely resembling that of the corresponding dispersed signal. However, it is important to note the deviations between the measured spectrum of the PM (solid red traces) and the dispersed signal (dotted blue traces), which are attributed to the nonideal quadratic approximation introduced in Eq. (2.2).

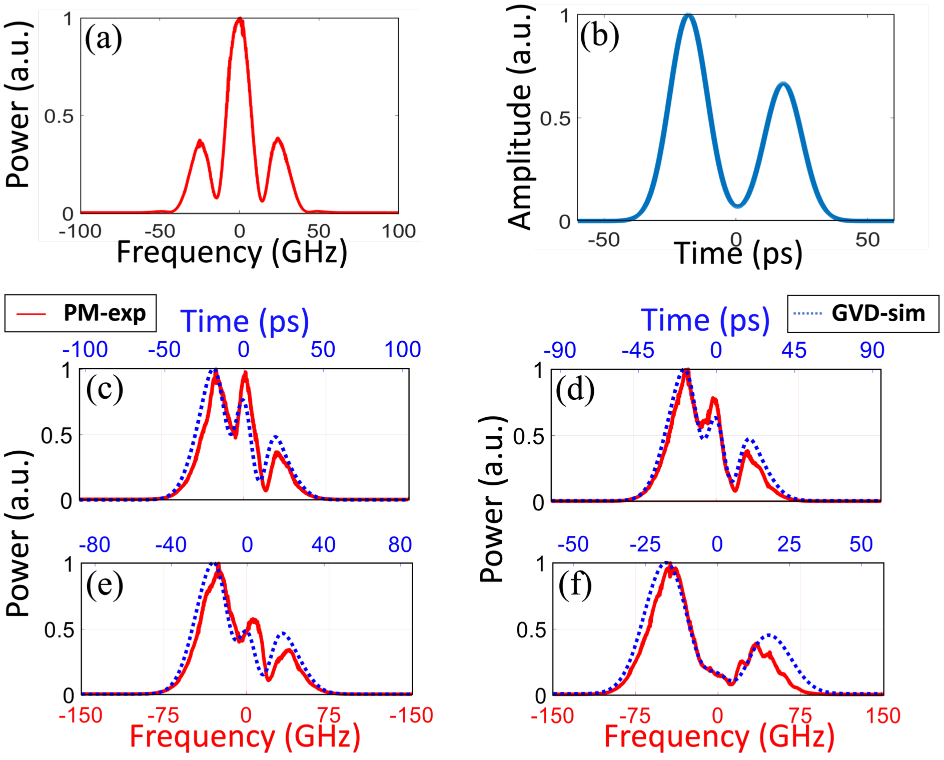

Figure 2.8. Results. (a) measured spectrum of the input pulse; (b) and the simulated temporal waveform; (c)-(e) measured spectra (solid red curve, bottom scale) at the output of the PM, compared with the simulated temporal waveforms after the corresponding amount of dispersion (dotted blue curve, top scale), with the relative frequency and time scaling defined in the text.

As previously discussed, these deviations become more significant, particularly at the edges of the waveform, as the modulation frequency increases.

For completeness, Fig. 2.8 shows additional results for an input temporal waveform that is shaped as two consecutive pulses with different intensities, each with a 12-ps FWHM time width, and separated by 36 ps. The measured spectrum and corresponding simulated temporal waveform are shown in Figs. 2.8 (a) and (b), respectively. In order to emulate different amounts of dispersion, in this case, we fix the modulation frequency at 10 GHz and we tune the modulation amplitude from 25 dBm to 30 dBm, corresponding to dispersive propagation through SMF lengths ranging from 4.77 km to 2.6 km, respectively, results shown in Figs. 2.8 (c)-(f). There is a good agreement between the measured modulated waveform spectra (solid red traces), and the numerically simulated temporal output waveforms (dotted blue traces) after propagation through the corresponding SMF lengths, considering that the time and frequency axis are scaled following the frequency-to-time mapping law defined above, Eq. (2.5). The results from Figs. 2.8 (f) to (c) show the evolution of the dispersion patterns from the Fresnel diffraction regime to nearly the Fraunhofer diffraction point. In this case, employing a high modulation frequency, i.e., 10 GHz, leads to a relatively small time aperture size. As a result, only the portion of the input optical signal within the time-lens aperture will undergo the desired quadratic phase, but all signal components outside this aperture will necessarily introduce aberrations to the resulting output frequency spectrum. This discrepancy aligns with the observed mismatch between the output spectrum of the PM and the dispersed waveform in Fig. 2.8.

2.5 Practical Application for Optimal Pulse Compression Conditions

High-quality ultra-short optical pulses, with time widths ranging from the picosecond to the femtosecond regime, are important for many applications in present and future high-speed communications systems [178], biomedical analysis [179], and optical metrology [180]. The implementation of ultra-short pulses usually involves temporal compression stage involving a dispersive medium, e.g., linear fiber Bragg gratings [181], arrayed waveguide gratings [182], or dispersion fibers [183], aimed at compensating the spectral phase variation of an original broadband signal to utilize all available frequency spectrum, i.e., to achieve the minimum pulse width corresponding to the original pulse frequency spectrum extension. The key for pulse compression is to find the optimal dispersion profile as per the original spectral phase variation. When the phase and amplitude information of the input pulse are unavailable, it is difficult to evaluate and realize the required amount of dispersion under the experimental conditions. Alternatively, we can evaluate the use of the proposed time-frequency duality mentioned above to find the needed dispersion profile for optimal compression of a chirped optical pulse. This is a very attractive method because of its tunability and simple implementation (using a temporal phase modulator).

For this purpose, we have firstly used this method to determine the precise GVD amount (both magnitude and sign) that is needed to achieve optimal compression of an incoming chirped optical temporal waveform, for which no information is available on its amplitude and phase profile. I reiterate that this would be useful in applications where precise characterization of an optical waveform's complex field profile is challenging, e.g., in short-pulse laser design [184]. We use the same system as shown in Fig. 2.6 to demonstrate this application. The signal spectrum was shaped by a programmable WS to obtain a linearly

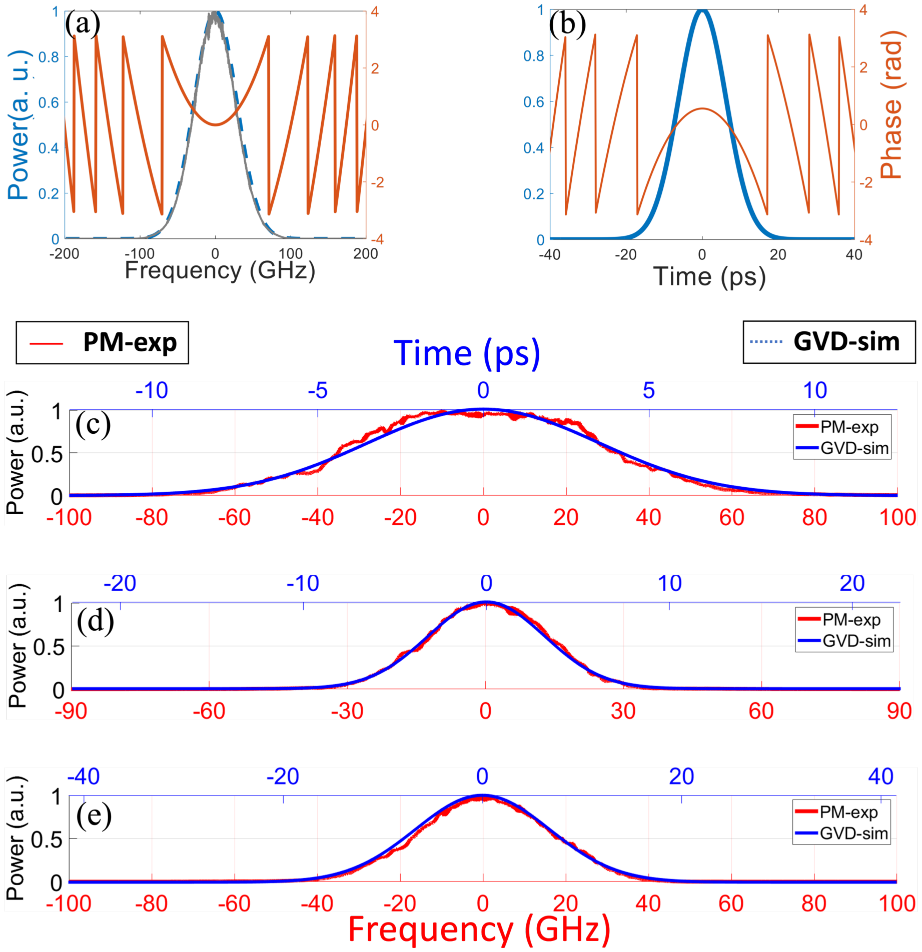

Figure 2.9. Results. (a) measured spectrum (grey curve), simulated spectrum (blue curve) and initial phase (orange curve) of the input pulse; (b) the simulated temporal waveform (blue curve) and temporal phase (red curve); (c)-(e) measured spectra (solid red curve, bottom scale) at the output of the PM, compared with the simulated temporal waveforms after the corresponding amount of dispersion (dotted blue curve, top scale), with the relative frequency and time scaling defined in the text. Notice that the same temporal axis is used here for representation of the different recovered waveforms to facilitate their comparison.

chirped Gaussian pulse with a temporal complex field $\hat{a}_{in}(t) = \exp\left[-\frac{(1+iC)}{2}\frac{t^2}{T_0{}^2}\right]$, where $T_0 = 9$ ps and the chirp parameter $\mathrm{C} = +2$. Specifically, Fig. 2.9 (a) shows the measured spectrum and spectral phase profile of this input pulse. Firstly, we set the modulation frequency and amplitude of the TL at 14 GHz and 30 dBm, respectively, to emulate pulse propagation through a 0.5-km length of dispersion-compensating fiber (DCF) with a dispersion parameter of β_2=$+39\ \mathrm{ps}^2/(\mathrm{rad}\cdot\mathrm{km})$. For this purpose, the input optical pulse must be centered around a valley of the sinusoidal RF signal; otherwise, the modulated output frequency spectrum indicates that the input optical pulse is temporally broadened regardless of the modulation chirp coefficient value. The red line in Fig. 2.9 (c) shows the measured optical spectrum of the modulated signal and the blue line is the corresponding simulated temporal waveform after propagation through the emulated DCF section, using the time-frequency mapping factor mentioned above. These results indicate that the FWHM temporal width of the pulse is compressed form ~18 ps to ~8 ps. In order to obtain further compression, we decreased the chirp coefficient to emulate a higher amount of dispersion. As seen in Fig. 2.9 (d), when the RF frequency and amplitude are set at 8.75 GHz and 33 dBm, corresponding to a 0.81-km length of the DCF, we achieve the maximum compression point, and in particular, the temporal FWHM of the output pulse is estimated to be ~5 ps. As expected, the total dispersion value corresponding to this optimal point (~$31.6\mathrm{ps}^2/\mathrm{rad}$) corresponds very nearly to the quadratic spectral phase imposed on the input pulse. When the modulating frequency is decreased to 6 GHz with a 33-dBm modulation amplitude (corresponding to a ~1.9-km DCF length), it can be seen from Fig. 2.9 (e) that the pulse width is now broadened. These results confirm that the proposed method provides a simple means to obtain an accurate estimate of the dispersion conditions for optimal pulse compression without the requirement for a full precise characterization of the input pulse to be compressed.

2.6 Conclusion

In this chapter, I have introduced and developed the fundamental components for signal analysis and processing to be used in my thesis. Specifically, I focus on the second-order dispersive medium and the time lens. By introducing their physical mechanism, main characteristics and practical implementations, a solid foundation has been established for the signal analysis and processing strategies as the heart of this thesis. Through mathematically analyzing the basic concept behind the equivalence between GVD propagation and TL modulation for any given input signal, I have provided a deep insight into the time-frequency relationship between these two units.

The discussed equivalence exploits the fact that the frequency spectrum of a given (input) waveform, following a suitable sinusoidal temporal phase modulation, exhibits the same shape as that of a dispersed version of the same temporal waveform after propagation through a prescribed amount of dispersion. The proposed approach represents a simple method to track the time-domain evolution of a dispersed optical waveform in a continuous fashion using a PM driven by a sinusoidal RF signal. The method requires no information on the complex profile of the input waveform, and the expected output temporal shape is observed along the optical frequency domain. The method could prove useful for analysis and design tasks of functionalities that involve GVD, such as for dispersion management, optical pulse compression, etc. In proof-of-concept experiments, we successfully tracked the dispersion-induced temporal evolution of different optical picosecond pulsed waveforms (e.g., a sinc-like temporal pulse and a double-pulse waveform) by tuning the frequency and/or amplitude of the phase modulation signal and observing the resulting shapes in the optical frequency domain. A good agreement was obtained between the measured spectra and predicted temporal shapes of the propagating waveform for different amounts of dispersion. As an application example, we utilized this method to determine the precise GVD amount (both magnitude and sign) that is needed to achieve optimal compression of an incoming chirped optical temporal waveform, for which no information was available on its amplitude and phase profile. This would be useful in applications where precise characterization of an optical waveform's complex field profile is challenging, e.g., in short-pulse laser design [184]. In the next chapter, I will present a time-frequency analysis method that is based on the time-lens and GVD processes described in this chapter.

3 TIME-MAPPED SPECTRAL ANALYSIS

In this chapter, I describe a novel temporal imaging technique for time-frequency (T-F) analysis of arbitrary signals with reconfigurable specifications. The key to this optimal design is to operate the system under so-called fractional Talbot conditions [193], i.e., to design the group-velocity dispersion (GVD) in such a way that the optical pattern at the output of the first dispersive line is a rate-multiplied copy of the input pulse train, thus achieving the desired uniform sampling of the signal under test in the modulation stage. I show here how this scheme can be designed to tailor at will the main performance specifications of the implemented spectrogram analysis, in terms of instantaneous bandwidth, and time and frequency resolutions, overcoming the central design trade-offs of the integer Talbot scheme. Furthermore, I propose an extension of this fractional Talbot design involving just temporal phase modulation of the SUT, leading to a simpler scheme that is also optimized in terms of energy efficiency. This latest design is related to the time-domain equivalent of a Talbot array illuminator (TAI) [193], a concept that has been recently used for optical pulse generation from continuous wave (CW) light [194] and Talbot passive amplification of arbitrary temporal waveforms [188]. This concept can be interpreted as a form of discretization of a conventional time lens (continuous quadratic phase modulation profile), allowing to effectively limit the maximum phase excursion to 2π while implementing a manipulation equivalent to a conventional time-lens with a total phase excursion up to 206.25π using a single electro-optic phase modulator.

3.1 Introduction

Precise knowledge of the evolving spectral characteristics of a waveform is fundamental to a wide range of fields including microwave photonics, Radar/Lidar technologies, telecommunications and biomedicine [5], [185], [186], [187], [188]. To obtain the most comprehensive representation of a signal of interest, the analysis is generally required to be done in real-time and without any gaps in the signal acquisition and processing. This effectively corresponds to measuring the joint time-frequency representation or spectrogram (SP) [188], [189], [190], [191], [192], [193], such that the spectral characteristics of the signal under test (SUT) are analyzed on time scales commensurate with the bandwidth of the analyzed waveform. Another key requirement for many of these applications is that the spectrum must be also captured with a sufficiently high definition, corresponding to a fine frequency resolution. Yet, it remains very challenging to capture the full spectrogram of Electromagnetic (EM) waves over a large analysis bandwidth (e.g., in the tens of GHz range and above) and with a simultaneous high frequency resolution (e.g., down to the MHz regime). In the case of radio and microwave signals, the most common solutions rely on electronic digital post-processing to implement multiple fast Fourier transform (FFT) algorithms. Although they can easily access frequency resolutions down to the kHz regime, the instantaneous operation bandwidth (or frequency span) remains limited to just a few hundreds of MHz [194]. On the other hand, photonic analog processing can overcome the analysis bandwidth limitation of electronic-based methods [189], [190], [191], [192], [193], [195], [196], [197], [198] but at the cost of a greatly impaired time or frequency resolution. As such, present photonic solutions are mainly based on temporal imaging schemes (or frequency-to-time mapping) using a linear electro-optic sampling or a time-lens process [8], [9], [10], [12], [13], [14], [15]. For instance, the Talbot design described in Chapter 1, for which the SUT is directly modulated on the input optical pulse train under the Nyquist criterion, has been demonstrated for continuously and gap-free time-mapped Fourier transform analysis. However, considering the practical requirements of the required devices in this scheme, particularly, group-velocity dispersion and detection speed, this approach is constrained to provide an instantaneous operation bandwidth just over a few GHz and with a limited number of analysis points along the frequency domain (typically, lower than ~10 analysis points). Moreover, the additional design conditions that need to be imposed in the Talbot scheme significantly affect the versatility of this scheme to tailor the specifications of the performed SP analysis. An alternative approach for a gap-free time-mapped spectrogram analysis has been recently proposed [173]. This approach can be interpreted as an extension of a time-lens Fourier transformer in which time lenses are consecutively implemented, adjacent to each other, while ensuring that each of the time-mapped spectra obtained at the system output remains temporally limited to a duration shorter than each lens aperture. The latest ensure that consecutive time-mapped spectra do not interfere with each other, enabling a straightforward mapping and recovery of the SUT spectrogram along the time domain. The time-lens spectrogram has been shown to enable performing spectrogram analysis over hundreds of GHz of instantaneous bandwidth using linear electro-optic modulation [173]. However, similarly to the Talbot spectrogram case, the time-lens spectrogram is also practically limited to provide a relatively coarse frequency resolution, with ~10 points per measured spectrum at best. This is due to the maximum phase excursion that can be achieved in practice through electro-optics modulation (limited to a few π). Whereas nonlinear optics implementations of similar designs might enable overcoming this main design trade-off, these would necessarily incur in excessive energy consumption and low efficiency. However, it remains challenging to capture the evolving spectrum of an incoming broadband signal at a nanosecond scale and with an ultrafine resolution [113], especially using an efficient linear-optics scheme.

To address this, a novel method will be introduced in this Chapter that employs phase-only linear optics manipulations, such that it is inherently highly sensitive and energy efficient. The proposed method can provide nanosecond-scale ultrahigh-definition spectral analysis, easily with hundreds of analysis points, simultaneously over a broadband analysis bandwidth, up to 92 GHz (i.e., corresponding to microwave frequencies up to 46-GHz) demonstrated in our work. In section 3.2, we obtain the principles and fundamental governing equations of the TAI spectrogram design using a more formal derivation, directly linked with the Talbot effect in dispersive optical fibers. We also show how this scheme can be designed to tailor at will the main performance specifications of the implemented SP analysis, in terms of instantaneous bandwidth, and time and frequency resolutions. The proposed design is validated through numerical simulations and experimental demonstrations. In particular, we experimentally demonstrate a time-mapped short time Fourier transform (STFT) based on phase-only modulation of the SUT (a temporal TAI design) that provides an outstanding performance, i.e., an instantaneous full analysis bandwidth up to ~92 GHz, a versatile frequency resolution down to ~110 MHz and an ultra-high processing speed, up to 1316×10^6 FTs per second, using widely available fiber-optics technologies.

3.2 Operation Principle

As described in Chapter 1, the Talbot-based spectrogram offers a simple way for time mapping a gap-free STFT of an incoming signal in an entirely continuous and real-time manner [191], [199]. As shown in Fig. 1.11 of Chapter 1, this design involves sampling the SUT (i.e., a microwave signal) with a periodic train of short (generally, unchirped) optical pulses under the Nyquist criterion followed by linear propagation through a suitable group-velocity dispersive line. Specifically, the dispersive line is designed to satisfy an integer Talbot self-imaging condition with respect to the pulse sampling rate. The system has been shown to map along the time domain the spectra of consecutive, heavily overlapped temporal sections of the SUT at the system output, with each time-mapped spectrum extending over a duration equal to the sampling pulse period. However, the key drawback of the integer Talbot scheme is the limited operation bandwidth (a few GHz at best) and limited number of analysis points along the frequency domain (typically, lower than ~10 analysis points).

To address this, we propose designing the dispersive lines to operate under fractional Talbot conditions [200], such that the optical signal on which the SUT is modulated is in fact a rate-multiplied copy of the input optical pulse train. The resulting scheme is shown in Fig. 3.1. For operation under fractional Talbot, the GVD in the system must satisfy the following condition [201]:

$$\ddot{\Phi}_0 = \frac{s}{q}\frac{{T_r}^2}{2\pi} \tag{3.1}$$

with q being any natural number and s being any integer co-prime with q. Notice that Eq. (3.1) with $q = 1$ is the integer Talbot condition. Under this condition, the input pulse train is exactly replicated at the output of the first dispersive line in the general scheme shown in Fig. 3.1. This implies that this first dispersive

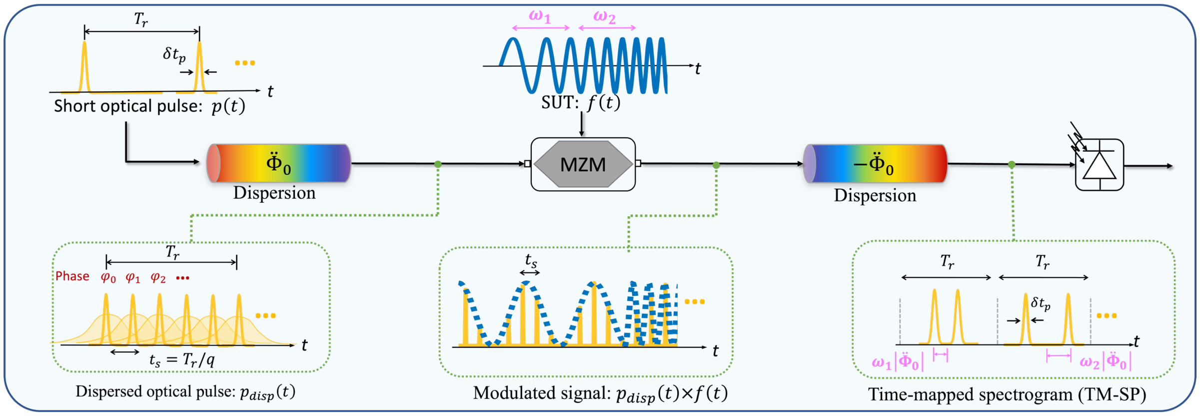

Figure 3.1.Basic principles of fractional Talbot-based schemes for time-mapped spectrogram, involving temporal sampling of the microwave SUT with a high-rate, Talbot phase-conditioned optical pulse train followed by fiber-optics group-velocity dispersion (GVD) and photo-detection.

line is unnecessary, leading to the Talbot spectrogram scheme described in Chapter 1, namely, involving a direct temporal sampling of the SUT with the input pulse train followed by propagation through the suitable amount of linear GVD. Under the fractional Talbot condition in Eq. (3.1) (with $q \geq 2$), the input pulse train is also self-imaged after propagation through the first dispersive line, in such a way that the dispersed optical signal is another pulse train in which the individual pulses are exact replicas of the input ones, with an envelope defined by $p(t)$, but repeating at an increased rate by the factor q. This means that the repetition period of the self-imaged pulse train after dispersion is $t_s = T_r/q$. In a practical design, the use of $|s| = 1$ ensures the most relaxed design condition. To ensure that a uniform rate-multiplied pulse train is produced, the reduced repetition period must still be longer than the full time-width of each individual pulse $\varDelta\nu_p$, namely, $t_s > 1/\varDelta\nu_p$. The SUT is then uniformly sampled by this short-pulse train with an increased rate (by the factor q with respect to the input pulses' rate). To be able to recover the STFT information, these consecutive time-mapped FTs must be sufficiently spaced apart to avoid any interference among them. Considering that the frequency-to-time mapping factor discussed before, $\Delta\omega_t \rightarrow \Delta t/\ddot{\Phi}_0$, is also determined by the dispersion factor $\ddot{\Phi}_0$, the time-mapped FT of any section of the SUT extends over a maximum duration of $|\ddot{\Phi}_0|\varDelta\omega_{SUT}$, where $\varDelta\omega_{SUT}$ is the full-width frequency bandwidth of the SUT. These two central design conditions can be mathematically expressed at once as follows:

$$\frac{1}{\Delta\nu_p} < t_s < \frac{1}{\Delta\upsilon_{SUT}} \tag{3.2}$$

where $\Delta\upsilon_{SUT} = \varDelta\omega_{SUT}/2\pi$ is the full spectral bandwidth of the SUT expressed in natural frequency units. The inequality to the right ensures no overlapping among consecutive time-mapped spectra at the system output. This inequality corresponds to the Nyquist criterion that must be satisfied in sampling a signal with a frequency bandwidth that is broader than $\Delta\upsilon_{SUT}$ [202]. We can easily confirm that the inequality to the left in Eq. (3.2) (condition for a gap-free analysis) is necessarily satisfied under the stated conditions for fractional self-imaging, considering that the resulting repetition period t_s must be longer than the full time-width of the individual pulses ($> 1/\Delta\nu_p$) to achieve a uniform rate-multiplied pulse train.

A key feature of a pulse train produced by fractional Talbot self-imaging is that a deterministic phase shift is induced pulse to pulse along the rate-multiplied train. The discrete and bounded temporal phase profile is based on the framework of the temporal TAI, according to the following expression [116]:

$$\varphi_n = -\sigma\pi n^2 \frac{p}{q} \tag{3.3}$$

where $\sigma = \pm 1$, n is a running integer index defining the temporal pulse number, and the integer parameter p depends on the rate-multiplication factor q and the parameter s in Eq. (3.1). In particular, the parameters p and s must satisfy the following congruence relationship: $ps = 1 + qe_q$, with $e_q = 1$ if q is odd and $e_q = 0$ if q is even. This feature of a fractional Talbot pulse train suggests an alternative implementation for generation of the pulse sequence used for sampling of the SUT. This sampling train could be produced by temporal phase modulation of a mode-locked optical pulse sequence directly generated with a repetition period t_s, in which the phase is shifted pulse to pulse according to the pattern in Eq. (3.3).

The proposed fractional Talbot design can be further simplified following the design illustrated in Fig. 3.2 (a). Let us assume that the individual optical pulses exhibit an ideal rectangular shape with a time width equal to the target output repetition period $t_s = T_r/q$. Mathematically, the individual pulse envelope can then be written as $p(t) \propto \mathrm{rect}(t/t_s)$, where $\mathrm{rect}(t/X)$ is an ideal rectangular function of duration equal to *X*, i.e., $\mathrm{rect}(t/X) = 1$, for $(-X/2) \leq t \leq (X/2)$, and $\mathrm{rect}(t/X) = 0$, for any other value of t. In this case, the fractional Talbot pulse train at the output of the dispersive line exhibits a uniform light distribution with a discrete temporal phase pattern following Eq. (3.3), as shown in Fig. 3.2 (a). This implies that the SUT must then be phase modulated according to the temporal profile in Eq. (3.3). This avoids the need for a temporal intensity sampling of the SUT and the corresponding amplitude modulation process. Fig. 3.2 (b) shows a proposed practical implementation of the resulting design. The SUT is first modulated into an optical carrier, e.g., a CW light. Notice that in general, the proposed system would perform SP analysis of the temporal complex envelope of an incoming optical waveform. The optical SUT is then phase modulated following the profile defined in Eq. (3.3). This can be implemented for instance using an electro-optic phase modulator (PM) driven by an electronic arbitrary waveform generator (AWG), as detailed in Chapter 1. The modulation signal from the AWG should be programmed to implement phase modulation according to the profile in Eq. (3.3). As illustrated in Fig. 3.2 (a), each discrete phase level should have a uniform value

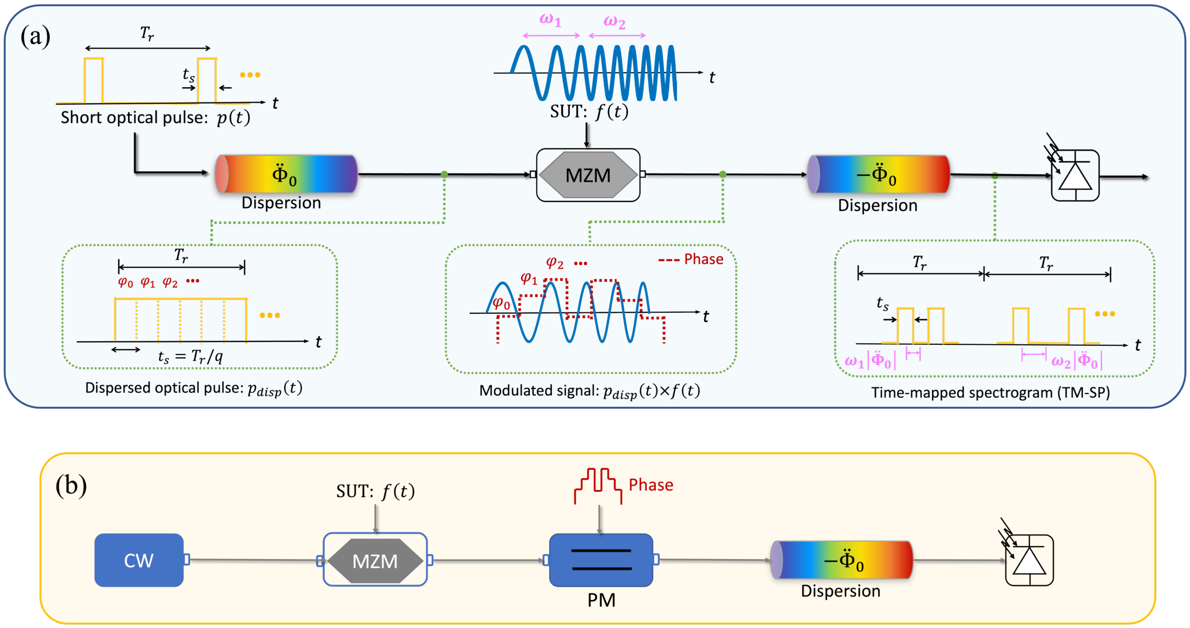

Figure 3.2. Principle of the proposed TAI-based spectrogram scheme. (a) Schematic of the proposed Talbot array illuminator (TAI) based configuration for real-time spectrogram analysis. (b) Practical implementation of the design in Fig. 3.2(a) using electro-optic phase modulation (PM) of the SUT on an optical carrier followed by fiber-optics GVD and photo-detection. In this latest case, the fractional Talbot phases can be electronically programmed.

extending over a duration equal to the repetition period t_s of the equivalent rate-multiplied pulse train. To avoid a large phase accumulation, requiring a large phase modulation excursion, the phases in Eq. (3.3) are more easily implemented modulus 2π, as shown in Fig. 3.2. This bounded phase overcomes the limitations associated with constraints in the maximum phase excursion that is possible with a practical temporal modulation device. In this case, the resultant phase pattern is periodic with a period equal to q (if the product pq is an even number) or $2q$ (if the product pq is an even number) [21], i.e., the resulting temporal phase modulation profile repeats periodically with a period equal to $T_r = qt_s$ or $2T_r = 2qt_s$, respectively. We recall that in general, the factor s is determined from the congruence relationship: $ps = 1 + qe_q$. In practice, the best performance is achieved when the factor s in Eq. (3.1) is fixed to have a magnitude equal to 1. For instance, when $s = 1$, the factor p in Eq. (3.3) must be fixed as follows: $p = 1$ if q is even, or $p = q + 1$ if q is odd. Here we chose q is odd, in such a way that the phase pattern in Eq. (3.3) repeats every q phase levels, or with a period $T_r = qt_s$. The resulting temporal TAI phase that is modulated on the PM can then be written:

$$\varphi_n = -\sigma\pi n^2 \frac{q-1}{q} \tag{3.4}$$

This phase function is wrapped to 2π and still give a modulation equivalent to a conventional time-lens with a total phase excursion of $\frac{\pi q}{4}$.

Subsequently, the phase-modulated SUT propagates through a linear dispersive line with a GVD equal to $-\ddot{\Phi}_0$ that satisfies the following condition:

$$\ddot{\Phi}_0 = \sigma \frac{q t_s^2}{2\pi}. \tag{3.5}$$

In practice, this spectral phase filtering can be implemented using a simple group-velocity dispersive line (e.g., an appropriate length of single-mode optical fibre).

As shown in Fig. 3.2 (a), the schematic of the proposed TAI-based time-mapped spectrogram simply consists of a PM to impart a discrete temporal phase according to Eq. (3.4) on the incoming signal. This phase modulated signal then propagates through a dispersive medium providing a GVD satisfying Eq. (3.5). The resulting temporal signal corresponds to consecutive time-mapped spectra of the signal after a photodiode. This scheme calculates the Fourier transform (FT) over each consecutive section of duration T_r of the input SUT, in such a way that the resulting consecutive spectra are mapped along the time domain, each extending over a time slot of duration T_r. This mapping is produced according to the frequency-to-time mapping law $\Delta\omega_t \rightarrow \Delta t/\ddot{\Phi}_0$, described in Eq. (1.5), where $\Delta\omega_t$ and Δt are the radial frequency of the input signal and time variable at the system output, both relative to the centre of each analysis window. The output temporal waveform of the proposed system is evaluated at each time slot $kT_r - \frac{T_r}{2} \leq t < kT_r + \frac{T_r}{2}$, with $k = 0, 1, 2, \ldots$, which represents the number of the time slot. Thus, the FT of each time-windowed version of the SUT can be obtained according to the frequency-to-time mapping factor with the central location of the temporal analysis window, running as kT_r. Specifically, the temporal waveform along the time slot centered at kT_r is just a time-mapped copy of the corresponding STFT of the SUT. In this manner, the entire dynamic spectrum of the SUT, when mapped along the time domain, is comprised within the corresponding analysis period. Thus, the input waveform section along each analysis window is consecutively Fourier transformed through a time-lens and dispersion based system. Specifically, the consecutive Fourier transforms are obtained by mapping the frequency spectrum of each of the corresponding adjacent signal sections along the time domain in a serial manner.

3.3 Design Trade-offs

In what follows, we provide an outline of the main design specifications and trade-offs of the temporal TAI (T-TAI) schemes for real-time spectrogram analysis. We target a design to perform a gap-free time-mapped spectrogram of a given SUT, extending over a maximum frequency bandwidth $\Delta\nu_{SUT}$ (instantaneous frequency bandwidth). This specification is ultimately limited by the operation bandwidth of the modulation devices in the system. Our goal is to perform the spectrogram analysis with a prescribed time or frequency resolution. We recall that the time (frequency) resolution of a given spectrogram distribution is defined as the minimum spacing between two different temporal (spectral) events of the SUT that can be clearly resolved in the obtained spectrogram [188]. The time and frequency resolution parameters are inversely related. The ratio between instantaneous bandwidth and frequency resolution provides an estimate of the number of points used in the performed spectral analysis. A key design specification is the photo-detection bandwidth, which will ultimately limit the achievable frequency resolution or number of frequency analysis points.

3.3.1 Main Design Requirements

Eq. (3.4) defines the required TAI phase consists of q phase levels eave of length t_s, forming a periodic pattern of length $T_r = qt_s$. T_r is the repetition period of the temporal phase, and t_s is the width of each bin in the temporal modulation pattern. The ratio T_r and t_s is a natural number q. We evaluate here the resulting specifications for the best performing case, i.e., when $|s| = 1$, though the obtained conclusions could be easily extrapolated to the cases when $|s| > 1$.

We recall that Eq. (3.2) defines the central design conditions of the scheme based on fractional Talbot conditions, including both the intensity sampling (or pulsed) scheme and the phase sampling (TAI) scheme. the inequality to the right in Eq. (3.2) ensures that the calculated consecutive spectra are sufficiently well separated as they are mapped along the time domain at the system output. This inequality corresponds to the Nyquist criterion of the implemented temporal sampling process on the SUT (intensity sampling for the pulsed design and phase sampling for the TAI design) [201], i.e., the sampling rate ($1/t_s$) must be higher than the SUT full bandwidth $\Delta\upsilon_{SUT}$. Thus, the maximum frequency extension of the input SUT, or instantaneous analysis bandwidth B of the implemented spectrogram, is just limited by the inverse of the time width t_s of each single-phase step in the modulation profile [189] , $B\sim 2\pi/t_s$. This latest condition ensures that the consecutive time-mapped spectra do not interfere with each other. Moreover, the signal frequency bandwidth must be within the spectrogram analysis bandwidth. This implies that [189]:

$$\Delta\upsilon_{SUT} \leq \frac{1}{t_s}, \tag{3.6}$$

where $\Delta\upsilon_{SUT}$ is the full bandwidth of the SUT expressed in natural frequency units. Thus, the full frequency bandwidth of the SUT is ultimately limited by the speed or bandwidth of the phase modulation apparatus, typically constrained by the bandwidth of the electronic used to generate the phase modulation waveforms. On the other hand, the rapid wrapping of the phase near the edges lead to stringent requirements for the modulation bandwidth [203]. The maximum number of points of the conducted spectral analysis is then defined as the full analysis bandwidth divided by the frequency resolution $N \sim B/\delta\omega_{res}$, where $\delta\omega_{res}$ is the frequency resolution. As discussed above, at the system output, consecutive time-mapped spectra are spaced by the period $T_r = qt_s$, in such a way that the processing speed (number of FTs calculated per unit of time) is determined by the inverse of this period, namely, $1/T_r = 1/(qt_s)$. A higher processing speed can then be achieved by fixing a shorter period T_r in the design (either by using a shorter t_s or a smaller q factor), but this would worsen the achieved frequency resolution, as discussed further below.

The required amount of dispersion following Eq. (3.5) produces a quadratic frequency dependent phase modulation that is the related to the designed parameter of the temporal phase. This implies that the temporal analysis window width is limited by the available dispersion. To achieve a narrower analysis window, we need to introduce a smaller amount of dispersion. According to Eq. (3.5), it is obvious that a smaller amount of dispersion can be realized by decreasing the width of the phase steps t_s. This would be limited by the maximum allowable bandwidth of the phase modulator and AWG, as described above. On the other hand, one could also reduce the analysis point q, while with sacrificing the analysis point, which is determined by the number of phase steps per period in the phase modulation pattern. Thus, the required amount of dispersion is determined by the TAI phase and can be adjusted by properly designing the related metrics of the system. In turn, this indicates that the proposed scheme offers a great versatility to tailor the performance specifications of the obtained spectrogram. Specifically, the system can be flexibly designed to achieve a target set of specifications, e.g., in terms of instantaneous frequency bandwidth, processing speed (or number of FTs per second), and the width of the analysis time window, which in turn determine the time and frequency resolutions. A detailed analysis of the design governing these performance metrics is provides below.

3.3.2 Spectrogram Time Resolution

As discussed in Chapter 1, the time resolution δt_{sp} of the performed spectrogram is given by the width of the analysis window, $|h(t)|^2$, which can be estimated as the width of the temporal intensity profile of the dispersed optical pulses. The reader can easily confirm that for a sufficiently large value of the q factor (e.g., $q > 10$), the GVD undergone by the input optical pulse train, defined in Eq. (3.1), satisfies the so-called temporal Fraunhofer condition with respect to each of the pulses in the sequence, $\left|\ddot{\Phi}_0\right| \gg \frac{\delta t_p{}^2}{2\pi}$, considering that the individual pulse duration δt_p should keep shorter than t_s (to avoid pulse overlapping after pulse rate multiplication at the output of the dispersive line). This implies that each of the individual pulses at the output of the dispersive line is a time-mapped version of the frequency spectrum of the input pulse, $p_{disp}(t) \propto P\left(\omega = t/\ddot{\Phi}_0\right)$ (with the variables t and ω being relative to the pulse's central time and frequency, respectively). As a result, the dispersed pulse intensity width (spectrogram time resolution) is well approximated by the width $\delta\omega_p$ of the energy spectrum of the input optical pulses $|P(\omega)|^2$ multiplied by the frequency-to-time scaling factor magnitude, $\delta t_{sp} \approx \left|\ddot{\Phi}_0\right| \delta\omega_p$.

For the phase sampling (TAI) case, Fig. 3.2, the spectrogram time resolution is determined by considering that the input optical pulse exhibits an ideal rectangular shape with a time width equal to the target sampling period $t_s = T_r/q$, i.e., $p(t) \propto \mathrm{rect}(t/t_s)$, see equivalent scheme in Fig. 3.2 (a). We recall that in a practical setup, this sampling period is determined by the duration of each of the individual discrete steps of the phase modulation profile. The FT of this pulse shape follows a *sinc* variation, and in particular, $P(\omega) \propto sin(\omega t_s/2)/\omega$. The spectral width of the corresponding energy spectrum $|P(\omega)|^2$ can be for instance estimated as the full width at half maximum of the main lobe of the squared *sinc* function. Thus, we assume the spectral width as $\delta\omega_p = 2\pi/t_s$. Using this estimate and the dispersion value in Eq. (3.5) (with $|s| = 1$), the time resolution is equal to the period of the sampling phase function:

$$\delta t_{sp} \approx q t_s = T_r \tag{3.7}$$

This result indicates that each temporal analysis window extends over a duration equal to the spacing between consecutive windows (T_r). Notice that the bandwidth of the SUT should satisfy Eq. (3.7) to ensure the full spectrum can be mapped to the temporal window T_r. In any case, the SP resolution is directly proportional to the period of the modulation phase function T_r. This implies that a sharper time resolution can be achieved by use of a shorter phase-modulation period T_r. In turn, this would result in a higher FT computation speed, though at the cost of a poorer frequency resolution (or the related smaller number of analysis points in the performed spectrogram).

3.3.3 Spectrogram Frequency Resolution

Recall that the frequency resolution of the computed spectrogram is defined as the minimum spacing between two different spectral events of the SUT that can be clearly resolved [188]. The frequency resolution ($\delta\omega_{res}$) also determines the number of points N_{freq} used for representation of each of the calculated signal spectra. Mathematically, the number of frequency points $N_{freq} < \Delta\omega_{SUT}/\delta\omega_{res}$, where $\Delta\omega_{SUT}$ is the full-width spectral bandwidth of the SUT and $\delta\omega_{res}$ is an estimate of the frequency resolution of the spectrogram captured at the system output. The best frequency resolution $\delta\omega_{res}^{optimal}$ offered by a spectrogram distribution is constrained by the uncertainty principle of the Fourier transform. This resolution is inversely proportional to the temporal duration of the analysis window $h(t)$ used for the STFT calculation (which in turns determine the spectrogram time resolution, as discussed above). As discussed, in the considered spectrogram schemes, the temporal analysis window is given by the dispersed optical pulse envelope. In most practical designs, a high q parameter ($q > 10$) is fixed, in which case the dispersed pulse envelope is approximately proportional to the input pulse spectrum, namely, $h(t) = p_{disp}(t) \propto P\big(\omega = t/\ddot{\Phi}_0\big)$. In this case, $FT\{h(t)\} \approx \ddot{\Phi}_0 p\big(t = -\ddot{\Phi}_0\omega\big)$, where $p(t)$ defines the temporal envelope of the input short pulses. Hence, the spectrogram frequency resolution is determined by the width δt_p of the temporal intensity profile of the input short pulses, $|p(t)|^2$, properly scaled along the frequency domain, i.e., $\delta\omega_{res}^{optimal} \approx \delta t_p/\big|\ddot{\Phi}_0\big|$.

In the phase sampling (TAI) design, Fig. 3.2, $\delta t_p = t_s$, such that the optimal frequency resolution is given by

$$\delta\omega_{res}^{optimal} \approx \frac{t_s}{|\ddot{\Phi}_0|} = \frac{2\pi}{T_r}\,. \tag{3.8}$$

Where we impose the condition in Eq. (3.5). This indicates that the frequency resolution is inversely related to the time resolution. This corresponds to a number of analysis points $N_{freq}^{optimal} < \varDelta\omega_{SUT}\big(\big|\ddot{\Phi}_0\big|/t_s\big) \approx \varDelta\nu_{SUT}T_r$. Considering further that the total bandwidth of the SUT is lower than the time-lens bandwidth, as per Eq. (3.6), we derive that the maximum number of analysis points is ultimately limited by the value of the factor q (ratio of the phase sampling period, T_r, to the duration of a phase sampling step, t_s):

$$N_{freq}^{optimal} < q = \frac{T_r}{t_s} \tag{3.9}$$

This latest equation indicates that a higher number of analysis points can be simply achieved by using a fractional Talbot phase sampling function with a longer number of phase levels.

The time-mapped spectra are subsequently measured with a photo-detection apparatus, which necessarily offers a limited time resolution δt_{PD} (inverse of its frequency bandwidth), thus further deteriorating the frequency resolution of the captured spectrogram (consecutive spectra). In particular, the effect of the photo-detector (PD) on the time-mapped spectrogram can be mathematically described through a temporal convolution of the temporal intensity profile at the system output, with the characteristic temporal impulse response of the PD, $r_{PD}(t)$ (real positive valued function) [204]. The optimal resolution in Eq. (3.8) is then smoothed (broadened) by the PD temporal response. To provide some estimates, we assume δt_p and δt_{PD} are the temporal widths (standard deviations) of the input pulse intensity waveform and PD impulse response, respectively. The resulting temporal width can be calculated by the convolution of these two functions [188], [202]:

$$\delta t_{res}^{PD} = \sqrt{{\delta t_p}^2 + {\delta t_{PD}}^2} \tag{3.10}$$

This latest width provides an estimate of the resolution with which each of the time-mapped spectral profiles is captured using a PD with a resolution δt_{PD}. In order to capture the time-mapped spectra with the estimated optimal resolution, and the corresponding maximum number of analysis points, the photo-detection device must provide a temporal resolution of the order of the pulse duration δt_p ($= t_s$, for the phase sampling design), which may pose practical challenges. If electro-optic phase modulation is used for practical implementation of the TAI scheme, Fig. 3.2 (b), it should be possible to capture the spectrogram with the predicted optimal frequency resolution using a high-bandwidth PD, as the bandwidth specifications are similar for available electro-optic modulation and photodetection devices. In a typical design procedure, the sampling step duration would be fixed to be the longest possible while satisfying the Nyquist criterion in Eq. (3.6), namely, $t_s \approx 1/\Delta\nu_{SUT}$, with $\Delta\nu_{SUT}$ being the maximum expected bandwidth for the SUT to be analyzed. The desired number of frequency analysis points would dictate q, i.e., the number of phase steps per period in the modulation function, which in turn would fix the sampling period $T_r = qt_s$. Hence, a larger number of analysis points requires a longer sampling period T_r, which translates into a reduced processing speed ($\sim 1/T_r$). A higher processing speed can then be achieved by fixing a shorter period T_r in the design (either by using a shorter t_s or a smaller q factor), but this would unavoidably worsen the achieved frequency resolution. Most importantly, a larger number of analysis points, implying a larger q, necessitates of a larger amount of GVD, since according to Eq. (3.5) (with $|s| = 1$):

$$\left|\ddot{\Phi}_0\right| = \frac{q{t_s}^2}{2\pi} \approx q\frac{1}{2\pi\Delta\nu_{SUT}{}^2} > \left(\frac{1}{2\pi\Delta\nu_{SUT}{}^2}\right) N_{freq}^{optimal}. \tag{3.12}$$

In deriving this latest inequality we have used Eq. (3.9). Hence, in practice, the number of analysis points (or frequency resolution) provided by the spectrogram analysis is ultimately limited by the achievable GVD amount (see following the numerical example and further discussions on this issue). The temporal phase modulation in the TAI spectrogram design, Fig. 3.2 (b), can be implemented using a PM driven by an electronic AWG.

3.3.4 Practical Implementation Considerations

The needed components in the proposed designs, i.e., CW light source, chromatic dispersion lines, electro-optic phase modulator, electronic arbitrary waveform generator and photo-detection device, are available in a wide variety of technology platforms. Fiber-optics technologies are particularly attractive because they offer a practical and compact implementation, which is also fully compatible with optical fiber communication devices and systems. CW laser can be designed and implemented to produce single-frequency source over a wide variety of specifications, with linewidth as narrow as several kilohertz or even sub-kilohertz, high output power up to kW range, and over a large range of wavelength regimes of. 1~3 μm [205]. Chromatic dispersion is inherently provided by conventional single-mode optical fibers (SMFs), such as those used for lightwave communications [206][36]. The time-mapped spectrogram systems typically require a large amount of dispersion over a broad frequency bandwidth (short pulse bandwidth), corresponding to hundreds of kilometers of a conventional SMF. This translates into important insertion losses (considering an insertion loss of ~0.4 dB/km at the typical telecommunication wavelength of 1,550nm). Devices are also available that can provide the needed dispersion-bandwidth specifications in more compact forms, i.e., with significantly lower losses, such as dispersion compensating fibers (DCFs) [207] or linearly chirped fiber Bragg gratings (LCFBGs) [208]. Specifically, ultra-broadband highly-dispersive LC-FBGs can have a fiber length below a meter and with total insertion losses < 3dB. The temporal modulation process can be implemented using electro-optic amplitude modulators, such as Mach-Zehnder modulators (MZMs) [204]. For proper operation, the SUT must be suitably biased (e.g., at the null transmission point, corresponding to the characteristic V_π of the modulator for a symmetric coupler design) and must be kept sufficiently small (e.g., much lower than V_π), to ensure that the modulated optical field is directly proportional to the SUT [209]. Notice that the linear relationship between the SUT and modulated optical field is a central assumption of the theoretical analysis presented above. Electro-optic MZMs offering modulation bandwidths exceeding 100 GHz [210] and with high extinction ratio over 47 dB [211] are currently available. Electro-optic PMs offering modulation bandwidths up to ~50 GHz are commercially available and technologies have been developed enabling electro-optic phase modulation over terahertz bandwidths [196]. The commercial AWG can provide up to 256 GSa/s sampling rates for generating the required multi-level temporal phase with narrow time width t_s, leading to a large operation bandwidth. A variety of photo-detection technologies are also available for light waves across a wide range of wavelengths and with bandwidths above 50 GHz (corresponding to time resolutions < 10ps) [212].

Practical components exhibit several nonidealities that may affect the theoretical performance of the time-mapped spectrogram scheme, including the following ones: (i) intensity and phase noise of the optical source [122], [213]; (ii) higher order dispersion terms and insertion losses of the group-velocity dispersive lines, as well as their power thresholds to avoid nonlinearities during signal propagation [206]; (iii) nonlinear response of the MZMs [204], [214]; (iv) sensitivity and noise characteristics of the photo-detection device [122], [204]. A practical scheme may also include different amplification devices, such as optical amplifiers to compensate for the insertion losses of the dispersive lines [122], [206] or electrical amplifiers to enhance the microwave SUT before electro-optic modulation. These amplification devices also introduce different forms of noise and/or nonlinear response, which may also affect the achieved performance. Overall, all these nonidealities may have an impact on the instantaneous bandwidth, and time and frequency resolutions offered by the spectrogram as well as on the dynamic range of the performed spectral analysis (minimum and maximum SUT energy spectrum levels that can be captured with a prescribed accuracy). A comprehensive evaluation of the effect of these nonideal effects on the achieved time-mapped spectrogram analysis is worth to seek.

3.4 Numerical Simulations

We report numerical simulation results firstly for the proposed TAI based real-time spectrogram analysis. Fig. 3.3 shows results from numerical simulations of the proposed scheme using phase sampling, as presented in Fig. 3.2 (b) (TAI spectrogram). We target realization of a real-time SP analysis with an instantaneous optical bandwidth up to 40 GHz (20 GHz radio frequency (RF) bandwidth) and a frequency resolution of 100 MHz, corresponding to >400 points of analysis per captured frequency spectrum. The microwave SUT is firstly modulated on CW light through a conventional intensity (e.g., MZM) modulator. We assume the bandwidth of the MZM to be 40 GHz with an extinction ratio (ER) of 37 dB, consistently with the parameters in the experiment reported below. The modulator is configured to achieve a carrier-free linear modulation of the SUT into the optical domain. A larger ER is desired to reduce the relative intensity ratio of the remaining optical carrier with respect to the SUT waveform, ensuring that the central-frequency component of the SUT spectrogram (mapped at the central reference time along each analysis window) is not significantly increased by the electro-optic modulation process, further details are discussed below. The optical SUT is then phase modulated according to the temporal profile in Eq. (3.4) with the following parameters. The time width of each of the discrete phase levels is assumed to be $t_s = 25$ ps, which can be realistically implemented using a phase modulation bandwidth < 40 GHz, and the parameters defining the fractional Talbot phase pattern are fixed to $s = -1$ and $q = 401$, which translates into a repetition period of the phase sampling function $T_r = t_s \times q \approx 10$ ns. These specifications are commensurate with available electronic AWGs and electro-optic phase modulators [204]. In the numerical studies reported here, we have modeled a phase modulation unit limited in bandwidth to 40 GHz. The following dispersive line introduces the GVD amount that is required by the main design condition in Eq. (3.5), namely, $-\ddot{\Phi}_0 = -\frac{q {t_s}^2}{2\pi} = 2.5 \times \frac{10^5}{2\pi}\,\mathrm{ps}^2/\mathrm{rad}$, i.e., with a magnitude equivalent to that of ~1,800 km of a standard single-mode fiber section, along a frequency bandwidth well above that of the phase-modulated waveform (> 40 GHz). In practice, such a dispersive line could be implemented using for instance a DCF section or a reflective LCFBG with a length in the tens-of-cm range [208]. This proposed design would consecutively map each calculated frequency spectrum over a time slot of 10-ns duration and with $q = 401$ analysis points, corresponding to an optimal frequency resolution of ~100 MHz. Capturing the spectrogram with this optimal frequency resolution requires using a photo-detector unit with a temporal resolution much sharper than ~25 ps. In the following numerical simulations, we assume and model a realistic photo-detector time resolution of $\delta t_{PD} \sim 16.5\ \mathrm{ps}$, corresponding to a detection bandwidth of 50 GHz, which enables approaching the optimal frequency resolutions for the performed SP analysis. The nominal time resolution of this first designed spectrogram analysis system is estimated to be about $T_r = 10$ ns (using the metric introduced above in Eq. (3.7)).

The simulated input SUT is specifically designed to evaluate the time and frequency resolutions of the performed time-mapped spectrogram (TM-SP), as well as to illustrate the potential of the proposed scheme for real-time spectral analysis of short interference and closely spaced frequency components. Fig. 3.3 (a) shows the 1-μs long microwave SUT, which is composed of a quadratically increasing frequency-chirp sinusoid, with a frequency increasing from 100 MHz to 20 GHz, and isolated interferences with varying frequency content and temporal durations. Specifically, we consider a set of interferences with durations ranging from 5 ns to 80 ns, and corresponding central frequencies ranging from of 2.5 GHz to 15 GHz. Fig. 3.3 (b) shows the average amplitude of the temporal waveform at the output of the TAI spectrogram system (i.e., magnitude of the output complex temporal envelope) after being captured with a 50-GHz PD. The TM-SP extends over the same total duration as the input signal, i.e., 1 μs. A zoom over different analysis periods (each with a duration T_r), corresponding to some of the interference locations along the output temporal waveform, is also shown in Fig. 3.3 (b). Notice that the proposed system maps along the time domain the corresponding full (double sideband) frequency spectrum every T_r, including both the positive and negative sides of the input SUT spectrum, according to the frequency-to-time mapping law defined above, $\Delta\omega = \Delta t / \ddot{\Phi}_0$ (where $\Delta\omega$ and Δt are calculated with respect to the center of the corresponding time slot). The corresponding frequency axis for each of the traces shown in the insets is represented in the top horizontal axis, following the time-to-frequency mapping law defined in the text. Notice that the recovered spectra are nearly symmetric around their central frequency, as expected for the analyzed real-valued SUT. As predicted, and as it can be observed from the insets in Fig. 3.3 (b), the temporal mapping enables identifying the frequency components of the SUT, namely the quadratic increasing frequency chirp term (denoted as 's') and the isolated frequency interferences (denoted as 'c_i' with i = 1, 2, 3, 4, …) at the expected temporal locations.

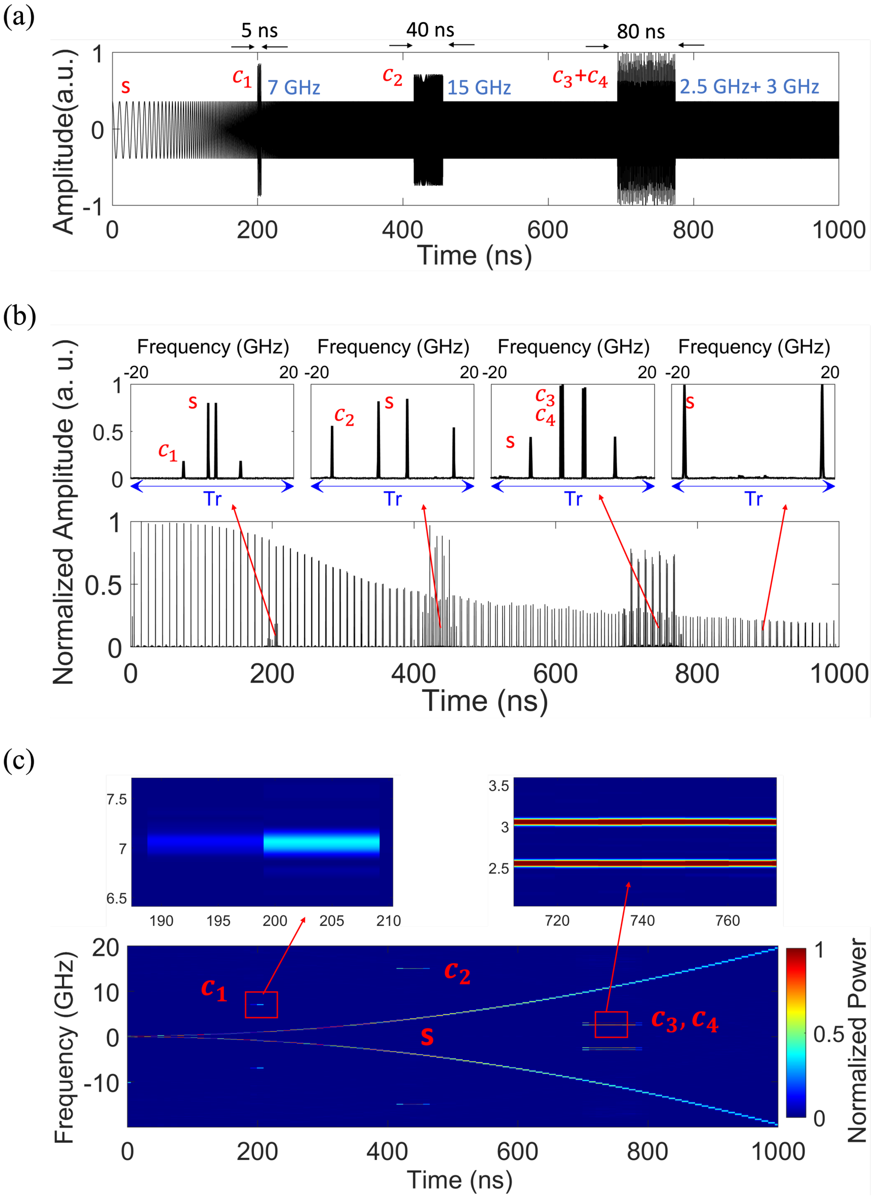

Figure 3.3. Numerical simulations of TAI-based time-mapped SP analysis of a microwave SUT. (a) Temporal trace of the signal under test (SUT), involving a quadratic frequency chirp component ('s') and several short-duration, narrowband interferences ('c1' - 'c4'). (b) Average amplitude of the temporal waveform at the output of the time-mapped spectrogram system. The inset plots show several zooms of the output waveform around four different relevant time slots, each extending over one analysis period (T_r). (c) 2D representation of the signal joint T-F energy distribution (SP) that is recovered from the output temporal trace, showing also two zooms of the obtained distribution around the T-F areas corresponding to some of the measured interferences.

Fig. 3.3 (c) shows a 2D representation of the signal joint T-F energy distribution (SP) that is recovered from the output temporal trace according to the time-to-frequency mapping defined above. The color code represents the relative intensity levels at each T-F location, see colormap at the right of the figure. The obtained SP shows the T-F distributions corresponding to the quadratic frequency-chirp component and the frequency interferences of the SUT at the prescribed time and frequency locations. The effect of the temporal analysis window on the obtained T-F patterns corresponding to the different interferences can be clearly observed in Fig. 3.3 (c): the amplitude of each of these patterns is reduced for a shorter duration of the interference event (below the time resolution level). We highlight that the obtained spectrogram enables recovering even the shortest (5-ns duration) interference term centered at 7 GHz (term ‘c_1’), see corresponding insets in Figs. 3.3 (b) and (c), even though this term is about two times shorter than the nominal time resolution of the recovered SP. Although the resulting temporal duration of the measured content c_1 is observed to be 10 ns rather than 5 ns, this is in consistent with the predicted time resolution of $T_r = 10$ ns. Thus, the proposed scheme can resolve the components with temporal duration narrower than the time resolution, but with the expected expansion in their observed time duration, which eventually matches the time resolution. It is also important to note that the frequency components of ‘c_3’ (centered at 3 GHz) and ‘c_4’ (centered at 2.5 GHz), spaced by 500 MHz, can be clearly discerned from each other, as shown in the corresponding insets of Fig. 3.3 (b) and (c), a result that is consistent with the predicted sub-GHz frequency resolution of the performed SP. Moreover, the output waveform follows the input signal SP at the exact same pace of the signal spectrum variations. Specifically, the changing signal FT in our example is calculated every 10 ns, i.e., at a speed of 100×10^6 FTs per second.

For evaluating the proposed system performance, the impact of the extinction ratio is studied. A main assumption in our numerical simulations is that the MZM used for the SUT is with high extinction ratio of 37 dB and it has the capability to suppress most of the energy of the carrier, allowing a clear observation of the time-mapped spectrogram of the SUT. Note that such high extinction ratio may not be practically available. In Fig. 3.4, we compare the output temporal waveform of the results in Fig. 3.3 by using a MZM with ER of 37 dB (blue solid curve) and 10 dB (orange dotted curve). A zoomed-in region over one analysis window is shown above to highlight the details, showing that a much lower ER affect the remaining

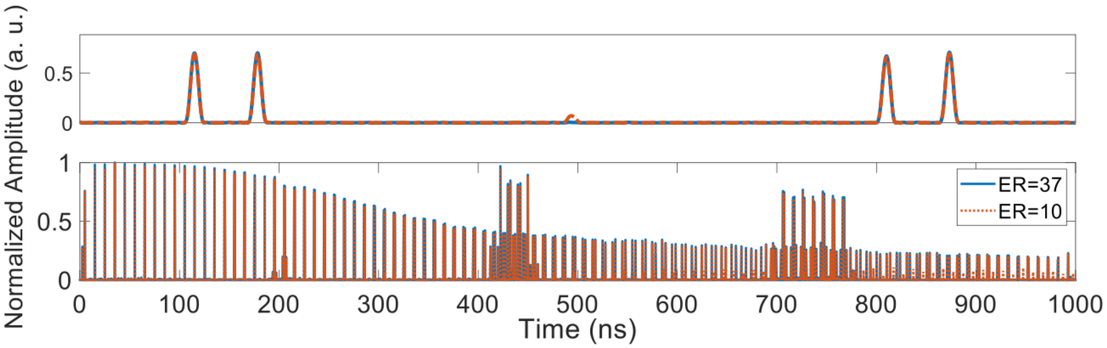

Figure 3.4. Numerical simulations of TAI-based time-mapped SP analysis of the same microwave SUT as shown in Fig. 3.3, while with 37-dB and 10-dB extinction ratio of the MZM.

amplitude of the DC voltage after detection. However, this is tolerable and is still much lower than the amplitude of the pulses representing the spectra of the SUT, allowing one to capture the spectrogram of the input.

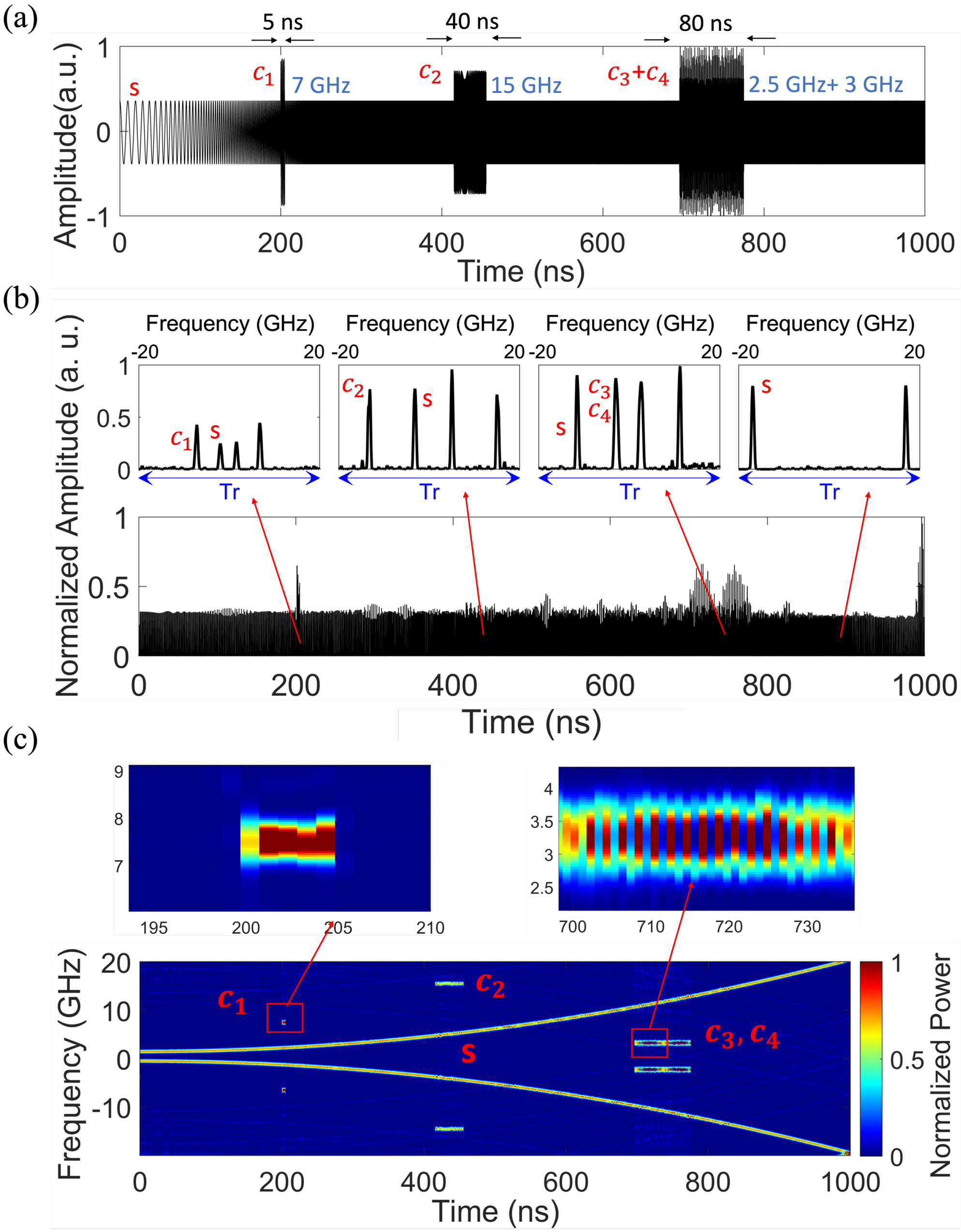

Figure 3.5. Numerical simulations of TAI-based time-mapped SP analysis of a microwave SUT, with the same captions as in Fig. 3. We show results for the analysis of the same SUT as in Fig. 3. The SP analysis system is now designed for q = 41 and T_r=1 ns, leading to an improved time resolution of the performed SP by about 10 times, and the corresponding deterioration in the obtained frequency resolution of the captured SP.

A key advantage of the proposed TAI-based real-time SP method is that the achieved time and frequency resolutions can be customized as desired by simply adjusting the repetition rate (or integer q) of the phase sampling function. This could be achieved by programming the AWG for generating the target phase modulation profile, while correspondingly adjusting the fiber dispersion value. We analyse the same SUT as above, while with different time and frequency resolution. Fig. 3.5 (b) shows the average amplitude of the output temporal waveform that is obtained for the same SUT when the period of the sampling pulses is decreased to $T_r \approx 1$ ns, while maintaining the rest of the specifications in the analysis system (e.g., sampling phase resolution $t_s = 25$ ps). As per the defined design conditions, a dispersive line providing a GVD amount equivalent to that of ~187 km of a standard single-mode fiber section is assumed. In Fig. 3.5 (b), a zoom over different analysis periods (each with a duration T_r), around different interference locations, show the respective time-mapped spectra. The modified phase-sampling function would produce a spectrogram with a sharper time resolution, to $\delta t_{sp} \sim 1$ ns, though with a deteriorated frequency resolution, $\delta\omega_{res} \sim 2\pi \times 1.2$ GHz. Fig. 3.5 (c) shows the 2D representation of the signal SP that is recovered from the output temporal trace. This analysis confirms that the reduced temporal analysis window duration can better intercept the shorter interferences (i.e., with an increased amplitude value, as compared with the 10-ns resolution case in Fig. 3.3), but with the expected deterioration in the frequency resolution. The change in the relative amplitude of the captured interferences can be clearly observed by comparing the results in Fig. 3.3 (b) and Fig. 3.5 (b), owing to the improved temporal resolution in the later case. To be more specific, from the insets in Fig. 3.5 (b), we observe that the 7-GHz interference 'c_1' of 5 ns duration is now resolved with a peak amplitude that is closer to that of the main chirp component ('s'), though with a broader width, corresponding to a poorer frequency resolution. In fact, in contrast to the results in Fig. 3.3, as shown in the insets of Fig. 3.5 (b) and (c), the two closely spaced frequency components 'c_3' and 'c_4' can be hardly discerned from each other, as their frequency spacing is now narrower than the nominal frequency resolution of the performed SP analysis. We attribute the notable background noise observed in the recorded spectrograms to the limited bandwidth of the phase modulator (i.e., 40 GHz), which leads to a distorted temporal phase profile compared with the designed ideal multi-level phase pattern.

3.5 Proof-of-concept Experimental Results

3.5.1 TM-SP of Non-stationary Microwave Signals Over 92-GHz Bandwidth

As discussed above, the proposed TAI-based spectrogram concept involves two main units: 1) temporal phase modulation, and 2) quadratic frequency dependent phase modulation. This system enables the analysis of high-speed electrical (e.g., microwave to mm-wave) signals by simply modulating the SUT

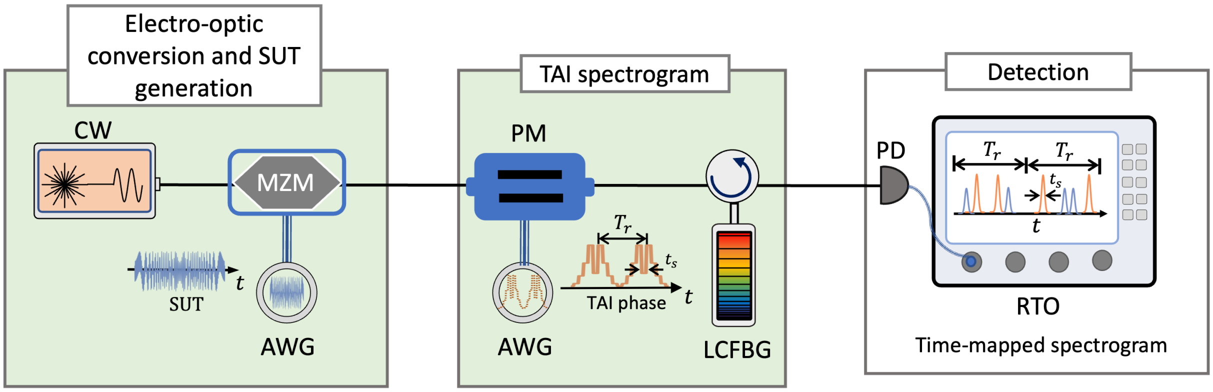

Figure 3.6. Principle and experimental setup for the proposed TAI spectrogram. The signal under test (SUT) is generated by an electrical arbitrary waveform generator (AWG). The electro-optic conversion stage up-converts the microwave signal into the optical domain by using an intensity modulator, so that the slowly varying envelope of an optical wave follows the microwave SUT profile. Following this, the TAI phase modulation along with reflective linearly chirped fibre Bragg grating (LCFBG) results in consecutively time-mapped Fourier transforms. A photodetector (PD) is used for conversion of the optical waveform to the electrical domain, and analog to digital conversion by a real-time oscilloscope. The computer reshapes the time-mapped spectrogram into a 2D image to be visualized.

on a CW light beam, as shown in Fig. 3.6. Here target analyzing a highly non-stationary microwave SUT using the phase sampling method (TAI spectrogram), however this proposed signal processing method can also be implemented for optical signal processing, which are beyond the scope of this thesis.

In order to experimentally verify the proposed TAI-based real-time spectrogram concept, a simple photonic-based scheme is designed for broadband waveforms analysis with advanced versatility. The experimental setup is illustrated in Fig. 3.6. The experimental setup follows the same general schematic used for simulations above. The optical carrier is generated from a tunable continuous wave laser (CoBrite-DX) with central wavelength of 1553.3 nm, which receives the electrical SUT for up-conversion to the optical domain. The customized high-speed microwave waveforms are generated using an electronic AWG with a sampling rate of 92-GS/s and analog bandwidth of 32 GHz (Keysight M8196A). A RF amplifier with a bandwidth of 50 GHz (Optilab MD-50) is used to boost the power of the SUT. The bias of the RF amplifier is carefully adjusted to ensure the linear amplification. The amplified SUT is then modulated on the optical carrier through an electro-optic MZM (EOSPACE, 40 GHz bandwidth and 37 dB extinction ratio). An optical polarization controller is used before the MZM to optimize the electro-optic modulation process. The modulator is biased at $V_\pi = 5.7\ V$ to achieve a carrier-free linear modulation, while within its linear region of operation, for modulating the SUT into the optical domain. An Erbium-Doped Fiber Amplifier (EDFA) is used to compensate for the loss along the system. The optical SUT then enters the TAI spectrogram unit, composed of a PM (40 GHz bandwidth) with a half-wave voltage of 3.1 V at 1 GHz (EOSPACE) driven by another channel of the same AWG and boosted by a 50-GHz RF amplifier (Optilab MD-50). The modulated temporal phase is designed as the required Talbot multi-level phase pattern that is satisfied Eq. (3.4). The TAI phase can be user-defined to achieve the customized specifications of the system, e.g., operation bandwidth, resolutions, and analysis points, as discussed above. Subsequently, the phase modulated light wave is linearly propagated through a reflective LCFBG, implementing the desired amount of group-velocity dispersion, according to Eq. (3.5) well over the full bandwidth of the optical modulated SUT. The temporal phase modulation profile and group-velocity dispersion are designed according to the conditions defined above. The temporal signal obtained at the output of the dispersive medium corresponds to consecutive time-mapped spectra of the input SUT within the analysis period T_r. For near-optimal recovery of the TM-SP, the output is measured by using a 50-GHz PD (Finisar XPDV2120R) to transfer the processed signal from the optical domain to the electrical domain. Then a 28-GHz real-time oscilloscope (RTO) is connected to capture the signals without averaging. The RTO is triggered through a reference signal from the electronic AWG with the same length of each incoming microwave SUT. The two-dimensional T-F energy representation is obtained from the one-dimensional temporal signal by vertically plotting each of the photo-detected intensity measurements of adjacent sections of the analysis window.

In a first experiment, we target verifying the largest operation bandwidth we can achieve through the available equipment. According to Eq. (3.7), a larger operation bandwidth requires a narrower width of the bins of the discrete temporal phase, which is limited by the largest sampling rate of the electronic AWG that is used for generating the required phase. According to the equipment we used, the shortest duration of a single-phase modulation step is set to t_s~ 10.8ps, enabling the analysis of signals with the maximum full frequency bandwidth of $1/t_s$ ~ 92 GHz (instantaneous analysis bandwidth of the performed spectrogram). The target number of analysis points per frequency spectrum is set to q = 139, corresponding to a temporal period for the phase modulation pattern of T_r = 1.5 ns. The theoretical phase modulation input into the

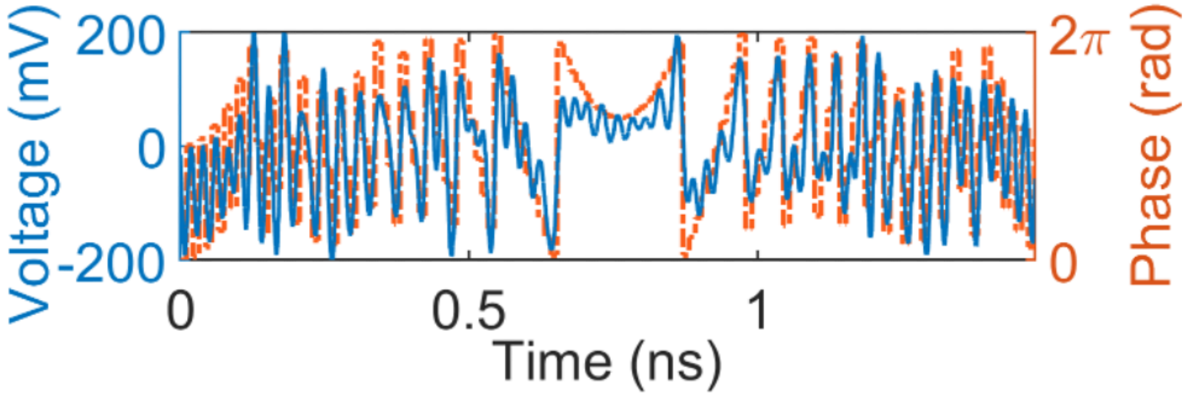

Figure 3.7. Theoretical and experimental TAI phases, where only one pattern can be seen over a single time lens aperture T_r of 1.5 ns. The function is wrapped to 2π and each discrete phase level has a width of t_s.

AWG is shown in orange dotted lines in Fig. 3.7. Shown in blue solid lines are the phase functions sent to the phase modulator, which is generated by the AWG and amplified by the 50-GHz RF amplifier (RFA). It is then recovered from a 70-GHz bandwidth electrical sampling oscilloscope (Tektronix CSA8200). In general, the shapes of the two phase profiles match well and are consistent with the designed specifications, showing a duration of 1.5 ns. The distortions between the theoretical and measured phase profile, especially in the fine details with sharp curves, are attributed to the limited analog bandwidth of the AWG and the RF amplifier. According to the study provided above, we estimate that this system would perform a spectrogram analysis with a theoretical frequency resolution of ~660 MHz. The phase modulated signal then propagates through a LCFBG providing a second-order dispersion $\ddot{\Phi}_0 \sim 2{,}600\ \mathrm{ps}^2/\mathrm{rad}$, with a magnitude that closely satisfies the fractional Talbot condition in Eq. (3.5). The temporal signal obtained at the output of the dispersive medium corresponds to consecutive time-mapped spectra of the input SUT within each analysis period T_r = 1.5 ns. As such, the signal FT is calculated every 1.5 ns, i.e., at a speed of 666×10^6 FTs per second.

To demonstrate the proposed 92 GH full bandwidth, we design a double-chirped microwave signal. Specifically, the SUT is composed two superimposed linearly-chirped sinusoidal waveforms of one varying from 0.67 to 46 GHz and vice versa for the other (here labeled S_1 and S_2, for reference further below), over a total duration of 136 ns. As the bandwidth of the SUT exceeds the limitation of the implemented RF amplifier, and MZM, the un-uniform frequency response will result in a non-flat shape of the signal. To ensure that the optical modulated signal exhibits a nearly flat amplitude over different frequency components, the microwave SUT is properly designed to pre-compensate for the spectral roll-off of the RF amplifier and MZM. Fig. 3.8 (a) shows the temporal waveform with pre-compensated amplitude of the SUT that was sent to the AWG. This is designed according to the response of RF amplifier and MZM to have a relatively large amplitude for high frequency contents. This pre-compensated signal generated from the AWG is firstly boosted by the RF amplifier and the amplified waveform is shown in Fig. 3.8 (b), showing a distorted amplitude caused by the non-flat response and nonlinearity of the RF amplifier. Fig. 3.8 (c) displays the photo-detected and measured temporal waveform of the optical modulated SUT at the output of the MZM, captured by a 70-GHz bandwidth electrical sampling oscilloscope, showing the signal with a nearly flat amplitude. The proposed TM-SP concept does not impose any fundamental limitation on the signal duration: the signal Fourier content is inherently time mapped in a continuous fashion as it propagates through the TM-SP system. The duration of each of the studied waveforms in our experimental examples was limited by the available memory of the instruments used for generation (AWG) and measurement (real-time scope) of waveforms. Additionally, in this way, the entire output signal could be captured with the real-time scope for subsequent off-line analysis and representation of the detected data (e.g., for the 2D time-frequency graphs).

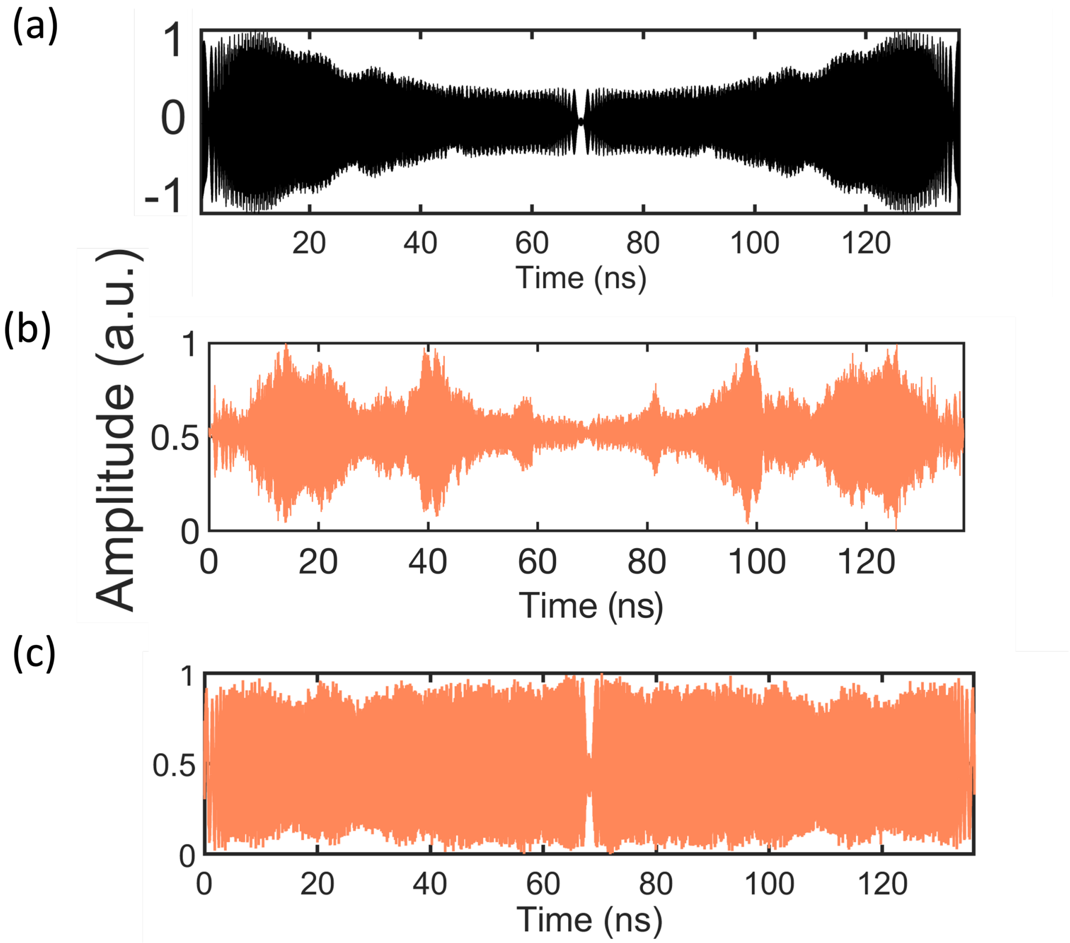

Figure 3.8. SUT with pre-compensated amplitude. The ~ 140-ns long signal under test (SUT) composed of two superimposed linearly-chirped waveforms over a 46 GHz frequency range is pre-compensated according to the response of the electro-optic Mach-Zehnder Modulator (MZM) and RF amplifier to ensure that the optical modulated signal exhibits a nearly flat amplitude. (a) Temporal waveform with pre-compensated amplitude of the SUT directly generated from the AWG. (b) Measured output of the RF amplifier, showing a distortion caused by the nonlinearity of the amplifier. (c) Photodetected and measured temporal waveform of the optical modulated SUT at the output of the MZM, captured by a 70-GHz bandwidth electrical sampling oscilloscope, showing the signal with a nearly flat amplitude.

Fig. 3.9 reports the results for analyzing this SUT, extending over a frequency range of ~46 GHz (full optical bandwidth of ~92 GHz), with the proposed method. The temporal waveform of the input signal that is at the output of RFA and sent to the MZM, with the zoomed-in traces corresponding to three different sections of the SUT are illustrated in Fig. 3.9 (a). The intensity of the numerically obtained spectrogram of the microwave SUT is shown in Fig. 3.9 (b), depicting the temporal evolution of the frequency spectrum. The microwave SUT is then modulated on the light source and the modulated optical signal is analysed by the TAI spectrogram. The temporal signal at the output of the TAI spectrogram unit is shown in Fig. 3.9 (c), with three different relevant zoomed-in regions periods (each with a duration of T_r) showing the details over different relevant time analysis periods. As expected, the proposed system maps the corresponding full (double sideband) frequency spectrum along the time domain every T_r, including both the positive and negative sides of the input SUT spectrum, according to the frequency-to-time mapping law defined above. We note that the TM-SP function exhibits a significant component at the center location of each analysis

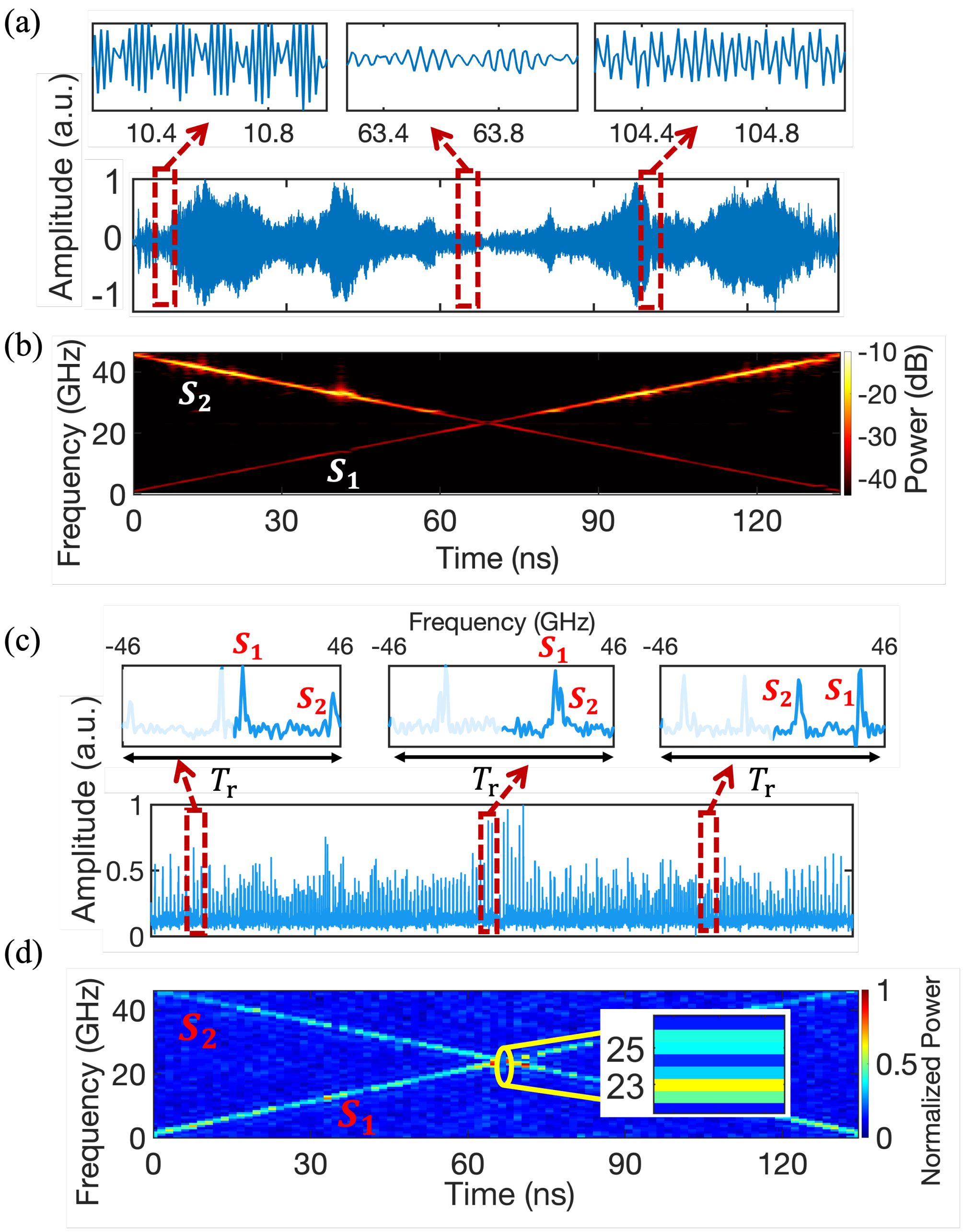

Figure 3.9. Demonstration of the proposal with 92 GHz bandwidth. (a) Temporal trace of the SUT, involving two linearly-chirped sinusoidal waveforms, one varying from 0.66 GHz to 46 GHz and vice versa for the other ('S1' and 'S2'), and the zoomed-in traces corresponding to three different sections of the SUT. (b) Intensity of the numerically obtained spectrogram of the SUT, depicting the temporal evolution of the frequency spectrum. (c) Measured TM-SP with several zooms around three different relevant time analysis periods. (d) 2D representation of the signal joint T-F distribution that is numerically rescaled from the output measured temporal trace of c, showing a close-up of the obtained distribution around near the cross point of the two chirped signals.

window, corresponding to the optical carrier frequency; however, this term is strongly attenuated in the representation of the TM-SP traces shown here to facilitate observation and interpretation of the obtained T-F distributions of the analyzed optical signals. Note that the equivalent frequency axis is marked at the top of each plot, according to the frequency-to-time mapping law described above. As predicted, and as it can be observed from the insets, the temporal mapping clearly identifies the frequency components of the two chirps, namely the linearly increasing (denoted as S_1) and decreasing (i.e., S_2), within each analysis window.

The captured temporal signal can be numerically reshaped into the common 2D spectrogram representation by simply plotting adjacent spectra vertically according to the frequency-to-time mapping, shown in Fig. 3.9 (d), clearly depicting the evolving frequency content of the individual chirps (i.e., S_1 and S_2) with a very high definition. The color code represents the relative amplitude levels at each T-F location, see colormap at the right of the figure. The recovered spectrogram is in excellent agreement with that expected for the input SUT. We reiterate that the evolving spectrogram is in fact recovered in a real-time manner, at the speed of the incoming SUT (notice that the input and output temporal patterns in Figs. 9 (a) and (c), respectively, extends over the same duration). A close-up of the obtained distribution around near the cross point of the two chirped signals is shown, two frequency contents (23 GHz and 25 GHz) separated with 2 GHz has been successfully distinguished, see detailed discussion below. In theory, each spectrum is measured with q = 139 analysis points, which corresponds to the ratio of the duration of an analysis period to the pulse width, or the ratio of the full bandwidth to the frequency resolution. Thus, we validate the main theoretical operation principle of the proposed method. The results confirm the capability of the demonstrated setup to provide a gap-free real-time spectral analysis with an instantaneous frequency bandwidth approaching 100 GHz, with 660-MHz frequency resolution, and1.5-ns time resolution, at a speed of 666×10^6 FTs per second, beyond the capabilities of current electronic DSP-based platforms.

To provide further evidence on the analysis of a more complicated signal, e.g., emulating an arbitrary incoming signal to be analyzed, we have performed results of a SUT that is specifically designed with a two-crossed linear chirps and random isolated frequency interferences. One of the two chirps varying from 0.67 to 20 GHz and vice versa for the other (labelled as S_1 and S_2, for reference further below) within the time interval from 0 to 130 ns. The set of interferences are considered with equal amplitude as that of the frequency chirp component, but with varying frequency content and temporal durations. Specifically, the frequency of the interferences varies from 5 GHz to 28 GHz and with different temporal durations ranging from 3 ns to 30.2 ns. This could be achieved by programming the AWG for generating the desired waveform. Fig. 3.10 (a) and (b) shows the digital SUT that was input to the MZM and the numerically computed spectrogram, respectively. We assume the same specifications for results in Fig. 3.9, i.e., $T_r \approx$

1.5 ns, $t_s = \frac{1}{92}$GHz, and q = 139, corresponding to the same maximum operation bandwidth (923 GHz), requiring the use of dispersion with the same specifications as in the above design example. This results in the same theoretical frequency resolution of 660 MHz. Fig. 3.10 (c) shows the measured output temporal

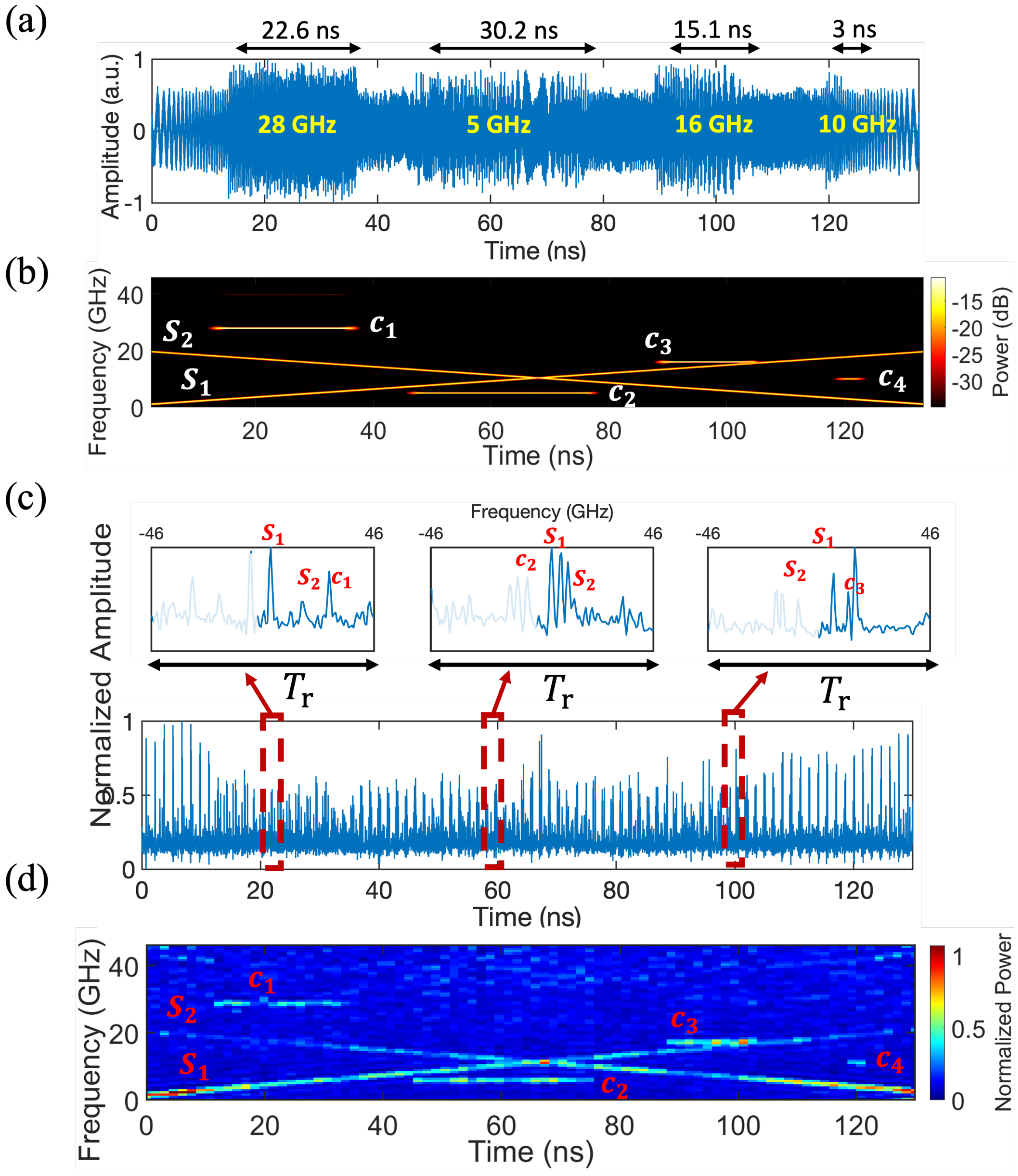

Figure 3.10. Demonstration of proposal with complicated SUT. (a) Temporal waveform of the SUT. (b) Numerical STFT spectrogram of the SUT. (c) The temporal waveform of the TM-SP. (d) 2D representation of the TM-SP.

waveform of the TAI spectrogram with zoomed-in regions over different analysis periods, each with a duration of T_r. To facilitate the evaluation of the obtained results, the captured temporal signal is numerically reshaped into a 2D time-frequency representation, Fig. 3.10 (d). As expected, the representation clearly depicts the evolving frequency content of the two chirps (S_1 and S_2) and the different interference terms (denoted as 'ci' with i = 1, 2, 3, …). Notice that the proposed system maps the corresponding full (double sideband) frequency spectrum along the time domain every T_r, including both the positive and negative sides of the input SUT spectrum, according to the frequency-to-time mapping law defined above. The equivalent frequency axis is shown at the top of each zoomed waveform. In order to clearly show the evolving frequency, here we only plot the positive spectra. These results clearly confirm that the proposed method allows on to resolve a sophisticated broadband microwave signal with random frequency events in a real-time fashion as long as they occur at the corresponding time locations. As shown in the insets of Fig. 3.10 (c), the two closely spaced frequency components 'S_1' and 'c3' can be clearly distinguished from each other. We also observe the 10-GHz content 'c4' of 3 ns duration is also resolved at the expected time location.

3.5.2 Evaluation of Time and Frequency Resolutions

In order to achieve this ideal performance, a photodetection bandwidth of the order of the SUT bandwidth (~46 GHz) would be needed. In practice, the frequency resolution, and thus, the number of

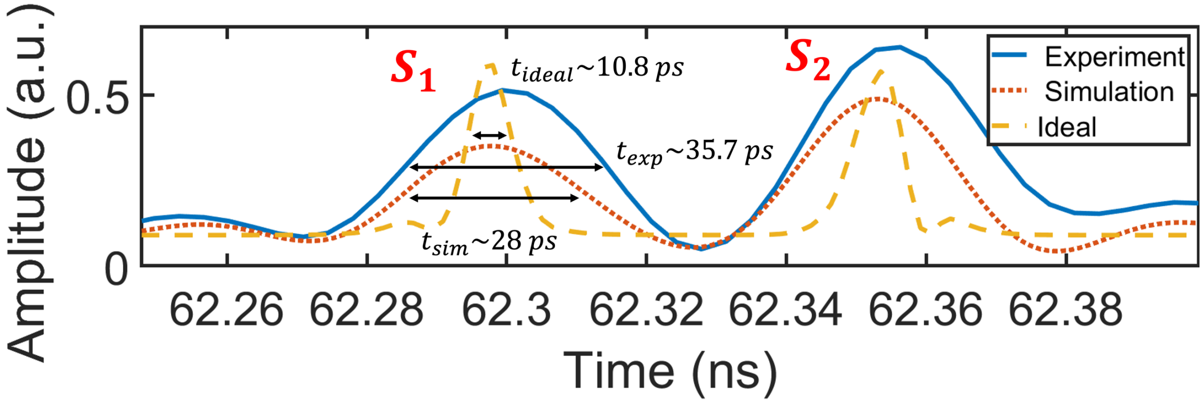

Figure 3.11. Demonstration of the deterioration of the frequency resolution. Comparison of a sample of the time-mapped spectrogram of the SUT in Fig. 9 for the simulation with ideal condition (yellow dashed), simulation with limited bandwidth of the equipment used in the experimental setup (orange dotted), and experimental results (blue solid). The amplitude FWHM of the measured pulse is Δt_{exp}=33 ps, similar to the simulated one with the same bandwidth limitation Δt_{sim}=28 ps, while the ideal width is Δt_{ideal}=10.8 ps. The broadening of the measured time-mapped spectrum is mainly attributed to the limited bandwidth of the real-time oscilloscope and photodiode used for analysis, and this measurement limitation impaired the frequency selectivity that could be experimentally verified with our experimental setup (with respect to the ideal prediction of a frequency resolution down to 660 MHz).

analysis points, is deteriorated by the reduced bandwidth of the photodetection system, which is limited by the 28-GHz bandwidth of the real-time scope used for digitization of the detected waveform. Specifically, the frequency resolution of the digitized spectrogram can be estimated by frequency-to-time mapping of the individual pulse widths (δt_{res}^{PD}) in the captured time-mapped spectra, following $\delta t_{res}^{PD}/(2\pi|\ddot{\Phi}_0|)$: the measured pulse width of ~35.7 ps (rather than ~10.8 ps, limited by the time resolution of the scope) translates into an effective frequency resolution of ~2 GHz, instead of the theoretically expected value of 660 MHz, resulting in the measurement of 46 analysis point per spectrum. To demonstrate the deterioration of the frequency resolution, we analyze a sample of the time-mapped spectrogram of the SUT in Fig. 3.9. A comparison of the temporal width of the output waveform between the simulation with ideal condition (yellow dashed), simulation with limited bandwidth of the equipment used in the experimental setup (orange dotted), and measured experimental results (blue solid) is shown in Fig. 3.11. The amplitude full-width at half-maximum (FWHM) of the measured pulse is Δt_{exp}=35.7 ps, similar to the simulated one with the same bandwidth limitation Δt_{sim}=28 ps, while the ideal width is $\Delta t_{ideal} = 10.8$ ps. The broadening of the measured TM-SP is mainly attributed to the limited bandwidth of the RTO and photodiode used for analysis, and this measurement limitation impaired the frequency selectivity that could be experimentally verified with our experimental setup (with respect to the ideal prediction of a frequency resolution down to 660 MHz).

The experimental results reported in Fig. 3.12 validate further the derived frequency resolution estimated. The SUT in Fig. 3.12 is designed to test whether the proposed setup with specifications shown above can follow the frequency resolution of ~2 GHz. Fig. 3.12 (a) shows the SUT consists of two closely spaced frequency tones (at 25 GHz and 27 GHz, respectively). Fig 12 (b) and (c) show the time-mapped waveform and the 2D spectrogram distribution of the analyzed signal, respectively. The close-up of the output temporal waveform and the recovered 2D spectrogram demonstrate a clear distinction between the two frequency contents and exhibits high stability over long time durations.

Indeed, as described above, we note that insufficient detection (or digitization) bandwidth leads to a temporal broadening of the spectrogram pulses, corresponding to a deterioration of the frequency resolution, while the maximum operation bandwidth and temporal resolution of the performed spectrogram analysis remain unaffected. Thus, a longer time resolution can be obtained by use of a longer analysis window, practically limited only by the dispersive line used in the system. As mentioned, the frequency resolution will however remain limited by the detection bandwidth. The highest frequency resolution offered by the system (inverse of the SP time resolution) can be exploited only if a detection stage is available with a sufficiently large bandwidth to capture the time-mapped spectrogram pulse time width (with no distortion).

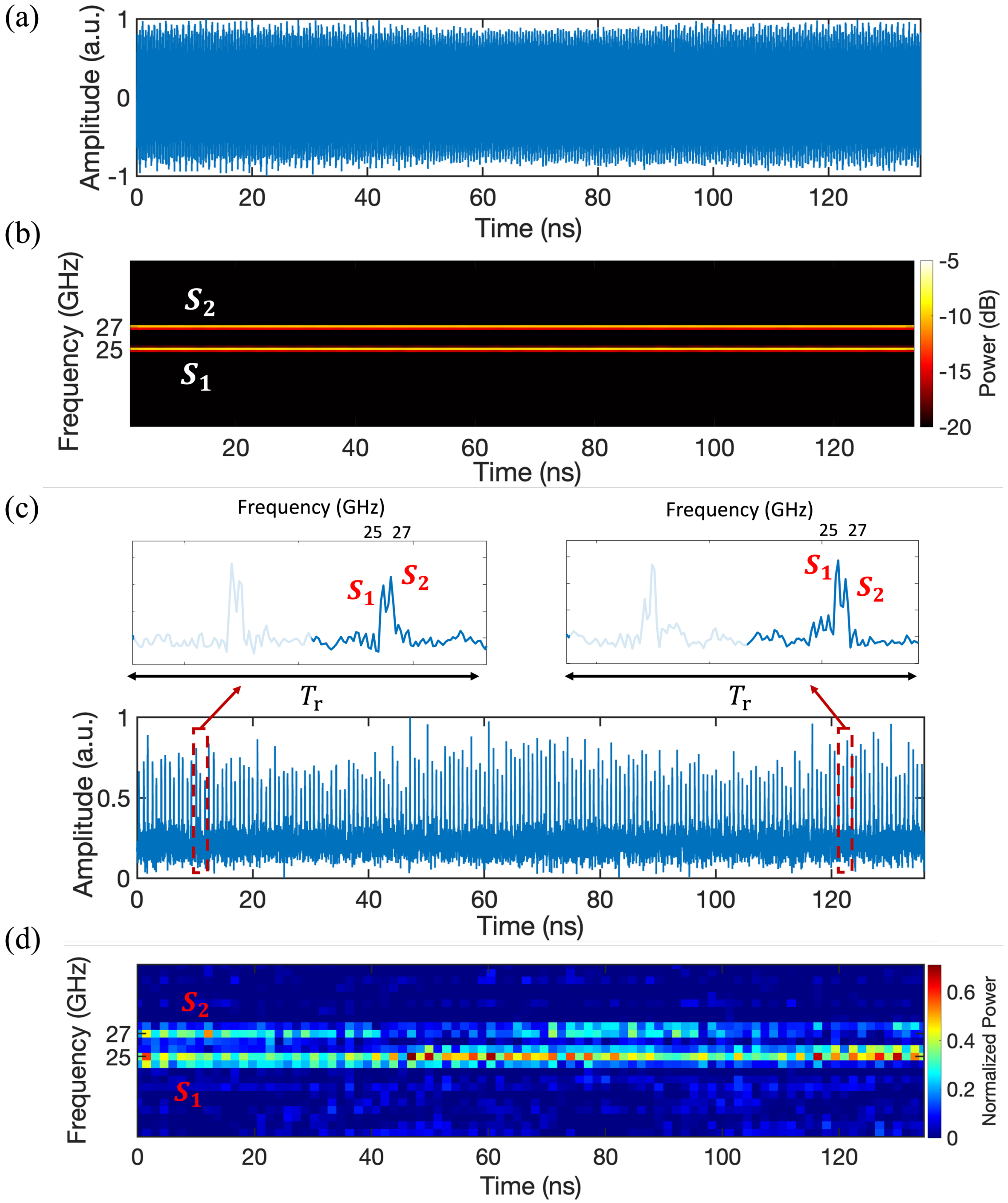

Figure 3.12. Experimental demonstration of the deteriorated frequency resolution. (a) The SUT employed for measuring the frequency resolution of the system is composed of two closely spaced frequency tones (at 25 and 27 GHz, respectively). (b) The numerical STFT of the SUT; (c)The measured time-mapped spectrogram with close-up, demonstrating a clear distinction between the two components. (d) 2D representation showcase they are clearly resolved by the TAI spectrogram.

3.5.3 Versatility of the Proposed TAI Spectrogram

As described above, the time and frequency resolution can be customized by programming the corresponding specifications of the temporal phase e.g., T_r. The time resolution of the obtained spectrogram is directly determined by the periodic length of the TAI phase T_r. As such, the simplest way to achieve a narrower time resolution is to decrease the phase modulation period. We demonstrated this with the same experimental setup and keep the same amount of dispersion (i.e., $\ddot{\Phi}_0 \sim 2{,}600\ \mathrm{ps}^2/\mathrm{rad}$) as the results shown in Fig. 3.9 and Fig. 3.10. Recall that the temporal phase and dispersion should satisfy Eq (3.1), in which case the parameters are designed according to the fixed dispersion. Hence, the TAI phase is adjusted with the time width of each of the discrete phase level is set with $t_s = \frac{1}{46}\mathrm{GHz} \approx 21.7\mathrm{ps}$ and period length of $T_r \approx 0.76\ ns$. This enables a theoretical analysis bandwidth of 46 GHz and an analysis window of 0.76 ns, corresponding to a time resolution of 0.76 ns. As such, the frequency resolution is $\delta\omega_{res} \sim 2\pi/T_r \sim 1.3$ GHz, which translate into a theoretical number of analysis points $q \approx 35$. The processing speed is 1316×10^6 FTs per second. The Theoretical (orange dotted curve) and experimental measure (blue solid curve) phase profiles are shown together in Fig. 3.13. Compared with the phase shown in Fig. 3.6, the distortion has been significantly improved. This is because the time width of each step is chosen to be wider which release the limitation of the AWG.

In the example reported here, the SUT is programmed to have a full bandwidth of 46 GHz. In particular, the SUT is composed of two superimposed linearly-chirped sinusoidal waveforms, one varying from 1.34 GHz to 23 GHz and vice versa for the other, labeled S_1 and S_2, respectively. This signal exhibits then a total optical bandwidth of ~46 GHz. The digitally generated waveform that was sent to the AWG for generation of the SUT and the measured modulated signal are shown in Fig. 3.14 (a), whereas the intensity of its numerically computed short-time Fourier transform (STFT) is shown in Fig. 3.14 (b). Fig. 3.14 (c)

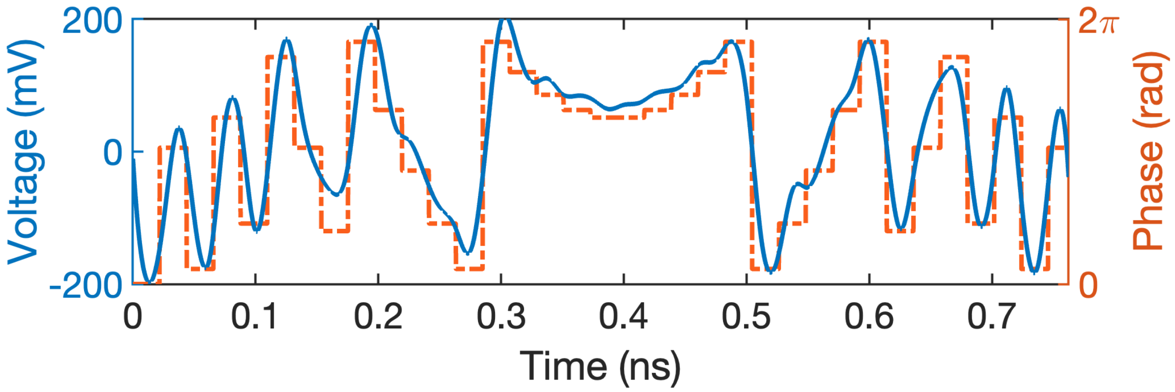

Figure 3.13. Theoretical and experimental TAI phases, where over the 0.76 ns only one pattern can be seen, representing one T_r. The function is wrapped to 2π and each discrete phase level has a width of t_s.

shows the measured output temporal waveform of the TAI spectrogram, with zoomed-in regions over different analysis periods, each with a duration of T_r. As predicted, the temporal mapping clearly shows the two different frequency components of the SUT (i.e., S_1 and S_2) along each analysis window. The 2D representation in Fig. 3.14 (d) was obtained from the output temporal trace by vertically plotting adjacent analysis windows and setting the frequency axis according to the frequency-to-time mapping law defined above. This representation clearly depicts the evolving frequency content of the two chirps. Notice that the proposed system maps the corresponding full (double sideband) frequency spectrum along the time domain

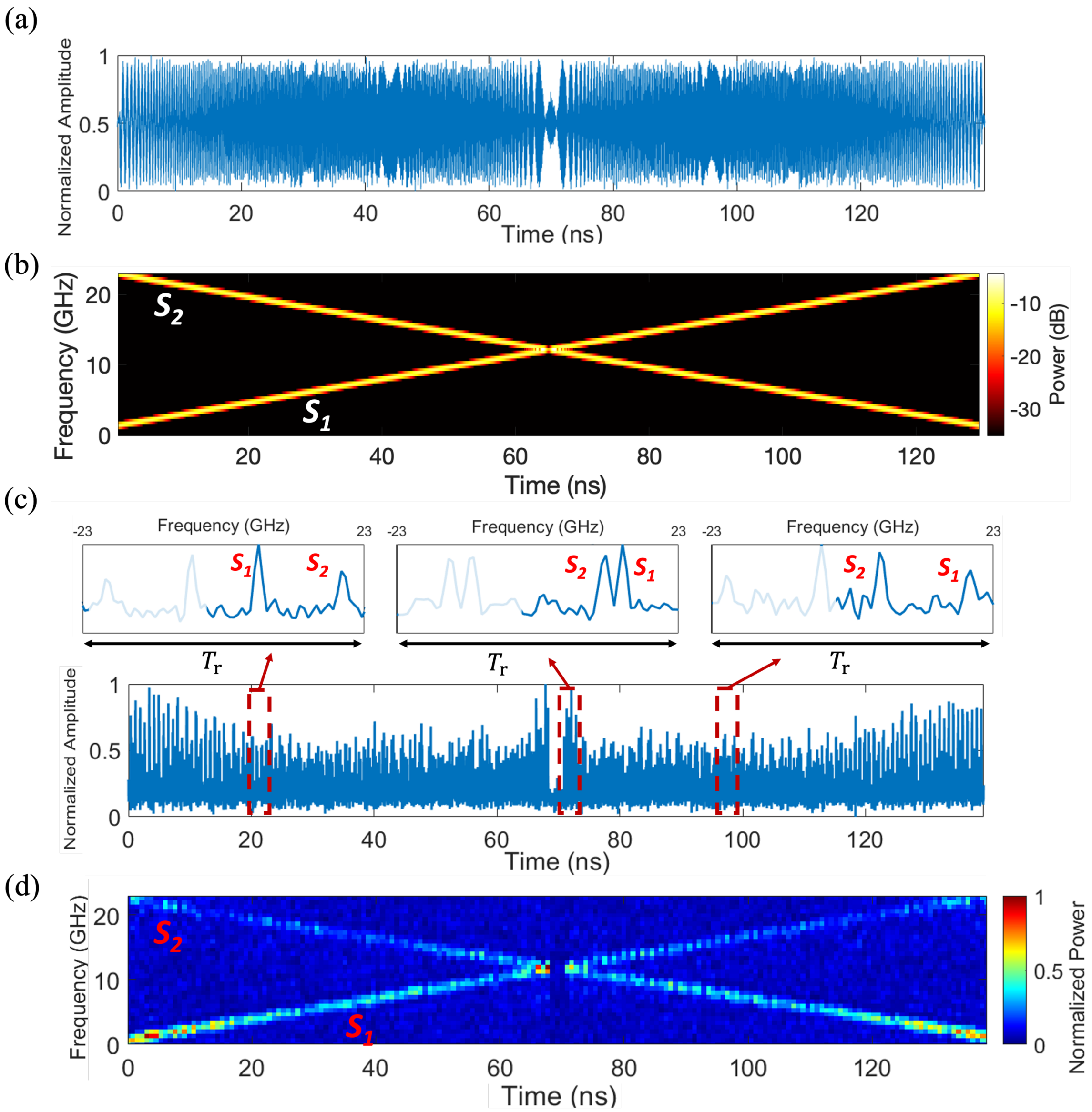

Figure 3.14. Experimental demonstration of the time-mapped spectrogram with time resolution of 0.76 ns. (a) Measured temporal waveform of the SUT. (b) Numerical STFT spectrogram of the SUT. (c) The temporal waveform at the output of the TAI-based TM-SP. (d) 2D representation off the TM-SP.

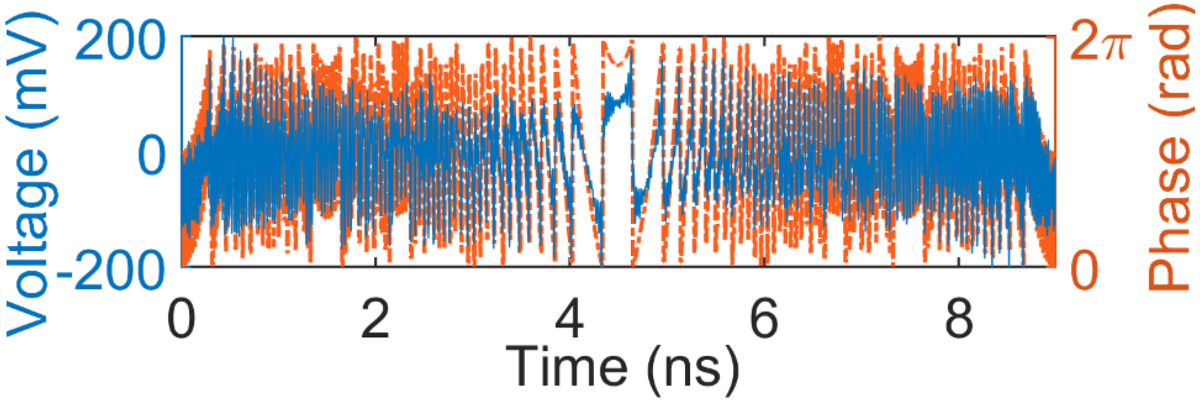

Figure 3.15. Theoretical and experimental TAI phases, where over the 9 ns only one pattern can be seen, representing one T_r. The function is wrapped to 2π and each discrete phase level has a width of t_s.

every T_r, including both the positive and negative sides of the input SUT spectrum, according to the frequency-to-time mapping law defined above. In order to clearly show the evolving frequency, here we only show the positive spectra. As expected, the reduced temporal analysis window duration results in a narrower time resolution, but with a deterioration in the frequency resolution. This result verifies the versatility of the time and frequency resolution of the proposed method through simply adjusting the temporal phase while maintain the experiments setup unchanged, which is realizable in practice.

We note that the specifications of the time-mapped spectrogram can also be achieved through adjusting temporal phase and the dispersion simultaneously. The frequency resolution is another important characteristic of a spectrogram as it gives a measure of how close two frequency components can be before they can no longer be resolved. To address this, we replace the LCFBG with a larger amount of dispersion $\ddot{\Phi}_0 \sim 15{,}494\ \mathrm{ps}^2/\mathrm{rad}$. The temporal phase modulation pattern is designed with $q = 836$ phase levels, each with a length of $t_s \sim 10.8$ ps and the period length is $T_r = 9$ ns, see Fig. 3.15. This allows us to achieve a narrower frequency resolution (i.e., $\delta\omega_{res} \sim 2\pi \times 110$ MHz) while maintaining the full analysis bandwidth to $1/t_s \sim 92$ GHz, corresponding to ~836 analysis points per spectrum. Based on this scheme, we process a highly non-stationary SUT consisting of two crossed linear chirps, one varying from 0.12 to 10 GHz and vice versa for the other (labelled as S_1 and S_2, for reference further below) within the time interval from 0 to 1 μs, and with different frequency interferences (c1-c4) of varying temporal durations. The frequency of the interferences varies from 8 GHz to 20 GHz. Fig. 3.16 (a) and (b) shows the digital SUT that was input to the MZM and the numerically computed spectrogram, respectively. As shown in Fig. 3.16 (c) and (d), the TM-SP enables an accurate identification of the individual chirps (i.e., S_1 and S_2) and frequency interferences of the SUT at the prescribe time and frequency locations, with the close-ups of the interference sections. The top axis in each zoomed plot corresponds to the equivalent relative frequency axis. Form the

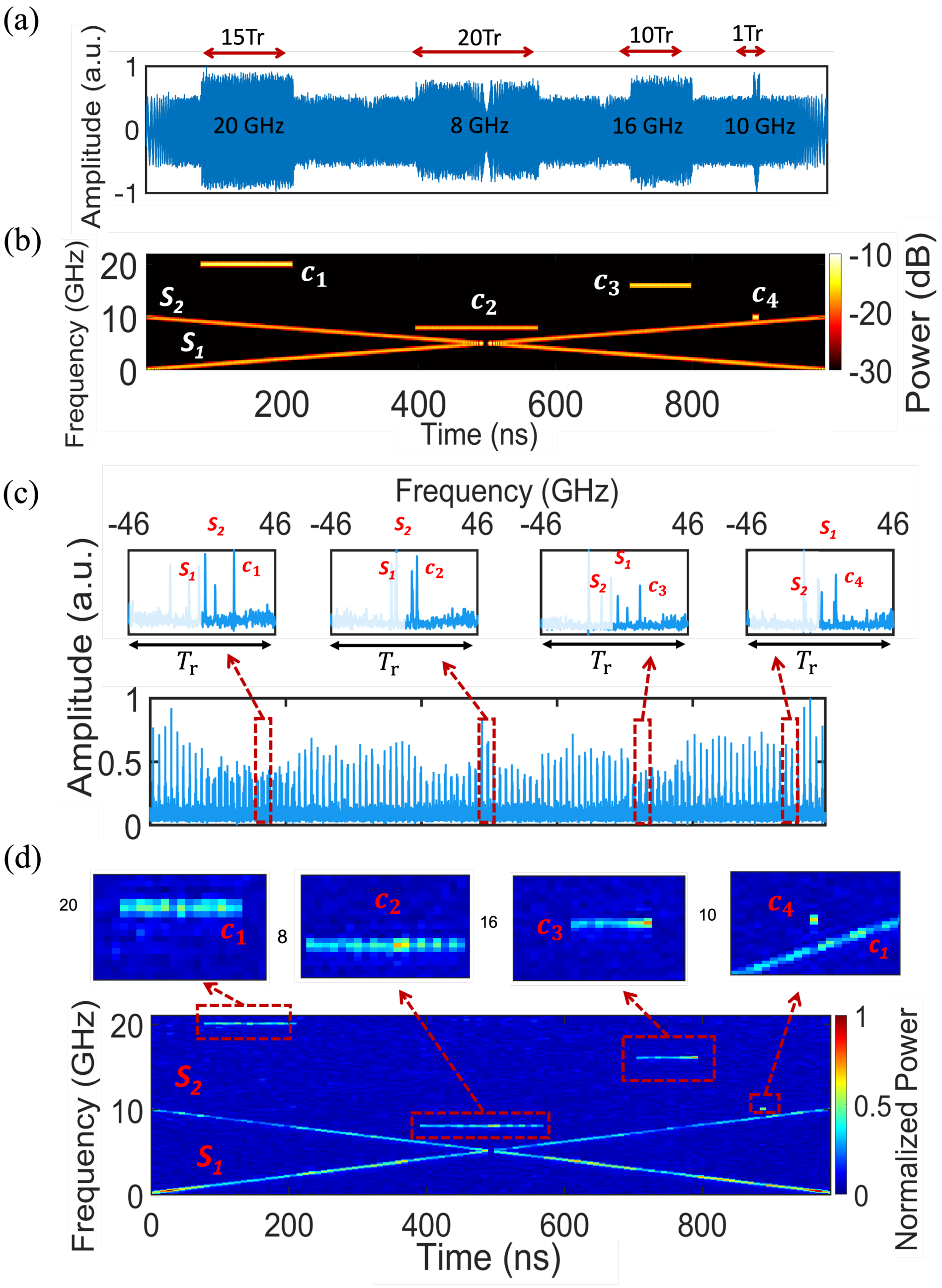

Figure 3.16. Experimental demonstration of fine frequency resolution. (a) Measured temporal waveform of the SUT, which is composed of two linear-chirped signals ('S_1' and 'S_2') and several interferences ('c1' – 'c4') with varying frequency location and temporal durations. (b) Intensity of the numerical STFT, or spectrogram, of the SUT. (c) Measured TM-SP trace at the output of the STFT scheme, with zooms-in around the location of the interferences, each zoomed waveform extending over on analysis period (T_r~9 ns). The top axis in each zoomed plot corresponds to the equivalent relative frequency axis. (d) A 2D representation of the measured TM-SP and the close-ups of the interference sections. The different frequency interference components are well discriminated even when extending over a duration as short as the analysis period (9 ns for 'c4').

insets in Fig. 3.16 (b), we notice that the interference c4 with frequency of 10 GHz and duration equal to T_r has been clearly resolved. This verifies the time resolution that can obtained through the designed specifications.

In this case, the inverse of the time window for this version of the TAI phase (9 ns) gives an extremely fine theoretical frequency resolution of 110 MHz, as well as large analysis bandwidth. However, the available photodetector and RTO acquisition bandwidth is not sufficient to reach the theoretical frequency resolution. Recalling the discussion on the frequency evaluation in Chapter 3, the limited detection bandwidth broadens the output pulse width, resulting in a deterioration of the frequency resolution. Specifically, the frequency resolution of the digitized spectrogram can be estimated by frequency-to-time mapping of the individual pulse widths in the captured time-mapped spectra, the measured pulse width of ~35.7 ps (rather than ~10.8 ps, limited by the time resolution of the scope) translates into an effective frequency resolution of $\delta\omega_{res} \approx 2\pi \times 400$ MHz, instead of the theoretically expected value of 110 MHz. To demonstrate this, we design a SUT composed of two sinusoidal signals with frequency spaced apart by the frequency resolution of 400 MHz. Fig. 3.17 (a) depicts the 2D spectrogram representation of the SUT (S_1: 12 GHz and S_2: 11.6 GHz, respectively). The inset shows the two frequency tones are clearly resolved.

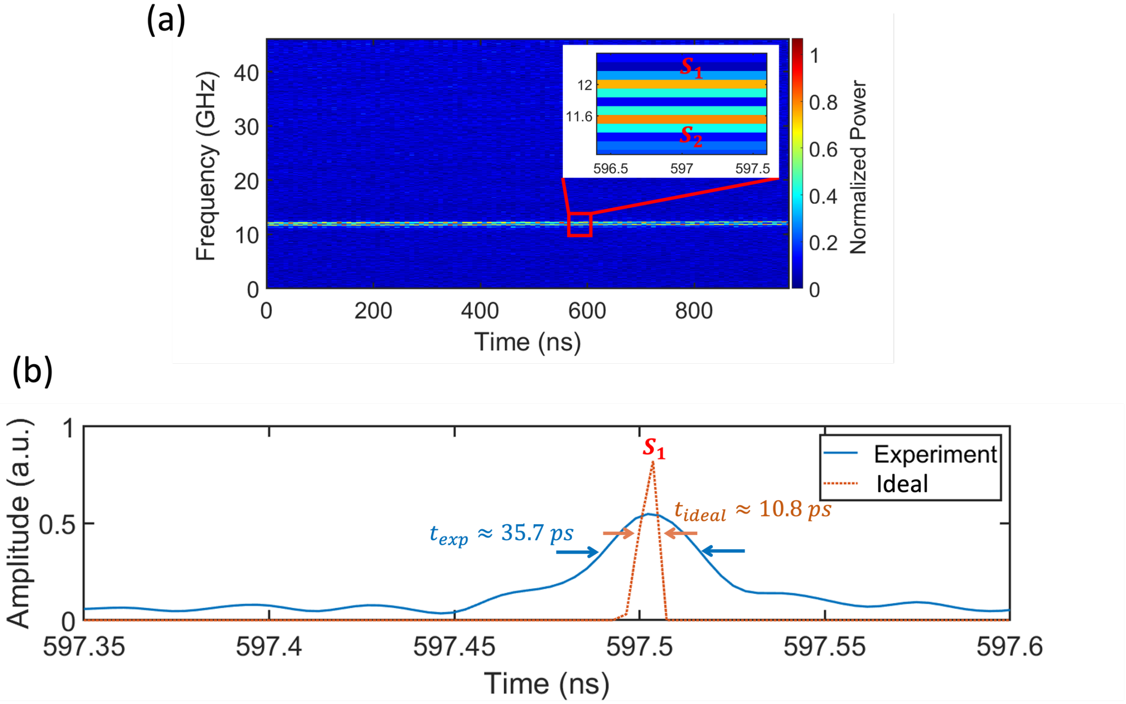

Figure 3.17. Experimental demonstration of the deteriorated frequency resolution. (a) 2D spectrogram representation of the SUT composed of two closely spaced frequency tones (S_1: 12 GHz and S_2: 11.6 GHz, respectively). (b) Comparison of a sample of the filtered time-mapped spectrogram for the simulation (orange dashed) and experimental results (blue solid). The experimental results are directly captured with a 28-GHz real-time oscilloscope. The amplitude Full width at half maximum (FWHM) of the measured pulse is Δt_{exp}=35.7 ps, while the ideal width is Δt_{ideal}=10.8 ps. The broadening of the measured time-mapped spectrum is attributed to the limited bandwidth of the real-time oscilloscope used for analysis, and this measurement limitation impaired the frequency selectivity that could be demonstrated with our experimental setup (with respect to the ideal prediction of a frequency resolution down to 110 MHz).

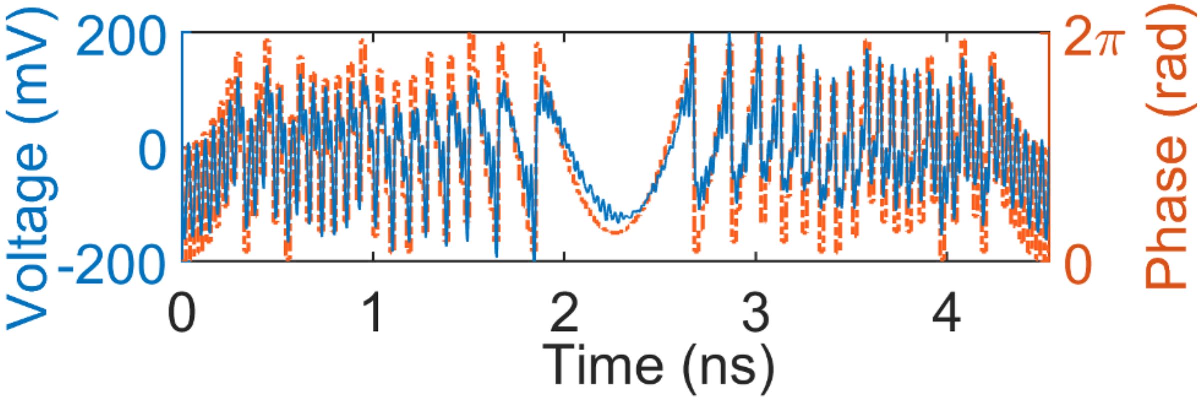

Figure 3.18. Theoretical and experimental TAI phases, where over the 4.5 ns only one pattern can be seen, representing one T_r. The function is wrapped to 2π and each discrete phase level has a width of t_s.

This can be further verified by measuring the pulse width of the obtained waveform. In Fig. 3.17 (b), a comparison of a sample of the time-mapped spectrogram for the simulation (orange dashed) and experimental results (blue solid) is shown. In order to clearly show the pulse width, here we only show the pulse representing S_1. The amplitude FWHM of the measured pulse is Δt_{exp} = 35.7 ps, while the ideal width is Δt_{ideal} = 10.8 ps. The broadening of the measured time-mapped spectrum is attributed to the limited bandwidth of the devices involved in the detection of the scheme. The results presented in Fig. 3.17 support the evaluation of the degradation of frequency resolution with 440 MHz (with respect to the ideal prediction of a frequency resolution down to 110 MHz).

The next results showcase the versatile time and frequency resolution based on the same scheme for the results shown in Fig. 3.16, through redesign the TAI phase. Here we set $t_s = 21.7\ ps$ enabling a theoretical analysis bandwidth of 46 GHz with frequency resolution of ~220 MHz, corresponding to a theoretical number of analysis points q = 207. Fig. 3. 18 illustrate the simulated and experimental measured phase profile. The subsequent needed second-order chromatic dispersion is given by the same LCFBG, providing $\ddot{\Phi}_0$ = 15,500 ps^2. As such, the frequency content of the SUT is analyzed over successive temporal sections, each with a duration of about T_r = 4.5 ns, and consecutively mapped along the time domain following the frequency-to-time mapping factor $\Delta\omega = \Delta t/|\ddot{\phi}|$. The microwave SUT, generated from another output of the electronic AWG, is composed of two crossed linear chirps, one varying from 0.23 to 15 GHz and vice versa for the other (labeled as S_1 and S_2, for reference further below) with different frequency interferences of varying temporal durations, over a total duration of ~323 ns. Fig. 3.19 (a) shows the digital samples of the SUT given to the AWG. The time-mapped spectrogram extends over the same total duration as the input signal, i.e., 323 ns, shown in Fig. 3.19 (b). Three different zoomed-in regions over different analysis periods, each extending over the duration of a single analysis window (T_r = 4.5 ns).

Temporal pulses representing two chirps (S_1 and S_2) and the different interferences are clearly observed in the corresponding time slots, e.g., interferences centered at 4 GHz (term 'c_2') and 16 GHz (term 'c_3,') in the second time window. Notice that the proposed system maps the corresponding full (double sideband) frequency spectrum along the time domain every T_r, including both the positive and negative sides of the input SUT spectrum, according to the frequency-to-time mapping law defined above. The equivalent frequency axis is shown at the top of each zoomed waveform. As predicted, the temporal mapping enables identifying the frequency components of the two chirped signals S_1 and S_2 and different interferences ($c_1, c_2, c_3,$ and c_4) in each analysis window. The captured temporal signal can then be numerically reshaped into the common 2D spectrogram representation by simply time-to-frequency scaling, shown in Fig. 3.19 (c). In order to clearly show the evolving frequency, here we only plot the positive spectra. The obtained 2D representation clearly depicts the evolving frequency content of the chirps (i.e., S_1 and S_2) and interference contents (i.e., $c_1, c_2, c_3,$ and c_4) with a very high definition. The color code represents the normalized intensity levels of the spectrogram distribution. In practice, the frequency resolution, and thus, the number of analysis points, is deteriorated by the reduced bandwidth of the detection system as mentioned above. Specifically, the frequency resolution of the digitized spectrogram can be estimated by frequency-to-time mapping of the individual pulse widths in the captured time-mapped spectra, the measured pulse width of ~35.7 ps (rather than ~22 ps, limited by the time resolution of the scope) translates into an effective frequency resolution of ~357 MHz, instead of the theoretically expected value of 220 MHz, corresponding to the analysis point of 182.

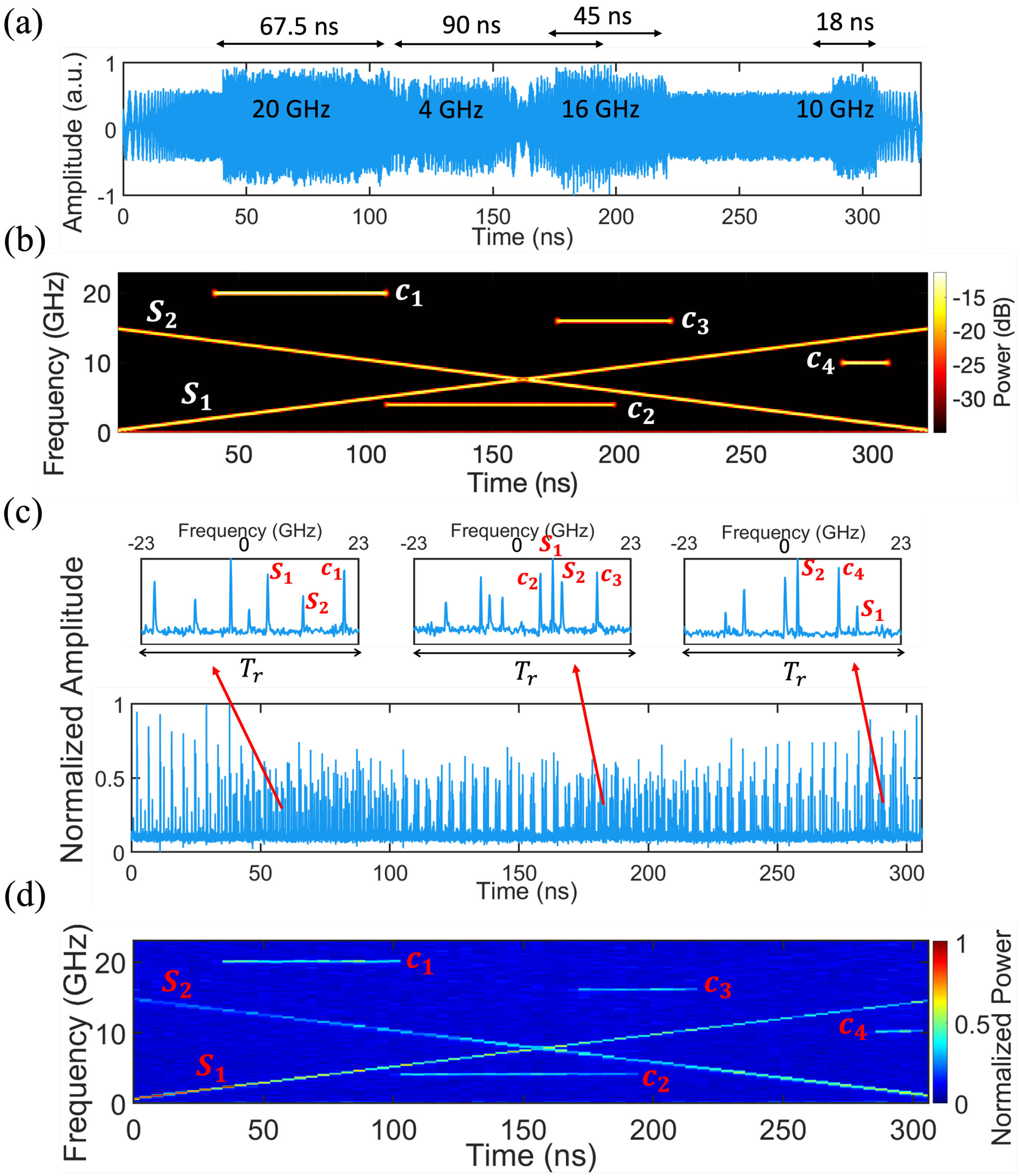

Figure 3.19. Experimental demonstration of TAI-based time-frequency analysis with time resolution of 4.5 ns and frequency resolution of 220 MHz. (a) Temporal trace of the SUT composed of two crossed chirp signals with interference components. (b) Numerical STFT of the SUT. (c) Temporal waveform of the T-TAI spectrogram with several zooms of different time analysis slots. (d) The 2D spectrogram representation that is numerically recovered from the measured output temporal trace.23

3.6 Conclusion

In this chapter, I proposed a framework for a time-frequency analyzer specifically targeted to microwave signals, using linear optics components, which provides the user with a high degree of versatility to customize the performance specifications depending on the demands of the application. Specifically, the T-F distribution is continuously mapped along the time domain through two basic units, temporal phase modulation and second-order dispersion. I showed a general mathematical analysis of the TAI-based spectrogram and discussed the trade-offs and versatility. With this architecture, I have presented the numerical simulations and experimental demonstrations to validate the theory. The TAI-based spectrogram has enabled real-time spectral analysis (RT-SA) of high-speed signals over a full bandwidth approaching 100 GHz, including the capability of intercepting random fast signals, with nanosecond time resolution and MHz-level frequency resolution. Moreover, the versatility in terms of time and frequency resolutions of the conducted analysis was demonstrated through simply adjusting the specifications of the TAI phase. I further anticipate the potential of the TAI-based spectrogram analysis over much higher instantaneous analysis bandwidths, to the THz range, by use of ultrabroadband electro-optic phase modulators [215] or nonlinear temporal phase modulation mechanisms, such as those based upon Kerr-based cross-phase modulation or four wave mixing in highly dispersive fibers or waveguides [206]. In the next chapter, I will process the obtained time-frequency distribution via widely-available temporal modulation techniques, enabling user-defined manipulation.

4 TIME-FREQUENCY PROCESSING

In this chapter, I propose a concept for user-defined real-time manipulation of the joint T-F distribution of electromagnetic waves directly in the analogue domain, ideally suited for operation on high-speed waves. This is based on the time-mapped spectrogram discussed in Chapter 3, allowing direct manipulation of the frequency contents in the time domain using temporal modulation methods. The proposed approach combines the versatility of the DSP approach with the performance (e.g., processing speed and bandwidth) of a photonic solution.

4.1 Introduction

A time-varying filter (TVF), which allows to manipulate the frequency spectrum of an incoming signal as it changes over time, is an essential building block in telecommunications [1], metrology [2], and radar systems [3]. By reconfiguring the spectral transfer function (or filter's response) over time, a TVF can provide a complete and precise manipulation of highly non-stationary signals, such as to suppress undesired time and/or frequency variant interferences or noise components along the incoming signal. Moreover, this capability is becoming increasingly important to achieve the desired advanced functionalities and overall performance in many modern and emerging applications, including next-generation telecommunication systems [74], [77] and intelligent remote sensing platforms (Radar and Lidar) [5], [75], [78]. For instance, towards improving the spectral efficiency of modern communication systems, cognitive radio and optical schemes are increasingly being employed [79], [80], requiring software-defined architectures that enable dynamic spectrum allocation and control. Sophisticated coding strategies are also needed where the desired information is encoded along the joint time-frequency (T-F) variations of the wave in a rapidly adaptable manner, such as for the case of ultrafast frequency-hoping systems [81]. Radar systems often operate in dynamic and challenging environments where reconfigurable manipulation of the frequency spectrum of the captured waves are highly desired to enhance the performance, versatility, and adaptability [5], [83]. In these applications, the required wave processing operations may include selecting or deselecting a set of frequency bands [89], filtering out some undesired interference or noise-like components from the incoming wave [60], or other more sophisticated manipulations on the complex wave spectrum [90]. The key feature is that these dedicated filtering operations need to be reconfigured at a very high speed, in a nanosecond scale or even faster [82], [90], while offering a set of specifications commensurate with the target performance, including operation over broad frequency bandwidths and with the needed time and frequency resolutions [92].

Full linear manipulation of the joint T-F distribution/short-time Fourier transform (STFT) of a given incoming signal requires the realization of a linear filter in which one can program and reconfigure the filter's spectral response in a user-defined, arbitrary manner, and at a speed as fast as the frequency resolution offered by the filter [71]. Arbitrary joint T-F filtering can be readily implemented using digital signal processing (DSP). However, this requires detection and digitization of the complex-field wave profile followed by conversion of the processed digital profile back into an analogue wave. Moreover, for a real-time wave manipulation, this procedure is very challenging when the wave variations are faster than just a few hundreds of MHz [216]. Alternatively, radio frequency (RF) filters [217], [218] have been demonstrated that enable discrete tuning of some of the filter's spectral response features (e.g., centre frequency and bandwidth), though over a limited operation bandwidth, up to a few GHz. Optical filtering offers much broader operation bandwidths, and technologies are available that allows for a versatile reconfigurability of the filter's spectral response [3], [219]. However, as discussed in Chapter 1, the reconfigurability speed of these schemes (typically in the kHz range) remains orders of magnitude slower than the frequency resolution they can offer (typically in the GHz range), thus being unsuited for general T-F signal manipulation tasks. As such, there have been important recent efforts towards the development of reconfigurable microwave TVFs implemented directly in the analog wave domain. A particularly interesting solution is that based on microwave photonic filter (MPF) systems, which can offer operation bandwidths above tens of GHz, and an important degree of flexibility and reconfigurability beyond that of their electrical filter counterparts [5,6]. Yet, MPFs remains limited in terms of their practical tuning speed and/or degree of reconfigurability. A continuous T-F filtering with a very high tuning speed based on temporal modulation of a time-mapped spectrogram based on the pulsed Talbot principle (See Chapter 1.3.1) was previously proposed [7]. However, consistently with the above-discussed constraints for this spectrogram analysis method, the processing bandwidth in this approach is inherently limited to a few GHz with only a few frequency analysis points. A technique that was also recently proposed is based on stimulated Brillouin scattering (SBS). Using this method, a MPF has been demonstrated to provide a fine frequency selectivity (e.g., tens of MHz) [220], but only the center frequency can be tuned and the requirement of a filter-controlling signal would introduce additional nonlinear components. On the other hand, the use of optical frequency combs has led to advances in rapid tuning speed and flexibility [63]. However, frequency tunability and bandwidth reconfigurability can be hardly achieved simultaneously using this methodology. Recently, a programmable photonic circuit based on waveguide meshes and phase shifters yielded filters with multiple responses [221]. However, tuning is relatively complex as it needs to control each phase actuator separately to achieve the desired filter response, and the tuning speed is inherently limited by the thermo-optic actuator (microsecond scales). Thus, it remains challenging for any of the MPFs proposed to date to provide the desired full combination of performance specifications. Some

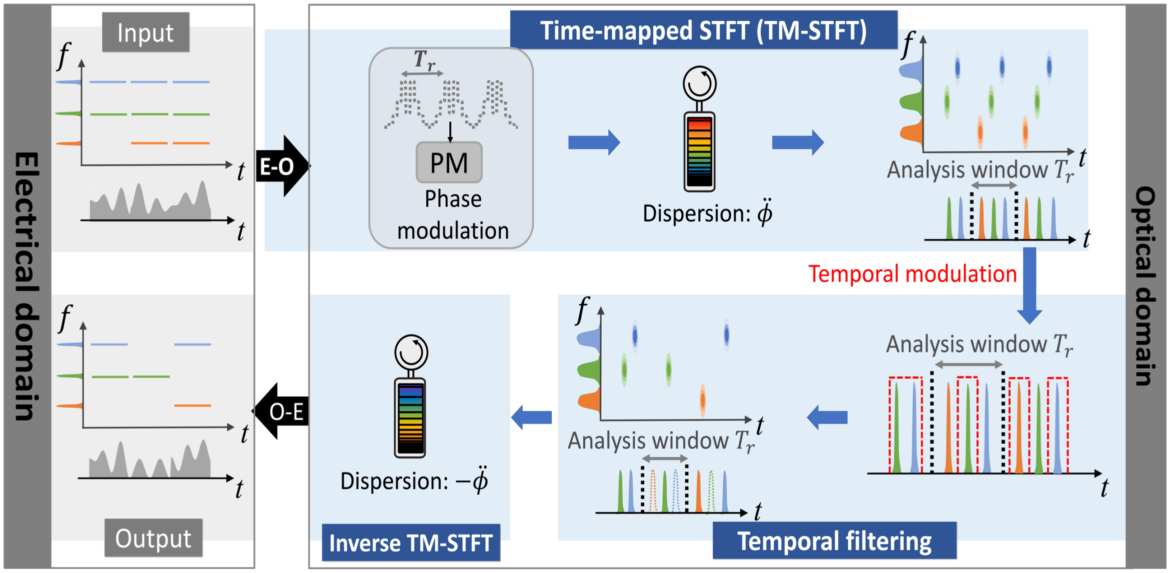

Figure 4.1. Principle of the proposed concept for user-defined joint T-F filtering of an EM wave. An input nonstationary microwave signal consists of three different frequency components. We consider that only two components are present in the first temporal segment of the signal to illustrate the case of an input non-stationary waveform. We show here how the proposed T-F filtering scheme can be designed to preserve/eliminate a prescribed set of frequency components in different signal temporal segments. For this purpose, the input microwave signal is first modulated on an optical carrier (electro-optic, E-O, conversion). The optical wave then undergoes two suitable phase transformations, implemented through temporal phase modulation with a discretized quadratic phase pattern followed by a quadratic spectral phase filtering with a group-velocity dispersive medium (e.g., a reflective chirped fibre Bragg grating). These phase transformations induce a continuous mapping of the time-varying frequency spectrum of the signal, or its two-dimensional (2D) joint T-F distribution, along the time domain. This distribution can then be easily manipulated at will using temporal modulation techniques (temporal filtering pattern indicated by the red-dashed traces). For the considered microwave photonics filtering scheme, recovering the processed wave simply involves compensating the input group-velocity dispersion and a photodetection step to transfer the optical processed wave back into the electrical domain.

of these methods are practically limited in regards to their degree of reconfigurability [63], [220], and/or on their operation bandwidth, to a few GHz at best [220], [222].

In the previous chapter, I have proposed and experimentally demonstrated the time-mapped spectrogram (TM-SP), involving mapping the T-F distribution (the STFT) of the incoming wave along the time domain, in a continuous and gapless manner [173], [201], [223], [224]. This in turns enables a user-defined manipulation of the wave's T-F distribution through use of any of the available temporal modulation techniques, As illustrated in Fig. 4.1. Specifically, I have demonstrated the Talbot array illuminator (TAI) spectrogram method for real-time and gapless time-frequency analysis of arbitrary incoming signals. Through this, the STFT, or spectrogram (SP), of the non-stationary signal is consecutively mapped along the time domain. As such, we gain direct access to the signals' changing spectral information, allowing for precise manipulation of the signal time-varying frequency content by using available temporal modulation methods, e.g., an electro-optic Mach-Zehnder modulator (MZM). This solution offers a notable design versatility to filter or modulate the specifications of the spectrogram within each time window. Using this concept, I conceive and demonstrate a photonics scheme for time-frequency processing of microwave and optical signals. A key aspect of this proposal is that since the time-mapped STFT is achieved using two consecutive phase transformations (along the temporal and spectral domains, respectively), the processed wave can be then recovered by simply applying the opposite phase manipulations. In practice, this platform allows us to achieve an arbitrary manipulation of the joint T-F distribution of the input microwave signal over a full bandwidth up to 92 GHz and with a fine frequency resolution, down to a few hundreds of MHz. Specifically, through implementation of the temporal filtering step using electro-optic modulation, the unit can be programmed electronically to provide any desired dynamic spectral response, with a reconfigurability speed inherently determined by the filter's frequency resolution, as needed for full manipulation of the wave T-F distribution. In this thesis, I demonstrate the use of this concept for realization of important functionalities beyond the potential of present technologies, including mitigation of nonstationary interference terms in broadband signals and the direct synthesis of high-speed waves with user-defined sophisticated T-F distributions.

4.2 Operation Principle

As illustrated in Fig. 4.2, the proposed time-varying frequency filtering system involves a cascade of the following elements: (i) electro-optic conversion of the SUT, (ii) Talbot array illuminator-based TM-SP unit, and (iii) a time-varying frequency (T-F) filter and signal regeneration unit. We recall the principle of TM-SP that has been described in Chapter 3. The microwave signal under test (SUT) is first converted to

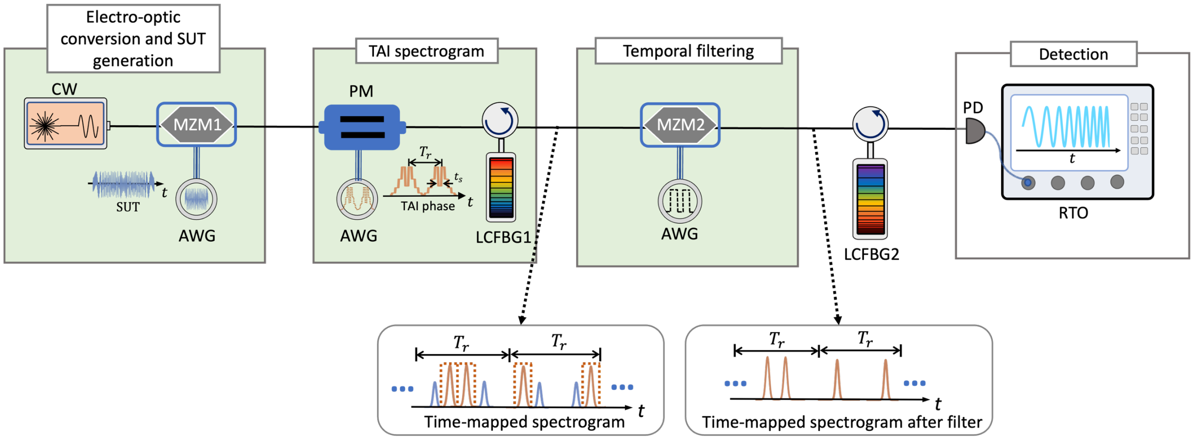

Figure 4.2. Principle and experimental setup of the proposed time-varying frequency filtering system. The scheme involves (i) converting the electrical signal to the optical domain (ii) TAI-based TM-SP and (ii) time-varying frequency filter. The dashes lines show the temporal filtering waveform designed to filter the target components (i.e., one of the chirp component) in the time-frequency domain.

the optical domain through a MZM (40 GHz bandwidth). The optical SUT is then processed to continuously map its STFT along the time domain, so-called TM-SP, using a TAI phase modulation design. For this purpose, the optical SUT is first phase modulated using an electro-optic phase modulator (PM) driven by an arbitrary waveform generator (AWG), providing a suitable Talbot multi-level phase pattern. Specifically, the phase pattern consists of q discrete steps, each with a length of t_s, according to the following expression: $\varphi_n = -\pi n^2 \frac{q-1}{q}$, for $n = 1, 2, \ldots, q$. This discrete phase pattern repeats periodically along the time domain with period length of $T_r = q t_s$. The duration of a single-phase step t_s determines the instantaneous analysis bandwidth of the performed STFT (or maximum SUT optical bandwidth) $B \sim 1/t_s$ and the temporal period of the phase pattern T_r defines the temporal resolution of this STFT analysis. The frequency resolution is inversely related to the temporal resolution $\delta\omega \sim 2\pi/T_r$, such that the number of analysis points is $q \approx \Delta\omega_s/\delta\omega$. Subsequently, the phase modulated signal is propagated through a linear dispersive element providing a second-order dispersion satisfying $\ddot{\Phi} = \frac{q t_s}{2\pi}$. Following this processing, the frequency spectra of successive sections of the SUT, are then consecutively mapped along the time domain, each within the corresponding analysis period of duration T_r, following the described frequency-to-time mapping law in Eq. (1.5) $\Delta\omega_t \rightarrow \Delta t/\ddot{\phi}$, where $\Delta\omega_t$ and Δt are relative to the centre of each analysis window. Subsequently, the signal's frequency spectrum information over every analysis window can be modulated (i.e., filtered) at will using a predesigned temporal modulation process, according to the above time-to-frequency mapping factor, effectively implementing the desired time-varying filtering process. In the experiments reported here, a second MZM is used to modify the time-mapped STFT. The user-defined temporal modulation pattern is generated by another channel of the same AWG, enabling electronically programmability of the filter's time-varying spectral response. Thus, the transfer function of the implemented time-varying filtering process can be reconfigured every T_r, i.e., at a tuning speed of T_r.

To process the time-mapped STFT waveform, the temporal modulation patterns are predesigned according to the frequency-to-time mapping law $\Delta\omega_t \rightarrow \Delta t/\ddot{\phi}$,. A set of 5 rectangular pulses is used to compose the filtering mask per analysis period of duration T_r. As such, the tuning speed is equal to the time resolution, T_r, which is inversely related to the frequency resolution, as mentioned above. This implies that a faster tuning speed can be achieved by use of a shorter period T_r. In turn, this would result in a higher processing speed, though at the cost of a poorer frequency resolution. In order to precisely manipulate the waveform with a resolution that is limited by the frequency resolution of the T-F distribution, a modulation time resolution is needed of the order of the TAI phase modulation step duration t_s. Note that the time width of the modulation pulse can be user-defined and adjusted accordingly. However, insufficient bandwidth of the time-domain filtering pattern (i.e., the use of wider filtering pulses) may result in a deterioration of the filter's frequency resolution, preventing for instance to be able to filter out one of the two-closely spaced frequencies, while the maximum bandwidth and time resolution of the performed filtering process remain essentially unaffected. In general, the temporal filtering mask can be mathematically expressed as:

$$h(t) = \sum_p \sum_k \left[a_{pk} \operatorname{rect}\left(\frac{t-\frac{T_r}{2} \pm \Delta t_{pk} + pT_r}{\Delta t_{filt}}\right) + \operatorname{rect}\left(\frac{t-\frac{T_r}{2} + pT_r}{\Delta t_{filt}}\right)\right]_{\Delta t_{pk} = \Delta\omega_{pk}/\ddot{\phi}} \tag{4.1}$$

where t defines the time variable of the temporal pattern, $\operatorname{rect}\left(\frac{t-T}{\Delta t}\right)$ denotes a rectangular function centered at T extending over a total duration of Δt, and pT_r identifies the central time location of each of the analysis periods (with $p = 0, \pm 1, \pm 2, ...$).

The first terms in the function in Eq. (4.1) define the modulation pattern for selecting the desired frequency components, where the parameter Δt_{filt} represents the time width of each of the rectangular pulses, which is chosen to be about t_s in our experiment, and Δt_{pk} is obtained from the frequency location $\Delta\omega_{pk}$ (relative to the center of the corresponding analysis window) of each of the different components (identified by $k = 0, 1, 2 ...$) to be selected from the spectrogram distribution in the p^{th} time slot, according to the frequency-to-time mapping law $\Delta\omega_t \rightarrow \Delta t/\ddot{\phi}$,. The factor a_{pk} defines the relative amount by which the corresponding frequency component is attenuated. The second summation term in the function defined in Eq. (4.1) corresponds to the location of the DC component (or carrier optical frequency) of the SUT, which needs to be maintained for realization of the processed waveform recovery step using the proposed scheme. We recall that this DC term exhibits a significant relative intensity and as such, it is eliminated in the 2D representation of the measured TM-SP distributions shown here to facilitate observation of the relevant components in the obtained T-F distributions. The temporal filtering profile defined by Eq. (4.1) can be customized by the designer in terms of the number of filtering pulses along every time slot, basic shape of the pattern, and the time width of each pulse. The relative intensity ratio of the unwanted frequency components with respect to the selected ones is mainly limited by the nominal extinction ratio of the modulation device used for practical implementation of the time filtering operation.

Finally, the filtered signal can be recovered by reverting the phase transformations used for realization of the TM-SP. For this purpose, we utilize a second dispersive line with the exact opposite dispersion of the first one (i.e., $-\ddot{\Phi}$) followed by photodetection to convert the signal back into microwave domain. An optical tuneable delay line is placed between the first linearly-chirped fiber Bragg grating (LCFBG) and the second MZM to synchronize the TM-SP trace of the SUT and the temporal filtering mask. It is worth to note that for the waveform recovery experiments, the optical carrier must be kept in the optical modulated SUT. As a result, the first MZM used for electrical-to-optical conversion of the SUT is biased to operate over its linear region.

4.3 Experimental Demonstration of Tunable Central Frequency

A proof-of-concept experiment is performed to demonstrate the proposed scheme with tunable central frequency based on the design illustrated in Fig. 4.2. As mentioned above, the time-mapped spectrogram discussed in Chapter 3 provides the access to process/filter the STFT of the SUT. By properly designing the filtering patter, here we showcase the filtering task for the results presented in Chapter 3. In the experiment, we use the same setup as for the time-mapped spectrogram of the SUT shown in Fig. 3.6, with the same specifications of the devices. The designed temporal filtering pattern is generated from one channel of the same AWG followed by a 40-GHz RF amplifier (MD-40). This filtering pattern is then modulated on the optical pulses after the first LCFBG, using a second MZM with 40 GHz bandwidth and 37 dB extinction ratio (EOSPACE) following an optical polarization controller. This MZM is biased at 6.2

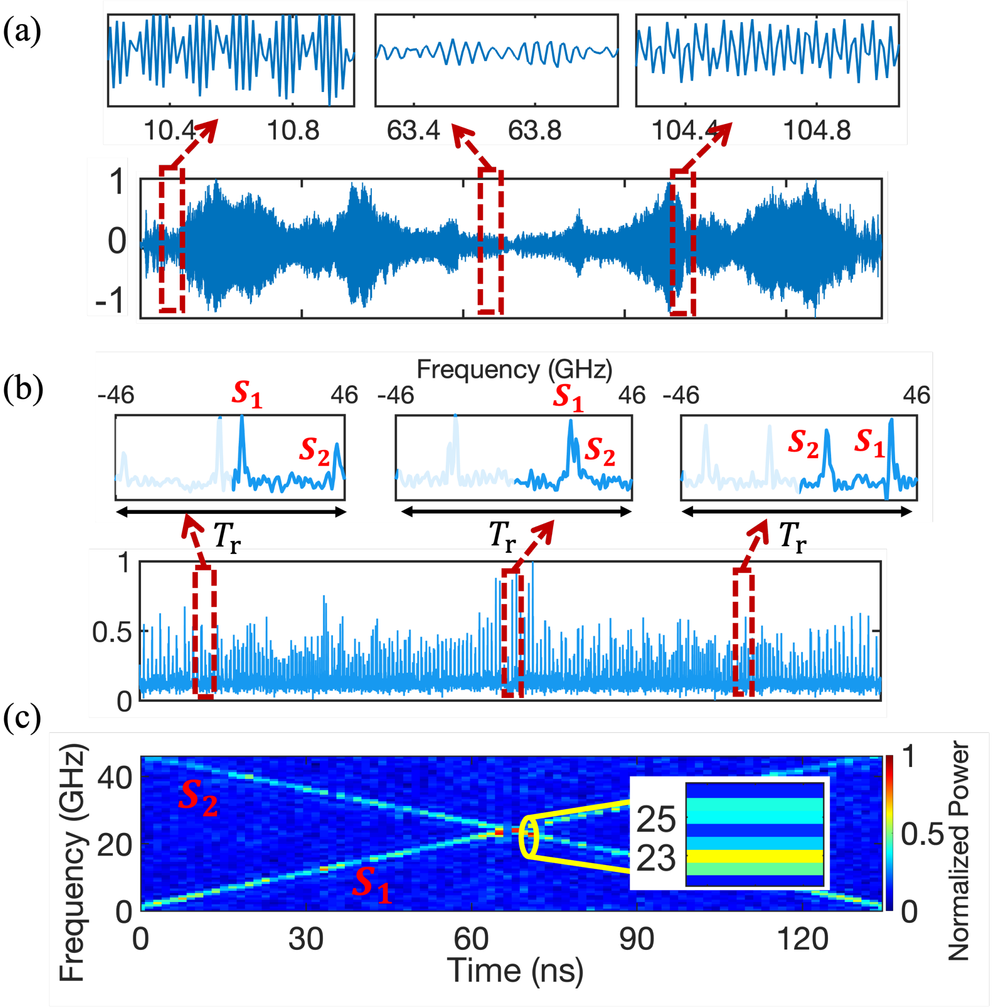

Figure 4.3. TAI-based time-frequency analysis of the results in Fig. 3.9: (a) Temporal trace of the SUT with pre-compensation, and the zoomed-in traces of different section of the SUT. (b) Time-mapped spectrogram of the SUT, with three zooms around different time window. (c) The 2D spectrogram representation.

V to achieve a high dynamic range. This enables electronic programmability of the filter's time-varying spectral response. Subsequently, the temporal T-F filtered waveform propagates through a second dispersive medium, implemented via another LCFBG with dispersion exactly opposite to that of the first one. The resulting filtered signal is recorded by a 50-GHz photodiode (PD) connected to a 28-GHz real-time oscilloscope (RTO).

To facilitate the evaluation, the first experimental results from Chapter 3 are used for the following temporal filtering. For clarity and completeness, I recall here the main results obtained for this signal, shown in Fig. 4.3. The SUT is composed of a double chirp with full bandwidth of 92 GHz (labeled S_1 and S_2 for each chirp). The temporal waveform of the SUT is shown in Fig. 4.3 (a). To analyze this SUT, we set the TAI phase consists of q = 139 phase levels each with a duration of t_s~ 10.8 ps, forming a periodic pattern of length T_r = 1.5 ns. A reflective LCFBG with second-order dispersion of $\ddot{\Phi}_0 \sim 2{,}600\ \mathrm{ps}^2/\mathrm{rad}$ is implemented for the TM-SP. This setup successfully maps the time-varying spectrum of the SUT along the time domain with analysis window of T_r = 1.5 ns, and 660-MHz frequency resolution, resulting in 139 analysis point. The measured TM-SP is presented in Fig. 4.3 (b), with zoomed-in regions showing the details over different analysis windows. The resulting 2D representation of the measured spectrogram of the SUT, depicted in Fig. 4.3 (c), illustrates the evolving frequency components of the two chirps. Subsequently, we target filtering in (i.e., selecting) a single linear chirp component from the double-chirped microwave signal [225].

To realize the desired T-F filtering operation, the time-mapped STFT is processed by a user-defined TVF with a frequency resolution of 660 MHz. This requires implementation of a time-domain filtering mask described in Eq. (4.1) with a time width of ~10.8 ps, commensurate with the specifications of available components. Specifically, the filtering mask is imposed on the time-mapped STFT through an electro-optic MZM driven by another channel of the AWG. In this example, the temporal filtering pattern, shown in Fig. 4.4 (a), is designed to select (i) the two temporal pulses corresponding to the target chirped waveform (i.e., negative and positive frequency components of S_1) from the four frequency components of the two crossing chirps and (ii) a central pulse to select the optical carrier. The filtering pattern is then reconfigured every T_r , i.e., at a tuning speed of $1/T_r$~660 MHz, of the order of the frequency resolution of the performed filtering operation. Three zoomed-in views of the temporal filtering pattern are shown in Fig. 4.4 (a), with each pulse width of t_s~ 10.8 ps, reconfigured every T_r = 1.5 ns. The varying time location of the filtering mask along each time slot aligns with the corresponding frequency terms of the increasing frequency-chirp

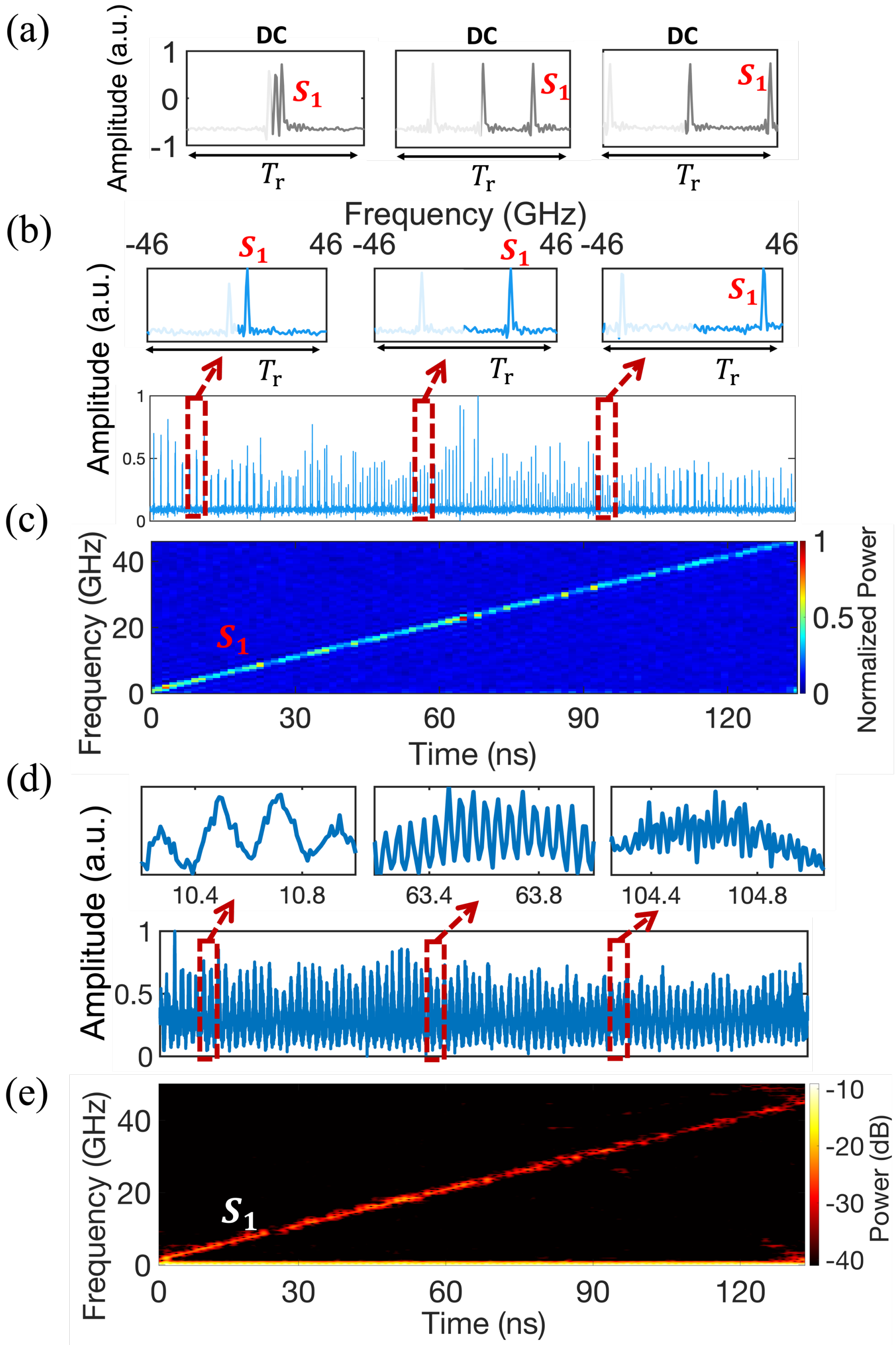

Figure 4.4. Experimental results of time-frequency filtering. (a) Three zooms of the temporal filtering pattern. (b) The time-mapped spectrogram after T-F filtering. (c) 2D representation of the filtered time-mapped spectrogram. (d) The recovered signal after the second dispersive element. (e) Numerical STFT spectrogram of the recovered signal.

component (S_1) to filter in this component from the SUT. Fig. 4.4 (b) shows the measured temporal waveform at the output of the MZM used for T-F filtering. The pulses representing the frequency components of S_2 are strongly reduced with respect to the S_1 components, as shown in the representation of the resulting TM-SP in Fig. 4.4 (c). It is clear that only the pulses representing the frequency components of S_1 along every time window are maintained. We recall that only the positive frequency axis is represented in the 2D spectrogram plots shown throughout this thesis for clarity. We also highlight the positive side of the spectrum for each zoomed-in waveform, corresponding to the same location as it is shown in Fig. 4.3 (b), with the equivalent frequency axis marked at the top of each plot. Finally, the microwave T-F-filtered waveform is recovered by passing through a second LCFBG with dispersion of $\ddot{\Phi}_0 \sim -2{,}600\ \mathrm{ps}^2/\mathrm{rad}$. The measured processed microwave signal is shown in Fig. 4.4 (d), with the same zoomed-in regions as the input shown in Fig. 4.3 (a). The corresponding numerical spectrogram of the processed measured signal is also shown in Fig. 4.4 (e). Compare with the results shown in Fig. 4.3, it is evident that S_2 is nearly supressed and a pure linear chirp with increasing frequency (component S_1) is successfully recovered.

The next result aims to illustrate the filter response with a different tuning speed and customized time widths for each temporal filtering pulse. To explore this, we use the same experimental setup with the amount of dispersion, $\ddot{\Phi}_0 \sim 2{,}600\ \mathrm{ps}^2/\mathrm{rad}$, as implemented in Fig. 4.4. However, we adjust the central frequency of the proposed filter with a different tuning speed compared to the scheme in Fig. 4.4. To evaluate this, the initial experimental results from Chapter 3 are employed for the subsequent temporal

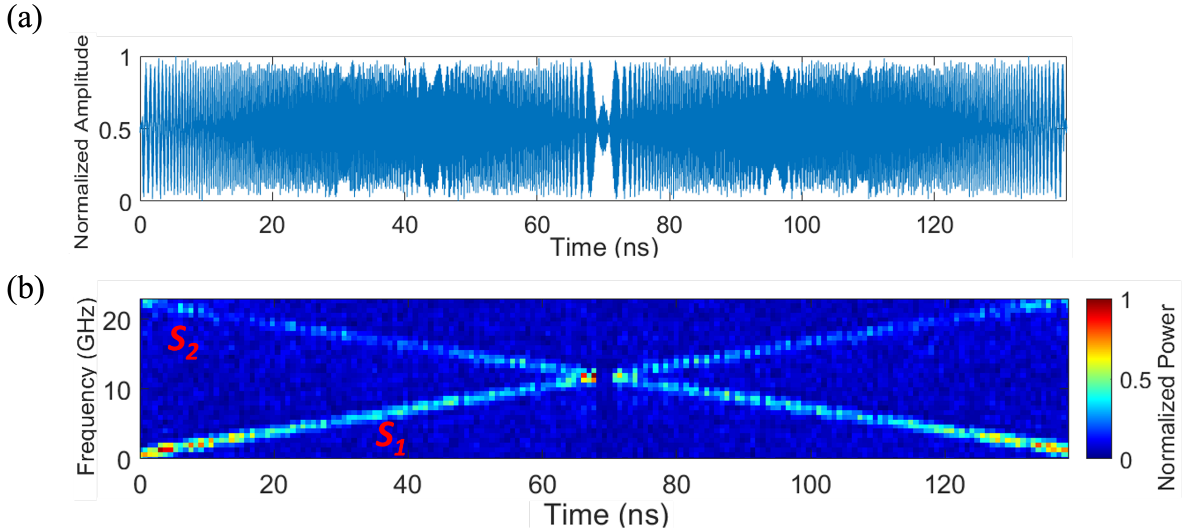

Figure 4.5. Experimental results of time-frequency analysis of two-chirps with instantaneous frequency of 23 GHz. (a) Temporal trace of the SUT with pre-compensation. (b) The 2D spectrogram representation of the time-mapped spectrogram.

filtering. For clarity and comprehensiveness, I reiterate the primary outcomes achieved for this signal, as depicted in Fig. 4.5. The SUT consists of two linearly-chirped sinusoidal waveforms with bandwidth of ~23 GHz, as depicted in Fig. 4.5 (a). In this configuration, the TAI phase is set to $t_s \approx 21.7$ps and the period length to $T_r \approx 0.76$ ns. Thus, the time-frequency distribution (STFT) of the SUT is continuously mapped onto the time domain every $T_r \approx 0.76$ ns, as shown in Fig. 4.5 (b). The frequency resolution of the obtained spectrogram is approximately 1.3 GHz. The TM-SP is then processed by the time-varying filter as follows. In order to eliminate one chirp component (S_2) from the two chirps, we manipulate the time-

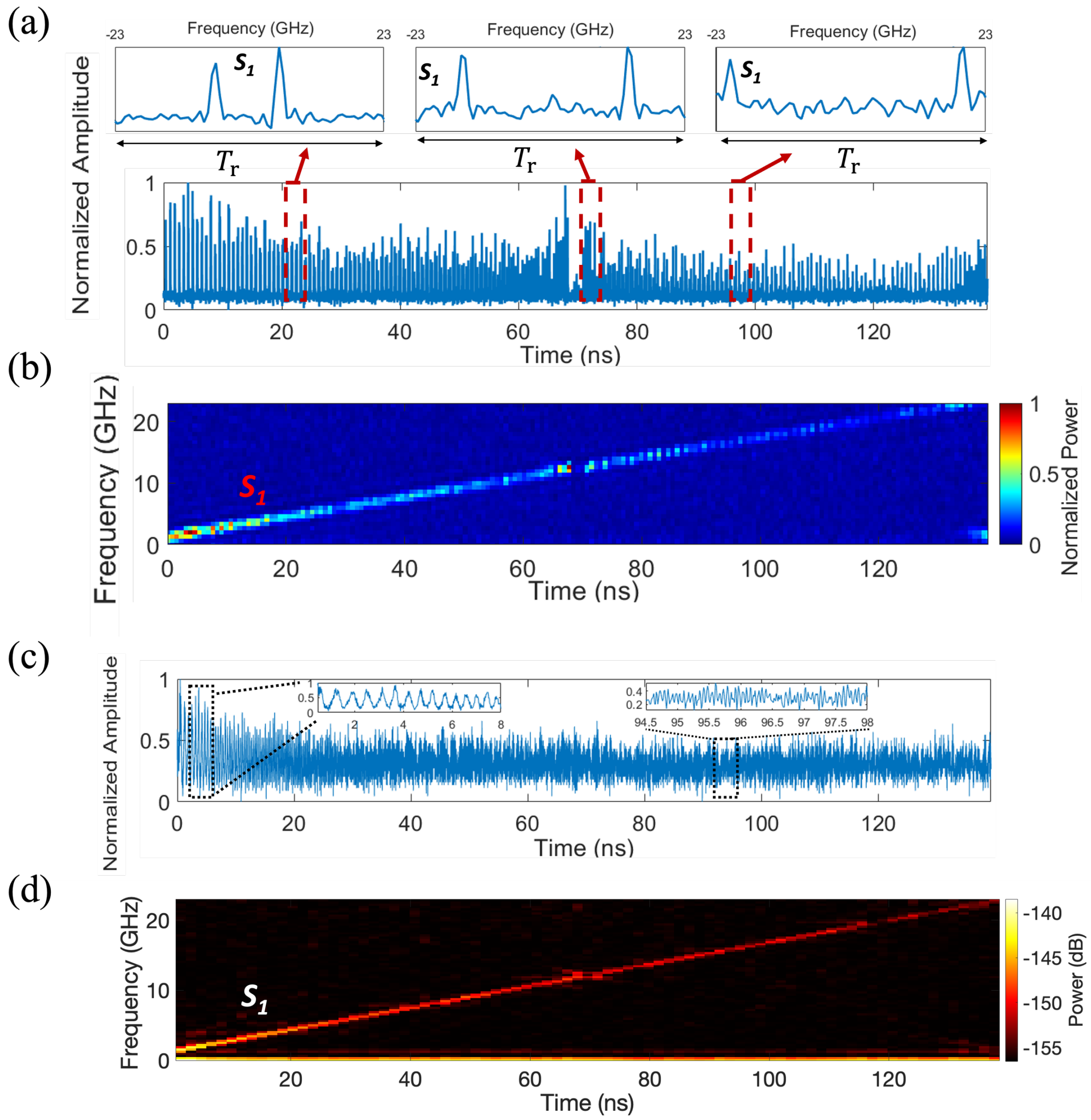

Figure 4.6. Experimental results after filtering. (a) The time-mapped spectrogram after T-F filtering. (b) 2D representation of the filtered time-mapped spectrogram. (c) The recovered signal after the second dispersive element. (d) Numerical STFT spectrogram of the recovered signal.

frequency distribution of the SUT along every analysis window of $T_r \approx 0.76$ ns, corresponding to a tuning speed of the implemented filtering operation of ~ 1.3 GHz. The temporal filtering pattern (i.e., rectangular passbands) is designed to select only one chirped waveform (i.e., S_1) from the two crossed chirps. This is done by dynamically varying the filter with a tuning speed of ~1.3 GHz and using an ~25-ps pulse width, corresponding to a filter passband equal to the frequency resolution of the TM-SP (i.e., ~1.3 GHz). Thus, the transfer-function profiles for the filter are programmed to select the desired linear chirped frequency components in every analysis time window T_r implementing the target time-variant filtering function. Fig. 4.6 (a) shows the measured T-F filtered waveform at the output of the second MZM. Notice that as designed, only the pulses representing the frequency components of S_1 are maintained. The corresponding 2D representation of this TM-SP is shown in Fig. 4.6 (b), again showing a clear decimation of the unwanted chirp. Finally, the T-F filtered temporal waveform is recovered after the second LCFBG, providing the exact opposite dispersion to the first LCFBG used for the TAI spectrogram. The recovered microwave signal is measured using a 50-GHz PD connected to a 28-GHz RTO, shown in Fig. 4.6 (c). The corresponding numerical spectrogram is also shown in Fig. 4.6 (d). Compared with the input, the output STFT spectrogram clearly confirms that the unwanted signal with decreasing frequency-chirp has been successfully decimated using the proposed T-F filtering system. Therefore, the proposed time-frequency filter has been demonstrated to have a tunable central frequency response and with a reconfigurable tuning speed.

4.4 Experimental Validation of User-defined Response for Interferences Mitigation

I have showed implementation of a basic bandpass filtering system in which the central frequency can be rapidly tuned. Here, I will experimentally demonstrate the capability of this method for user-defined time-varying filtering in which the spectral response can be electronically programmed at will to have several filtering pulses along every time slot and precise time-frequency selectivity. Specifically, we showcase here the application of this method for mitigation of unwanted time-varying frequency interferences from a sophisticated (double chirped) broadband microwave signal. To facilitate the evaluation, the captured results in Fig. 3.10 of Chapter 3 are used for the following temporal filtering. For the sake of clarity and completeness, the main results obtained for this signal are reiterated here in Fig. 4.7. The SUT consists of two crossed linear chirps, one varying from 0.67 to 20 GHz and vice versa for the other (labelled as as S_1 and S_2) within the time interval from 0 to 130 ns, and with different frequency

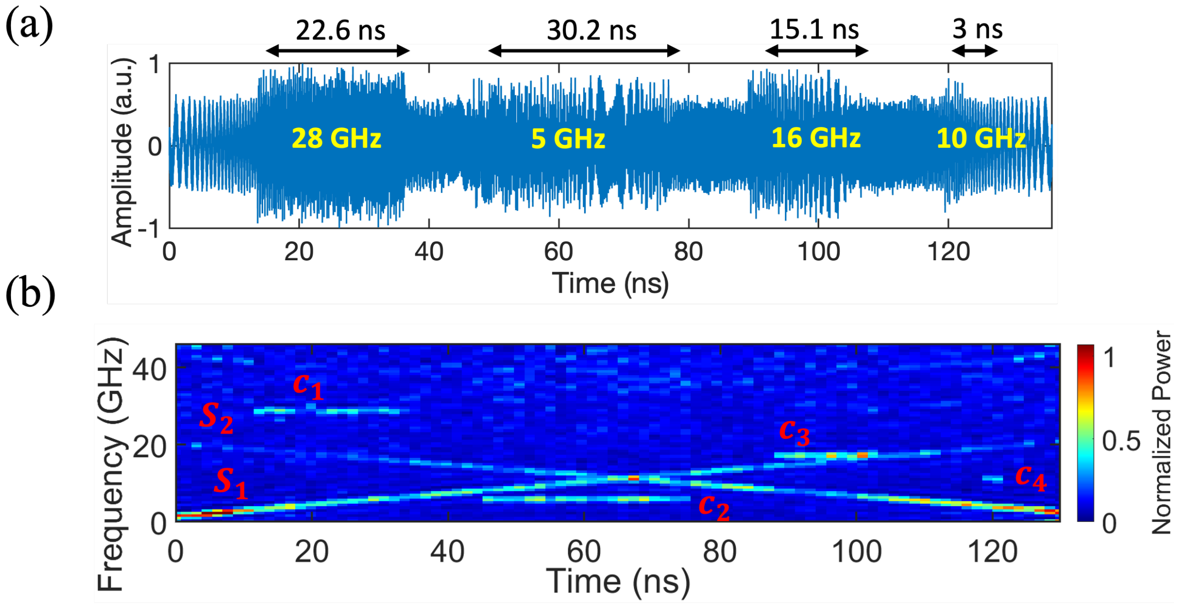

Figure 4.7. Experimental results of TAI-based time-frequency analysis: (a) Temporal trace of the SUT with pre-compensation. (b) The 2D spectrogram representation of the time-mapped spectrogram.

interferences of varying temporal durations. The frequency of the interferences varies from 5 GHz to 28 GHz. A LCFBG is employed to provide the needed second-order chromatic dispersion $\ddot{\Phi}_0 \sim 2{,}600\ \mathrm{ps}^2/\mathrm{rad}$. The TM-SP has been analysed with analysis period of $T_r \approx 1.5$ ns and frequency resolution of 660 MHz. The output temporal waveform and the 2D time-frequency representation clearly depicts the evolving frequency content of the two chirps (S_1 and S_2) and the different interference terms, shown in Fig. 4.7 (b). The temporal waveform is then modulated by the user-defined filtering pattern through a second MZM. The temporal filtering mask is designed to be composed of rectangular shapes as in Eq. (4.1), each with a

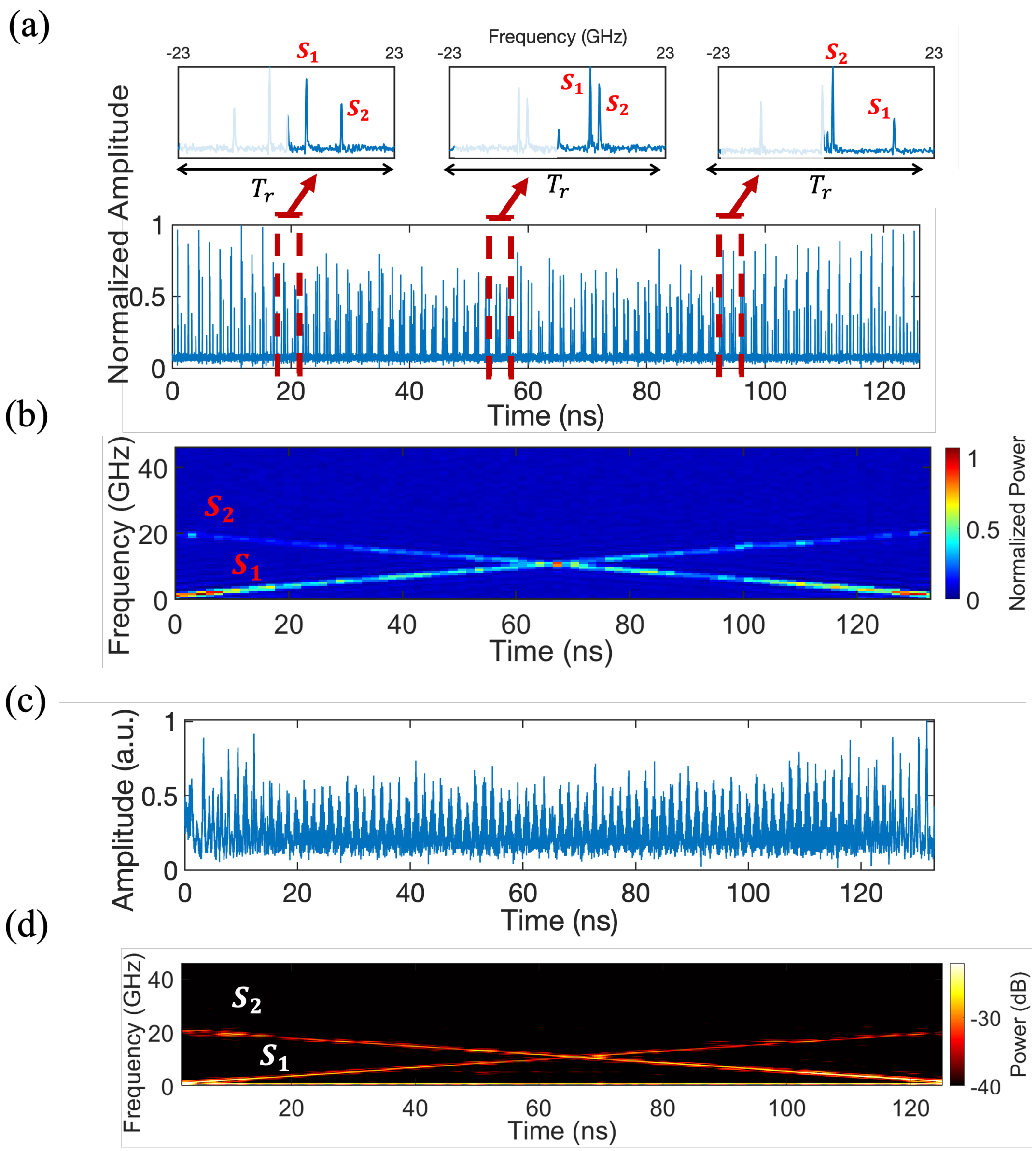

Figure 4.8. Experimental results of the T-F manipulation. (a) The time-mapped spectrogram after T-F filtering. (b) 2D representation of the filtered time-mapped spectrogram. (c) The recovered signal after the second dispersive element. (d) Numerical STFT spectrogram of the recovered signal.

temporal width equal to t_s, corresponding to a filter passband equal to the frequency resolution $\delta\omega_{res} \sim 2\pi \times 660$ MHz of the time-mapped spectrogram. To eliminate the interferences while maintain the two chirps, the design of a multi-passband filtering mask is required to consist of five square-like pulses along every analysis period: two pulses for each of the chirped components to be filtered in, with the inter-pulse spacing adjusted every analysis period (T_r) to select the four pulses corresponding to the two chirped signals, and one central pulse to select the optical carrier. Thus, the response of the filter can be effectively programmed every $T_r = 1.5$ ns. The output of the second MZM used for time filtering is shown in Fig. 4.8 (a) and the corresponding zoomed-in regions clearly confirm that the pulses representing the interference terms have been greatly mitigated while the ones corresponding to the chirped signal terms, S_1 and S_2, are maintained nearly undistorted. The 2D representation is shown in Fig. 4.8 (b), again showing a clear reduction of the unwanted interferences. Finally, a second LCFBG with dispersion of $\ddot{\Phi}_0 \sim -2{,}600\ \mathrm{ps}^2/\mathrm{rad}$ is used for dispersion compensation and the recovered microwave signal is measured using a 50-GHz PD connected to a 28-GHz RTO, shown in Fig. 4.8 (c). The corresponding numerical spectrogram is also shown in Fig. 4.8 (d). Compared with the input, the output STFT spectrogram clearly confirms that the unwanted interferences have been successfully mitigated using the proposed T-F filtering system.

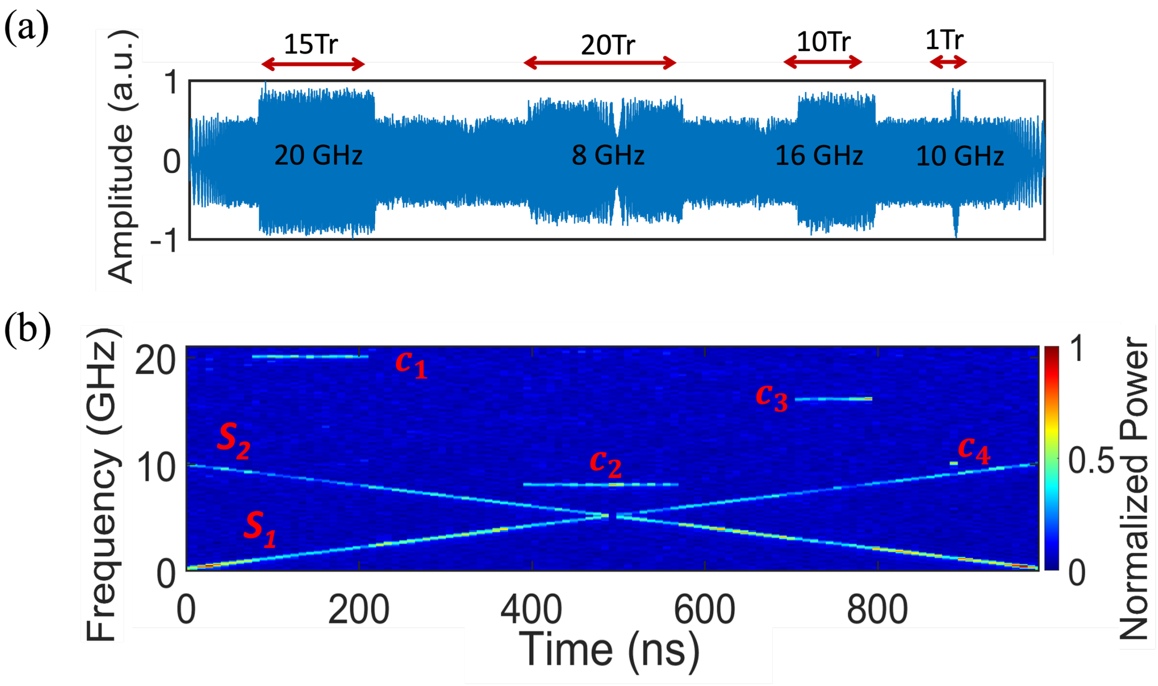

Figure 4.9. Experimental results of TAI-based time-frequency analysis. (a) Temporal trace of the SUT with pre-compensation. (b) The 2D spectrogram representation of the time-mapped spectrogram.

The next results aim to realize a time-frequency filter with fine frequency selectivity (i.e., 110 MHz). To facilitate the evaluation, the captured results in Fig. 3.16 of Chapter 3 are used for the following temporal filtering. For clarity and completeness, I recall here the main results obtained for this signal, shown in Fig. 4.9. Fig. 4.9 (b) shows that the spectrum of the SUT is mapped along the time domain every $T_r \sim 9$ ns with a frequency resolution of 110 MHz. To obtain the fine frequency resolution, we use a LCFBG with the amount of dispersion $\ddot{\Phi}_0 \sim 15{,}494\ \mathrm{ps}^2/\mathrm{rad}$. The resulting time-mapped spectrogram enables an accurate identification of the individual chirps (i.e., S_1 and S_2) and frequency interferences of the SUT at the expected time and frequency locations, as depicted in Fig. 4.9 (b), providing the capability of precise frequency manipulation for the following temporal filtering step. Thus, we target removing a set of undesired frequency-changing interferences along a broadband double-chirped signal. In order to select the two chirped waveforms (S_1 and S_2), two rectangular pulses with varying time locations according to the frequency-to-time mapping factor are implemented in every analysis time window T_r. The temporal width of each filtering pulse is set as $t_s \sim 10.8$ ps to precisely manipulate the corresponding time-mapped

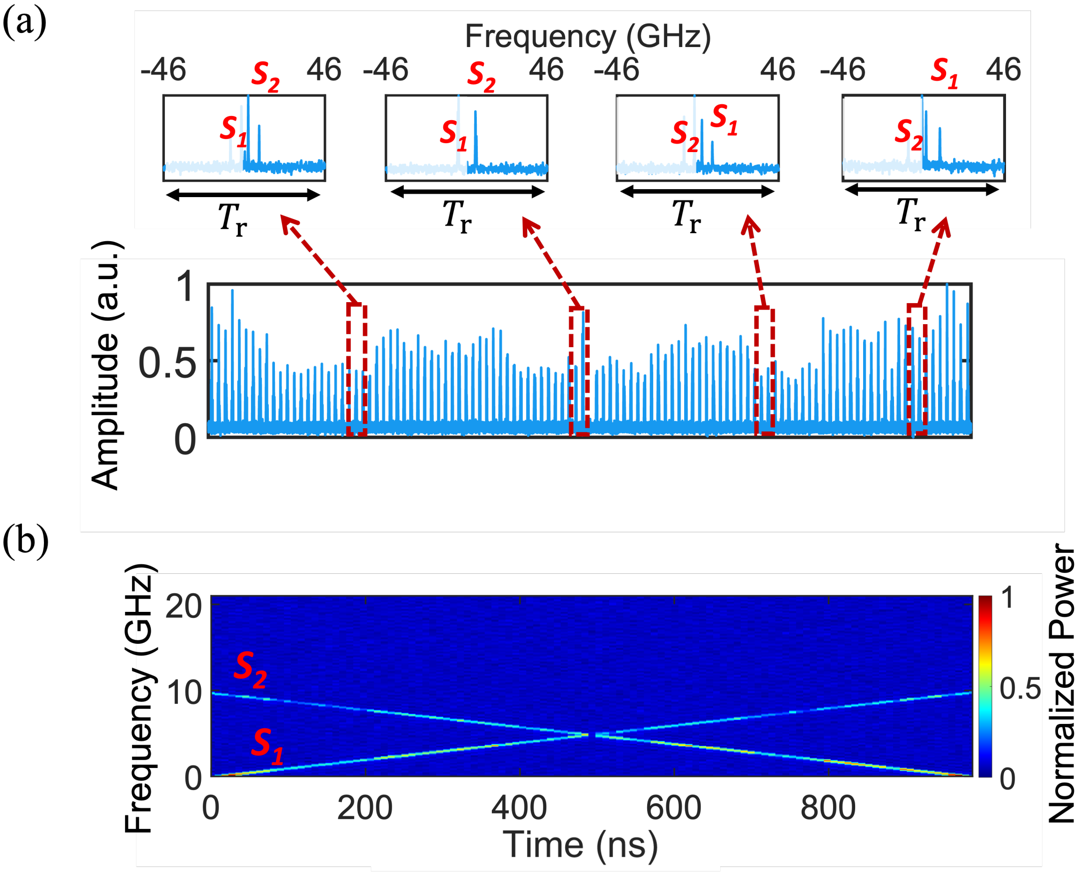

Figure 4.10. Experimental results of the T-F manipulation. (a) The time-mapped spectrogram after T-F filtering. (b) 2D representation of the filtered time-mapped spectrogram.

waveform. Fig. 4.10 (a) and (b) show the measured TM-SP trace after the temporal filtering process, as well as the corresponding 2D representation. As expected, the system performs a sufficiently high selectivity to efficiently remove interference c_4 which is spaced by 1 GHz with respect to the double-chirped waveform.

4.5 Evaluation of Frequency Response of the T-F Filter

To provide further evidence on the reconfigurability of the spectral response that is provided by the demonstrated time-varying filtering scheme, in terms of the passband shape, bandwidth, and tuning frequency, we have performed a standard characterization of the RF spectral response of the microwave photonics filtering scheme in Fig. 4.11. This characterization has been carried out under different temporal filtering specifications, i.e., by programming the corresponding modulation pattern. based on the setup shown in Fig. 4.11. A continuous wave (CW) optical carrier centered at 1553.5 nm is used as the optical source. A 50 GHz bandwidth vector network analyzer (VNA) is implemented to provide the RF signal with a frequency swept from 10 MHz to 50 GHz. The RF signal is modulated on the electro-optic modulator after a RF amplifier. An erbium-doped fiber amplifier (EDFA) at the output of MZM is used to compensate for the loss. The optical signal is then sent to the TM-SP step and the temporal filtering. The 92 GS/s electrical AWG is used to provide the TAI phase and pre-designed temporal filtering pattern. In order to

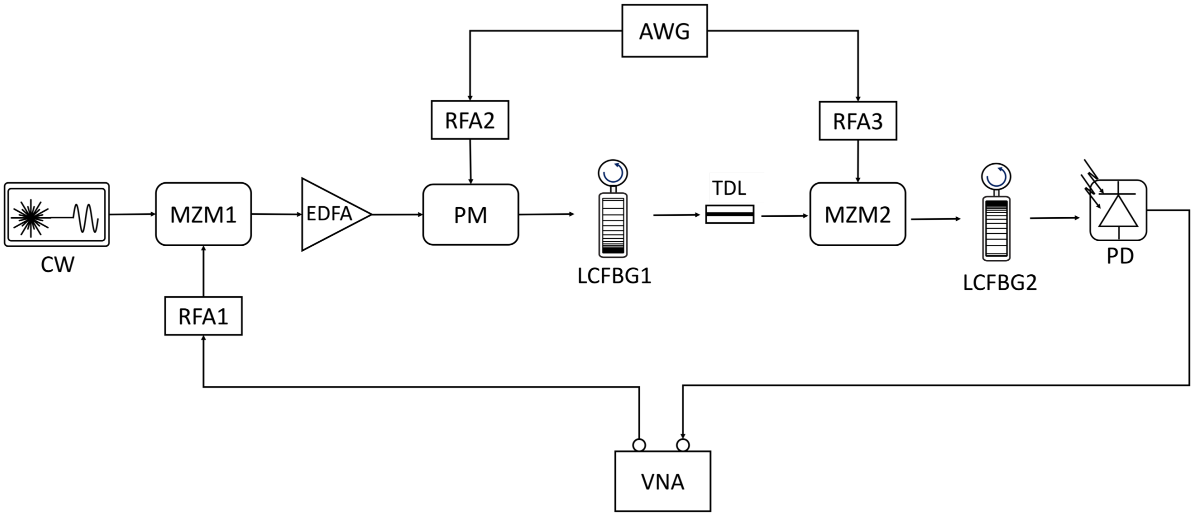

Figure 4.11. The setup for measuring the spectral amplitude response of the implemented microwave photonic filter using a standard scheme based on an VNA. MZM: electro-optic Mach-Zehnder Modulator, EDFA: Erbium-Doped Fiber Amplifier, PM: electro-optic Phase Modulator, RFA: RF Amplifier, AWG: Arbitrary Waveform Generator, LCFBG: Linearly-Chirped Fiber Bragg Grating, TDL: optical Tunable Delay Line, PD: Photo-Diode, RTO: Real-Time Oscilloscope, VNA: Vector Network Analyzer.

demonstrate the characterization of the proposed filter with the largest operation bandwidth, the TAI phase is set with single step width of $t_s \sim$ 10.8ps, enabling the analysis of signals with the maximum full frequency bandwidth of $1/t_s \sim$ 92 GHz. The temporal period for the temporal phase pattern is T_r = 1.5 ns, corresponding to a tunable frequency of ~ 666 MHz. A LCFBG with $\ddot{\Phi}_0 \sim 2{,}600\ \mathrm{ps}^2/\mathrm{rad}$ is used. Note that an optical tunable delay line is used to ensure the time-mapped spectrogram is align with the filtering mask. The manipulated signal is then recovered through a second LCFBG with the opposite dispersion of the first one and a 50-GHz photodetector. The recovered microwave signal is connected to the input of the VNA to measure the frequency response of the system.

The measured S_{21} parameters from the VNA for different filtering responses are shown in Fig. 4.12. As previously discussed, the central frequency, bandwidth, and shape of the proposed filter can be dynamically reconfigured through designing the temporal filtering pattern. In Fig. 4.12 (a), we target demonstrating the tunable central frequency of the filter response. Accordingly, we program the temporal filtering waveform to consist of a set of rectangular-like shape pulses, each with a temporal width of $5 \times t_s$. The time location of these pulses varies according to the frequency-to-time mapping factor discussed before to achieve different central frequencies. This configuration corresponds to a bandpass spectral response

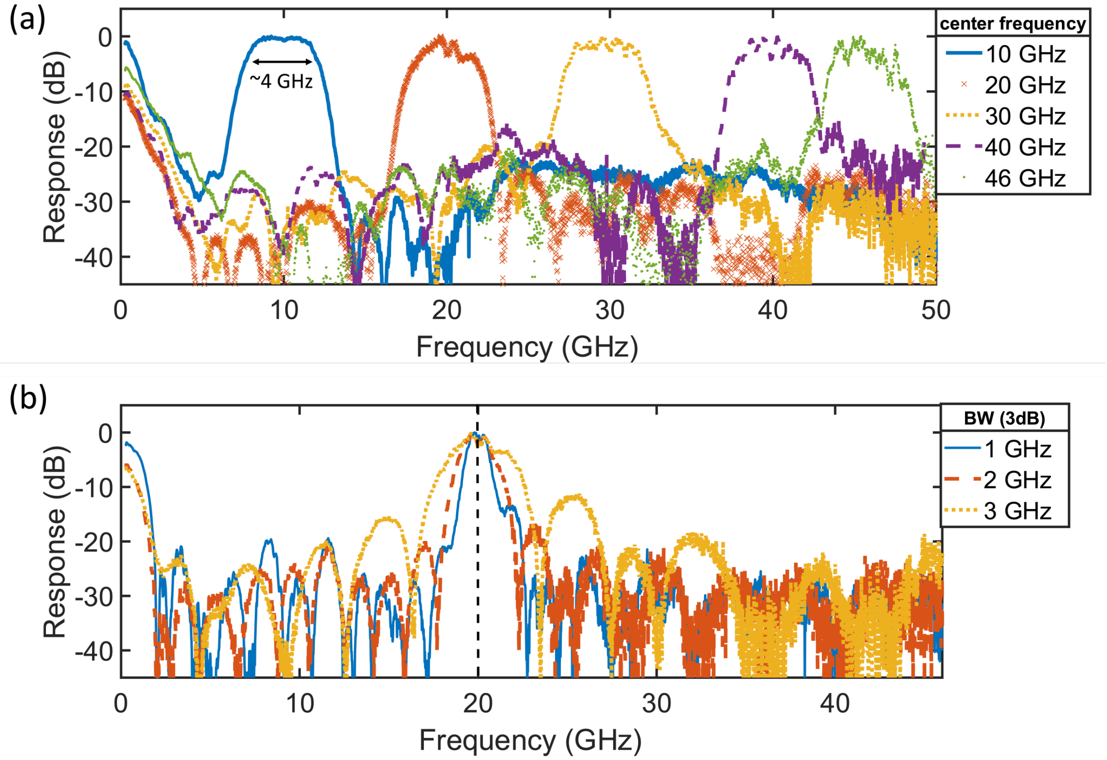

Figure 4.12. Measured frequency response of the demonstrated microwave photonics filter, with (a) reconfigurable center frequency, (b) bandwidth and shape.

with 3-dB bandwidth of 4 GHz and a tunable center frequency ranging from 10 to 46 GHz. The measured frequency response clearly shows the tuning of the central frequency, with a consistent passband passband of 4 GHz.

To further highlight the versatility of our proposed scheme, i.e., the capability of reconfigurable response shape and frequency bandwidth, we re-design the filtering pattern with a sinc-like shape pulse. Results in Fig. 4.12 (b) confirm that the corresponding frequency response of the system also follows a sinc-like shape. The temporal width of the pulse ranges from 10.8 ps to 32.4 ps, corresponding to the measured tunable bandwidth from 1 GHz to 3 GHz. In this case, we fix the time location of the filtering pulse within each time window at the position corresponding to 20 GHz. Consequently, the measured frequency response is centered at 20 GHz and with different passbands.

Thus, we have demonstrated that the proposed filtering system exhibits the anticipated broad operation bandwidth, and reconfigurable frequency response in terms of central frequency, passband, shape, and tuning speed. It is worth noting that the frequency and bandwidth tuning is performed in discrete steps in Fig. 4.12, though generally, continuous tuning could be achieved by properly designing the filtering pattern.

4.6 Experimental Demonstration of T-F Filtering with an Arbitrary Response

In a final experiment, we showcase the capability of the proposed method to reshape at will the joint T-F distribution of an input stationary broadband wave (Fig. 4.13). The scheme is now reconfigured to achieve a time resolution (and analysis period) of $T_r \sim 4.5$ ns, corresponding to a frequency resolution of ~220 MHz, and a full analysis bandwidth of $1/t_s \sim 46$ GHz. The input SUT is a train of sinc-like pulses, periodically spaced by $T_r/3$, purposely designed to exhibit a nearly uniform joint T-F energy distribution along its entire duration and full bandwidth (~46 GHz). The measured temporal waveform of the SUT and the numerical STFT are shown in Fig. 4.13, which is composed of periodic sinc-like pulses, forming a nearly uniform spectrogram distribution, over a frequency range up to 23 GHz (positive side) along a duration of ~300 ns. An arbitrary prescribed 2D image can then be inscribed along the joint T-F energy distribution of the wave within the resolution specifications of the performed T-F filtering scheme.

It is important to consider that the filtering pattern generated by the AWG fundamentally operates on vectors. Hence, in order to reshape the spectrogram into the desired 2D image pattern, we need to flat the

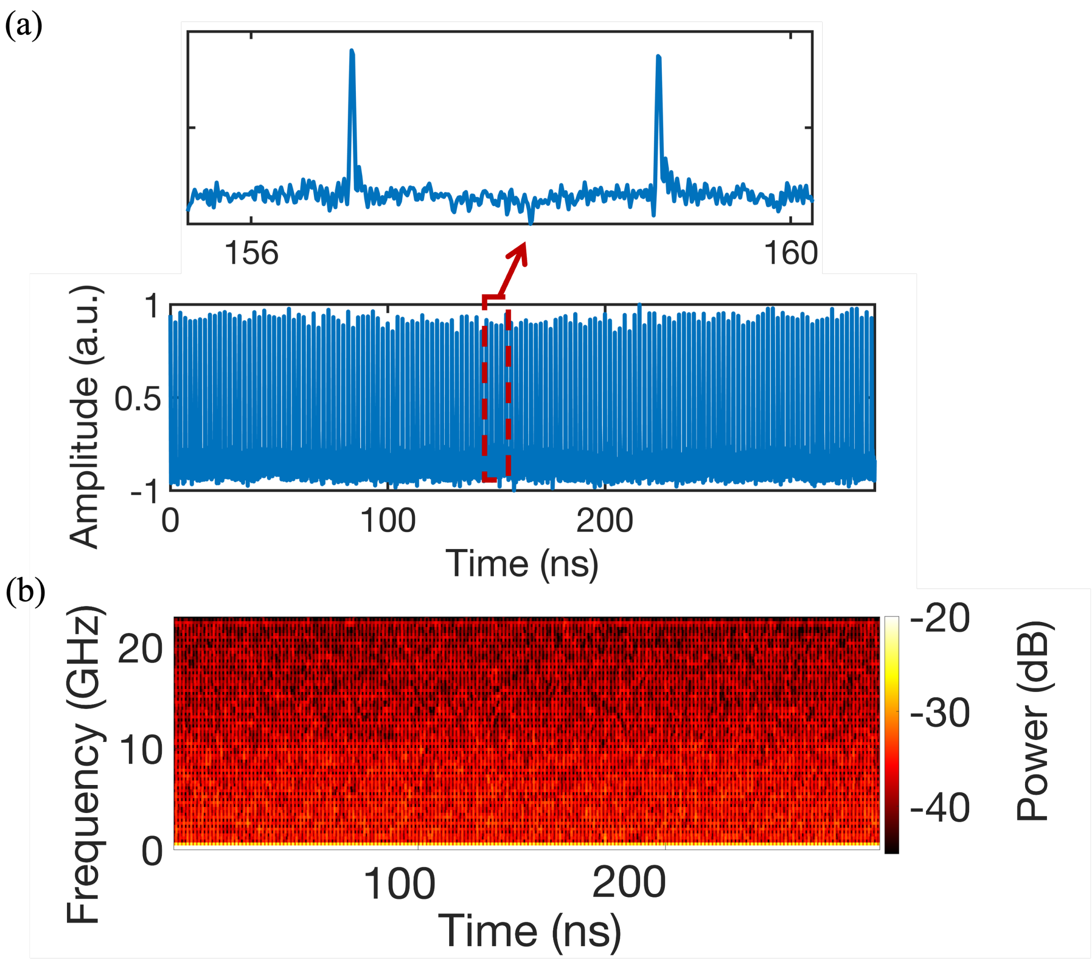

Figure 4.13. Measured temporal waveform and numerical STFT of the SUT, which is composed of periodic sinc-like pulses, forming a nearly uniform spectrogram distribution.

2D image into a 1D vector. The detailed flattening process is illustrated in Fig. 4.14. The target filtering image pattern (e.g., Mona Lisa painting) is first resized into a new matrix. The number of columns in this new matrix is equal to the total number of analysis temporal periods and the number of the rows is determined by the total number of frequency points per analysis period in the target 2D T-F representation. The resized matrix is then unfolded to form a 1D vector by connecting each unfolded slice sequentially. This resulting vector is subsequently programmed into the electronic AWG to generate the target temporal filtering pattern. The designed filtering pattern is modulated onto the TM-SP of the SUT. The output is then processed to have the frequency spectrum information along every prescribed analysis period T_r, according to the frequency-to-time mapping factor. Then the output (1D vector) is folded along every analysis period to be a matrix, following the inverse procedure to the initial unfolding method. The final result is the 2D representation after the target user-defined filtering.

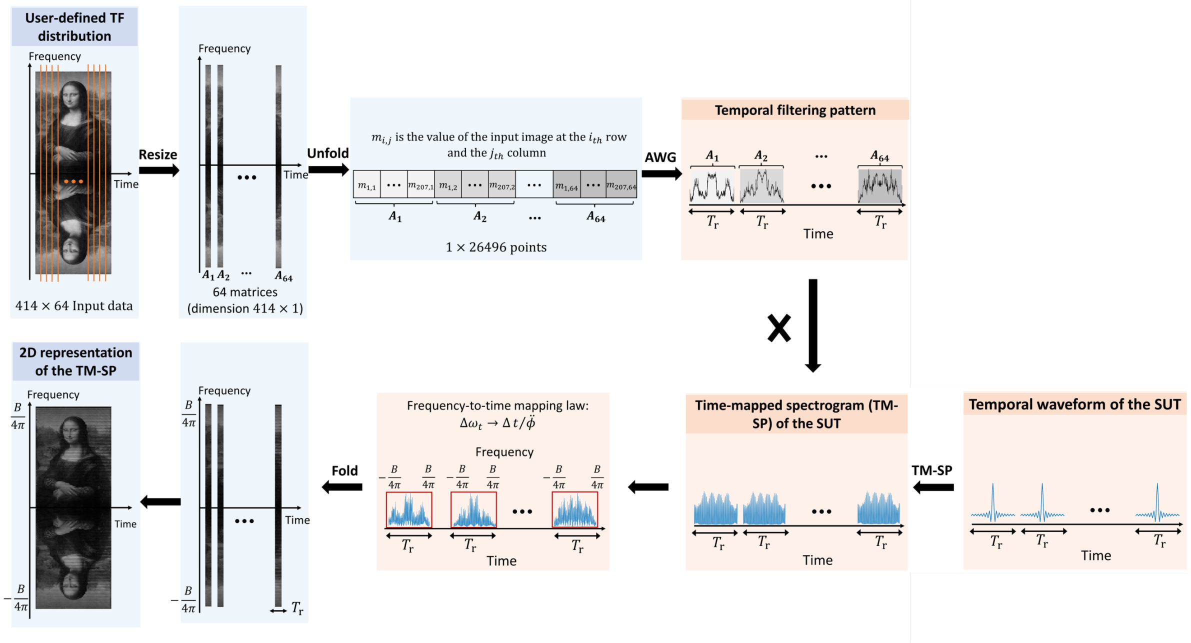

Figure 4.14. Diagram illustrating the flattening method for image filtering pattern and formation of the 2D representation of the TM-SP.

In a first example, we successfully re-shape the wave T-F distribution into a 2D pattern that resembles an image of the Mona Lisa painting, see Fig. 4.15. The filtering pattern is directly transferred from the image of the Mona Lisa painting. We firstly converted the image from RGB to grayscale and employed normalization of the intensity (i.e., 1 for white and 0 for black). In this case, our goal is to map the target image into the 2D joint T-F representation, and we recall that this 2D representation is obtained by vertically plotting the frequency spectrum profile of adjacent temporal analysis windows. As such, the image matrix needs to be resized to have the same number of samples per column as the vertical samples per analysis period in the 2D T-F representation, according to the specifications of the performed TM-SP (i.e., 414 samples in our case); accordingly, the row samples must be fixed to be equal to the total number of analysis periods (64 samples in our case). The temporal filtering pattern can then be obtained by unfolding the 2D matrix into a 1D vector, as described above. Fig. 4.15 (a) is the measured 1D temporal filtering mask mapped from the 2D image of the Mona Lisa painting used to manipulate the T-F distribution of the SUT, and a zoom of the user-defined temporal filtering pattern of arbitrary shape, showing that the temporal filtering can be programmed with arbitrary customized waveform. The 2D representation of the TM-SP trace that is measured after the temporal filtering is illustrated in Fig. 4.15 (b), showing that the synthesized spectrogram closely follows the contour of the target image. The result confirms that the joint T-F distribution of the processed wave has a contour proportional to that of the Mona Lisa image, though with the expected degraded resolution mainly due to the down-sampling implemented in the filtering mask generation process, and the limited bandwidth of the 28-GHz scope used for capturing the TM-SP traces.

In a second instance, we use the same SUT, Fig. 4.13, and design a temporal filtering pattern, aimed at synthesizing a T-F distribution following a 2D image of the Chinese character “中”, Fig. 4.16 (a). The filtering mask is designed to craft a joint T-F distribution resembling the Chinese character shown at the top left. For this purpose, the temporal filtering pattern consists of a sequence of square-like passband pulses with suitable varying widths and centre locations, according to the desired frequency spectrum profile along each of the consecutive analysis periods. To give an example, as shown in the zoomed-in-region in Fig. 4.16 (a), the temporal filtering pattern is designed to select the frequency band from 2 GHz to 16 GHz in the 38th to 40th time slot, forming the central vertical line of the character, corresponding to a passband total

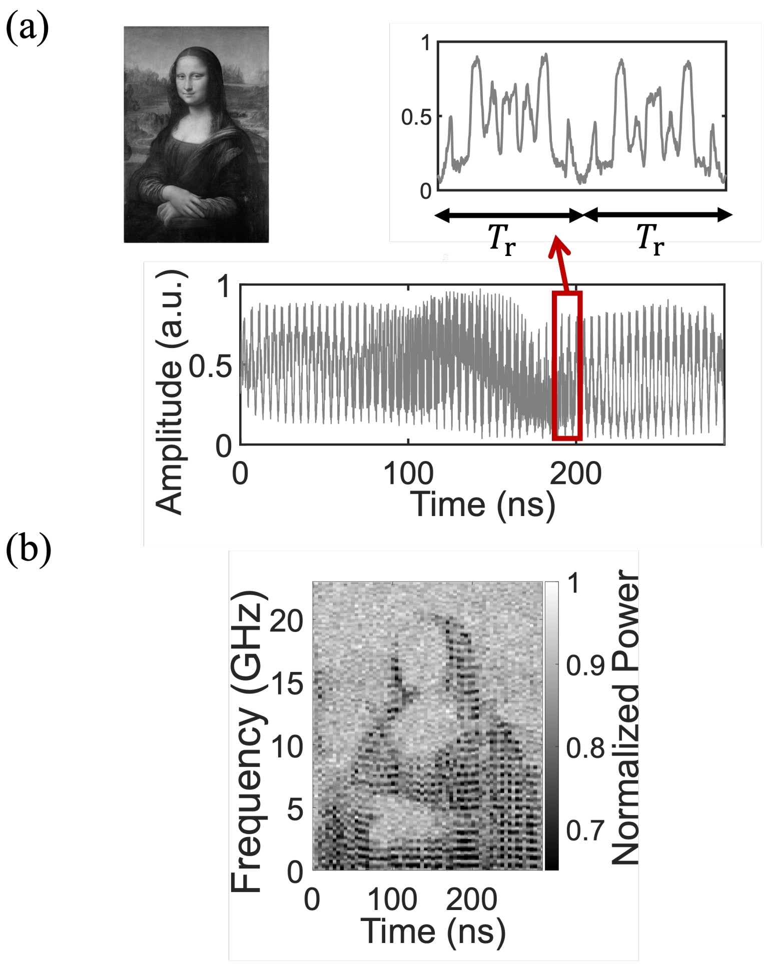

Figure 4.15. Demonstration of user-defined direct synthesis of the wave joint T-F distribution. (a) 1D temporal filtering mask mapped from the 2D image of the Mona Lisa painting used to manipulate the T-F distribution of the SUT, and a zoom of the user-defined temporal filtering pattern of arbitrary shape. (b) The 2D representation of the TM-SP trace that is measured after the temporal filtering, showing that the synthesized spectrogram closely follows the contour of the target image.

time width of ~ 64 × t_s. While in the 12th to 14th and 60th to 62nd time slot, the frequencies 5-13 GHz are selected to delineate the left and right vertical lines of the character. Between the 14th to 60st time slots, the frequency bands 5-7 GHz and 11-13 GHz have been filtered in to form the two horizontal lines. The short pulses at the edge of each time window are purposedly introduced to facilitate the synchronization between the filtering mask and TM-SP. The 2D representation of the TM-SP trace that measured after the temporal filtering is shown in Fig. 4.16 (b), confirming that the synthesized spectrogram closely resembles the target character.

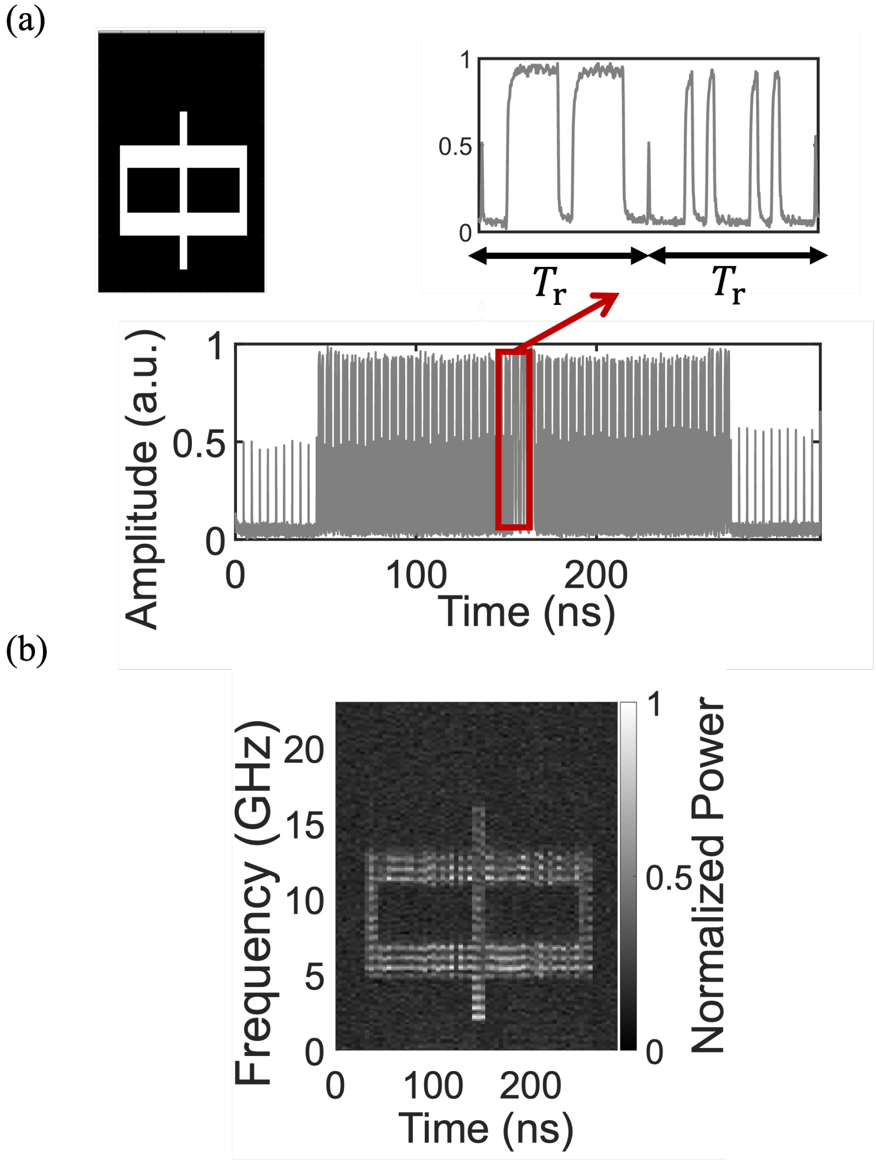

Figure 4.16. Demonstration of user-defined direct synthesis of the wave joint T-F distribution. (a) the filtering mask is now designed to craft a joint T-F distribution resembling the Chinese character shown at the top left. (b) The 2D representation of the TM-SP trace that is measured after the temporal filtering, confirming the synthesized spectrogram resembles the target character.

4.7 Conclusion

In this chapter, I have demonstrated a technique to manipulate the T-F distribution of the signals. In Chapter 3, the T-F distribution (the STFT) of the incoming wave has been successfully mapped along the time domain, in a continuous and gapless manner, which in turns enables a user-defined manipulation of the T-F distribution through an electro-optic MZM, providing a simple and remarkable versatility way to customize the manipulation. The operation principle was discussed and has been experimentally demonstrated through manipulating a wave over broad bandwidths, with high temporal and frequency resolutions and an unprecedented degree of versatility. I further demonstrate application of this scheme for mitigation of rapidly changing frequency interference terms along a high-speed wave and the direct synthesis of fast waveforms with customized T-F distributions. The reported method represents a significant advancement in the quest for manipulation of the T-F properties of EM waves and it fulfills the stringent requirements for many modern and emerging applications.

As such, I anticipate the potential of application of this same concept or similar strategies nearly across the entire EM spectrum. It would be relatively straightforward to utilize the demonstrated fibre-optics scheme for processing ultrafast light waves with frequency bandwidths well beyond those reported here, into the THz regime and above. Towards this aim, we envision the use of nonlinear optics mechanisms, such as cross-phase modulation or four-wave mixing [226], in dedicated optical fibres or waveguides for implementation of the needed temporal phase modulation process at much higher speeds. Realization of the scheme in compact integrated-waveguide formats would be potentially feasible, though we anticipate that a main challenge may be that of on-chip integration of the group-velocity dispersive lines [227]. The proposed concept represents a significant advancement towards manipulation and control of the T-F properties of EM waves, and we believe that it will prove particularly useful for realization of the cognitive and software-defined paradigms in future wireless and optical communications, intelligent remote sensing platforms and other systems based on broadband microwave, THz or optical waves.

In the proof-of-concept experiments, the filtering pattern is pre-designed accordingly to manipulate the incoming signal. In this case, the frequency components of the incoming signal need to be precisely known in advance. As such, this approach is ideally suited for applications where the signal characteristics are predetermined, such as in frequency hopping communication systems[81], [228] or chirped radar platforms[86]. Moreover, our approach also holds promise for processing unknown incoming waveforms through generation of the filtering pattern on-the-fly, either in the digital domain or in an entirely analogue manner.

This work demonstrates advanced versatility based on a photonic method and with low latency, making it well-suited for real-time high-speed signal analysis and processing. The proposed photonic method outperforms DSP engines by orders of magnitude. Nonetheless, it is worth noting that our proposed scheme relies on high-speed electro-optic modulators and electronic AWGs, which may translate into a significant cost and power consumption in practical implementations. However, the performance benefits of our proposed system, including high-resolution, real-time TF manipulation over tens of GHz bandwidth, outweigh the added complexity and cost. Equivalent performance specifications achieved through, e.g., DSP approaches, would require channelizing a ~40 GHz bandwidth signal into smaller few-GHz bandwidths segments [229], as each DSP unit has limited real-time operation bandwidth. In turn, this would translate into a considerable cost and complexity for the resulting overall DSP system. Thus, the low latency advantage, and the capability to handle such high-frequency waves in a real-time manner and with notable versatility make our proposed scheme particularly interesting for advanced applications.

5 CONCLUSIONS AND FUTURE PROSPECTS

5.1 Conclusions

This thesis discusses the equivalence between time-lens (TL) modulation and group-velocity dispersion (GVD) propagation as a foundation for real-time spectral analysis. The primary focus is on two main topics: time-frequency analysis and manipulation. The proposed scheme generally relies on frequency-to-time mapping using phase-only modulation of the incoming signal, combined with spectral filtering through temporal modulation. These proposed methods offer great versatility, with a large operational bandwidth and fine resolution.

Chapter 2 introduced the mathematical principle of the two main devices: second-order dispersive medium and time-lens, used in the proposed signal analysis and processing method. The physical mechanism, main characteristics and practical implementations have been analyzed, providing a deep understanding of these two units. Based on this, the relationship between time and frequency has been explored and the equivalence between GVD propagation and TL modulation for any given input signal is proposed. The equivalence exploits the fact that the frequency spectrum of a given (input) waveform, following a suitable sinusoidal temporal phase modulation, exhibits the same shape as that of a dispersed version of the same temporal waveform after propagation through a prescribed amount of dispersion. The numerical and experimental results confirm the time-frequency duality. As an application example, we utilized this method to determine the precise group-velocity dispersion (GVD) amount (both magnitude and sign) that is needed to achieve optimal compression of an incoming chirped optical temporal waveform, for which no information was available on its amplitude and phase profile.

In Chapter 3, a practical photonic-based platform for real-time spectrogram analysis was proposed and demonstrated, using the two units discussed in Chapter 2, i.e., time-lens and dispersive medium. The general mathematical analysis and trade-offs of the TAI-based spectrogram were discussed. A number of numerical and experimental results were performed to verify the features of the proposed scheme. The demonstrated Talbot Array Imaging (TAI) based spectrogram has achieved unprecedented performance specifications, namely

- Real-time analysis bandwidth up to ~ 100 GHz,
- Temporal resolution into the nanosecond regime,
- Fine frequency resolution down to the MHz level,
- User-defined reconfigurable specifications.

These performance specifications fulfill critical requirements of the time-frequency analysis for a wide range of applications, including communications, Radar/Lidar technologies, telecommunications and biomedicine. Moreover, the performance specifications of the TAI-based spectrogram achieved in this doctoral project can easily be upgraded over much higher instantaneous analysis bandwidths, to the THz range, by use of ultrabroadband electro-optic phase modulators (PM) [215] or nonlinear temporal phase modulation mechanisms, such as those based upon Kerr-based cross-phase modulation or four wave mixing in highly dispersive fibers or waveguides [206].

The obtained time-frequency distribution was subsequently manipulated in Chapter 4 by using an electro-optic Mach-Zehnder modulator (MZM). As the time-frequency (T-F) distribution of the incoming wave has been successfully mapped along the time domain, in a continuous and gapless manner, which in turns enables a user-defined manipulation of the T-F distribution directly in the time domain. The time-frequency manipulation has been demonstrated with broad operation bandwidth, high temporal and frequency resolutions and an unprecedented degree of versatility. Applications of this scheme for mitigation of rapidly changing frequency interference terms along a high-speed wave and the direct synthesis of fast waveforms with customized T-F distributions were also demonstrated. The reported method represents a significant advancement in the quest for manipulation of the T-F properties of Electromagnetic (EM) waves and it fulfills the stringent requirements for many modern and emerging applications.

5.2 Future Prospects

5.2.1 Noise Mitigation of Time-varying Signals

One potential application of the proposed time-frequency processing is to mitigate noise in time-varying signals. In practical applications, optical signals are usually mixed with various types of noise, including out-of-band noise, in-band noise, and interference from other signals. To address the latter two distortions and increase the signal to noise ratio (SNR), a time-varying filter is essential [60], [230], [231]. One possible scenario is illustrated in Fig. 5.1 (a). The incoming chirped microwave signal contains significant background noise, making it difficult to identify the frequency components of the signal. In the proposed scheme, the spectrogram of the degraded chirped signal is first mapped along the time domain using the TAI-based signal processing approach. To mitigate the noise and improve the SNR, an intensity modulator driven by a temporal filtering profile is utilized to filter out the target frequency components. Afterwards, the filtered signal is recovered by a reverse dispersive unit. As such, signal to noise ratio could be significantly improved after the recovery of the signal.

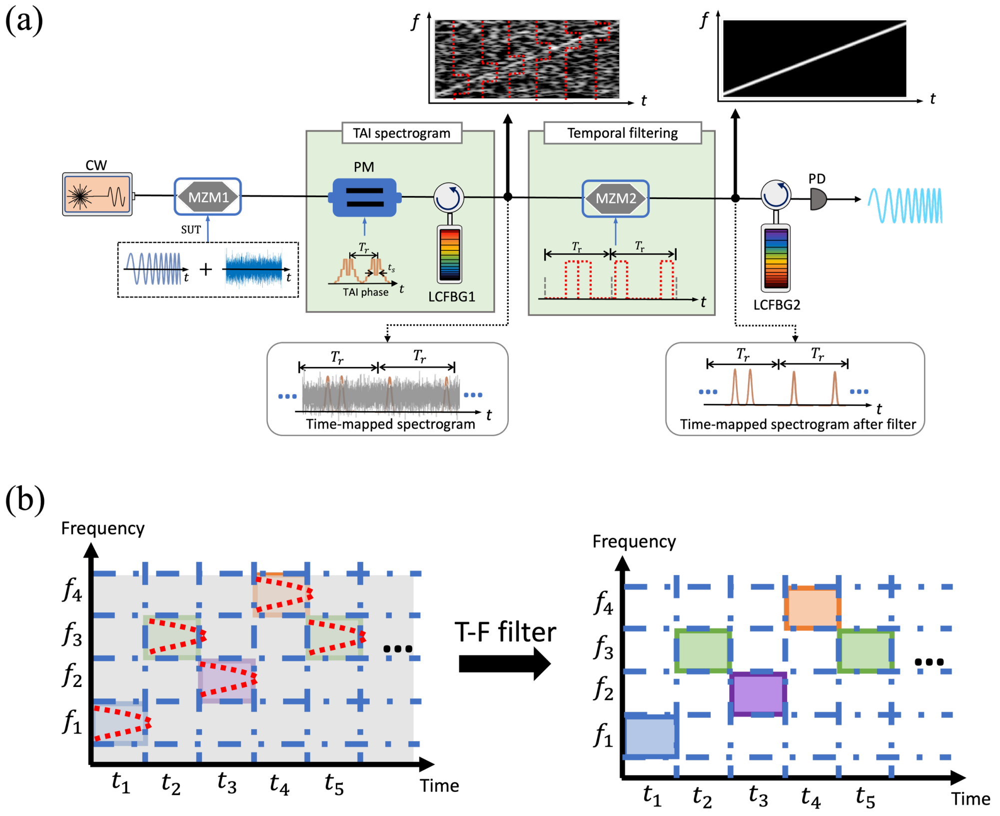

Figure 5.1. Noise mitigation based on the time-frequency filter. (a) Schematic of background noise of the input microwave signal. (b) Schematic of filtering noise of frequency hopping.

Another crucial application of the time-frequency filter is to improve the SNR of frequency hopping systems. In a frequency hopping system, different frequency channels are assigned for different users at different time, increasing the overall communication capacity of emerging wireless systems [81]. Frequency hopping communication systems have been widely used to enhance information security in data transmission, satellite communications, and radar systems, etc [81], [232], [233]. Emerging next-generation communication systems require a higher hopping speed within nanoseconds and wider hopping frequency bandwidth wider than tens of gigahertz. Therefore, a time-varying filter with a rapid tuning speed and wide operation bandwidth is highly demanded. Our proposed time-varying filter has a potential to further improve the SNR in high-speed frequency hopping systems. A more detailed conceptual illustration is shown in Fig. 5.1 (b). Frequency channels from f_1 to f_4 are allocated to one user within a given time window (e.g., f_1 at t_1, and f_3 at t_2). In practice, the received signal is mixed with in-band noise. To increase the SNR, the time-varying filter can be designed to filter out the specific frequency channels within the given time window, thus improving the SNR for the post processing.

5.2.2 Time-varying Filter for Phase-encoded Signal

In the aforementioned time-varying filter, only a reverse GVD unit is utilized to compensate the phase distortion induced by the first GVD unit during the stage of the time-mapped spectrogram. However, the TL phase profile still remains in the processed optical signal, which is converted into electrical domain after the detection. As such, the proposed scheme can only process the amplitude-encoded microwave signals. To extend the capability of the proposed time-frequency manipulation to complex signals (i.e., signals with both amplitude and phase information), an additional TL is needed in the recovery process. The schematic of this enhanced approach is shown in Fig. 5.2. The time-mapped spectrogram of the incoming optical signal is first achieved through a time lens and a GVD unit. Afterwards, an intensity modulator/phase

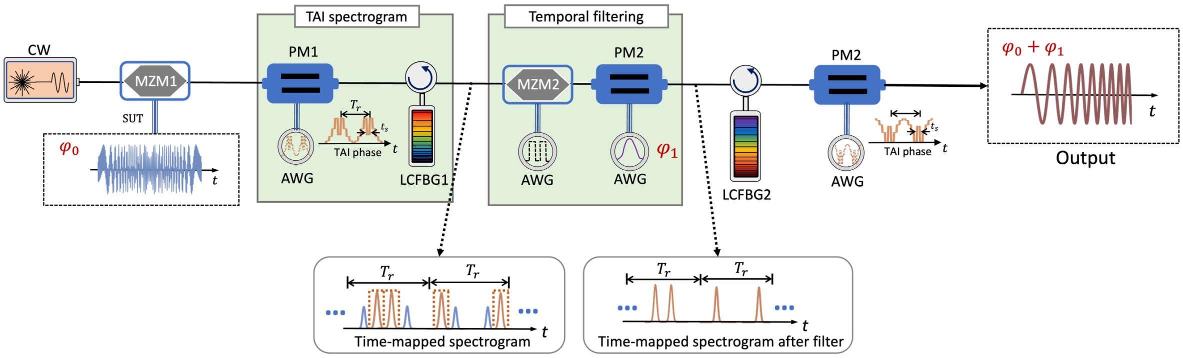

Figure 5.2. Time-frequency filtering of complex signal. Schematic of manipulating amplitude and phase of the SUT.

modulator is employed to perform the temporal filtering, which can mitigate the intensity and/or manipulate the phase information of specific frequency components. Finally, the filtered optical signal is recovered by implementing a reverse GVD unit and a PM. Note that the second PM is utilized to compensate the phase profile induced by the time lens in the time-mapped spectrogram stage. Compared to the initial time-varying filtering scheme, this advance configuration can manipulate both the intensity and phase information of the incoming time-varying signal at the will, providing greater flexibility and functionality.

5.2.3 Toward the Analysis and Processing of Ultrafast Optical Signal

The practical implementation of the temporal phase modulation (TPM) process faces significant technological limitations. Typically, multilevel TPM is achieved using an PM driven by an electronic arbitrary waveform generator to create the required phase profile, as described in Chapter 3. However, the sophisticated phase patterns required often demand bandwidths that exceed the capabilities of current state-of-the-art digital-to-analog converters.

To overcome this challenge, nonlinear optical processes, such as those used in TL systems, can be employed. For instance, ultrafast TLs have been implemented using cross-phase modulation (XPM) and four-wave mixing (FWM) [234].These techniques involve coupling the signal of interest with a carefully designed pump derived from a periodic short-pulse optical source. Recently, it has been demonstrated that nonlinear XPM and FWM in optical fibers can be utilized to achieve an ultrafast implementation of TPM, surpassing the speeds of electro-optic approaches by orders of magnitude. An XPM-based discrete-multilevel TPM was first demonstrated through a tailored pulse-shaping process, where a pump with an intensity profile matching the required TPM is created [235]. This design, which restricts the phase to below 2π, requires significantly less power than a traditional XPM-based parabolic TL [235] . Alternatively, ultrafast TPM can be achieved using FWM [236]. In this method, the pump is generated by increasing the repetition rate of a short-pulse train by the analysis point of q as it propagates through a GVD medium that satisfies a fractional self-imaging condition. This creates a pump with a discrete multilevel phase profile proportional to the desired TPM, which is then transferred to the idler through the FWM process. This approach has been applied in temporal TAI [235], [237]. As such, it can be anticipated that the optical time-varying filter could process ultrafast optical signal by replacing the conventional PM based TLs with the nonlinear effects-bases TLs.

6 BIBLIOGRAPHIE

[1] J. Capmany, B. Ortega, and D. Pastor, “A tutorial on microwave photonic filters,” *J. Light. Technol.*, vol. 24, no. 1, pp. 201–229, Jan. 2006, doi: 10.1109/JLT.2005.860478.

[2] S. V. Vaseghi, *Advanced Digital Signal Processing and Noise Reduction*. John Wiley & Sons, 2008.

[3] A. M. Weiner, “Ultrafast optical pulse shaping: A tutorial review,” *Opt. Commun.*, vol. 284, no. 15, pp. 3669–3692, Jul. 2011, doi: 10.1016/j.optcom.2011.03.084.

[4] L. Tan and J. Jiang, *Digital Signal Processing: Fundamentals and Applications*. Academic Press, 2018.

[5] Shilong Pan and Y. Zhang, “Microwave Photonic Radars,” *J. Lightwave Technol.*, vol. 38, no. 19, pp. 5450–5484, Oct. 2020.

[6] L. Tan and J. Jiang, *Digital Signal Processing: Fundamentals and Applications*. Academic Press, 2018.

[7] A. Papandreou-Suppappola, *Applications in Time-Frequency Signal Processing*. CRC Press, 2018.

[8] “Terahertz modulation of the Faraday rotation by laser pulses via the optical Kerr effect | Nature Photonics.” Accessed: Jun. 17, 2024. [Online]. Available: https://www.nature.com/articles/nphoton.2015.249

[9] A. P. Goutzoulis, *Design and Fabrication of Acousto-Optic Devices*. CRC Press, 2021.

[10] P. J. Winzer and R.-J. Essiambre, “Advanced optical modulation formats,” in *Optical Fiber Telecommunications V B (Fifth Edition)*, in Optics and Photonics. , Burlington: Academic Press, 2008, pp. 23–93. doi: 10.1016/B978-0-12-374172-1.00002-3.

[11] G. P. Agrawal, *Fiber-Optic Communication Systems*. John Wiley & Sons, 2012.

[12] R. Hui and M. O’Sullivan, *Fiber-Optic Measurement Techniques*. Academic Press, 2022.

[13] Y. Shen, R. Bootsman, M. S. Alavi, and L. C. N. de Vreede, “A Wideband IQ-Mapping Direct-Digital RF Modulator for 5G Transmitters,” *IEEE J. Solid-State Circuits*, vol. 57, no. 5, pp. 1446–1456, May 2022, doi: 10.1109/JSSC.2022.3144362.

[14] C. Wang *et al.*, “Integrated lithium niobate electro-optic modulators operating at CMOS-compatible voltages,” *Nature*, vol. 562, no. 7725, Art. no. 7725, Oct. 2018, doi: 10.1038/s41586-018-0551-y.

[15] A. Chen and E. Murphy, *Broadband Optical Modulators: Science, Technology, and Applications*. CRC Press, 2011.

[16] S. Kumar and M. J. Deen, *Fiber Optic Communications: Fundamentals and Applications*. John Wiley & Sons, 2014.

[17] H. M. El-Hageen, P. G. Kuppusamy, A. M. Alatwi, M. Sivaram, Z. A. Yasar, and A. N. Z. Rashed, “Different modulation schemes for direct and external modulators based on various laser sources,” *Journal of Optical Communications*, vol. 44, no. s1, pp. s697–s706, Dec. 2023, doi: 10.1515/joc-2020-0029.

[18] “Multi-function Mach-Zehnder modulator for pulse shaping and generation.” Accessed: Mar. 19, 2024. [Online]. Available: https://opg.optica.org/oe/fulltext.cfm?uri=oe-24-19-22239&id=350120

[19] M. Plewicki, F. Weise, S. M. Weber, and A. Lindinger, “Phase, amplitude, and polarization shaping with a pulse shaper in a Mach-Zehnder interferometer,” *Appl. Opt., AO*, vol. 45, no. 32, pp. 8354–8359, Nov. 2006, doi: 10.1364/AO.45.008354.

[20] P. Ghelfi, F. Scotti, F. Laghezza, and A. Bogoni, “Photonic Generation of Phase-Modulated RF Signals for Pulse Compression Techniques in Coherent Radars,” *J. Lightwave Technol.*, vol. 30, no. 11, pp. 1638–1644, Jun. 2012, doi: 10.1109/JLT.2012.2187879.

[21] I. Morohashi, T. Sakamoto, N. Sekine, A. Kasamatsu, and I. Hosako, “Ultrashort optical pulse source using Mach–Zehnder-modulator-based flat comb generator,” *Nano Communication Networks*, vol. 10, pp. 79–84, Dec. 2016, doi: 10.1016/j.nancom.2016.07.012.

[22] G. P. Agrawal, *Fiber-Optic Communication Systems*. John Wiley & Sons, 2012.

[23] L.-S. Yan, Q. Yu, T. Luo, A. E. Willner, and X. S. Yao, “Compensation of higher order polarization-mode dispersion using phase modulation and polarization control in the transmitter,” *IEEE Photon. Technol. Lett.*, vol. 14, no. 6, pp. 858–860, Jun. 2002, doi: 10.1109/LPT.2002.1003117.

[24] Zhiyu Chen, Lianshan Yan, Hengyun Jiang, Wei Pan, Bin Luo, and Xihua Zou, “Dispersion Compensation in Analog Photonic Link Utilizing a Phase Modulator,” *J. Lightwave Technol.*, vol. 32, no. 23, pp. 4642–4647, Dec. 2014, doi: 10.1109/JLT.2014.2362916.

[25] “Third-order dispersion compensation using a phase modulator | IEEE Journals & Magazine | IEEE Xplore.” Accessed: Mar. 19, 2024. [Online]. Available: https://ieeexplore.ieee.org/abstract/document/1213575

[26] J. Azaña, N. K. Berger, B. Levit, and B. Fischer, “Broadband Arbitrary Waveform Generation Based on Microwave Frequency Upshifting in Optical Fibers,” *J. Lightwave Technol., JLT*, vol. 24, no. 7, p. 2663, Jul. 2006.

[27] H. Chi and J. Yao, “Symmetrical waveform generation based on temporal pulse shaping using amplitude-only modulator,” *Electronics Letters*, vol. 43, no. 7, pp. 415–417, Mar. 2007, doi: 10.1049/el:20073808.

[28] M. Li, J. Azaña, N. Zhu, and J. Yao, “Recent progresses on optical arbitrary waveform generation,” *Front. Optoelectron.*, vol. 7, no. 3, pp. 359–375, Sep. 2014, doi: 10.1007/s12200-014-0470-y.

[29] G. Sinatkas, T. Christopoulos, O. Tsilipakos, and E. E. Kriezis, “Electro-optic modulation in integrated photonics,” *Journal of Applied Physics*, vol. 130, no. 1, p. 010901, Jul. 2021, doi: 10.1063/5.0048712.

[30] H. Sepehrian, J. Lin, L. A. Rusch, and W. Shi, “Silicon Photonic IQ Modulators for 400 Gb/s and Beyond,” *J. Lightwave Technol., JLT*, vol. 37, no. 13, pp. 3078–3086, Jul. 2019.

[31] Y. Ogiso *et al.*, “Over 67 GHz Bandwidth and 1.5 V Vπ InP-Based Optical IQ Modulator With n-i-p-n Heterostructure,” *J. Lightwave Technol., JLT*, vol. 35, no. 8, pp. 1450–1455, Apr. 2017.

[32] *Handbook of optics. 2: Devices, measurements, and properties*, 2. ed. New York: McGraw-Hill, 1995.

[33] X. Li, C. Yang, Q. Ye, Y. Chong, and Z. Zhou, “A simple method for measuring the RF halfwave voltage of phase modulators,” in *2013 5th IEEE International Symposium on Microwave, Antenna, Propagation and EMC Technologies for Wireless Communications*, Oct. 2013, pp. 343–346. doi: 10.1109/MAPE.2013.6689817.

[34] F. Arab Juneghani *et al.*, “Thin-Film Lithium Niobate Optical Modulators with an Extrapolated Bandwidth of 170 GHz,” *Advanced Photonics Research*, vol. 4, no. 1, p. 2200216, 2023, doi: 10.1002/adpr.202200216.

[35] F. Valdez, V. Mere, X. Wang, and S. Mookherjea, “Integrated O- and C-band silicon-lithium niobate Mach-Zehnder modulators with 100 GHz bandwidth, low voltage, and low loss,” *Opt. Express*, vol. 31, no. 4, p. 5273, Feb. 2023, doi: 10.1364/OE.480519.

[36] C. Wang, M. Zhang, B. Stern, M. Lipson, and M. Lončar, “Nanophotonic lithium niobate electro-optic modulators,” *Opt. Express, OE*, vol. 26, no. 2, pp. 1547–1555, Jan. 2018, doi: 10.1364/OE.26.001547.

[37] M. Thomaschewski, V. A. Zenin, S. Fiedler, C. Wolff, and S. I. Bozhevolnyi, “Plasmonic Lithium Niobate Mach–Zehnder Modulators,” *Nano Lett.*, vol. 22, no. 16, pp. 6471–6475, Aug. 2022, doi: 10.1021/acs.nanolett.2c00714.

[38] A. V. Oppenheim, A. S. Willsky, and S. H. Nawab, *Signals & systems (2nd ed.)*. USA: Prentice-Hall, Inc., 1996.

[39] F. Jin and S. Cao, “Automotive Radar Interference Mitigation Using Adaptive Noise Canceller,” *IEEE Trans. Veh. Technol.*, vol. 68, no. 4, pp. 3747–3754, Apr. 2019, doi: 10.1109/TVT.2019.2901493.

[40] M. Vaezi, Z. Ding, and H. V. Poor, *Multiple Access Techniques for 5G Wireless Networks and Beyond*. Cham: Springer International Publishing, 2019. doi: 10.1007/978-3-319-92090-0.

[41] S. Ranathive, K. V. Kumar, A. N. Z. Rashed, M. S. F. Tabbour, and T. V. P. Sundararajan, “Performance Signature of Optical Fiber Communications Dispersion Compensation Techniques for the Control of Dispersion Management,” *J. Opt. Commun.*, vol. 43, no. 4, pp. 611–623, Oct. 2022, doi: 10.1515/joc-2019-0021.

[42] R. J. Cameron, C. M. Kudsia, and R. R. Mansour, *Microwave Filters for Communication Systems: Fundamentals, Design, and Applications*. John Wiley & Sons, 2018.

[43] “Alan V. Oppenheim, Alan S. Willsky, with S. Hamid-Signals and Systems-Prentice Hall (1996).pdf.” Accessed: Mar. 25, 2024. [Online]. Available: https://eee.guc.edu.eg/Courses/Communications/COMM401%20Signal%20&%20System%20Theory/Alan%20V.%20Oppenheim,%20Alan%20S.%20Willsky,%20with%20S.%20Hamid-Signals%20and%20Systems-Prentice%20Hall%20(1996).pdf

[44] R. J. Cameron, C. M. Kudsia, and R. R. Mansour, *Microwave Filters for Communication Systems: Fundamentals, Design, and Applications*. John Wiley & Sons, 2018.

[45] J.-S. G. Hong and M. J. Lancaster, *Microstrip Filters for RF / Microwave Applications*. John Wiley & Sons, 2004.

[46] V. Kalyani and V. Sharma, “Different types of Optical Filters and their Realistic Application,” *Journal of Management Engineering and Information Technology*, vol. 3, Jun. 2016.

[47] A. M. Weiner, “Femtosecond pulse shaping using spatial light modulators,” *Review of Scientific Instruments*, vol. 71, no. 5, pp. 1929–1960, May 2000, doi: 10.1063/1.1150614.

[48] B. H. Ahmad, M. H. Mazlan, M. N. Husain, Z. Zakaria, and N. A. Shairi, “MICROSTRIP FILTER DESIGN TECHNIQUES: AN OVERVIEW,” vol. 10, no. 2, 2015.

[49] I. C. Hunter, L. Billonet, B. Jarry, and P. Guillon, “Microwave filters-applications and technology,” *IEEE Trans. Microwave Theory Techn.*, vol. 50, no. 3, pp. 794–805, Mar. 2002, doi: 10.1109/22.989963.

[50] P. Pramanick and P. Bhartia, *Modern RF and Microwave Filter Design*. Artech House, 2016.

[51] “waveshaper_family.pdf.” Accessed: Mar. 20, 2024. [Online]. Available: https://www.epsglobal.com/Media-Library/EPSGlobal/Products/files/finisar/roadm-fws-optoelectronic/waveshaper_family.pdf?ext=.pdf

[52] C. Psomas and I. Krikidis, “RC Filter Design for Wireless Power Transfer: A Fourier Series Approach,” *IEEE Signal Processing Letters*, vol. 29, pp. 597–601, 2022, doi: 10.1109/LSP.2022.3148673.

[53] K. Song, W. Chen, S. R. Patience, Y. Chen, A. M. Iman, and Y. Fan, “Compact Wide-Frequency Tunable Filter With Switchable Bandpass and Bandstop Frequency Response,” *IEEE Access*, vol. 7, pp. 47503–47508, 2019, doi: 10.1109/ACCESS.2019.2908453.

[54] M. Saint-Laurent *et al.*, “A 28 nm DSP Powered by an On-Chip LDO for High-Performance and Energy-Efficient Mobile Applications,” *IEEE J. Solid-State Circuits*, vol. 50, no. 1, pp. 81–91, Jan. 2015, doi: 10.1109/JSSC.2014.2371454.

[55] S. Hou *et al.*, “Programmable Optical Filter in Thin-Film Lithium Niobate with Simultaneous Tunability of Extinction Ratio and Wavelength,” *ACS Photonics*, vol. 10, no. 11, pp. 3896–3900, Nov. 2023, doi: 10.1021/acsphotonics.3c00574.

[56] R. Kashyap, *Fiber Bragg Gratings*. Academic Press, 2009.

[57] S. Mandal, K. Dasgupta, T. K. Basak, and S. K. Ghosh, “A generalized approach for modeling and analysis of ring-resonator performance as optical filter,” *Optics Communications*, vol. 264, no. 1, pp. 97–104, Aug. 2006, doi: 10.1016/j.optcom.2006.02.028.

[58] J. Philip, T. Jaykumar, P. Kalyanasundaram, and B. Raj, “A tunable optical filter,” *Meas. Sci. Technol.*, vol. 14, no. 8, pp. 1289–1294, Aug. 2003, doi: 10.1088/0957-0233/14/8/314.

[59] J. Capmany and D. Novak, “Microwave photonics combines two worlds,” *Nature Photon*, vol. 1, no. 6, pp. 319–330, Jun. 2007, doi: 10.1038/nphoton.2007.89.

[60] D. Ma and Y. Chen, “Time-varying microwave photonic filter for arbitrary waveform signal-to-noise ratio improvement,” *Opt. Lett.*, vol. 47, no. 9, pp. 2186–2189, May 2022, doi: 10.1364/OL.455019.

[61] D. Marpaung *et al.*, “Low-power, chip-based stimulated Brillouin scattering microwave photonic filter with ultrahigh selectivity,” *Optica*, vol. 2, no. 2, pp. 76–83, Feb. 2015, doi: 10.1364/OPTICA.2.000076.

[62] N. Shi, X. Zhu, S. Sun, W. Li, N. Zhu, and M. Li, “Fast-Switching Microwave Photonic Filter Using an Integrated Spectrum Shaper,” *IEEE Photonics Technology Letters*, vol. 31, no. 3, pp. 269–272, Feb. 2019, doi: 10.1109/LPT.2019.2892470.

[63] V. R. Supradeepa *et al.*, “Comb-based radiofrequency photonic filters with rapid tunability and high selectivity,” *Nat. Photon.*, vol. 6, no. 3, Art. no. 3, Mar. 2012, doi: 10.1038/nphoton.2011.350.

[64] L. Cohen, *Time-frequency analysis*. in Prentice Hall signal processing series. Englewood Cliffs, N.J: Prentice Hall PTR, 1995.

[65] P. Flandrin, M. Amin, S. McLaughlin, and B. Torresani, “Time-Frequency Analysis and Applications [From the Guest Editors],” *IEEE Signal Process. Mag.*, vol. 30, no. 6, pp. 19–150, Nov. 2013, doi: 10.1109/MSP.2013.2270229.

[66] B. Boashash, *Time-Frequency Signal Analysis and Processing: A Comprehensive Reference*. Academic Press, 2015.

[67] “H101397.pdf.” Accessed: Mar. 25, 2024. [Online]. Available: http://sutlib2.sut.ac.th/sut_contents/H101397.pdf

[68] S. Pan and Y. Zhang, "Microwave Photonic Radars," *J. Lightwave Technol.*, vol. 38, no. 19, pp. 5450–5484, Oct. 2020, doi: 10.1109/JLT.2020.2993166.

[69] L. Romero Cortés, D. Onori, H. Guillet De Chatellus, M. Burla, and J. Azaña, "Towards on-chip photonic-assisted radio-frequency spectral measurement and monitoring," *Optica*, vol. 7, no. 5, p. 434, May 2020, doi: 10.1364/OPTICA.383247.

[70] Hongjian Sun, A. Nallanathan, Cheng-Xiang Wang, and Yunfei Chen, "Wideband spectrum sensing for cognitive radio networks: a survey," *IEEE Wireless Commun.*, vol. 20, no. 2, pp. 74–81, Apr. 2013, doi: 10.1109/MWC.2013.6507397.

[71] B. Boashash, *Time-Frequency Signal Analysis and Processing: A Comprehensive Reference*. Academic Press, 2015.

[72] D. Griffin and J. Lim, "Signal estimation from modified short-time Fourier transform," *IEEE Transactions on Acoustics, Speech, and Signal Processing*, vol. 32, no. 2, pp. 236–243, Apr. 1984, doi: 10.1109/TASSP.1984.1164317.

[73] J. Norgard and G. L. Best, "The Electromagnetic Spectrum," in *National Association of Broadcasters Engineering Handbook*, 11th ed., Routledge, 2017.

[74] Y. I. A. Al-Yasir, N. Ojaroudi Parchin, R. A. Abd-Alhameed, A. M. Abdulkhaleq, and J. M. Noras, "Recent Progress in the Design of 4G/5G Reconfigurable Filters," *Electronics*, vol. 8, no. 1, Art. no. 1, Jan. 2019, doi: 10.3390/electronics8010114.

[75] P. Ghelfi *et al.*, "A fully photonics-based coherent radar system," *Nature*, vol. 507, no. 7492, Art. no. 7492, Mar. 2014, doi: 10.1038/nature13078.

[76] W. A. Majid *et al.*, "A Bright Fast Radio Burst from FRB 20200120E with Sub-100 Nanosecond Structure," *ApJL*, vol. 919, no. 1, p. L6, Sep. 2021, doi: 10.3847/2041-8213/ac1921.

[77] H. Sun, A. Nallanathan, C.-X. Wang, and Y. Chen, "Wideband spectrum sensing for cognitive radio networks: a survey," *IEEE Wirel. Commun.*, vol. 20, no. 2, pp. 74–81, Apr. 2013, doi: 10.1109/MWC.2013.6507397.

[78] H. Shao *et al.*, "An Investigation of Spectral Band Selection for Hyperspectral LiDAR Technique," *Electronics*, vol. 9, no. 1, Art. no. 1, Jan. 2020, doi: 10.3390/electronics9010148.

[79] B. Wang and K. J. R. Liu, "Advances in cognitive radio networks: A survey," *IEEE J. Sel. Top. Signal Process.*, vol. 5, no. 1, pp. 5–23, Feb. 2011, doi: 10.1109/JSTSP.2010.2093210.

[80] I. de Miguel *et al.*, "Cognitive dynamic optical networks," *J. Opt. Commun. Netw.*, vol. 5, no. 10, pp. A107–A118, Oct. 2013, doi: 10.1364/JOCN.5.00A107.

[81] Q. Liu and M. P. Fok, "Ultrafast and Wideband Microwave Photonic Frequency-Hopping Systems: A Review," *Appl. Sci.*, vol. 10, no. 2, Art. no. 2, Jan. 2020, doi: 10.3390/app10020521.

[82] Y. Sun, S. Wang, J. Chen, and G. Wu, "Fast and large-range frequency hopping receiving based on simultaneous photonic filtering and digitizing," *Opt. Lett.*, vol. 46, no. 4, pp. 749–752, Feb. 2021, doi: 10.1364/OL.415003.

[83] G. Serafino *et al.*, "Toward a New Generation of Radar Systems Based on Microwave Photonic Technologies," *J. Light. Technol.*, vol. 37, no. 2, pp. 643–650, Jan. 2019, doi: 10.1109/JLT.2019.2894224.

[84] S. Pan, X. Ye, Y. Zhang, and F. Zhang, "Microwave Photonic Array Radars," *IEEE Journal of Microwaves*, vol. 1, no. 1, pp. 176–190, Jan. 2021, doi: 10.1109/JMW.2020.3034583.

[85] W. Zhang *et al.*, “A system-on-chip microwave photonic processor solves dynamic RF interference in real time with picosecond latency,” *Light Sci Appl*, vol. 13, no. 1, p. 14, Jan. 2024, doi: 10.1038/s41377-023-01362-5.

[86] S. Alland, W. Stark, M. Ali, and M. Hegde, “Interference in Automotive Radar Systems: Characteristics, Mitigation Techniques, and Current and Future Research,” *IEEE Signal Processing Magazine*, vol. 36, no. 5, pp. 45–59, Sep. 2019, doi: 10.1109/MSP.2019.2908214.

[87] M. Rameez, M. I. Pettersson, and M. Dahl, “Interference Compression and Mitigation for Automotive FMCW Radar Systems,” *IEEE Sensors Journal*, vol. 22, no. 20, pp. 19739–19749, Oct. 2022, doi: 10.1109/JSEN.2022.3204505.

[88] C. Waldschmidt, J. Hasch, and W. Menzel, “Automotive Radar — From First Efforts to Future Systems,” *IEEE Journal of Microwaves*, vol. 1, no. 1, pp. 135–148, Jan. 2021, doi: 10.1109/JMW.2020.3033616.

[89] S. R. Thummaluru, M. Ameen, and R. K. Chaudhary, “Four-Port MIMO Cognitive Radio System for Midband 5G Applications,” *IEEE Trans. Antennas Propag.*, vol. 67, no. 8, pp. 5634–5645, Aug. 2019, doi: 10.1109/TAP.2019.2918476.

[90] H.-J. Kim, D. E. Leaird, and A. M. Weiner, “Rapidly Tunable Dual-Comb RF Photonic Filter for Ultrabroadband RF Spread Spectrum Applications,” *IEEE Trans. Microw. Theory Tech.*, vol. 64, no. 10, pp. 3351–3362, Oct. 2016, doi: 10.1109/TMTT.2016.2599162.

[91] L. Huang, R. Li, S. Liu, P. Dai, and X. Chen, “Centralized Fiber-Distributed Data Communication and Sensing Convergence System Based on Microwave Photonics,” *Journal of Lightwave Technology*, vol. 37, no. 21, pp. 5406–5416, Nov. 2019, doi: 10.1109/JLT.2019.2935903.

[92] E. H. W. Chan and R. A. Minasian, “High-Resolution Tunable RF/Microwave Photonic Notch Filter With Low-Noise Performance,” *J. Light. Technol.*, vol. 29, no. 21, pp. 3304–3309, Nov. 2011, doi: 10.1109/JLT.2011.2167957.

[93] “6G: The Next Horizon,” *https://www-file.huawei.com/-/media/corp2020/pdf/tech-insights/1/6g-white-paper-en.pdf?la=en*.

[94] F. Khan and M. I. Younis, “RF MEMS electrostatically actuated tunable capacitors and their applications: a review,” *J. Micromech. Microeng.*, vol. 32, no. 1, p. 013002, Dec. 2021, doi: 10.1088/1361-6439/ac3cd5.

[95] P. S. R. Diniz, E. A. B. da Silva, and S. L. Netto, *Digital Signal Processing: System Analysis and Design*. Cambridge University Press, 2010.

[96] M. Portnoff, “Implementation of the digital phase vocoder using the fast Fourier transform,” *IEEE Trans. Acoust., Speech, Signal Process.*, vol. 24, no. 3, pp. 243–248, Jun. 1976, doi: 10.1109/TASSP.1976.1162810.

[97] X. Yang, M. Kawamata, and T. Higuchi, “Approximations of IIR periodically time-varying digital filters,” *IEE Proceedings - Circuits, Devices and Systems*, vol. 142, no. 6, pp. 387–393, Dec. 1995.

[98] M. Soudan and C. Vogel, “On the correction of linear time-varying systems by means of time-varying FIR filters,” in *2011 IEEE 54th International Midwest Symposium on Circuits and Systems (MWSCAS)*, Seoul, Korea (South): IEEE, Aug. 2011, pp. 1–4. doi: 10.1109/MWSCAS.2011.6026377.

[99] J. L. H. Webb, "Transposed FIR filter structure with time-varying coefficients for digital data resampling," *IEEE Trans. Signal Process.*, vol. 48, no. 9, pp. 2594–2600, Sep. 2000, doi: 10.1109/78.863063.

[100] T. Rohlev and C. Loeffler, "Invertible periodically time-varying digital filters," in *ICASSP '87. IEEE International Conference on Acoustics, Speech, and Signal Processing*, Dallas, TX, USA: Institute of Electrical and Electronics Engineers, 1987, pp. 2380–2383. doi: 10.1109/ICASSP.1987.1169919.

[101] P. Okoniewski and J. Piskorowski, "Stability analysis of linear time-varying IIR filter with equalized group delay characteristic," in *2013 18th International Conference on Methods & Models in Automation & Robotics (MMAR)*, Miedzyzdroje: IEEE, Aug. 2013, pp. 46–50. doi: 10.1109/MMAR.2013.6669879.

[102] M. Cherniakov, *An Introduction to Parametric Digital Filters and Oscillators*. John Wiley & Sons, 2003.

[103] Y. Salathé *et al.*, "Low-Latency Digital Signal Processing for Feedback and Feedforward in Quantum Computing and Communication," *Phys. Rev. Applied*, vol. 9, no. 3, p. 034011, Mar. 2018, doi: 10.1103/PhysRevApplied.9.034011.

[104] B. A. Shenoi, *Introduction to Digital Signal Processing and Filter Design*. John Wiley & Sons, 2005.

[105] I. Verbauwhede, P. Schaumont, C. Piguet, and B. Kienhuis, "Architectures and design techniques for energy efficient embedded DSP and multimedia processing," in *Automation and Test in Europe Conference and Exhibition Proceedings Design*, Feb. 2004, pp. 988-993 Vol.2. doi: 10.1109/DATE.2004.1269022.

[106] J.-H. Hwang, M.-Y. Lee, C.-Y. Jeong, and C. Yoo, "Active-RC channel selection filter tunable from 6 kHz to 18 MHz for software-defined radio," in *2005 IEEE International Symposium on Circuits and Systems (ISCAS)*, May 2005, pp. 4803-4806 Vol. 5. doi: 10.1109/ISCAS.2005.1465707.

[107] H. Islam, S. Das, T. Bose, and T. Ali, "Diode Based Reconfigurable Microwave Filters for Cognitive Radio Applications: A Review," *IEEE Access*, vol. 8, pp. 185429–185444, 2020, doi: 10.1109/ACCESS.2020.3030020.

[108] R. A. Minasian, "Photonic signal processing of microwave signals," *IEEE Trans. Microwave Theory Techn.*, vol. 54, no. 2, pp. 832–846, Feb. 2006, doi: 10.1109/TMTT.2005.863060.

[109] D. Marpaung, C. Roeloffzen, R. Heideman, A. Leinse, S. Sales, and J. Capmany, "Integrated microwave photonics," *Laser & Photonics Reviews*, vol. 7, no. 4, pp. 506–538, 2013, doi: 10.1002/lpor.201200032.

[110] J. Capmany, J. Mora, I. Gasulla, J. Sancho, J. Lloret, and S. Sales, "Microwave Photonic Signal Processing," *J. Lightwave Technol.*, vol. 31, no. 4, pp. 571–586, Feb. 2013, doi: 10.1109/JLT.2012.2222348.

[111] J. Yao, "Microwave Photonics," *J. Lightwave Technol.*, vol. 27, no. 3, pp. 314–335, Feb. 2009, doi: 10.1109/JLT.2008.2009551.

[112] X. Xie, J. Li, F. Yin, K. Xu, and Y. Dai, "STFT Based on Bandwidth-Scaled Microwave Photonics," *J. Lightwave Technol., JLT*, vol. 39, no. 6, pp. 1680–1687, Mar. 2021.

[113] P. Zuo, D. Ma, and Y. Chen, "Short-Time Fourier Transform Based on Stimulated Brillouin Scattering," *J. Lightwave Technol.*, vol. 40, no. 15, pp. 5052–5061, Aug. 2022, doi: 10.1109/JLT.2022.3174552.

[114] “Real-time gap-free dynamic waveform spectral analysis with nanosecond resolutions through analog signal processing | Nature Communications.” Accessed: Mar. 25, 2024. [Online]. Available: https://www.nature.com/articles/s41467-020-17119-2

[115] S. R. Konatham, H. G. de Chatellus, and J. Azaña, “Photonics-Based Real-Time Spectrogram Analysis of Broadband Waveforms,” *J. Lightwave Technol., JLT*, vol. 38, no. 19, pp. 5356–5367, Oct. 2020.

[116] J. Azaña and X. Zhu, “Optical Time-Mapped Spectrograms (I): From the Time-Lens Fourier Transformer to the Talbot-Based Design,” *J. Lightwave Technol.*, vol. 41, no. 14, pp. 4609–4623, Jul. 2023, doi: 10.1109/JLT.2023.3243531.

[117] “All-Optical Short-Time Fourier Transform Based on a Temporal Pulse-Shaping System Incorporating an Array of Cascaded Linearly Chirped Fiber Bragg Gratings.” Accessed: Jun. 20, 2024. [Online]. Available: https://ieeexplore.ieee.org/abstract/document/5959187?casa_token=0UsTbRGcwl0AAAAA:3sTVlgsEtejiEqY2cRqulrJYi8il5tnHfzBdZU8r_0IE2jea8mwOKR1NKBF4nsHA6LU4GIo_TQ

[118] A. Nuruzzaman, O. Boyraz, and B. Jalali, “Time-stretched short-time Fourier transform,” *IEEE Transactions on Instrumentation and Measurement*, vol. 55, no. 2, pp. 598–602, Apr. 2006, doi: 10.1109/TIM.2006.864246.

[119] P. Zuo, D. Ma, and Y. Chen, “Short-Time Fourier Transform Based on Stimulated Brillouin Scattering,” *Journal of Lightwave Technology*, vol. 40, no. 15, pp. 5052–5061, Aug. 2022, doi: 10.1109/JLT.2022.3174552.

[120] J. Li *et al.*, “Low-Latency Short-Time Fourier Transform of Microwave Photonics Processing,” *Journal of Lightwave Technology*, vol. 41, no. 19, pp. 6149–6156, Oct. 2023, doi: 10.1109/JLT.2023.3279261.

[121] R. E. Saperstein, D. Panasenko, and Y. Fainman, “Demonstration of a microwave spectrum analyzer based on time-domain optical processing in fiber,” *Opt. Lett., OL*, vol. 29, no. 5, pp. 501–503, Mar. 2004, doi: 10.1364/OL.29.000501.

[122] A. M. Weiner, *Ultrafast Optics*. John Wiley & Sons, 2011.

[123] S. Thomas, A. Malacarne, F. Fresi, L. Potì, and J. Azaña, “Fiber-Based Programmable Picosecond Optical Pulse Shaper,” *J. Lightwave Technol., JLT*, vol. 28, no. 12, pp. 1832–1843, Jun. 2010.

[124] S. Thomas, A. Malacarne, F. Fresi, L. Potì, A. Bogoni, and J. Azaña, “Programmable fiber-based picosecond optical pulse shaper using time-domain binary phase-only linear filtering,” *Opt. Lett., OL*, vol. 34, no. 4, pp. 545–547, Feb. 2009, doi: 10.1364/OL.34.000545.

[125] J. Azana and M. A. Muriel, “Temporal self-imaging effects: theory and application for multiplying pulse repetition rates,” *IEEE J. Select. Topics Quantum Electron.*, vol. 7, no. 4, pp. 728–744, Sep. 2001, doi: 10.1109/2944.974245.

[126] “Alan V. Oppenheim, Alan S. Willsky, with S. Hamid-Signals and Systems-Prentice Hall (1996).pdf.” Accessed: Mar. 25, 2024. [Online]. Available: https://eee.guc.edu.eg/Courses/Communications/COMM401%20Signal%20&%20System%20Theory/Alan%20V.%20Oppenheim,%20Alan%20S.%20Willsky,%20with%20S.%20Hamid-Signals%20and%20Systems-Prentice%20Hall%20(1996).pdf

[127] J. Philip, T. Jaykumar, P. Kalyanasundaram, and B. Raj, “A tunable optical filter,” *Meas. Sci. Technol.*, vol. 14, no. 8, pp. 1289–1294, Aug. 2003, doi: 10.1088/0957-0233/14/8/314.

[128] "Multipurpose silicon photonics signal processor core | Nature Communications." Accessed: Jun. 19, 2024. [Online]. Available: https://www.nature.com/articles/s41467-017-00714-1

[129] "Programmable wavelength filter with double ring loaded MZI | Scientific Reports." Accessed: Jun. 19, 2024. [Online]. Available: https://www.nature.com/articles/s41598-021-04598-6

[130] A. M. Weiner, "Femtosecond pulse shaping using spatial light modulators," *Review of Scientific Instruments*, vol. 71, no. 5, pp. 1929–1960, May 2000, doi: 10.1063/1.1150614.

[131] J. Yao, "Photonics to the Rescue: A Fresh Look at Microwave Photonic Filters," *IEEE Microwave*, vol. 16, no. 8, pp. 46–60, Sep. 2015, doi: 10.1109/MMM.2015.2441594.

[132] M. Sagues, R. García Olcina, A. Loayssa, S. Sales, and J. Capmany, "Multi-tap complex-coefficient incoherent microwave photonic filters based on optical single-sideband modulation and narrow band optical filtering," *Opt. Express*, vol. 16, no. 1, p. 295, 2008, doi: 10.1364/OE.16.000295.

[133] A. Ortigosa-Blanch, J. Mora, J. Capmany, B. Ortega, and D. Pastor, "Tunable radio-frequency photonic filter based on an actively mode-locked fiber laser," *Opt. Lett., OL*, vol. 31, no. 6, pp. 709–711, Mar. 2006, doi: 10.1364/OL.31.000709.

[134] X. Xue *et al.*, "Programmable Single-Bandpass Photonic RF Filter Based on Kerr Comb from a Microring," *J. Lightwave Technol.*, vol. 32, no. 20, pp. 3557–3565, Oct. 2014, doi: 10.1109/JLT.2014.2312359.

[135] J. Sancho *et al.*, "Integrable microwave filter based on a photonic crystal delay line," *Nat Commun*, vol. 3, no. 1, p. 1075, Sep. 2012, doi: 10.1038/ncomms2092.

[136] M. Song, C. M. Long, R. Wu, D. Seo, D. E. Leaird, and A. M. Weiner, "Reconfigurable and Tunable Flat-Top Microwave Photonic Filters Utilizing Optical Frequency Combs," *IEEE Photon. Technol. Lett.*, vol. 23, no. 21, pp. 1618–1620, Nov. 2011, doi: 10.1109/LPT.2011.2165209.

[137] W. Li, M. Li, and J. Yao, "A Narrow-Passband and Frequency-Tunable Microwave Photonic Filter Based on Phase-Modulation to Intensity-Modulation Conversion Using a Phase-Shifted Fiber Bragg Grating," *IEEE Trans. Microwave Theory Techn.*, vol. 60, no. 5, pp. 1287–1296, May 2012, doi: 10.1109/TMTT.2012.2187678.

[138] H. Sun *et al.*, "Reconfigurable microwave photonic filter based on a quantum dash mode-locked laser," *Opt. Lett., OL*, vol. 47, no. 5, pp. 1133–1136, Mar. 2022, doi: 10.1364/OL.451185.

[139] X. Zhu, F. Chen, H. Peng, and Z. Chen, "Novel programmable microwave photonic filter with arbitrary filtering shape and linear phase," *Opt. Express*, vol. 25, no. 8, p. 9232, Apr. 2017, doi: 10.1364/OE.25.009232.

[140] C. Wang, "Dispersive Fourier Transformation for Versatile Microwave Photonics Applications," *Photonics*, vol. 1, no. 4, Art. no. 4, Dec. 2014, doi: 10.3390/photonics1040586.

[141] J. Ge and M. P. Fok, "Optically Controlled Fast Reconfigurable Microwave Photonic Dual-Band Filter Based on Nonlinear Polarization Rotation," *IEEE Trans. Microwave Theory Techn.*, vol. 65, no. 1, pp. 253–259, Jan. 2017, doi: 10.1109/TMTT.2016.2614295.

[142] J. Ge and M. P. Fok, "Passband switchable microwave photonic multiband filter," *Sci Rep*, vol. 5, no. 1, p. 15882, Nov. 2015, doi: 10.1038/srep15882.

[143] "Continuously tunable and reconfigurable microwave photonic multiband filter based on cascaded MZIs | IEEE Conference Publication | IEEE Xplore." Accessed: Mar. 23, 2024. [Online]. Available: https://ieeexplore.ieee.org/abstract/document/8116149

[144] J. S. Fandiño, P. Muñoz, D. Doménech, and J. Capmany, "A monolithic integrated photonic microwave filter," *Nature Photon*, vol. 11, no. 2, pp. 124–129, Feb. 2017, doi: 10.1038/nphoton.2016.233.

[145] S. Fu *et al.*, "SOA Nonlinear Polarization Rotation With Linear Polarization Maintenance: Characterization and Applications," *IEEE J. Select. Topics Quantum Electron.*, vol. 14, no. 3, pp. 816–825, 2008, doi: 10.1109/JSTQE.2008.919281.

[146] J. Ge and M. P. Fok, "Ultra High-Speed Radio Frequency Switch Based on Photonics," *Sci. Rep.*, vol. 5, no. 1, Art. no. 1, Nov. 2015, doi: 10.1038/srep17263.

[147] J. Ge, D. A. Garon, Q. Liu, and M. P. Fok, "Reconfigurable microwave photonic spectral shaper," in *2019 Optical Fiber Communication Conference (OFC)*, Optica Publishing Group, Mar. 2019, p. W2A.36. doi: 10.1364/OFC.2019.W2A.36.

[148] O. Daulay *et al.*, "Programmable Integrated Microwave Photonic Filter using a Modulation Transformer and a Double-Injection Ring Resonator," in *2021 European Conference on Optical Communication (ECOC)*, Sep. 2021, pp. 1–4. doi: 10.1109/ECOC52684.2021.9605964.

[149] C. Porzi, M. Reza, P. Ghelfi, M. Sorel, and A. Bogoni, "Silicon-on-Insulator Microwave Photonic Filter With Widely Tunable and Reconfigurable Flat-Top Bandpass Functionality," *J. Lightwave Technol.*, vol. 40, no. 20, pp. 6666–6675, Oct. 2022.

[150] G. Han, S. Li, X. Xue, and X. Zheng, "Photonic time-frequency filter based on the software-defined time-frequency prism," *Opt. Lett.*, vol. 47, no. 14, pp. 3576–3579, Jul. 2022, doi: 10.1364/OL.457157.

[151] G. P. Agrawal, *Applications of Nonlinear Fiber Optics*. Academic Press, 2008.

[152] P. Ciąćka, A. Rampur, A. Heidt, T. Feurer, and M. Klimczak, "Dispersion measurement of ultra-high numerical aperture fibers covering thulium, holmium, and erbium emission wavelengths," *J. Opt. Soc. Am. B*, vol. 35, no. 6, p. 1301, Jun. 2018, doi: 10.1364/JOSAB.35.001301.

[153] L. Chang, S. Liu, and J. E. Bowers, "Integrated optical frequency comb technologies," *Nat. Photon.*, vol. 16, no. 2, pp. 95–108, Feb. 2022, doi: 10.1038/s41566-021-00945-1.

[154] A. F. Sayed, F. M. Mustafa, A. A. M. Khalaf, and M. H. Aly, "Spectral width reduction using apodized cascaded fiber Bragg grating for post-dispersion compensation in WDM optical networks," *Photon Netw Commun*, vol. 41, no. 3, pp. 231–241, Jun. 2021, doi: 10.1007/s11107-021-00926-y.

[155] M. Aliee, M. H. Mozaffari, and H. Saghaei, "Dispersion-flattened photonic quasicrystal optofluidic fiber for telecom C band operation," *Photonics and Nanostructures - Fundamentals and Applications*, vol. 40, p. 100797, Jul. 2020, doi: 10.1016/j.photonics.2020.100797.

[156] M. Karpiński, M. Jachura, L. J. Wright, and B. J. Smith, "Bandwidth manipulation of quantum light by an electro-optic time lens," *Nature Photon*, vol. 11, no. 1, pp. 53–57, Jan. 2017, doi: 10.1038/nphoton.2016.228.

[157] M. Martyanov, I. Mukhin, I. Kuzmin, and S. Mironov, “Compact pulse shaper based on a tilted volume Bragg grating,” *Opt. Lett., OL*, vol. 47, no. 3, pp. 557–560, Feb. 2022, doi: 10.1364/OL.448275.

[158] C. Schnébelin and H. G. de Chatellus, “Spectral interpretation of Talbot self-healing effect and application to optical arbitrary waveform generation,” *Opt. Lett., OL*, vol. 43, no. 7, pp. 1467–1470, Apr. 2018, doi: 10.1364/OL.43.001467.

[159] M. Narimousa, M. Sabaeian, S. M. M. Ghahfarrokhi, and O. Panahi, “Second-order interferometric autocorrelation for measuring group velocity dispersion and pulse broadening of femtosecond pulses,” *Appl. Opt., AO*, vol. 57, no. 18, pp. 5011–5018, Jun. 2018, doi: 10.1364/AO.57.005011.

[160] T. Herr, M. L. Gorodetsky, and T. J. Kippenberg, “Dissipative Kerr Solitons in Optical Microresonators,” in *Nonlinear Optical Cavity Dynamics*, John Wiley & Sons, Ltd, 2016, pp. 129–162. doi: 10.1002/9783527686476.ch6.

[161] A. M. Weiner, *Ultrafast Optics*. John Wiley & Sons, 2011.

[162] E. R. Andresen, C. Finot, D. Oron, and H. Rigneault, “Spectral Analog of the Gouy Phase Shift,” *Phys. Rev. Lett.*, vol. 110, no. 14, p. 143902, Apr. 2013, doi: 10.1103/PhysRevLett.110.143902.

[163] J. Azana and M. A. Muriel, “Real-time optical spectrum analysis based on the time-space duality in chirped fiber gratings,” *IEEE J. Quantum Electron.*, vol. 36, no. 5, pp. 517–526, May 2000, doi: 10.1109/3.842092.

[164] R. Salem, M. A. Foster, and A. L. Gaeta, “Application of space–time duality to ultrahigh-speed optical signal processing,” *Adv. Opt. Photon., AOP*, vol. 5, no. 3, pp. 274–317, Sep. 2013, doi: 10.1364/AOP.5.000274.

[165] J. Azana and M. A. Muriel, “Real-time optical spectrum analysis based on the time-space duality in chirped fiber gratings,” *IEEE J. Quantum Electron.*, vol. 36, no. 5, pp. 517–526, May 2000, doi: 10.1109/3.842092.

[166] J. Azaña, N. K. Berger, B. Levit, and B. Fischer, “Spectral Fraunhofer regime: time-to-frequency conversion by the action of a single time lens on an optical pulse,” *Appl. Opt., AO*, vol. 43, no. 2, pp. 483–490, Jan. 2004, doi: 10.1364/AO.43.000483.

[167] R. Salem, M. A. Foster, and A. L. Gaeta, “Application of space–time duality to ultrahigh-speed optical signal processing,” *Adv. Opt. Photon., AOP*, vol. 5, no. 3, pp. 274–317, Sep. 2013, doi: 10.1364/AOP.5.000274.

[168] J. Huh and J. Azaña, “All-Optical Reconfigurable Signal Processing Based on Cross Phase Modulation Time Lensing,” *IEEE Photonics Technology Letters*, vol. 29, no. 10, pp. 826–829, May 2017, doi: 10.1109/LPT.2017.2687826.

[169] J. Schröder *et al.*, “Aberration-free ultra-fast optical oscilloscope using a four-wave mixing based time-lens,” *Optics Communications*, vol. 283, no. 12, pp. 2611–2614, Jun. 2010, doi: 10.1016/j.optcom.2010.02.019.

[170] J. Azaña, N. K. Berger, B. Levit, and B. Fischer, “Spectral Fraunhofer regime: time-to-frequency conversion by the action of a single time lens on an optical pulse,” *Appl. Opt., AO*, vol. 43, no. 2, pp. 483–490, Jan. 2004, doi: 10.1364/AO.43.000483.

[171] M. Yu *et al.*, “Integrated femtosecond pulse generator on thin-film lithium niobate,” *Nature*, vol. 612, no. 7939, pp. 252–258, Dec. 2022, doi: 10.1038/s41586-022-05345-1.

[172] M. A. Foster, R. Salem, D. F. Geraghty, A. C. Turner-Foster, M. Lipson, and A. L. Gaeta, "Silicon-chip-based ultrafast optical oscilloscope," *Nature*, vol. 456, no. 7218, pp. 81–84, Nov. 2008, doi: 10.1038/nature07430.

[173] B. Crockett, C. M. L. Rowe, and J. Azaña, "Capturing ultra-broadband complex-fields of arbitrary duration using a real-time spectrogram," *APL Photonics*, vol. 8, no. 6, p. 066108, Jun. 2023, doi: 10.1063/5.0145961.

[174] B. H. Kolner and M. Nazarathy, "Temporal imaging with a time lens," *Opt. Lett., OL*, vol. 14, no. 12, pp. 630–632, Jun. 1989, doi: 10.1364/OL.14.000630.

[175] K. D. Rao, *Signals and Systems*. Cham: Springer International Publishing, 2018. doi: 10.1007/978-3-319-68675-2.

[176] X. Zhu, L. R. Cortés, and J. Azaña, "Group-velocity dispersion emulator using a time lens," *Opt. Lett., OL*, vol. 46, no. 23, pp. 5974–5977, Dec. 2021, doi: 10.1364/OL.444211.

[177] J. Azana, N. K. Berger, B. Levit, and B. Fischer, "Spectro-Temporal Imaging of Optical Pulses With a Single Time Lens," *IEEE Photon. Technol. Lett.*, vol. 16, no. 3, pp. 882–884, Mar. 2004, doi: 10.1109/LPT.2004.823702.

[178] Y. Han, Y. Guo, B. Gao, C. Ma, R. Zhang, and H. Zhang, "Generation, optimization, and application of ultrashort femtosecond pulse in mode-locked fiber lasers," *Progress in Quantum Electronics*, vol. 71, p. 100264, May 2020, doi: 10.1016/j.pquantelec.2020.100264.

[179] X. Cheng, D. S. Gunawardena, C.-F. J. Pun, J. Bonefacino, and H.-Y. Tam, "Single nanosecond-pulse production of polymeric fiber Bragg gratings for biomedical applications," *Opt. Express, OE*, vol. 28, no. 22, pp. 33573–33583, Oct. 2020, doi: 10.1364/OE.408744.

[180] Y. Shimizu, L.-C. Chen, D. W. Kim, X. Chen, X. Li, and H. Matsukuma, "An insight into optical metrology in manufacturing," *Meas. Sci. Technol.*, vol. 32, no. 4, p. 042003, Feb. 2021, doi: 10.1088/1361-6501/abc578.

[181] J. He *et al.*, "Femtosecond laser line-by-line inscription of apodized fiber Bragg gratings," *Opt. Lett., OL*, vol. 46, no. 22, pp. 5663–5666, Nov. 2021, doi: 10.1364/OL.441888.

[182] W. Zhang *et al.*, "Review of pulse compression gratings for chirped pulse amplification system," *OE*, vol. 60, no. 2, p. 020902, Feb. 2021, doi: 10.1117/1.OE.60.2.020902.

[183] F. Köttig, D. Schade, J. R. Koehler, P. S. J. Russell, and F. Tani, "Efficient single-cycle pulse compression of an ytterbium fiber laser at 10 MHz repetition rate," *Opt. Express, OE*, vol. 28, no. 7, pp. 9099–9110, Mar. 2020, doi: 10.1364/OE.389137.

[184] V. Ginzburg *et al.*, "11 fs, 1.5 PW laser with nonlinear pulse compression," *Opt. Express, OE*, vol. 29, no. 18, pp. 28297–28306, Aug. 2021, doi: 10.1364/OE.434216.

[185] L. R. Chen, P. Moslemi, Z. Wang, M. Ma, and R. Adams, "Integrated Microwave Photonics for Spectral Analysis, Waveform Generation, and Filtering," *IEEE Photonics Technology Letters*, vol. 30, no. 21, pp. 1838–1841, Nov. 2018, doi: 10.1109/LPT.2018.2861703.

[186] L. R. Cortés, D. Onori, H. G. de Chatellus, M. Burla, and J. Azaña, "Towards on-chip photonic-assisted radio-frequency spectral measurement and monitoring," *Optica, OPTICA*, vol. 7, no. 5, pp. 434–447, May 2020, doi: 10.1364/OPTICA.383247.

[187] X. Zou, B. Lu, W. Pan, L. Yan, A. Stöhr, and J. Yao, "Photonics for microwave measurements," *Laser & Photonics Reviews*, vol. 10, no. 5, pp. 711–734, 2016, doi: 10.1002/lpor.201600019.

[188] P. G. Stoica, R. Moses, P. Stoica, and R. L. Moses, *Spectral analysis of signals*. Upper Saddle River, NJ: Pearson, Prentice Hall, 2005.

[189] P. Zuo, D. Ma, and Y. Chen, “Short-Time Fourier Transform Based on Stimulated Brillouin Scattering,” *Journal of Lightwave Technology*, vol. 40, no. 15, pp. 5052–5061, Aug. 2022, doi: 10.1109/JLT.2022.3174552.

[190] C. Zhang, J. Xu, P. C. Chui, and K. K. Y. Wong, “Parametric spectro-temporal analyzer (PASTA) for real-time optical spectrum observation,” *Sci Rep*, vol. 3, no. 1, p. 2064, Jun. 2013, doi: 10.1038/srep02064.

[191] S. R. Konatham *et al.*, “Real-time gap-free dynamic waveform spectral analysis with nanosecond resolutions through analog signal processing,” *Nat Commun*, vol. 11, no. 1, p. 3309, Jul. 2020, doi: 10.1038/s41467-020-17119-2.

[192] B. Crockett, M. L. Connor Rowe, and J. Azaña, “Real-time spectral characterization of THz-bandwidth waveforms by unwrapping a time-lens spectrogram,” in *2023 Photonics North (PN)*, Jun. 2023, pp. 1–2. doi: 10.1109/PN58661.2023.10223063.

[193] X. Xie, J. Li, F. Yin, K. Xu, and Y. Dai, “STFT Based on Bandwidth-Scaled Microwave Photonics,” *J. Lightwave Technol., JLT*, vol. 39, no. 6, pp. 1680–1687, Mar. 2021.

[194] B. Crockett, L. R. Cortés, R. Maram, and J. Azaña, “Optical signal denoising through temporal passive amplification,” *Optica, OPTICA*, vol. 9, no. 1, pp. 130–138, Jan. 2022, doi: 10.1364/OPTICA.428727.

[195] J. Huh and J. Azana, “All-Optical Reconfigurable Signal Processing Based on Cross Phase Modulation Time Lensing,” *IEEE Photon. Technol. Lett.*, vol. 29, no. 10, pp. 826–829, May 2017, doi: 10.1109/LPT.2017.2687826.

[196] H. Guillet De Chatellus, L. R. Cortés, and J. Azaña, “Optical real-time Fourier transformation with kilohertz resolutions,” *Optica*, vol. 3, no. 1, p. 1, Jan. 2016, doi: 10.1364/OPTICA.3.000001.

[197] A. Mahjoubfar, D. V. Churkin, S. Barland, N. Broderick, S. K. Turitsyn, and B. Jalali, “Time stretch and its applications,” *Nature Photon*, vol. 11, no. 6, pp. 341–351, Jun. 2017, doi: 10.1038/nphoton.2017.76.

[198] H. Huang *et al.*, “Experimental observation of the spectral self-imaging effect with a four-wave mixing time lens,” *Opt. Lett., OL*, vol. 48, no. 6, pp. 1522–1525, Mar. 2023, doi: 10.1364/OL.485428.

[199] J. Azaña and X. Zhu, “Optical Time-Mapped Spectrograms (I): From the Time-Lens Fourier Transformer to the Talbot-Based Design,” *Journal of Lightwave Technology*, vol. 41, no. 14, pp. 4609–4623, Jul. 2023, doi: 10.1109/JLT.2023.3243531.

[200] L. Romero Cortés, R. Maram, H. Guillet de Chatellus, and J. Azaña, “Arbitrary Energy-Preserving Control of Optical Pulse Trains and Frequency Combs through Generalized Talbot Effects,” *Laser & Photonics Reviews*, vol. 13, no. 12, p. 1900176, 2019, doi: 10.1002/lpor.201900176.

[201] J. Azaña, X. Zhu, C. Rowe, and B. Crockett, “Optical Time-Mapped Spectrograms (II): Fractional Talbot Designs,” *J. Light. Technol.*, pp. 1–12, 2023, doi: 10.1109/JLT.2023.3260706.

[202] A. V. Oppenheim, A. S. Willsky, and S. H. Nawab, *Signals & Systems*. Pearson Educación, 1997.

[203] C. R. Fernández-Pousa, R. Maram, and J. Azaña, “CW-to-pulse conversion using temporal Talbot array illuminators,” *Opt. Lett., OL*, vol. 42, no. 13, pp. 2427–2430, Jul. 2017, doi: 10.1364/OL.42.002427.

[204] B. E. A. Saleh and M. C. Teich, *Fundamentals of Photonics*. John Wiley & Sons, 2019.

[205] S. Fu *et al.*, “Review of recent progress on single-frequency fiber lasers [Invited],” *J. Opt. Soc. Am. B, JOSAB*, vol. 34, no. 3, pp. A49–A62, Mar. 2017, doi: 10.1364/JOSAB.34.000A49.

[206] G. P. Agrawal, “Nonlinear Fiber Optics,” in *Nonlinear Science at the Dawn of the 21st Century*, vol. 542, P. L. Christiansen, M. P. Sørensen, and A. C. Scott, Eds., in Lecture Notes in Physics, vol. 542. , Berlin, Heidelberg: Springer Berlin Heidelberg, 2000, pp. 195–211. doi: 10.1007/3-540-46629-0_9.

[207] L. Grüner-Nielsen *et al.*, “Dispersion-Compensating Fibers,” *J. Lightwave Technol., JLT*, vol. 23, no. 11, p. 3566, Nov. 2005.

[208] J. Azana and M. A. Muriel, “Real-time optical spectrum analysis based on the time-space duality in chirped fiber gratings,” *IEEE Journal of Quantum Electronics*, vol. 36, no. 5, pp. 517–526, May 2000, doi: 10.1109/3.842092.

[209] M. L. Farwell, W. S. C. Chang, and D. R. Huber, “Increased linear dynamic range by low biasing the Mach-Zehnder modulator,” *IEEE Photonics Technology Letters*, vol. 5, no. 7, pp. 779–782, Jul. 1993, doi: 10.1109/68.229804.

[210] X. Wang, P. O. Weigel, J. Zhao, M. Ruesing, and S. Mookherjea, “Achieving beyond-100-GHz large-signal modulation bandwidth in hybrid silicon photonics Mach Zehnder modulators using thin film lithium niobate,” *APL Photonics*, vol. 4, no. 9, p. 096101, Sep. 2019, doi: 10.1063/1.5115243.

[211] Y. Ogiso, Y. Tsuchiya, S. Shinada, S. Nakajima, T. Kawanishi, and H. Nakajima, “High Extinction-Ratio Integrated Mach–Zehnder Modulator With Active Y-Branch for Optical SSB Signal Generation,” *IEEE Photonics Technology Letters*, vol. 22, no. 12, pp. 941–943, Jun. 2010, doi: 10.1109/LPT.2010.2047854.

[212] E. M. Gallo *et al.*, “Picosecond response times in GaAs/AlGaAs core/shell nanowire-based photodetectors,” *Applied Physics Letters*, vol. 98, no. 24, p. 241113, Jun. 2011, doi: 10.1063/1.3600061.

[213] “Timing jitter and phase noise of mode-locked fiber lasers.” Accessed: Mar. 25, 2024. [Online]. Available: https://opg.optica.org/oe/fulltext.cfm?uri=oe-18-5-5041&id=196138

[214] C.-T. Lin, J. (Jyehong) Chen, S.-P. Dai, P.-C. Peng, and S. Chi, “Impact of Nonlinear Transfer Function and Imperfect Splitting Ratio of MZM on Optical Up-Conversion Employing Double Sideband With Carrier Suppression Modulation,” *J. Lightwave Technol., JLT*, vol. 26, no. 15, pp. 2449–2459, Aug. 2008.

[215] M. Burla *et al.*, “500 GHz plasmonic Mach-Zehnder modulator enabling sub-THz microwave photonics,” *APL Photonics*, vol. 4, no. 5, p. 056106, May 2019, doi: 10.1063/1.5086868.

[216] “RSA7100B.” Accessed: Jun. 22, 2024. [Online]. Available: https://www.tek.com/en/datasheet/rsa7100b-rsa7100b-spectrum-analyzer-datasheet

[217] F. Khan and M. I. Younis, “RF MEMS electrostatically actuated tunable capacitors and their applications: a review,” *J. Micromech. Microeng.*, vol. 32, no. 1, p. 013002, Dec. 2021, doi: 10.1088/1361-6439/ac3cd5.

[218] K. Song, W. Chen, S. R. Patience, Y. Chen, A. M. Iman, and Y. Fan, “Compact Wide-Frequency Tunable Filter With Switchable Bandpass and Bandstop Frequency Response,” *IEEE Access*, vol. 7, pp. 47503–47508, 2019, doi: 10.1109/ACCESS.2019.2908453.

[219] D. Pérez-López, A. López, P. DasMahapatra, and J. Capmany, “Multipurpose self-configuration of programmable photonic circuits,” *Nat. Commun.*, vol. 11, no. 1, Art. no. 1, Dec. 2020, doi: 10.1038/s41467-020-19608-w.

[220] D. Ma and Y. Chen, “Time-varying microwave photonic filter for arbitrary waveform signal-to-noise ratio improvement,” *Opt. Lett., OL*, vol. 47, no. 9, pp. 2186–2189, May 2022, doi: 10.1364/OL.455019.

[221] D. Pérez-López, A. López, P. DasMahapatra, and J. Capmany, “Multipurpose self-configuration of programmable photonic circuits,” *Nat Commun*, vol. 11, no. 1, Art. no. 1, Dec. 2020, doi: 10.1038/s41467-020-19608-w.

[222] S. R. Konatham, B. Crockett, L. R. Cortés, and J. Azaña, “On-the-fly continuous time varying frequency filtering of broadband microwave signals,” in *45th European Conference on Optical Communication (ECOC 2019)*, Sep. 2019, pp. 1–4. doi: 10.1049/cp.2019.0837.

[223] S. R. Konatham *et al.*, “Real-time gap-free dynamic waveform spectral analysis with nanosecond resolutions through analog signal processing,” *Nat. Commun.*, vol. 11, no. 1, Art. no. 1, Jul. 2020, doi: 10.1038/s41467-020-17119-2.

[224] X. Zhu, B. Crockett, C. M. L. Rowe, and J. Azaña, “Photonics-enabled Nanosecond Scale Real-time Spectral Analysis with 92-GHz Bandwidth and MHz resolution,” in *2023 Optical Fiber Communication Conference (OFC)*, Optica Publishing Group, Mar. 2023, p. M1J.5. doi: 10.1364/OFC.2023.M1J.5.

[225] X. Zhu, B. Crockett, C. M. L. Rowe, H. Sun, and J. Azaña, “Agile Manipulation of the Time-Frequency Distribution of High-Speed Electromagnetic Waves,” *Nature Communications*, 2024.

[226] M. P. Fernandez, S. Kaushal, B. Crockett, L. A. Bulus-Rossini, P. A. Costanzo-Caso, and J. Azaña, “An Ultra-Fast Temporal Talbot Array Illuminator,” *J. Light. Technol.*, pp. 1–9, 2023, doi: 10.1109/JLT.2023.3247168.

[227] S. Kaushal, A. Aadhi, A. Roberge, R. Morandotti, R. Kashyap, and J. Azaña, “All-fibre phase filters with 1-GHz resolution for high-speed passive optical logic processing,” *Nat. Commun.*, vol. 14, no. 1, Art. no. 1, Mar. 2023, doi: 10.1038/s41467-023-37472-2.

[228] “On the Anti-Interference Tolerance of Cognitive Frequency Hopping Communication Systems | IEEE Journals & Magazine | IEEE Xplore.” Accessed: Aug. 05, 2024. [Online]. Available: https://ieeexplore.ieee.org/abstract/document/9149671

[229] B. H. M and K. A. Gupta, “Wideband Digital Channelizer based on Spectrum Sensing,” in *2020 Third International Conference on Advances in Electronics, Computers and Communications (ICAECC)*, Dec. 2020, pp. 1–6. doi: 10.1109/ICAECC50550.2020.9339512.

[230] H.-J. Kim, D. E. Leaird, and A. M. Weiner, “Rapidly Tunable Dual-Comb RF Photonic Filter for Ultrabroadband RF Spread Spectrum Applications,” *IEEE Transactions on Microwave Theory and Techniques*, vol. 64, no. 10, pp. 3351–3362, Oct. 2016, doi: 10.1109/TMTT.2016.2599162.

[231] M. Jiang, G. Liao, Z. Yang, Y. Liu, and Y. Chen, "Tunable Filter Design for Integrated Radar and Communication Waveforms," *IEEE Communications Letters*, vol. 25, no. 2, pp. 570–573, Feb. 2021, doi: 10.1109/LCOMM.2020.3033119.

[232] S. Wei, M. Zhang, G. Wang, X. Sun, L. Zhang, and D. Chen, "Robust Multi-Frame Joint Frequency Hopping Radar Waveform Parameters Estimation Under Low Signal-Noise-Ratio," *IEEE Access*, vol. 7, pp. 177198–177210, 2019, doi: 10.1109/ACCESS.2019.2936418.

[233] K. Wu, J. A. Zhang, X. Huang, and Y. J. Guo, "Frequency-Hopping MIMO Radar-Based Communications: An Overview," *IEEE Aerospace and Electronic Systems Magazine*, vol. 37, no. 4, pp. 42–54, Apr. 2022, doi: 10.1109/MAES.2021.3081176.

[234] Y. Zhao *et al.*, "Repetition rate multiplication control of micro-combs assisted by perfect temporal Talbot effect," *APL Photonics*, vol. 5, no. 4, p. 046102, Apr. 2020, doi: 10.1063/1.5139599.

[235] M. P. Fernández *et al.*, "Nonlinear time-lens with improved power efficiency through a discrete multilevel pump," *Opt. Lett., OL*, vol. 45, no. 13, pp. 3557–3560, Jul. 2020, doi: 10.1364/OL.396342.

[236] "All-Optical Parametric-Assisted Oversampling and Decimation for Signal Denoising Amplification - Fernandez - 2023 - Laser & Photonics Reviews - Wiley Online Library." Accessed: Jun. 29, 2024. [Online]. Available: https://onlinelibrary.wiley.com/doi/full/10.1002/lpor.202200711

[237] M. P. Fernández, S. Kaushal, B. Crockett, L. A. Bulus-Rossini, P. A. Costanzo-Caso, and J. Azaña, "Combined parametric and denoising passive amplification by FWM-based oversampling and Talbot-based decimation," in *2023 Optical Fiber Communications Conference and Exhibition (OFC)*, Mar. 2023, pp. 1–3. doi: 10.1364/OFC.2023.M1J.7.